

Remote Sensing and Modeling of Atmospheric Dust and Studying Its Impact on Environment, Weather, and Climate

Guest Editors: Hesham El-Askary, Seon K. Park, Slobodan Nickovic, and Mian Chin





Remote Sensing and Modeling of Atmospheric Dust and Studying Its Impact on Environment, Weather, and Climate

Advances in Meteorology

Remote Sensing and Modeling of Atmospheric Dust and Studying Its Impact on Environment, Weather, and Climate

Guest Editors: Hesham El-Askary, Seon K. Park,
Slobodan Nickovic, and Mian Chin



Copyright © 2015 Hindawi Publishing Corporation. All rights reserved.

This is a special issue published in “Advances in Meteorology.” All articles are open access articles distributed under the Creative Commons Attribution License, which permits unrestricted use, distribution, and reproduction in any medium, provided the original work is properly cited.

Editorial Board

José Antonio Adame, Spain
Cesar Azorin-Molina, Spain
Guillermo Baigorria, USA
Marina Baldi, Italy
Abderrahim Bentamy, France
Massimo A. Bollasina, UK
Stefania Bonafoni, Italy
Isabella Bordi, Italy
Alex Cannon, Canada
Claudio Carbone, Italy
Dominique Carrer, France
Charles Chemel, UK
Annalisa Cherchi, Italy
James Cleverly, Australia
Jill S. M. Coleman, USA
Gabriele Curci, Italy
Mladjen Ćurić, Serbia
Klaus Dethloff, Germany
Panuganti C. S. Devara, India
Julio Diaz, Spain
Arona Diedhiou, France
Stefano Dietrich, Italy
Eugenio Domínguez Vilches, Spain
Antonio Donateo, Italy
Igor Esau, Norway
Stefano Federico, Italy
Enrico Ferrero, Italy
Rossella Ferretti, Italy
Roberto Fraile, Spain
Charmaine Franklin, Australia
Jan Friesen, Germany

María Ángeles García, Spain
Herminia García Mozo, Spain
Eduardo García-Ortega, Spain
Luis Gimeno, Spain
Jorge E. Gonzalez, USA
Ismail Gultepe, Canada
Rafiq Hamdi, Belgium
Adel Hanna, USA
Hiroyuki Hashiguchi, Japan
Tareq Hussein, Jordan
Bradley G. Illston, USA
Ivar S A Isaksen, Norway
Yasunobu Iwasaka, Japan
Pedro Jiménez-Guerrero, Spain
Kuruvilla John, USA
Charles Jones, USA
Hann-Ming H. Juang, USA
George Kallos, Greece
Harry D. Kambezidis, Greece
Nir Y. Krakauer, USA
Simon O. Krichak, Israel
Hisayuki Kubota, Japan
Haim Kutiel, Israel
Richard Leaitch, Canada
Monique Leclerc, USA
Ilan Levy, Israel
Gwo-Fong Lin, Taiwan
Anthony R. Lupo, USA
Paolo Madonia, Italy
Andreas Matzarakis, Germany
Samantha Melani, Italy
Nicholas Meskhidze, USA

Christophe Messenger, France
Mario Marcello Miglietta, Italy
Takashi Mochizuki, Japan
Andrea Montani, Italy
Goro Mouri, Japan
Brian R. Nelson, USA
Efthymios I. Nikolopoulos, USA
Sandip Pal, USA
Giulia Panegrossi, Italy
Giulia Pavese, Italy
Kyaw T. Paw, USA
Olivier P. Prat, USA
Sara C. Pryor, USA
Philippe Ricaud, France
Tomeu Rigo, Spain
Filomena Romano, Italy
Jose Antonio Ruiz-Arias, Spain
Haydee Salmun, USA
Pedro Salvador, Spain
Arturo Sanchez-Lorenzo, Spain
Andres Schmidt, USA
Shraddhanand Shukla, USA
Fiona Smith, UK
Francisco J. Tapiador, Spain
Yoshihiro Tomikawa, Japan
Tomoo Ushio, Japan
R. Van Der Velde, The Netherlands
Sergio M. Vicente-Serrano, Spain
Francesco Viola, Italy
Alastair Williams, Australia
Olga Zolina, France

Contents

Remote Sensing and Modeling of Atmospheric Dust and Studying Its Impact on Environment, Weather, and Climate, Hesham El-Askary, Seon K. Park, Slobodan Nickovic, and Mian Chin
Volume 2015, Article ID 854968, 2 pages

Investigation of Three-Dimensional Evolution of East Asian Dust Storm by Modeling and Remote Sensing Measurements, Jiawei Li and Zhiwei Han
Volume 2015, Article ID 483476, 12 pages

Study of Aerosols' Characteristics and Dynamics over the Kingdom of Saudi Arabia Using a Multisensor Approach Combined with Ground Observations, Ashraf Farahat, Hesham El-Askary, and Abdulaziz Al-Shaibani
Volume 2015, Article ID 247531, 12 pages

Studying Air Pollutants Origin and Associated Meteorological Parameters over Seoul from 2000 to 2009, Sunmin Park, Hesham El-Askary, Ismail Sabbah, Hanbin Kwak, Anup K. Prasad, Woo-Kyun Lee, and Menas Kafatos
Volume 2015, Article ID 704178, 12 pages

Origin and Distribution of PAHs in Ambient Particulate Samples at High Mountain Region in Southern China, Peng-hui Li, Yan Wang, Yu-hua Li, Hong-li Li, and Xianliang Yi
Volume 2015, Article ID 245438, 8 pages

Atmospheric Error Correction of the Laser Beam Ranging, J. Saydi, A. Lotfalian, M. Abedi, J. Khalilzadeh, and H. Saghafifar
Volume 2014, Article ID 294741, 6 pages

Dust Identification over Arid and Semiarid Regions of Asia Using AIRS Thermal Infrared Channels, Hui Xu, Tianhai Cheng, Donghai Xie, Jiaguo Li, Yu Wu, and Hao Chen
Volume 2014, Article ID 847432, 16 pages

Source Allocation of Long-Range Asian Dusts Transportation across the Taiwan Strait by Innovative Chemical-Assisted Identification Methods, Yi-Hsiu Jen, Yi-Chi Liu, Iau-Ren Ie, Chung-Shin Yuan, and Chung-Hsuang Hung
Volume 2014, Article ID 268037, 10 pages

Ground-Based Polarimetric Remote Sensing of Dust Aerosol Properties in Chinese Deserts near Hexi Corridor, Hua Xu, Zhengqiang Li, Donghui Li, Li Li, Xingfeng Chen, Yisong Xie, Kaitao Li, Cheng Chen, and Yuhuan Zhang
Volume 2014, Article ID 240452, 10 pages

Editorial

Remote Sensing and Modeling of Atmospheric Dust and Studying Its Impact on Environment, Weather, and Climate

Hesham El-Askary,^{1,2,3} Seon K. Park,^{4,5,6,7} Slobodan Nickovic,^{8,9,10} and Mian Chin¹¹

¹ Schmid College of Science and Technology, Chapman University, Orange, CA 92866, USA

² Center of Excellence in Earth Observing, Chapman University, Orange, CA 92866, USA

³ Department of Environmental Sciences, Alexandria University, Moharam Bek, Alexandria 21522, Egypt

⁴ Department of Environmental Science and Engineering, Ewha Womans University, Seoul 120-750, Republic of Korea

⁵ Department of Atmospheric Science and Engineering, Ewha Womans University, Seoul 120-750, Republic of Korea

⁶ Severe Storm Research Center, Ewha Womans University, Seoul 120-750, Republic of Korea

⁷ Center for Climate/Environment Change Prediction Research, Ewha Womans University, Seoul 120-750, Republic of Korea

⁸ Institute for Atmospheric Physics, The University of Arizona, Tucson, AZ 85721, USA

⁹ South East European Virtual Climate Change Center, Republic Hydrometeorological Service, Kneza Viseslava 66, 11000 Belgrade, Serbia

¹⁰ Institute of Physics, 11080 Belgrade, Serbia

¹¹ Atmospheric Chemistry and Dynamics Laboratory, NASA Goddard Space Flight Center, Code 614, Greenbelt, MD 20771, USA

Correspondence should be addressed to Hesham El-Askary; elaskary@chapman.edu

Received 23 June 2015; Accepted 23 June 2015

Copyright © 2015 Hesham El-Askary et al. This is an open access article distributed under the Creative Commons Attribution License, which permits unrestricted use, distribution, and reproduction in any medium, provided the original work is properly cited.

Aerosols have been regarded as one of the major constituents of the atmosphere and have a wide range of impacts at different levels, scales, and sectors. Remote sensing and modeling of the atmospheric dust storms, supported by ground observations, are critical in analyzing, characterizing, and assessing many impacts in terms of dust mineralogical composition, interaction with clouds and radiation, optical and chemical characteristics, major sources of emission, mix-up with anthropogenic, sea-salt, and biomass aerosols during long range transport, and deposition. Studies of dust storms and their impact on the local and regional environment and climate, using space observations (Moderate Resolution Imaging Spectroradiometer (MODIS), Atmospheric Infrared Sounder (AIRS), Multiangle Imaging Spectroradiometer (MISR), Cloud-Aerosol Lidar and Infrared Pathfinder Satellite Observation (CALIPSO), Polarization and Anisotropy of Reflectances for Atmospheric Science coupled with Observations from a Lidar (PARASOL), Scanning Imaging Absorption spectrometer for Atmospheric Chartography (SCIAMACHY), Ozone Monitoring Instrument (OMI), etc.), ground measurements (Aerosol Robotic Network (AERONET), sky

radiometers, sunphotometer, lidar systems, and chemical analysis), and modeling (SKIRON, Dust Regional Atmospheric Model (DREAM), Navy Aerosol Analysis and Prediction System (NAAPS), etc.), have addressed some of these issues. The studies included in this special issue are mainly concerned with ground-based, satellite observations and modeling of aerosol related events of natural or anthropogenic origin over climatically sensitive areas influenced by dust storms, such as Korea, China, and Saudi Arabia.

S. K. Park et al. investigated the temporal characteristics of major air pollutants collected from 44 air quality stations over the city of Seoul, Korea, namely, nitrogen dioxide, carbon monoxide, particular matter at 10 microns, and sulfur dioxide (SO₂), between 2000 and 2009. Ground data were correlated with satellite based observations collected from Moderate Resolution Imaging Spectroradiometer as well as the AERONET ground stations. They showed that anthropogenic aerosols are dominant in the summer season even though the concentration was lower than the other seasons which can be attributed to natural and anthropogenic sources, as well as changing meteorological factor.

P. Li et al. studied the origin and distribution of polycyclic aromatic hydrocarbons (PAHs) originating from natural and/or anthropogenic sources in ambient particulate samples at high mountain region in southern China to understand their deposition and transport. Local meteorology including atmospheric pressure, relative humidity, and ambient temperature with backward trajectory analysis suggested that particulate samples measured at the Mount Heng region were predominantly associated with the air masses from southern China. They found out that vehicular emission, coal combustion, industry emission, and unburned fossil fuels were suggested to be the PAHs sources at Mount Heng site.

A. Farahat et al. covered aerosol distribution and characteristics using satellite based observations over four regions in Saudi Arabia using satellite and ground observations for the period April 2003–January 2013. The study includes cities in the north western, western, and eastern provinces of Saudi Arabia and in the Rub' al Khali desert or Empty Quarter. Satellite and ground observations showed that the dust season extends from April to August with prominent peaks yet with high anthropogenic contribution in late summer and early fall. Analysis shows an increase in the aerosol concentration during March 2009 which could be attributed to a major dust storm during that time.

J. Li and Z. Han shed the light on the three-dimensional evolution of an East Asian dust storm during 23–26 April 2009 by utilizing a Regional Air Quality Model System (RAQMS) and satellite measurements. Modeled spatial distributions of Aerosols Optical Depth (AOD) and vertical profiles of aerosol extinction coefficient during the dust storm were compared with MODIS and CALIPSO data, demonstrating that RAQMS was able to reproduce the 3D structure and the evolution of the dust storm reasonably well.

Y.-H. Jen et al. allocated sources of the long range transport of Asian dust across Taiwan using innovative chemical-assisted identification techniques. They combined chemical composition with the enrichment factor and the grey relational analysis to identify the potential sources of eighteen different Asian dust storms. Back trajectory analysis highlighted the source soils to be from Inner Mongolia with a high similarity with the outputs obtained from the chemical based techniques.

H. Xu et al. studied dust aerosol properties near Hexi Corridor in the Chinese deserts using polarimetric measurements from a ground-based sunphotometer. They found out that the partial occurrence of calcite or hematite in the soil of Minqin or the influence of anthropogenic aerosols containing carbon affected aerosol characteristics as evident from the aerosol optical properties, angstrom exponent, and the single scattering albedo.

H. Xu et al. used thermal observations of AIRS in conjunction with visible observations of MODIS and Cloud-Aerosol Lidar with Orthogonal Polarization (CALIOP) for dust identification over the arid and semiarid regions of Asia. This is owed to the fact that dust generated in northern China exerts significant influences on regional air quality, weather, and climate.

J. Saydi et al. tackled the issue of increasing the laser ranging accuracy by ray tracing using atmospheric models

based on surface measurements of pressure, temperature, and relative humidity. They studied the atmospheric effects on the laser beam by using the principles of laser ranging and performing atmospheric corrections for 0.532, 1.3, and 10.6 microns through the weather conditions of Tehran, Isfahan, and Bushehr in Iran. They found that the laser ranging error decreased by increasing the laser emission angle.

Hesham El-Askary
Seon K. Park
Slobodan Nickovic
Mian Chin

Research Article

Investigation of Three-Dimensional Evolution of East Asian Dust Storm by Modeling and Remote Sensing Measurements

Jiawei Li and Zhiwei Han

Key Laboratory of Regional Climate-Environment for Temperate East Asia (RCE-TEA), Institute of Atmospheric Physics (IAP), Chinese Academy of Sciences (CAS), Beijing 100029, China

Correspondence should be addressed to Zhiwei Han; hzw@mail.iap.ac.cn

Received 3 June 2014; Accepted 16 September 2014

Academic Editor: Hesham El-Askary

Copyright © 2015 J. Li and Z. Han. This is an open access article distributed under the Creative Commons Attribution License, which permits unrestricted use, distribution, and reproduction in any medium, provided the original work is properly cited.

The three-dimensional evolution of an East Asian dust storm during 23–26 April 2009 was investigated by utilizing a regional air quality model system (RAQMS) and satellite measurements. This severe dust storm hit Mt. Tai in east China with daily mean PM_{10} concentration reaching $1400 \mu\text{g}/\text{m}^3$ and the model captured the PM_{10} variation reasonably well. Modeled spatial distributions of AOD and vertical profiles of aerosol extinction coefficient during the dust storm were compared with MODIS and CALIPSO data, demonstrating that RAQMS was able to reproduce the 3D structure and the evolution of the dust storm reasonably well. During early days of the dust storm, daily mean dust-induced AOD exceeded 2.0 over dust source regions (the Gobi desert and the Taklamakan desert) and was in a range of 1.2–1.8 over the North China Plain, accounting for about 98% and up to 90% of total AOD over corresponding areas, respectively. The top of the dust storm reached about 8 km over east China, with high dust concentration locating at around 40°N . Dust aerosol below 2 km was transported southeastward off the Gobi desert while dust above 2 km was transported out of China along 40° – 45°N .

1. Introduction

Dust aerosol is one of the most important aerosol components because it is a major contributor to global atmospheric aerosol loading and optical thickness. Recent estimates of its global source strength range from 1000 to 5000 Mt/year with highly varied spatial-temporal distribution [1]. When surface wind speeds are strong enough, dust particles are injected into the atmosphere from source regions and then subjected to long-range transport [2–6], degrading air quality and even disturbing regional climate. For example, Huang et al. found that dust aerosol can heat the air over Taklamakan desert by a maximum of 5 K/day in summertime [7]; Lau et al. found that dust can be a cause of East Asian monsoon anomaly [8].

East Asia is one of the major dust source regions in the world. There are two major sources, namely, the Taklamakan desert in west China and the Gobi desert across south Mongolia and north China. Dust storms are most active in springtime [3, 4]. Severe dust storms not only exert significant impacts on East Asia itself but also can reach as far as the west coast of North America [9]. Several methods have been

used to understand the evolution and the impact of East Asian dust storm on atmospheric environment and climate. In situ sampling (e.g., [4, 10]) and remote sensing by ground-based lidar (e.g., [11]) and by satellite (e.g., [9]) are primary methods in understanding sources, optical properties, compositions, and spatial distributions of dust storm. Since 2006, a new instrument, the space-based two-wavelength, polarization-sensitive backscatter lidar, the Cloud-Aerosol Lidar with Orthogonal Polarization (CALIOP) on board the Cloud-Aerosol Lidar and Infrared Pathfinder Satellite Observations (CALIPSO) satellite began to provide continuous global measurements of aerosol vertical distribution with high spatial resolution [12]. This instrument provides a top-down view to investigate the vertical structure of aerosols including dust. Based on CALIPSO measurements, some studies have investigated vertical characteristics and spatial-temporal variation of dust storms (e.g., [13, 14]). Numerical model is another important scientific tool in understanding dust related problems because it is able to represent and interpret the complex processes and mechanisms of dust evolution. A number of dust models have been established and applied

to investigate dust's generation, long-range transport, climate effects, and perturbation to atmospheric chemistry in East Asia (e.g., [5, 6, 15–17]).

In this paper, we studied the three-dimensional structure and evolution of dust storm over East Asia in April 2009 by utilizing a regional air quality model system (RAQMS), mainly focusing on the dust storm period during 23–26 April. In situ observations at the summit of the Mt. Tai (locating in east China), satellite retrievals of aerosol optical depth (AOD), and space-based lidar measurements are collected and used to verify model simulations and investigate the transport process of the dust storm. Spatial distributions of dust aerosol and dust-induced AOD, as well as vertical distribution of dust extinction coefficient during the dust storm period, were further discussed.

2. Model Description

The regional air quality model system (RAQMS) is a three-dimensional Eulerian model constructed on a terrain-following spherical coordinate system. The model contains a series of key processes related to atmospheric pollutants including emission, advection, diffusion, multiphase chemistry, dry deposition, and wet scavenge [6, 17]. The SAPRC99 (Statewide Air Pollution Research Center) mechanism proposed by Carter [18] was applied to account for gas phase chemistry. The ISORROPIA II model had been embedded into RAQMS to represent the thermodynamic equilibrium processes among inorganic aerosols [19]. A bulk yield scheme was used to deal with the formation of secondary organic aerosol (SOA) [20]. Heterogeneous reactions between dust aerosol and gases had also been considered [21]. Inorganic and carbonaceous aerosols were assumed to fit the log-normal distribution and settle in fine mode. Soil dust and sea salt aerosols were represented by a sized-segregated submodule including key processes for dust and sea salt such as generation, dry deposition, and wet scavenging, in which dust was divided into 10 size bins ranging from $0.43\ \mu\text{m}$ to $42\ \mu\text{m}$ and sea salt was divided into 8 size bins ranging from $0.43\ \mu\text{m}$ to $17.5\ \mu\text{m}$ [6]. Dry deposition of gaseous species was parameterized based on the method of Walmsley and Wesely [22] except gas phase sulfate whose dry deposition velocities was calculated by the approach of Walcek et al. [23]. Dry deposition velocities of aerosols were calculated as the inverse of total resistances plus the gravitational settling term [6]. The subgrid cloud mixing, scavenging of gas species, and aqueous chemistry were similar to those used in the second-generation regional acid deposition model [24]. Below-cloud scavenging of aerosols between cloud base and ground surface was parameterized based on an expression of scavenging rate that is a function of precipitation rate and collision efficiency of particle by hydrometeor [6]. Inorganic aerosols were treated as internally mixed, whereas black carbon, organic carbon, dust, and sea salt were treated as externally mixed with inorganic components. The kappa parameterization [25] was adopted to account for the hygroscopic growth of aerosol diameter. Aerosol optical properties such as extinction, single scattering albedo, and asymmetry

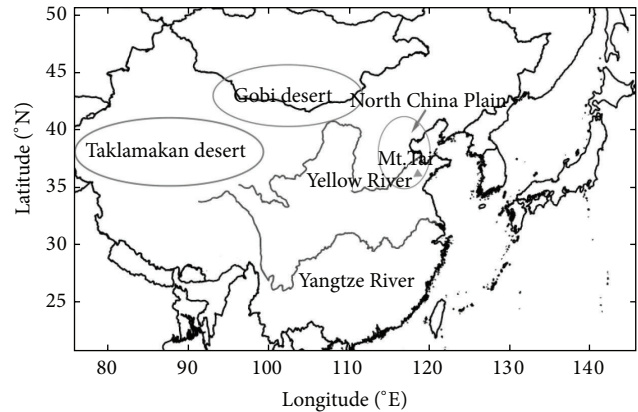


FIGURE 1: Model domain, location of Mt. Tai, and major landmarks.

factor were calculated by a Mie-theory-based method [26]. The RAQMS model had already been facilitated in a number of studies concerning regional environmental problems in East Asia such as tropospheric ozone, acid deposition, and dust storm [6, 17, 27].

In this work the RAQMS was facilitated with a horizontal resolution of $0.5^\circ \times 0.5^\circ$. Twelve vertical layers stretch unequally from ground to about 10 km (the intermediate heights of each layer are about 50 m, 150 m, 300 m, 500 m, 750 m, 1500 m, 2500 m, 3500 m, 4500 m, 6000 m, 7500 m, and 8950 m). The model domain covers most areas of East Asia including most China, the Korean Peninsula, Japan, Mongolia, and the West Pacific, ranging between 75°E to 145°E and 20°N to 50°N (Figure 1).

Monthly varied anthropogenic emission inventories for CO (carbon monoxide), NO_x (nitrogen oxides), SO_2 (sulfur dioxide), BC (black carbon), POC (primary organic carbon), NMVOCs (non-methane volatile organic compounds), and primary particulate matters (emitted from industry, construction, exposed surface, etc.) were obtained from MEIC (Multi-resolution Emission Inventory for China) model provided by Tsinghua University (<http://meicmodel.org>) for China and from US NASA's (National Aeronautics and Space Administration) INTEX-B (Intercontinental Chemical Transport Experiment-Phase B) project [28] for the rest of the domain. The MEIC inventory was used to represent emission condition in 2009, and the INTEX-B inventory was based on the year 2006. Monthly biomass burning emissions were obtained from the Global Fire Emission Database version 3.1 based on the year 2009 [29].

The nonhydrostatic, fifth-generation mesoscale model (MM5) was applied to provide meteorological fields of wind, temperature, humidity, and other parameters to drive RAQMS. Four-dimensional data assimilation (FDDA) technique was used when running MM5 to enhance the simulation accuracy of key meteorological parameters. NCEP (National Centers for Environmental Prediction) reanalysis data with temporal resolution of 6 hours and spatial resolution of $1^\circ \times 1^\circ$ were used to provide initial and boundary conditions of MM5.

3. Observations

Daily PM₁₀ samples were collected in a 24-hour interval from 27 March to 26 April 2009 at the summit of a mountain site (Mt. Tai, 36.27°N, 117.10°E, 1545 m a.s.l., Figure 1) in east China. On 24 April an intensive dust storm arrived in Mt. Tai, during which PM₁₀ sampling time was changed into 3–6 hours. Information of this observation data such as instruments and analytical method was documented in detail in Wang et al. [10].

Daily AOD data at 550 nm from MODIS (Moderate-Resolution Imaging Spectroradiometer) on board Aqua satellite was collected. Two AOD products, namely, the Level-3 MODIS “Land and Ocean” AOD product and the Level-3 “Deep Blue Land only” AOD product, were used for model validation during the dust storm period. The “Land and Ocean” product can provide retrievals on areas out of the dust source regions including ocean and east/south China, but it cannot provide sufficient retrievals over desert areas. The “Deep Blue Land only” product, however, can provide retrievals over the entire continent including desert areas theoretically, but this product does not provide any retrieval over ocean. Using these two products at the same time can obtain as much AOD information about this dust storm as possible. Both products are in the resolution of 1° × 1°. The retrieval time of MODIS on board Aqua is around 13:30 (Local Standard Time). The MODIS instrument is also on board another satellite Terra; however, during this dust storm period, data quality of retrievals from MODIS-Terra was too low to be used, so MODIS-Terra data were not used in this work.

Vertical distributions of aerosol and cloud information were measured by the space-based lidar CALIOP on board the CALIPSO satellite [12]. The CALIOP Level 2 aerosol profile products (ver. 3.01) containing aerosol profile extinction coefficient at 532 nm were obtained and used in this study to verify modeled aerosol extinction coefficient profiles. The horizontal resolution of the CALIOP Level 2 aerosol profile product is 5 km and the vertical resolution is 60 m. The lidar signal inversion is started from around 30 km down to the ground surface. Atmospheric Volume Description (AVD) flag and Cloud-Aerosol Discrimination (CAD) score that were contained in the Level 2 product were used to screen out aerosol extinction coefficient profiles containing cloud signals by the method described in the user's guide webpage (http://www-calipso.larc.nasa.gov/resources/calipso_users_guide/tools/index.php). CALIOP measurements are available both at daytime and nighttime. Considering data quality, one profile was selected per day within the model domain on days 23, 24, and 26 and two profiles were used on day 25.

4. Model Validations

4.1. Comparison with Ground-Level PM₁₀ Observation at Mt. Tai. Comparison between simulated and observed daily concentrations of PM₁₀ and inorganic components at Mt. Tai from 27 March to 26 April 2009 are presented in Figure 2. The model reproduced the magnitude and temporal variation

of PM₁₀ concentration at this site and correctly captured the arrival of the dust storm on 23 April, the peak on 24 April, and its passing after 25 April. The observation revealed that the strength of this dust storm was so strong that daily mean PM₁₀ concentration reached as high as ~1400 μg/m³ and the maximum concentration approached ~1800 μg/m³ (sampling interval of 3 hours). The model captured such characteristics, predicting daily PM₁₀ to be ~1600 μg/m³. During the observation period, mean PM₁₀ concentrations from observation and simulation were 201 μg/m³ and 200 μg/m³, respectively, with correlation coefficient of 0.92. For sulfate, nitrate, and ammonium, the model generally reproduced the temporal variations but tended to underpredict their daily concentrations, which could be attributed to the relatively coarse model resolution that cannot distinguish their emission gradients between urban and mountain areas. Besides, the chemical mechanism of nitrate is too complex and cannot be well treated in atmospheric chemistry models, which is also a reason resulting in the relatively poor performance for nitrate. For instance, heterogeneous reactions between gaseous precursors (HNO₃, N₂O₅, NO₂, etc.) and atmospheric aerosols (dust and other aerosol types) [21] and the impact of HONO chemical mechanism [30] are not well understood nowadays. It should be mentioned that nitrate and nitrogen oxides are also often poorly predicted in present chemical transport models [27, 31]. During the sampling period, mean observed concentrations of sulfate, nitrate, and ammonium were 16.7 μg/m³, 20.1 μg/m³, and 12.0 μg/m³, respectively, while those from model simulation were 13.5 μg/m³, 15.2 μg/m³, and 7.4 μg/m³. The comparison with observation at Mt. Tai showed that a severe dust storm hit east China during 23–26 April and demonstrated that RAQMS reproduced the impact of this dust storm on east China properly on both aspects of timing and strength. In the following sections, model comparisons with remote sensing measurements will be focused on the dust storm period.

4.2. Comparison with MODIS Retrieved AOD. Figure 3 shows daily AOD retrievals from MODIS on board the Aqua satellite and model results. Simulated AOD was sampled according to corresponding MODIS retrievals. From Deep Blue MODIS retrieval (Figure 3(c)), the dust storm occurred on 23 April over the Gobi desert; as a result, AOD over the Gobi desert was about 2.0–3.2. Meanwhile, large amount of dust was also generated over the Taklamakan desert, resulting in maximum AOD of approaching 4.0. The model correctly reproduced locations of high AOD centers over these deserts but with some overprediction (Figure 3(d)). Dust aerosol was nearly the only contributor to total AOD over dust source regions, with percentage contribution of up to 98% over the two deserts estimated by the model (shown in Figures 3(b) and 3(d) are fractional values).

The main body of the dust storm originated from the Gobi desert moved southeastward to the North China Plain on 24 April, exerting significant influences on this area. Both MODIS retrievals (Figures 3(a) and 3(c)) and simulations (Figures 3(b) and 3(d)) revealed the high AOD center over the North China Plain with the value in a range of 1.2 to around

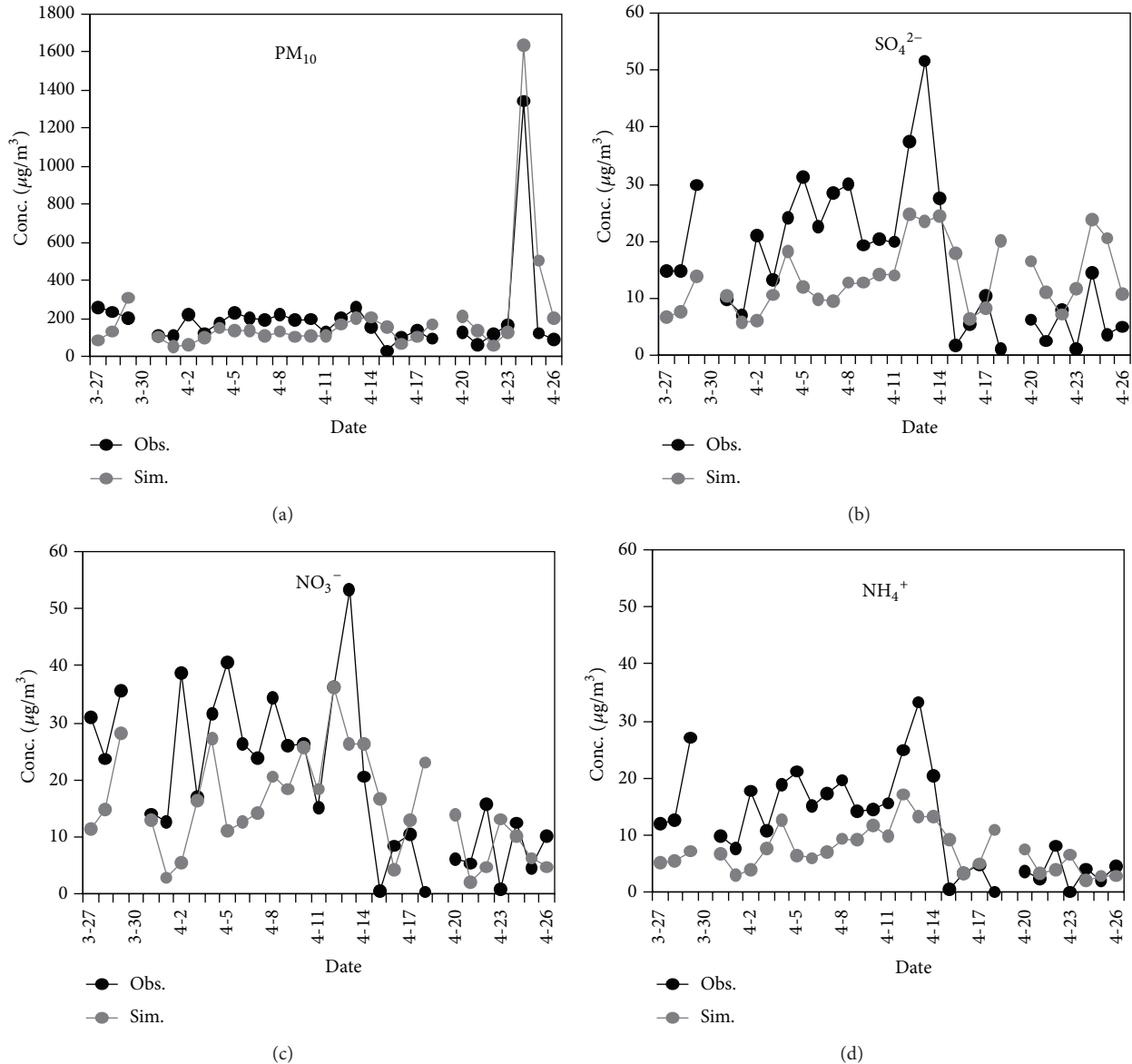


FIGURE 2: Comparisons between observed and simulated ground-level daily mean concentrations of PM_{10} , sulfate (SO_4^{2-}), nitrate (NO_3^-), and ammonium (NH_4^+) at Mt. Tai.

3.6; meanwhile, both retrievals and simulations showed that AOD over the Taklamakan desert was in a range of 1.0–4.0. The contribution of dust to total AOD still remained at a high level. The model estimation of the percentage contribution of dust was up to 90% over most areas of the North China Plain and >90% over the Taklamakan desert.

The body of the dust storm moved further southward on 25 April but with weaker strength. MODIS retrieval indicated that on 25 April, high AOD appeared over south China (areas south of the middle and lower reaches of the Yangtze River) with values of about 1.2–2.0 (Figure 3(a)). The model reproduced the magnitude and the distribution pattern of AOD over these areas (Figure 3(b)). However, the model slightly underpredicted AOD over the Taklamakan desert and parts of the North China Plain (Figures 3(c) and 3(d)). On

this day, the contribution of dust to total AOD became smaller over east China, the estimated percentages ranged from 40% to 60% over high AOD areas on south China. It should be noticed that there was a branch of dust over northeast China which was not depicted as clear as the main body of the dust storm in satellite figures due to the relatively smaller AOD values and insufficient valid retrieval data there, and the model reproduced this branch.

This dust storm almost finished on 26 April. Both MODIS (Figure 3(a)) and RAQMS (Figure 3(b)) indicated that high AOD mainly appeared over south China, with values decreased to a range of 0.8–1.6, and dust accounted for only about 40% of total AOD over large portions of these areas. The model underpredicted AOD over the Taklamakan desert on this day (Figures 3(c) and 3(d)).

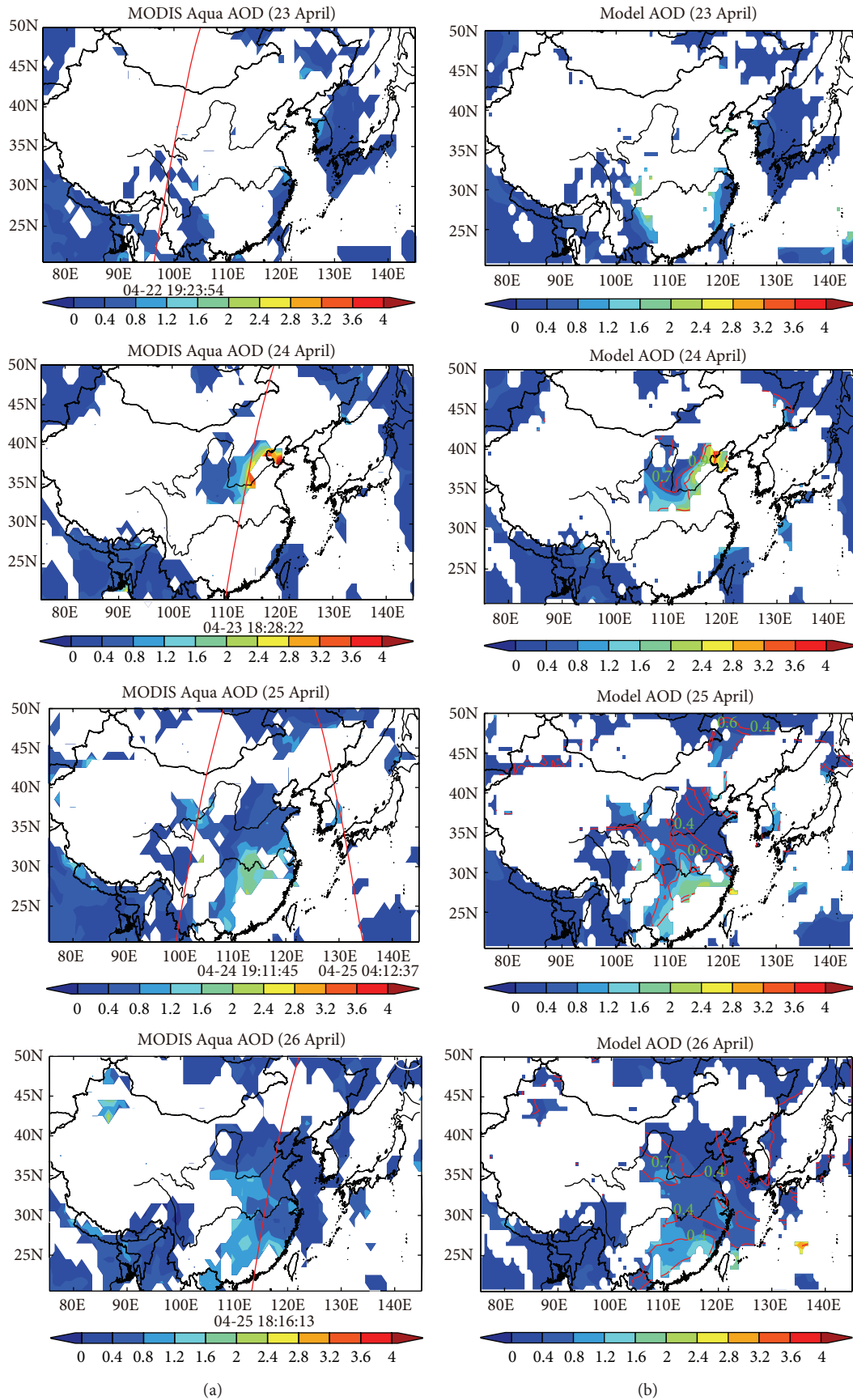


FIGURE 3: Continued.

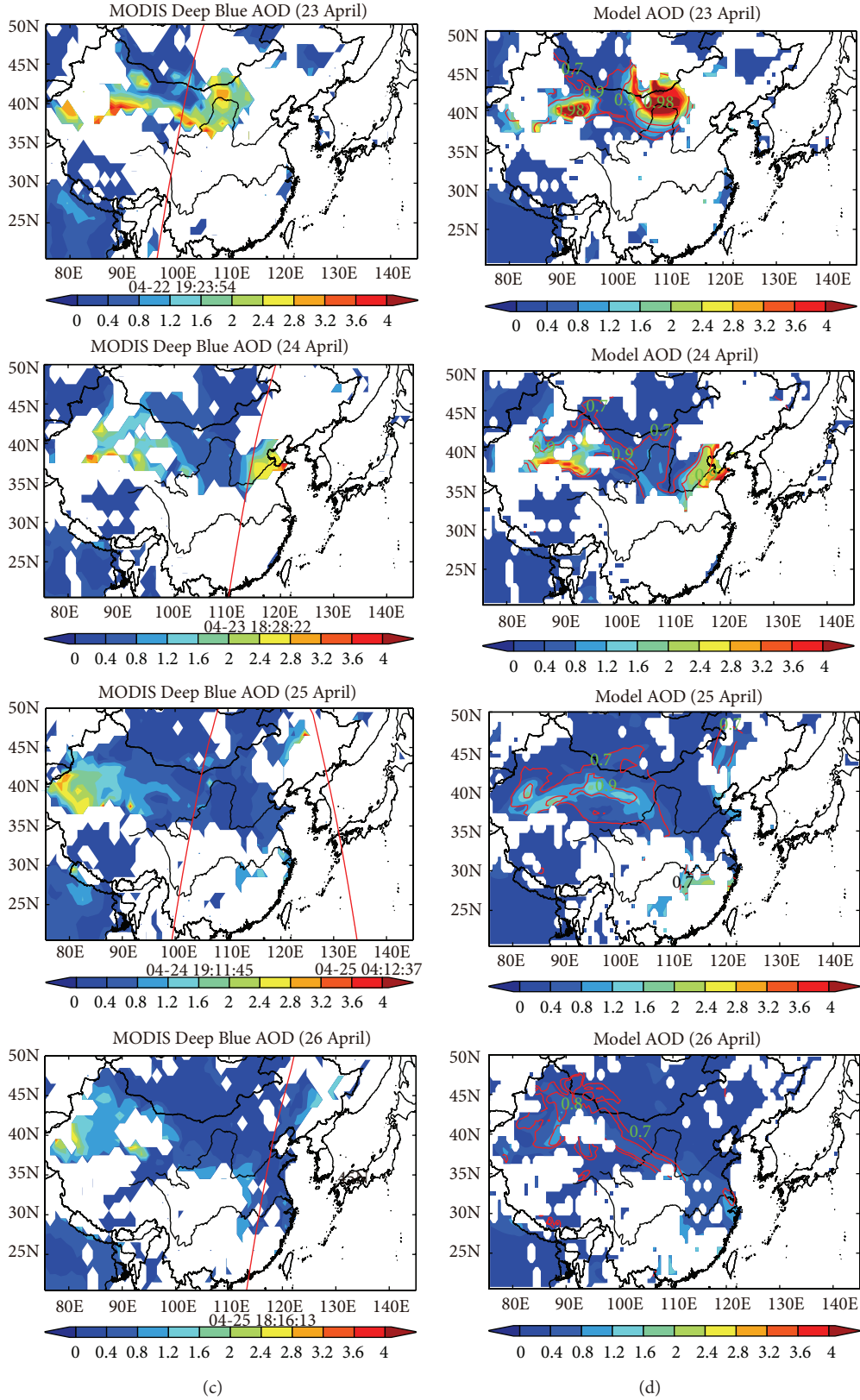


FIGURE 3: AOD from MODIS and the model at 550 nm during 23 to 26 April 2009 (LST): (a) MODIS Aqua “Land and Ocean” AOD product; (b) modeled AOD sampling according to (a); (c) MODIS Aqua “Deep Blue Land only” AOD product; (d) modeled AOD sampling according to (c). CALIPSO orbit paths (red lines) and path times (at the bottom of each path, UTC time, MM-DD HH:MM:SS) are presented in MODIS AOD figures ((a), (c)). Fractional contributions of dust to total AOD are indicated in modeled AOD figures ((b), (d), red contour lines with light blue numbers).

4.3. Comparison with CALIOP Products. The orbit of the CALIPSO satellite that approximately crossed the body of the dust storm was selected for each day (see Figures 3(a) and 3(c)) to depict the vertical evolution of the dust transport. Figure 4 presents profiles of aerosol subtype information (left column) and aerosol extinction coefficient at 532 nm from CALIOP measurements (middle column) and simulated vertical distributions of aerosol extinction coefficient at 550 nm (right column). As this study mainly focuses on dust aerosol, fractional contributions of dust to total aerosol extinction estimated by the model were also displayed. The main body of a dust plume was assumed to have the fractional value of greater than 0.7 in this study.

On 23 April when the dust storm occurred in the Gobi desert, the CALIPSO satellite flew across this dust source region. Along this orbit (Figure 4(a)), a pure dust plume was detected by CALIOP in the range of about 37°N to 45°N and between altitudes of about 1 km to 8 km (left column in Figure 4(a)). The corresponding distribution of measured aerosol extinction coefficient (middle column in Figure 4(a)) showed the largest values ($\geq 1.0 \text{ km}^{-1}$) locating around 40°N and relatively large values ($0.3\text{--}1.0 \text{ km}^{-1}$) locating between 40°N and 45°N at lower altitudes (1–3 km), indicating most dust aerosol distributed below about 3 km. Right column in Figure 4(a) was the vertical distribution of simulated aerosol extinction coefficients and fractional contributions of dust to total aerosol extinction coefficient greater than 0.7. It is found that the model reasonably reflected the span (37°–45°N) and the elevation (from surface to about 7 km) of the dust plume, reproducing the largest aerosol extinction coefficient center at around 40°N within 3 km, but the model seemed to underestimate measurements. It should be noted that the CALIOP retrieved aerosol extinction coefficients $\geq 1.0 \text{ km}^{-1}$ (in red color in the middle column of Figure 4) are of higher uncertainties that it can be used to reflect dust plume qualitatively rather than quantitatively.

On the midnight of 24 April (UTC time, the afternoon of 23 April), the CALIPSO satellite crossed the North China Plain which was affected by the main body of the dust storm (see Figure 3). Aerosols classified as pure dust by CALIOP located between 35°N and 40°N and stretched from surface to about 10 km (left column in Figure 4(b)). Measured aerosol extinction coefficients $\geq 1.0 \text{ km}^{-1}$ were found to stretch from surface to about 3 km within the latitude band of 35°–40°N, but the values decreased sharply to about 0.1 km^{-1} above 4 km, indicating that most dust aerosols were restricted within this altitude (middle column in Figure 4(b)). The model reasonably simulated the location (35°N to about 42°N) and the vertical extension (from surface to 8 km) of the dust plume but overestimated the total aerosol extinction coefficient above 4 km (right column in Figure 4(b)).

The presented CALIOP aerosol profiles on the midnight of 25 April (Figure 4(c)) belong to an orbit path crossing the tail-end of the dust storm (Figure 3). As detected by CALIOP, dust aerosol located between 35°N and 40°N and between 1 km and 10 km (left column in Figure 4(c)), with high aerosol extinction coefficient center (about $0.4\text{--}1.0 \text{ km}^{-1}$) appearing at the altitude of around 3 km (middle

column in Figure 4(c)). The model simulated the location and the vertical distribution of dust aerosol reasonably well (right column in Figure 4(c)); however, although the model simulated the largest contribution of dust to total aerosol extinction coefficient at 2–3 km (fractional value of ≥ 0.9), it underestimated the intensity of this high aerosol extinction coefficient center revealed by CALIOP.

CALIOP retrievals and simulations along another orbit path crossing the west Pacific Ocean at noon of 25 April (see Figures 3(a) and 3(c)) are shown in Figure 4(d). The main body of the dust storm was found at about 35°–40°N around 2–4 km (left and middle columns in Figure 4(d)). The model reasonably reproduced the main features of the dust plume (right column in Figure 4(d)). Both CALIOP measurement and simulation indicated that there was dust plume transported out of the continent between latitudes of about 35°–40°N at altitude of 2–4 km on 25 April. The analysis of MODIS and CALIOP retrievals revealed that the dust storm transported in two directions; one was a southeastward pathway from the Gobi desert to south China; the other one was an eastward pathway from source region to the west Pacific Ocean.

The CALIPSO orbit path also passed over the tail-end of the dust plume on 26 April (see Figures 3(a) and 3(c)). The detected dust plume could be divided into two major parts, namely, (1) 25°–30°N, below 3 km, and (2) 30°–35°N, from surface to 10 km (left column in Figure 4(e)), with aerosol extinction coefficients of about $0.3\text{--}1.0 \text{ km}^{-1}$ and about 0.1 km^{-1} , respectively (middle column in Figure 4(e)). The corresponding simulated aerosol extinction coefficient was generally consistent with the measurement features of the dust plume, but the model seemed to underestimate the contribution of dust to aerosol extinction coefficient for the 2nd part of the plume below 3 km (right column in Figure 4(e)). The model also reproduced the dust plume extending vertically from surface to about 8 km in between 35° and 45°N (right column), which was classified as “polluted dust” by CALIOP (left column).

The comparisons made in Section 4 demonstrated that RAQMS was able to represent the temporal, horizontal, and vertical evolution of the dust storm during 23 to 26 April, 2009, reasonably well. This supports the reliability of model analysis of dust structure and its evolution process in the following section.

5. Three-Dimensional Structure of the Dust Storm and Its Evolution Process

Figure 5(a) presents the daily mean ground-level dust concentration and dust-induced AOD during the dust storm period, and Figure 5(b) shows the daily mean vertical distribution of dust concentration and dust extinction coefficient for east China (zonal average from 105°E to 125°E). At the outbreak of the dust storm (23 April), large amount of dust aerosol was generated on the Gobi desert and the Taklamakan desert, with the maximum daily surface concentration exceeding 8 mg/m^3 over the two source regions. Dust aerosol resulted in maximum daily mean dust-induced

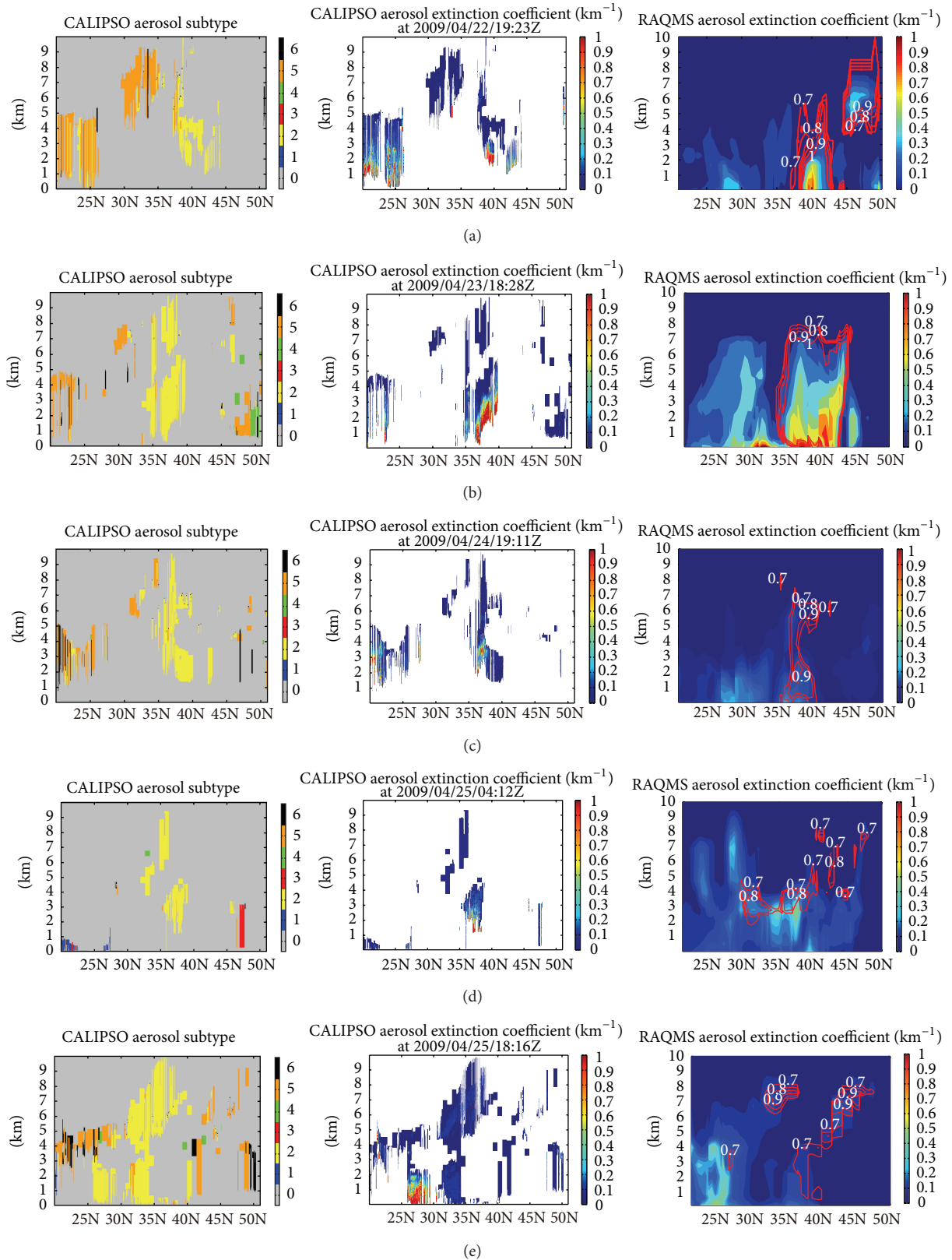


FIGURE 4: Left column: vertical distributions of aerosol subtype from CALIOP measurements (0 = not applicable, 1 = clean marine, 2 = dust, 3 = polluted continental, 4 = clean continental, 5 = polluted dust, and 6 = smoke); middle column: vertical distributions of aerosol extinction coefficient at 532 nm from CALIOP; right column: simulated aerosol extinction coefficient at 550 nm. Red contours overlaid on simulation results are fractional contributions of dust to total aerosol extinction coefficient. Dates in figure titles are local standard time while orbit times in figure titles are coordinated universal time.

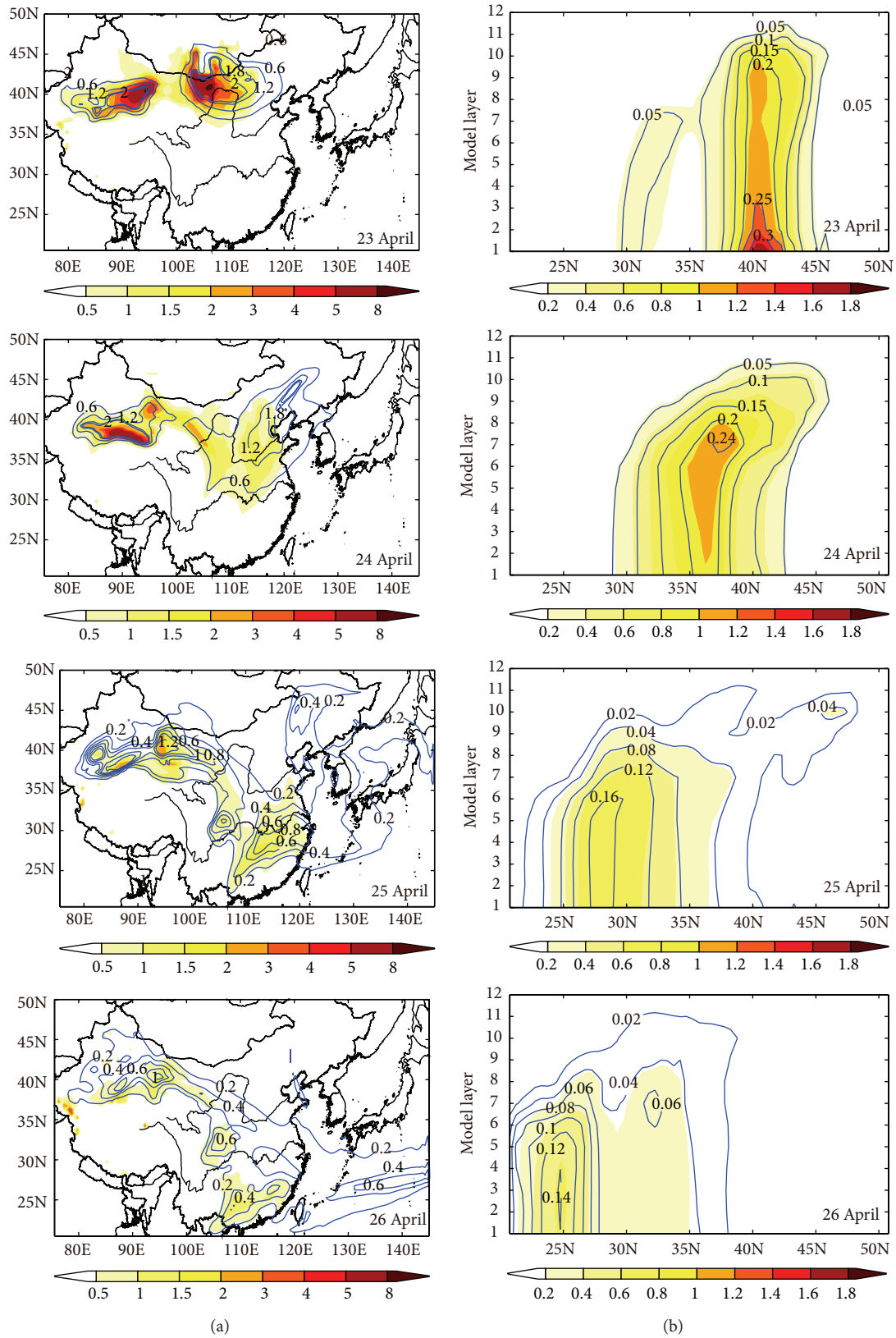


FIGURE 5: Daily mean (a) surface dust concentration (mg/m^3) and dust-induced AOD (blue contours with numbers) and (b) sectional average over $105^\circ\text{--}125^\circ\text{E}$ of dust concentration (mg/m^3) and dust extinction coefficient (km^{-1} , blue contours with numbers) for the dust storm period (23–26 April) from model simulation.

AOD of up to 2.0 over these two deserts. The vertical profile of dust concentration for east China shows that there was a dust concentration center at about 40°–41°N, with the largest concentration ($>1.4 \text{ mg/m}^3$) and extinction coefficient ($>0.3 \text{ km}^{-1}$) situated below about 200 m (the 2nd model layer). The top of the dust storm exceeded 8 km (11th layer), with high dust concentration ($\geq 1.0 \text{ mg/m}^3$) and large dust aerosol extinction coefficient ($\geq 0.2 \text{ km}^{-1}$) extending from surface to near 7 km (10th layer) due to vertical mixing.

On 24 April, the main body of the dust storm transported southeastward off the Gobi desert, resulting in daily mean surface dust concentration of about $1.0\text{--}1.5 \text{ mg/m}^3$ and daily mean dust AOD of $1.2\text{--}1.8$ over most areas of the North China Plain. Dust concentration and dust AOD could be in ranges of $1.0\text{--}1.5 \text{ mg/m}^3$ and $0.6\text{--}1.2$ over the middle and lower reaches of the Yellow River on this day. It should be noticed that there was another large AOD center ($1.2\text{--}1.8$) with sharp gradient locating over northeast China where there was very low ground-level dust concentration; that is because a branch of dust was transported eastward off the Gobi desert at higher altitudes. High dust concentration of about $1.0\text{--}1.2 \text{ mg/m}^3$ stretched straight from near surface to about 2 km (6th–7th layers) at around 36°N. Above 2 km, the dust concentration center shifted north to nearly 39°N. High dust concentrations mainly appeared at higher altitudes (such as 2–4 km) rather than at the surface on this day, resulting in the largest dust extinction coefficient of about 0.24 km^{-1} appearing at about 2.5 km (7th layer).

The main body of the dust storm transported to south China on 25 April, leading to ground-level dust concentration of $0.5\text{--}1.5 \text{ mg/m}^3$ over south of middle and lower reaches of the Yangtze River. At the meantime, the high center of dust-induced AOD moved accordingly to south China but the value decreased to about $0.4\text{--}0.8$. The high AOD center over northeast China remained there but the maximum value decreased sharply from about 1.8 to 0.4. The top of the dust storm (dust concentration $\geq 0.2 \text{ mg/m}^3$) lowered to about 4.5 km (9th layer) over east China. High dust concentration in vertical direction decreased to $0.6\text{--}0.8 \text{ mg/m}^3$ between about 26°–32°N, with dust extinction coefficient also weakened to about $0.12\text{--}0.16 \text{ km}^{-1}$. Dust concentration as well as dust extinction coefficient was higher at around 2.5 km (7th layer) than at the surface in between 35° and 40°N. The high dust extinction coefficient center over northeast China was found at about 6 km (10th layer), with the maximum value of about 0.04 km^{-1} . Vertical distribution patterns of dust concentration and dust extinction coefficient for 24 and 25 April reveal that the transport pathway of the dust storm split into two over east China: the low altitude pathway (below 2 km) was in a southeastward direction from the Gobi desert to south China while the high altitude pathway (above 2 km) was in an eastward direction from source region to the west Pacific Ocean along 35°–40°N, consistent with comparisons between satellite measurements and simulations in Sections 4.2 and 4.3. Wind directions varied at different altitudes were the reason. On these two days, wind directions at altitudes below 2 km over east China were dominated by north wind, resulting in southward transport of dust aerosols; however,

at altitudes above 2 km, the westerly and northwesterly controlled east China; as a result, dust aerosols were conveyed from the Gobi desert to the west Pacific Ocean between 35° and 40°N (figures of the wind field were not shown).

The dust storm moved further south on 26 April, with lower ground-level concentration ($0.5\text{--}1.0 \text{ mg/m}^3$) and smaller coverage. As a result, dust-induced AOD decreased to about $0.2\text{--}0.4$ over south China. The top of the dust storm also further decreased to near 2.5 km (7th layer). The high dust center located at around 25°N, with daily concentration of about $0.4\text{--}0.6 \text{ mg/m}^3$ and dust extinction coefficient of about $0.12\text{--}0.14 \text{ km}^{-1}$. The dust storm episode was actually finished on this day.

During this dust storm period (23–26 April, 2009), the model estimated that a total of $2.24 \times 10^4 \text{ Gg}$ dust particles were generated over the Gobi desert and the Taklamakan desert. About 50% ($1.12 \times 10^4 \text{ Gg}$) of emitted dust particles were redeposited onto the ground by dry deposition process. The dry deposition amount of dust was about $5\text{--}15 \text{ g/m}^2$ over dust source regions and the amount decreased sharply to less than 0.5 g/m^2 over downwind areas such as south China and the West Pacific Ocean. The removal of dust due to wet scavenging process accounted for about 16% of generated dust particles. Different from dry deposition, wet scavenge mainly occurred over downwind areas such as north China, the middle and lower reaches of the Yangtze River, and the West Pacific Ocean. The amount of wet scavenged dust was estimated to be in the range of about $0.5\text{--}10 \text{ g/m}^2$ over these downwind areas. The rest 34% emitted dust was subjected to long-range transport.

6. Conclusion

The three-dimensional evolution of a dust storm occurring over East Asia from 23 to 26 April 2009 was investigated by using the regional model RAQMS. Major focuses of this study have been placed on model validation and analyses of dust storm evolution. A variety of observational data including in situ ground-level PM_{10} and inorganic aerosol observations at Mt. Tai, aerosol optical depth (AOD) retrievals from MODIS, and profile aerosol extinction coefficient and aerosol subtype information from CALIOP were used to evaluate the model performance and investigate the evolution of the dust storm. Comparing with ground-level observations at Mt. Tai, the model well reproduced the magnitude of the dust storm on 23–26 April, predicting maximum daily PM_{10} concentration of $\sim 1600 \mu\text{g/m}^3$, close to the observed daily PM_{10} concentration peak of $\sim 1400 \mu\text{g/m}^3$. During the whole observation period (27 March–26 April), the mean PM_{10} concentrations at Mt. Tai for observation and simulation were $201 \mu\text{g/m}^3$ and $200 \mu\text{g/m}^3$, respectively, with correlation coefficient of 0.92. The model also reasonably reproduced concentration levels of inorganic aerosol components at Mt. Tai. Comparison with MODIS retrievals demonstrated that the model performed well on reproducing the magnitude and the distribution pattern of AOD during the dust storm period, and comparison with CALIOP measurements showed that the model was able to reasonably simulate the vertical distribution of aerosol

extinction coefficient. Model validation indicated that the model was capable of reproducing the three-dimensional structure and the evolution of the dust storm, capturing major features of the dust storm reasonably well.

The dust storm was originated from the Gobi desert. During the early days of the dust storm, the ground-level daily dust concentration could be higher than 8 mg/m^3 over dust source regions and $1.0\text{--}1.5 \text{ mg/m}^3$ over the North China Plain, resulting in daily mean dust-induced AOD to be as high as 2.0 over desert areas and in a range of $1.2\text{--}1.8$ over vast areas of the North China Plain. As a result, dust-induced AOD could account for 98% and up to 90% of total AOD over desert areas and parts of north China, respectively, during the first two days of the dust storm. The top of the dust storm could reach as high as about 8 km at the beginning, with high dust concentration ($\geq 1.0 \text{ mg/m}^3$) and large dust aerosol extinction coefficient ($\geq 0.2 \text{ km}^{-1}$) extending from surface to about 7 km. Vertical distribution of dust concentration also showed that the transport pathway of this dust storm was split into two, dust aerosols at lower altitude (below 2 km) were transported southeastward from the Gobi desert to south China while aerosols at higher altitude (above 2 km) were transported eastward out of China along $35^\circ\text{--}40^\circ\text{N}$. During last days of the dust storm, although the ground-level dust concentration, dust-induced AOD, and the altitude of dust top over south China were all decreased obviously, the contribution of dust to total AOD was still approaching 40% over these areas, implying the important implications of the dust storm on radiative forcing in southern parts of China. During this dust storm period (23–26 April, 2009), a total of $2.24 \times 10^4 \text{ Gg}$ dust aerosols were estimated to be generated over East Asia, about 50% and 16% of them were removed by dry deposition and wet scavenging processes, respectively, and 34% of them were subjected to long-range transport.

Conflict of Interests

The authors declare that there is no conflict of interests regarding the publication of this paper.

Acknowledgments

This study was supported by the National 973 Project of China (2014CB953703) and the National Natural Science Foundation of China (Grant no. 41375151). The authors would like to thank Professor Gehui Wang for providing observation data at Mt. Tai and the MODIS science data support team for maintaining and providing MODIS AOD retrievals. The CALIOP data were obtained from the NASA Langley Research Center Atmospheric Sciences Data Center.

References

- [1] I. N. Sokolik and O. B. Toon, "Direct radiative forcing by anthropogenic airborne mineral aerosols," *Nature*, vol. 381, no. 6584, pp. 681–683, 1996.
- [2] I. Tegen, S. P. Harrison, K. Kohfeld, I. C. Prentice, M. Coe, and M. Heimann, "Impact of vegetation and preferential source areas on global dust aerosol: Results from a model study," *Journal of Geophysical Research D: Atmospheres*, vol. 107, no. 21, article 4576, 2002.
- [3] Y. Shao and C. H. Dong, "A review on East Asian dust storm climate, modelling and monitoring," *Global and Planetary Change*, vol. 52, no. 1–4, pp. 1–22, 2006.
- [4] X. Y. Zhang, S. L. Gong, Z. X. Shen et al., "Characterization of soil dust aerosol in China and its transport and distribution during 2001 ACE-Asia: 1. Network observations," *Journal of Geophysical Research D: Atmospheres*, vol. 108, no. 9, article 4261, 2003.
- [5] S. L. Gong, X. Y. Zhang, T. L. Zhao, I. G. McKendry, D. A. Jaffe, and N. M. Lu, "Characterization of soil dust aerosol in China and its transport and distribution during 2001 ACE-Asia: 2. Model simulation and validation," *Journal of Geophysical Research D: Atmospheres*, vol. 108, no. 9, 2003.
- [6] Z. Han, H. Ueda, K. Matsuda et al., "Model study on particle size segregation and deposition during Asian dust events in March 2002," *Journal of Geophysical Research D: Atmospheres*, vol. 109, no. 19, article 19205, 2004.
- [7] J. Huang, Q. Fu, J. Su et al., "Taklimakan dust aerosol radiative heating derived from CALIPSO observations using the Fu-Liou radiation model with CERES constraints," *Atmospheric Chemistry and Physics*, vol. 9, no. 12, pp. 4011–4021, 2009.
- [8] K. M. Lau, M. K. Kim, and K. M. Kim, "Asian summer monsoon anomalies induced by aerosol direct forcing: the role of the Tibetan Plateau," *Climate Dynamics*, vol. 26, no. 7–8, pp. 855–864, 2006.
- [9] R. B. Husar, D. M. Tratt, B. A. Schichtel et al., "Asian dust events of April 1998," *Journal of Geophysical Research D: Atmospheres*, vol. 106, no. 16, pp. 18317–18330, 2001.
- [10] G. Wang, J. Li, C. Cheng et al., "Observation of atmospheric aerosols at Mt. Hua and Mt. Tai in central and East China during spring 2009—part I: EC, OC and inorganic ions," *Atmospheric Chemistry and Physics*, vol. 11, no. 9, pp. 4221–4235, 2011.
- [11] N. Sugimoto, A. Shimizu, I. Matsui et al., "Study of Asian dust phenomena in 2001–2003 using a network of continuously operated polarization lidars," *Water, Air, and Soil Pollution: Focus*, vol. 5, no. 3–6, pp. 145–157, 2005.
- [12] D. M. Winker, M. A. Vaughan, A. Omar et al., "Overview of the CALIPSO mission and CALIOP data processing algorithms," *Journal of Atmospheric and Oceanic Technology*, vol. 26, no. 11, pp. 2310–2323, 2009.
- [13] I. Uno, K. Yumimoto, A. Shimizu et al., "3D structure of Asian dust transport revealed by CALIPSO lidar and a 4DVAR dust model," *Geophysical Research Letters*, vol. 35, no. 6, Article ID L06803, 2008.
- [14] K. Eguchi, I. Uno, K. Yumimoto et al., "Trans-pacific dust transport: Integrated analysis of NASA/CALIPSO and a global aerosol transport model," *Atmospheric Chemistry and Physics*, vol. 9, no. 9, pp. 3137–3145, 2009.
- [15] Y. Shao, Y. Yang, J. Wang et al., "Northeast Asian dust storms: Real-time numerical prediction and validation," *Journal of Geophysical Research D: Atmospheres*, vol. 108, no. 22, Article ID 4691, 2003.
- [16] Z. Han, J. Li, W. Guo, Z. Xiong, and W. Zhang, "A study of dust radiative feedback on dust cycle and meteorology over East Asia by a coupled regional climate-chemistry-aerosol model," *Atmospheric Environment*, vol. 68, pp. 54–63, 2013.
- [17] J. Li, Z. W. Han, and R. J. Zhang, "Model study of atmospheric particulates during dust storm period in March 2010 over East

- Asia,” *Atmospheric Environment*, vol. 45, no. 24, pp. 3954–3964, 2011.
- [18] W. P. L. Carter, “Documentation of the SAPRC-99 chemical mechanism for VOC reactivity assessment,” Final Report Contract no. 92-329 and 95-308, California Air Resources Board, 2000.
- [19] C. Fountoukis and A. Nenes, “ISORROPIAII: a computationally efficient thermodynamic equilibrium model for K^+ – Ca^{2+} – Mg^{2+} – NH_4^+ – Na^+ – SO_4^{2-} – NO_3^- – Cl^- – H_2O aerosols,” *Atmospheric Chemistry and Physics*, vol. 7, no. 17, pp. 4639–4659, 2007.
- [20] D. A. Lack, X. X. Tie, N. D. Bofinger, A. N. Wiegand, and S. Madronich, “Seasonal variability of secondary organic aerosol: a global modeling study,” *Journal of Geophysical Research D: Atmospheres*, vol. 109, no. 3, Article ID D03203, 2004.
- [21] J. W. Li and Z. W. Han, “A modeling study of the impact of heterogeneous reactions on mineral aerosol surfaces on tropospheric chemistry over East Asia,” *Particulate Chemistry*, vol. 8, no. 5, pp. 433–441, 2010.
- [22] J. L. Walmsley and M. L. Wesely, “Modification of coded parametrizations of surface resistances to gaseous dry deposition,” *Atmospheric Environment*, vol. 30, no. 7, pp. 1181–1188, 1996.
- [23] C. J. Walcek, R. A. Brost, J. S. Chang, and M. L. Wesely, “ SO_2 , sulfate and HNO_3 deposition velocities computed using regional landuse and meteorological data,” *Atmospheric Environment*, vol. 20, no. 5, pp. 949–964, 1986.
- [24] J. S. Chang, R. A. Brost, I. S. A. Isaksen et al., “A three-dimensional Eulerian acid deposition model: physical concepts and formulation,” *Journal of Geophysical Research*, vol. 92, no. 12, pp. 14681–14700, 1987.
- [25] M. D. Petters and S. M. Kreidenweis, “A single parameter representation of hygroscopic growth and cloud condensation nucleus activity,” *Atmospheric Chemistry and Physics*, vol. 7, no. 8, pp. 1961–1971, 2007.
- [26] X. Han, M. Zhang, Z. Han, J. Xin, and X. Liu, “Simulation of aerosol direct radiative forcing with RAMS-CMAQ in East Asia,” *Atmospheric Environment*, vol. 45, no. 36, pp. 6576–6592, 2011.
- [27] Z. Han, T. Sakurai, H. Ueda et al., “MICS-Asia II: model intercomparison and evaluation of ozone and relevant species,” *Atmospheric Environment*, vol. 42, no. 15, pp. 3491–3509, 2008.
- [28] Q. Zhang, D. G. Streets, G. R. Carmichael et al., “Asian emissions in 2006 for the NASA INTEX-B mission,” *Atmospheric Chemistry and Physics*, vol. 9, no. 14, pp. 5131–5153, 2009.
- [29] G. R. van der Werf, J. T. Randerson, L. Giglio et al., “Global fire emissions and the contribution of deforestation, savanna, forest, agricultural, and peat fires (1997–2009),” *Atmospheric Chemistry and Physics*, vol. 10, no. 23, pp. 11707–11735, 2010.
- [30] Y. Li, J. An, M. Min, W. Zhang, F. Wang, and P. Xie, “Impacts of HONO sources on the air quality in Beijing, Tianjin and Hebei Province of China,” *Atmospheric Environment*, vol. 45, no. 27, pp. 4735–4744, 2011.
- [31] H. Hayami, T. Sakurai, Z. Han et al., “MICS-Asia II: model intercomparison and evaluation of particulate sulfate, nitrate and ammonium,” *Atmospheric Environment*, vol. 42, no. 15, pp. 3510–3527, 2008.

Research Article

Study of Aerosols' Characteristics and Dynamics over the Kingdom of Saudi Arabia Using a Multisensor Approach Combined with Ground Observations

Ashraf Farahat,^{1,2} Hesham El-Askary,^{3,4,5} and Abdulaziz Al-Shaibani⁶

¹Department of Prep Year Physics, College of Applied and Supporting Studies, King Fahd University of Petroleum and Minerals, Dhahran 31261, Saudi Arabia

²Department of Physics, Faculty of Science, Alexandria University, Moharam Beek, Alexandria 21522, Egypt

³Schmid College of Science and Technology, Chapman University, Orange, CA 92866, USA

⁴Center of Excellence in Earth Systems Modeling and Observations, Chapman University, Orange, CA 92866, USA

⁵Department of Environmental Science, Faculty of Science, Moharam Beek, Alexandria University, Alexandria 21522, Egypt

⁶Department of Earth Science, King Fahd University of Petroleum and Minerals, Dhahran 31261, Saudi Arabia

Correspondence should be addressed to Hesham El-Askary; elaskary@chapman.edu

Received 25 August 2014; Revised 28 November 2014; Accepted 9 December 2014

Academic Editor: Slobodan Nickovic

Copyright © 2015 Ashraf Farahat et al. This is an open access article distributed under the Creative Commons Attribution License, which permits unrestricted use, distribution, and reproduction in any medium, provided the original work is properly cited.

This study covers various aspects of the aerosol distribution and characteristics, namely, optical depth climatology, absorption characteristics, and their microphysical properties over four regions in Saudi Arabia using satellite and ground observations including MODIS/Terra and Aqua, OMI, MISR/Terra, AERONET, and CALIPSO for the period April 2003–January 2013. The study includes cities in the North Western, Western, Eastern provinces of Saudi Arabia and in the Rub al Khali desert or Empty Quarter. Satellite and ground observations showed that the dust season extends from April to August with prominent peaks yet with high anthropogenic contribution late summer and early fall. Analysis shows an increase in the aerosol concentration during March 2009 which could be attributed to a major dust storm during that time. Comparing the AOD time series over regions 1–3 and region 4 (desert) we observe monthly and annual variability with no recurrence pattern over the years. The Aqua Deep Blue AOD₅₅₀ data shows a single peak pattern that occurs over region 4 during the spring season known for its frequent dust events. OMI data shed the light on the presence of higher air pollution levels over region 3, representing the oil rich eastern province of Saudi Arabia.

1. Introduction

Aerosols' impact on the regional climate and their ultimate connections to the Earth's global climate system and hence forcing has been observed through their optical and microphysical properties [1–5]. Thus, improving our understanding of aerosol properties and characterization is imperative especially over mega and highly populated cities where aerosols have major impacts on human health [6–9]. The kingdom of Saudi Arabia is one of the major sources of aerosols in the world, including natural and anthropogenic components [10, 11]. Yet, it still lacks for better characterization of its atmospheric aerosols properties with significant shortage of

in situ observations. Over the Middle East, dust sources extend from the north of the Tigris-Euphrates basin to the coast of Oman, yet dust activity is quite complex and widely impacted by seasonal variability [12]. Temporal and spatial characteristics of Saudi Arabian dust storms, with focus on associated air parcel trajectories, have been investigated using dust concentrations and geochemistry of aerosols, station, and gridded weather observations and remotely sensed aerosol observations [13–15].

Using PM₁₀ concentrations, recorded by the King Abdel Aziz City for Science & Technology (KACST) monitoring network during 2000–2003, nine local and four external dust sources have been identified, in association with seven

types of dust storms, triggered by seasonal distribution of meteorological conditions, yet dominated by Haboob (~42%) and Shamal (~37%). A thorough investigation of one of the most intense dust storms experienced in Saudi Arabia over the last two decades that struck Riyadh and lasted several hours on March 10th, 2009 was conducted [16]. Significant changes of aerosol and meteorological parameters were observed with air pressure rapidly increasing by 4 hPa, temperature decreasing by 6 °C, relative humidity increasing from 10% to 30%, Aerosol Optical Depth (AOD) at 550 nm increasing from 0.396 to 1.71, and Angstrom Exponent (AE) rapidly decreasing from 0.192 to -0.078. On the other hand, seasonality and aerosols' concentration variability impacting cloud properties and serving as condensation nuclei were studied over the Arabian Sea using satellite and ground observations [17, 18], and over other surrounding locations in Northern Africa and Gulf region [19–29]. According to [18] seasonal variations are clearly found in the shape and magnitude of the volume size distribution of the coarse size mode due to dust emission.

A model for PM_{10} dust emission was constructed by [30], using the concept of a threshold friction velocity which is dependent on surface roughness that in turn was correlated with geomorphology or soil properties. This was applied for Kuwait, Iraq, Syria, Saudi Arabia, the United Arab Emirates, and Oman. The model results agreed quantitatively with measurements at four locations in Saudi Arabia and one in Kuwait for one major dust event ($>1000 \mu g/m^3$). On the other hand [31] incorporated a two-stream scattering scheme based on the delta-Eddington approximation into the Florida State University Limited Area Model for computing the shortwave radiative fluxes due to dust aerosols over the Saudi Arabian region and to study their impact on synoptic-scale systems and the diurnal cycle over the region. The average diameter of dust particles collected during a dust storm at various heights near Riyadh was tested by [32]. It was found that most of the particle size distributions can be described by a lognormal or normal distribution depending on the storm condition and height. The average diameter of sand/dust particles decreases with the increase of height according to a power law.

In this paper, we present a detailed climatological analysis of the optical and microphysical aerosol properties using satellite observations over four main selected regions in Saudi Arabia; criteria of selection follow, highlighted in Figure 1. Furthermore, we discuss patterns of aerosol transport and characteristics during the significant March 10, 2009 dust storm as well as aerosol optical and physical characteristics as an extension of the work performed by [16]. Data from two Aerosol RObotic NETwork (AERONET) ground based stations, namely, the Solar Village (long: 46.397 lat. 24.907) and MASDAR (long. 54.617 lat. 24.442) (indicated by 5 and 6, resp., in Figure 1), are also used for validation purposes. The two stations are yet not included in our four selected regions of interest but are seen of great importance for comparison between deserts and urban areas. Aerosols in general have regional behavior and long-range transport may be a factor; therefore, using the ground data is seen as a needed addition.

Region 1 represents the North Western (NW) cities of Saudi Arabia, where temperature ranges from ~46 °C during

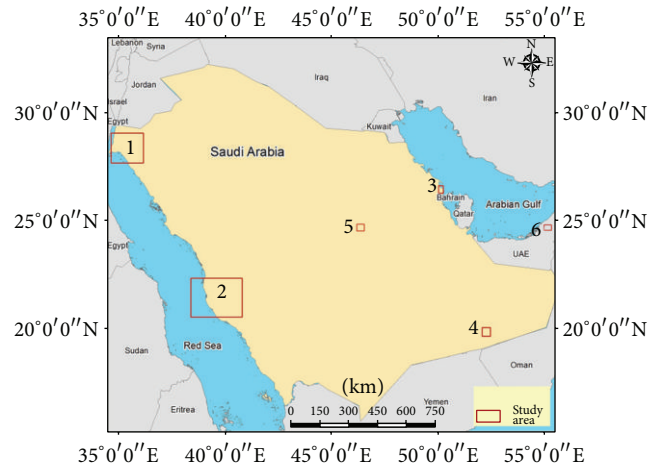


FIGURE 1: Map of Saudi Arabia including the four regions considered in this study represented by the cities of Tabuk, Mecca, and Dhahran and Rub al Khali (Empty Quarter) Desert. AERONET Solar Village and MASDAR locations are indicated by 5 and 6.

summer to ~-6 °C during winter, with rain fall during the winter months from November to March. The NW region has small population of less than 600,000 and contains the Tabuk industrial city on an area of 1.4 million square meter and known for its petrochemical, plastic, aluminum, and steel industries. Region 2 represents the Western Province (WP) of Saudi Arabia that includes three major cities, namely, Jeddah, Mecca, and Madinah known for their high population especially during Muslims' pilgrimage season (Hajj), which is said to be the largest people gathering in the world with more than 2 million visits per year. Particulate pollution is a serious problem in the city of Mecca and in the neighboring regions due to particles emitted by traffic during the Hajj season [33, 34]. Moreover, the city of Mecca is located in a valley in approximately the middle of the Sarawat mountain range that produces large concentrations of airborne sand and anthropogenic aerosols. The WP retains its very warm temperature in winter ~18 °C increasing to ~40 °C during summer, with sparse rain falls between November and January. Region 3 represents the East province (EP) of Saudi Arabia, containing one of the largest industrial complexes in the Middle East including steel mill, oil refinery, world's largest desalination plants, electric power, and petrochemical products such as plastic and fertilizers. The climate of the EP is tropically hot and relatively humid with temperature ranging from ~46 °C during the summer to ~13 °C during the winter [35]. Finally, region 4 is located at the southern Saudi Arabia and represents the Rub al Khali Desert or Empty Quarter (EQ). The EQ is a massive source of aerosols as it covers an area of ~560,000 km² with daily maximum temperature reaching as high as 56 °C and receiving annual rainfall of less than 30 mm.

2. Data Sets and Methods

In this work we utilized aerosol measurements from a number of sensors to leverage the wide variety of aerosol

parameters available from these sensors, which include the Moderate Resolution Imaging Spectroradiometer (MODIS) aboard the Terra and Aqua satellites and the Ozone Monitoring Instrument (OMI) on the Aura satellite to investigate the aerosol optical properties; the Multi-angle Imaging SpectroRadiometer (MISR) instrument on Terra to examine microphysical properties of the aerosols including size and shape; Cloud-Aerosol Lidar and Infrared Pathfinder (CALIOP) sensor on CALIPSO satellite to identify different aerosol types and vertical distribution. Ground-based measurements used in this analysis include the multiyear aerosol AERONET measurements [36] at two sites mentioned above. The HYSPLIT (Hybrid Single-Particle Lagrangian Integrated Trajectory) model version 4 was used to generate air mass forward trajectories. The HYSPLIT model is the latest version of an integrated system for computing air parcel trajectories, dispersion, and deposition simulations [37]. The above-mentioned data will be used to characterize the apparent complex dynamics of the aerosols over the Kingdom that are dominated by coarse mode dust aerosols from the desert, modified and mixed with fine anthropogenic aerosol.

2.1. MODIS/Terra and MODIS/Aqua. MODIS/Terra and MODIS/Aqua instruments provide a number of validated aerosol products that include AOD at 10 km resolution over water and over land [38, 39]. The AOD uncertainty is ± 0.05 ($\pm 0.15 * \text{AOD}$) over land and ± 0.03 ($\pm 0.05 * \text{AOD}$) over ocean. Uncertainty in the monthly average fine fraction aerosol optical depth is $\pm 20\%$ [38]. Over the desert region we use the Deep Blue product rather than the standard AOD product because the latter is retrieved using the dark-target approach [40] at near-infrared wavelengths (2.1 and 3.8 μm) [41]. The two blue channels (0.412 and 0.470 μm) allow the Deep Blue algorithm to be more sensitive to aerosols over bright surfaces for which surface reflectance is relatively small to infer aerosol properties [42]. The MODIS Deep Blue algorithm primarily uses the UV channels to provide aerosol retrievals over deserts and other areas where the operational cannot. The uncertainties of the Deep Blue product are reported to be around 25–30% [43]. The recent release of a new 3-km resolution aerosol product in the MODIS Collection 6 dataset [44] is highly advantageous for studying small regions such as those highlighted in the present study.

2.2. MISR/Terra. MISR/Terra operational aerosol retrievals performed at 17.6 km horizontal resolution include some information about particle size, shape, and single-scattering albedo, in addition to AOD which will be used in this study [45–48]. A global comparison of coincident MISR and AERONET sunphotometer data showed that overall, about 70% to 75% of MISR AOD retrievals fall within 0.05 or $20% * \text{AOD}$, and about 50% to 55% are within 0.03 or $10% * \text{AOD}$, except at sites where dust or mixed dust and smoke are commonly found [48, 49]. Here, we have analyzed the Level 3 monthly aerosol product averaging select Level 1 and Level 2 parameters over daily, monthly, seasonal, and annual time periods from January 2003 to August 2009 to study aerosols shape and size.

2.3. CALIPSO. CALIPSO is a Franco-American mission that supplies a unique dataset of atmospheric vertical profiles measured by CALIOP on-board the satellite with a 30-m vertical resolution. CALIPSO data releases began in mid-June 2006 and include Level 1 radiances, a Level 2 vertical feature mask, and cloud and aerosol layer products [50].

2.4. OMI/Aura. OMI/Aura provides the (UltraViolet Aerosol Index) UVAI data [51–53]. The UVAI is a product of the standard OMI aerosol retrieval, which indicates the UV absorbing aerosols [53]. Absorbing aerosols such as carbonaceous aerosols, desert dust, and volcanic ash above the boundary layer yield positive UVAI values (>1), whereas nonabsorbing small particle aerosols yield small negative values [53]. Absorbing aerosols in the boundary layer may produce small UVAI values (<0.5) that make it difficult to separate their signal from the background noise. Given the large size (13×24 km at nadir) of the OMI pixels, subpixel cloud contamination is a persistent problem resulting in the overestimation of AOD and underestimation of the single-scattering coalbedo [53].

2.5. AERONET. AERONET federation of Cimel sunphotometers provide daytime AOD measurements every 15-min on average covering the 340–1600 nm wavelength range with typical AOD uncertainties of ± 0.015 [36, 54, 55]. AERONET AODs are derived from direct-beam solar measurements, and some information about particle size and indices of refraction are derived from sky-scans which will be used in this study from the stations mentioned in Section 1.

3. Results and Discussion

3.1. Analysis of Aerosol Optical Depth (AOD). In this study, the MODIS Terra and Aqua AOD data were acquired to investigate the aerosols load, characteristics, extent, and temporal variability over three Saudi Arabian subregions including Tabuk (34.70°E to 36.21°E and 27.60°N to 28.99°N); Mecca (38.42°E to 40.82°E and 20.50°N to 22.28°N), and Dhahran (49.98°E to 50.19°E and 26.21°N to 26.56°N) (Figure 1). These regions are selected to represent the NW, W, and E areas of Saudi Arabia, respectively, for spatial representation of aerosols behavior. Figures 2(a), 2(b), and 2(c) show the AOD monthly mean at 550 nm over Tabuk, Mecca, and Dhahran from April 2003 till January 2013. Figure 2(d) shows the monthly Deep Blue at 550 nm over Rub al Khali (Empty Quarter) Desert (52°E to 52.4°E and 19.6°N to 20°N) during the same period. Due to the relatively small reflectance over the Rub al Khali Desert, we used the Deep Blue algorithm for its larger sensitivity to aerosols over bright surfaces as discussed in Section 2.1. Comparing the AOD monthly data over the four regions shows monthly and annual variability with no recurrence pattern over the years. A sudden increase in the aerosol concentration is observed during 2009 over region 3 (EP) that can be attributed to the major March 2009 dust event in Saudi Arabia as well as to some industrial activities in that region [14]. This significant observed increase in the AOD concentration average values over Dhahran (Figure 2(c)) during 2008–2009 yet has

TABLE 1: Annual AOD means for Terra and Aqua over regions 1–3 and for Aqua Deep Blue over region 4 (desert).

Year	Annual mean of Terra AOD			Annual mean of Aqua AOD			Aqua Deep Blue AOD
	Regions			Regions			Regions
	1	2	3	1	2	3	4
2003	0.24 ± 0.02	0.47 ± 0.05	0.56 ± 0.11	0.21 ± 0.02	0.42 ± 0.04	0.47 ± 0.07	0.29 ± 0.04
2004	0.23 ± 0.02	0.35 ± 0.02	0.40 ± 0.04	0.20 ± 0.02	0.33 ± 0.02	0.38 ± 0.03	0.20 ± 0.02
2005	0.24 ± 0.02	0.40 ± 0.07	0.43 ± 0.04	0.22 ± 0.01	0.35 ± 0.03	0.37 ± 0.03	0.24 ± 0.03
2006	0.24 ± 0.01	0.36 ± 0.03	0.41 ± 0.03	0.22 ± 0.02	0.35 ± 0.03	0.40 ± 0.03	0.28 ± 0.04
2007	0.26 ± 0.03	0.38 ± 0.03	0.51 ± 0.06	0.20 ± 0.02	0.38 ± 0.02	0.44 ± 0.04	0.27 ± 0.03
2008	0.25 ± 0.02	0.41 ± 0.04	0.66 ± 0.10	0.20 ± 0.02	0.44 ± 0.05	0.63 ± 0.11	0.32 ± 0.06
2009	0.24 ± 0.02	0.38 ± 0.03	0.65 ± 0.10	0.19 ± 0.01	0.38 ± 0.03	0.71 ± 0.12	0.26 ± 0.04
2010	0.29 ± 0.02	0.39 ± 0.05	0.48 ± 0.05	0.27 ± 0.02	0.42 ± 0.06	0.48 ± 0.05	0.24 ± 0.03
2011	0.22 ± 0.01	0.40 ± 0.04	0.53 ± 0.07	0.20 ± 0.02	0.44 ± 0.06	0.50 ± 0.07	0.31 ± 0.05
2012	0.27 ± 0.04	0.40 ± 0.04	0.52 ± 0.07	0.24 ± 0.03	0.44 ± 0.05	0.50 ± 0.06	0.33 ± 0.05

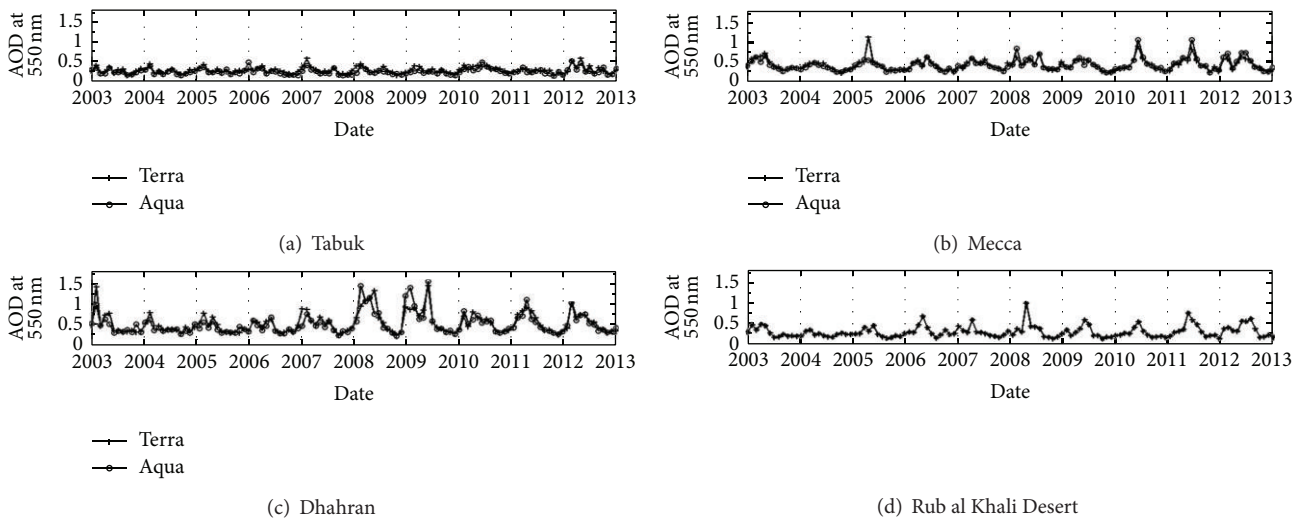


FIGURE 2: Time series plot of MODIS AOD at 550 nm using Terra and Aqua over (a) Tabuk, (b) Mecca, and (c) Dhahran and Aqua Deep Blue data over (d) Rub al Khali (Empty Quarter) Desert.

a slight impact on Mecca (Figure 2(b)) as compared to Rub Al Khali (Figure 2(d)) implying the local nature of this event. On the other hand, the Aqua Deep Blue AOD₅₅₀ data over Rub al Khali Desert (Region 4) (Figure 2(d)) shows a single peak pattern annually taking place during the spring season during which dust events are dominant. Table 1 shows the average AOD with the standard errors over regions 1–4. To examine the AOD background level over the Kingdom, monthly means climatology over regions 3 and 4 using MODIS standard AOD and Deep Blue, respectively, at 550 nm is calculated and represented (Figures 3(a) and 3(b)) with standard vertical error bars of the monthly mean values. The monthly MODIS climatological means shows a cycle with minimum AOD during autumn and winter months and then peaks during spring and summer months. The maximum annual mean AOD₅₅₀ from Aqua and Terra is $\sim 0.82 \pm 0.06$, $\sim 0.72 \pm 0.05$, respectively, while the minimum annual mean is $\sim 0.28 \pm 0.06$, $\sim 0.28 \pm 0.05$, respectively. It is clear that there is still a relatively high AOD background observed over the selected regions which can be associated with the industrial

pollution and petrochemical industry active in region, which is typical of industrial cities in developing countries [7, 56, 57].

Such high background AOD levels would have an indirect impact on the local climate and precipitation levels. Hence, the relation between the mean precipitation rate and AOD levels is investigated and as a result, monthly climatology of the mean precipitation rate over region 3 is additionally plotted to (Figure 3(a)) during the period 2003–2013. Minimum precipitation rates during the summer and maximum during the winter are observed. During March–April and September–November we find that the effect of precipitation on aerosols concentration is not clear owing to the indirect effects as compared with other studies over the Mediterranean basin where precipitation rate was shown as one of the strongest removal processes for atmospheric aerosols in winter [58]. As presented in Figure 3(a) the precipitation rate is very low ranging from 0.02 to 0.04 mm/month; hence, precipitation might have a lower contribution to the wet deposition of aerosols. The possible cause for the lower AOD values

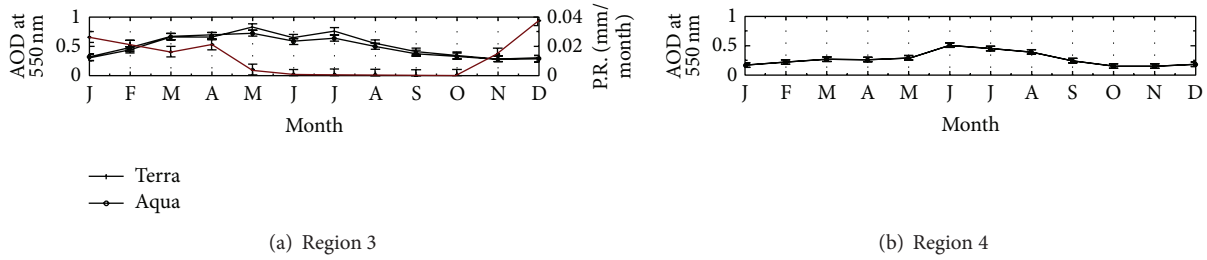


FIGURE 3: Climatology MODIS monthly AOD means over (a) region 3 (EP) from Terra and Aqua (2003–2013), the right axis is for the precipitation rate of the EP for the same period, (b) region 4 (Rub al Khali) with standard deviations.

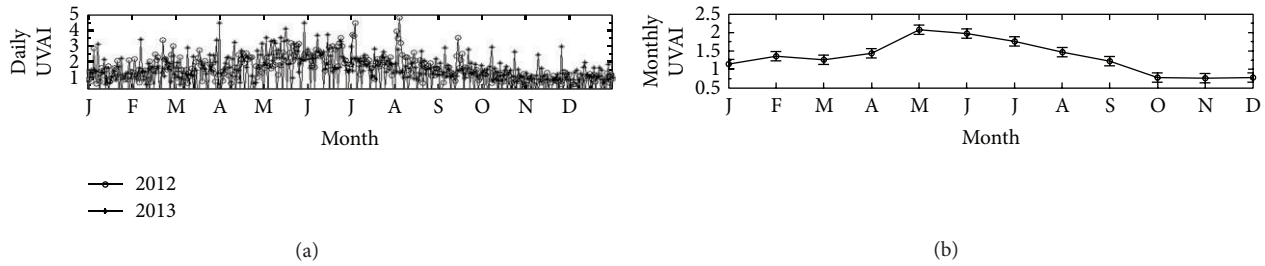


FIGURE 4: (a) The monthly climatology means of UVAI over region 3 (EP) for 2012-2013 and (b) is Daily OMI UVAI for 2012-2013. The vertical bars represent standard errors.

can be precipitation over the source regions or precipitation during the aerosol travel from source to the observation site. If this is not the case, the most probable cause is the seasonal change of the wind stream pattern, which advects the aerosols from the source regions to the observation site as well as higher summer AODs due to accumulation of fine aerosol particles in summer [58]. It is noteworthy that annual dust and anthropogenic pollutants are the main emission sources during March–April and September–November periods. Despite the fact that the available precipitation data suffer from errors, they still can be used for long time averaging [59].

Terra mean AOD results were higher than Aqua during May–August; however the difference is not significantly high, consistent with [38] where they showed that there is no significant difference between Terra and Aqua results. The monthly climatology means over Rub al Khali Desert (Region 4) displays a maximum AOD_{550} value of 0.5035 ± 0.03 and a minimum of 0.1469 ± 0.03 representing lower monthly AOD as compared to that over region 3. This is attributed to the industrial activities and local air pollution over region 3.

3.2. Absorbing Aerosol Characteristics, Vertical Structure, and Subtypes. Absorbing aerosols, originating from arid areas, have long-range transport capability, during which they usually interact with urban/industrial pollutants and other aerosols under various meteorological conditions. Such transport results in a complex mixing scenario among different aerosols, affecting the climate system radiative balance directly and indirectly [2, 60]. To detect and quantify these aerosols, such as carbonaceous and mineral dust, the near-UV aerosol sensing is adequate since they absorb ultraviolet (UV) radiation.

The UVAI data used in this study are sensitive to dust vertical distribution, wind-transport, and the dust size distributions, which is a reasonable approach for arid environments [61]. Figures 4(a) and 4(b) present the daily OMI UVAI variations for 2012–2013 and monthly climatology means of the two-year period over region 3 (EP). We observe perennial positive values indicating the existence of absorbing aerosols all year round [62]. The daily UVAI observations highlight a monthly component during the 2-year period with a clear spike during late spring and summer seasons which is evident from the UVAI monthly climatology showing maxima of 2.1 ± 0.13 in May (Figure 4(b)). The high UVAI values during May are consistent with large AOD values observed from the MODIS data (Figure 3(a)) as compared to those observed over region 4. This leads us to believe in the presence of higher air pollution levels over region 3, representing the oil rich eastern province of Saudi Arabia. It is evident that MODIS AOD and UVAI show a similar pattern in aerosol variability (Figures 3 and 4) yet with sharper AOD peaks during summer. This is owed to the UVAI sensitivity to aerosol layer height [62], where the dust aerosols exist in a wider range of altitudes than possible anthropogenic aerosols, which are confined to the planetary boundary layer (PBL) [26, 28], where UVAI tends to be insensitive to these boundary layer aerosols [63]. This mixing scenario between aerosols of natural and anthropogenic origin is observed from the aerosols vertical backscatter and subtypes obtained from CALIPSO which is quite useful here for observing weak aerosol layers and thin clouds by detecting optical depths of 0.01 or less [64]. In Figure 5, the vertical profiles of the atmosphere up to 20 km, represented by total attenuated backscatter at 532 nm, are shown as CALIPSO overpasses the Eastern part of inland Saudi Arabia on 11 March (Figure 5(a))

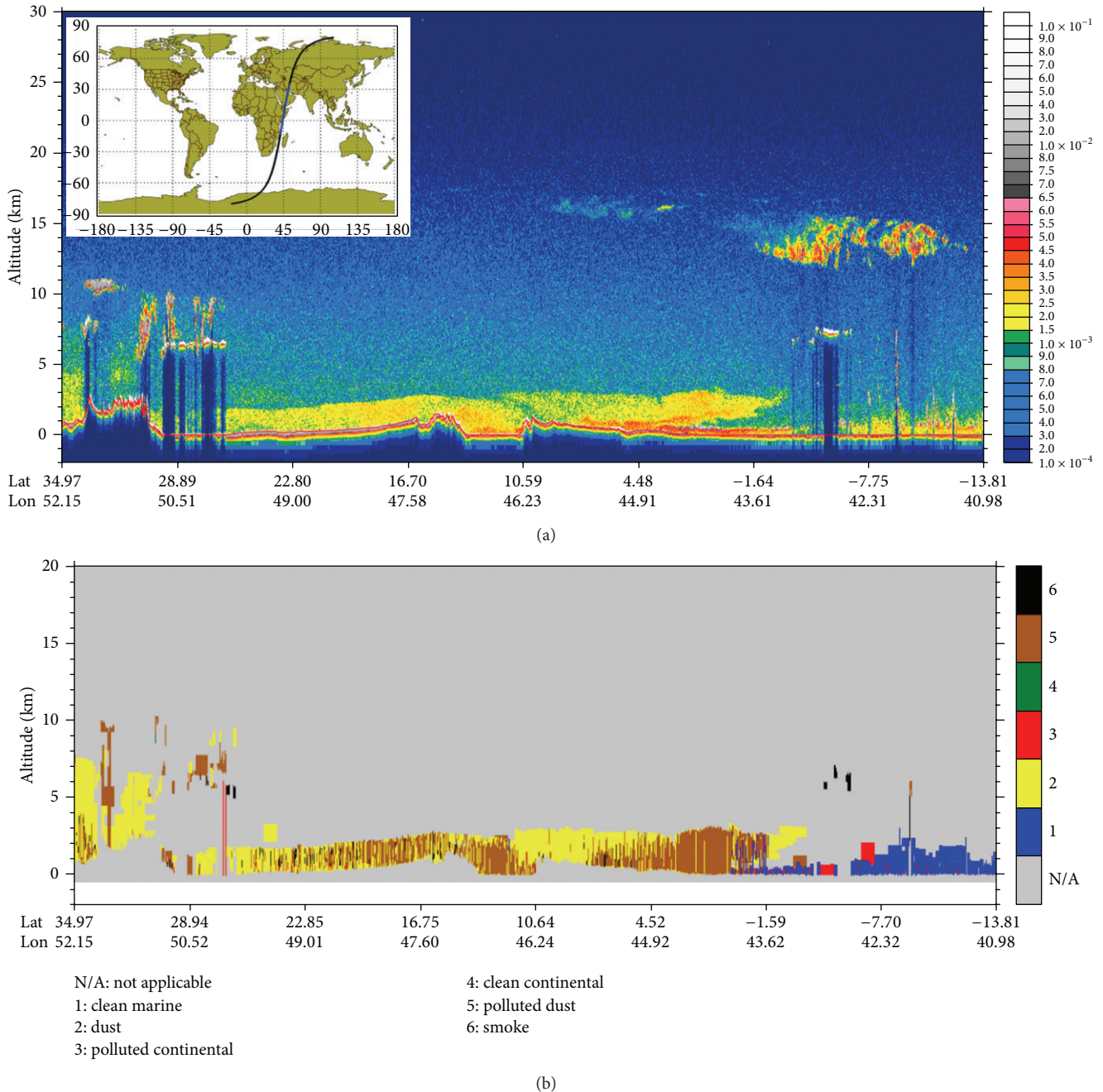


FIGURE 5: CALIPSO (a) total attenuated backscatter at 532 nm of a dust storm event as measured by the night-time CALIPSO overpass over the inland Saudi Arabia (at 2238 to 2251 UTC 11 March 2008) and (b) aerosol subtype over the same area. The surface elevation is shown as a thick black line. The inset map shows the path of CALIPSO overpass over the globe (black line) and the study region (red line).

during nighttime, while Figure 5(b) showed the most abundant aerosol types over selected areas shown in Figure 5(a). The profile clearly shows the vertical structure of a major SDS over the study regions. On 11 March, high concentration of aerosol reached high >5 km over the northern Eastern region and up to 2-3 km over the central and southern areas in the Eastern inland Saudi Arabia, including surrounding Gulf States. Areas in Eastern Africa are mostly covered by clouds, which show extremely high backscatter (topped white) and

block backscatter from the atmosphere (Deep Blue) below them. Mixed cloud layers are observed over region of interest mainly dominated by dust and polluted dust starting at very high altitudes reflecting the fine mode fraction particles distribution which is mainly abundant over the northern part. The major SDS was also identified in other parameters obtained from CALIPSO, such as perpendicular attenuated backscatter (532 nm), total attenuated backscatter at 1064 nm, attenuated color ratio, and depolarization ratio (not shown).

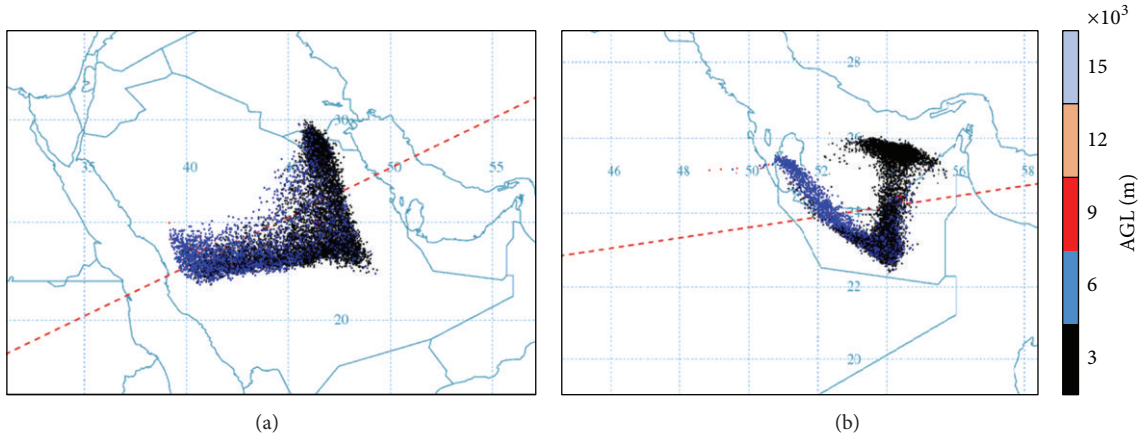


FIGURE 6: HYSPLIT backward trajectory dispersion starting from (a) Solar Village, (b) MASDAR ends on March 09, 2009 13:00 UTC. Heights are indicated by the legend bar.

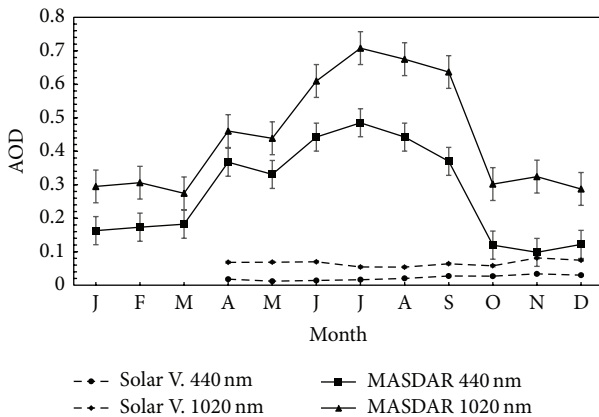


FIGURE 7: AERONET AOD observations at 440 and 1020 nm from April 2012 to May 2013 using Solar Village and MASDAR stations. The vertical bars represent standard errors.

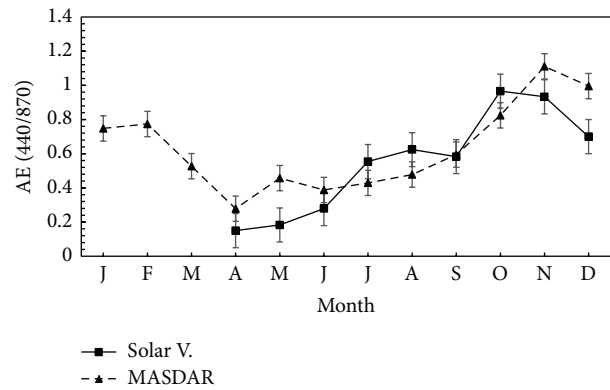


FIGURE 8: AERONET AE observations using MASDAR from April 2012 to May 2013 using MASDAR station. The vertical bars represent standard errors.

3.3. *Microphysical Properties.* AERONET ground-based measurements of AOD data at 440 nm and 1020 nm are analyzed for the available periods of April 2012–December 2012 for Solar Village and from June 2012 till May 2103 for MASDAR to verify satellite data as discussed in Sections 1 and 2.5. As previously discussed we considered the Solar Village location as an AOD representative over desert, while the MASDAR one to represent the AOD over the EP of Saudi Arabia. Moreover, the HYSPLIT backward trajectories shown in Figures 6(a) and 6(b) emphasize the fact that regions 3 and 4 are one of the possible sources of aerosols received at the Solar Village and MASDAR, respectively. The observations from both stations at 440 nm show maxima of 0.71 in July and a minimum of 0.27 in March over MASDAR and a maxima of 0.08 in November and a minimum of 0.05 in August over Solar Village (Figure 7). The high July AOD value (0.71) over MASADR showed a close agreement with the July AOD value (0.76) retrieved from Aqua over the EP, which confirms a general agreement between satellite and MASDAR AOD observations. However, such agreement was

not established between the August AOD value (0.39) from Aqua over region 4 as compared to the AOD low value (0.05) recorded by the Solar Village station. This is expected owing to aerosols deposition taking place as they move from Rub al Khali to the Solar Village for a long distance (Figure 6(a)). It is clear that the AOD values at 440 nm are higher than those at 1020 nm since the longer wavelength is greatly affected by water-vapor absorption and hence is used to derive the total water-vapor column [24].

We use the AERONET AE (440/870) to identify the aerosol origin being natural, anthropogenic, or mixed over regions 3 and 4 of Saudi Arabia where small AE values are associated with large dust particles (natural origin) as compared to large AE values representing small size aerosols (anthropogenic/mixed) (Figure 8). The results show small AE values during spring (mostly desert dust) and larger AE values are observed during July–December mainly associated with smaller particles over MASDAR and Solar Village reflecting a more mixed scenario over both locations. This is attributed to the fact that pollutants as well as mixed aerosols with dust are quite common over Arabia. This is further

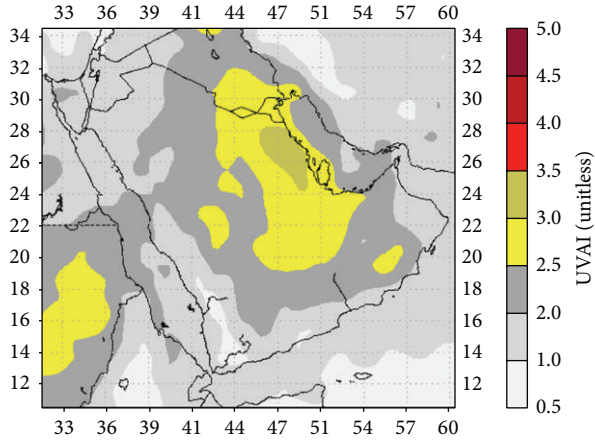


FIGURE 9: OMI UVAI image over Saudi Arabia on March 09, 2009.

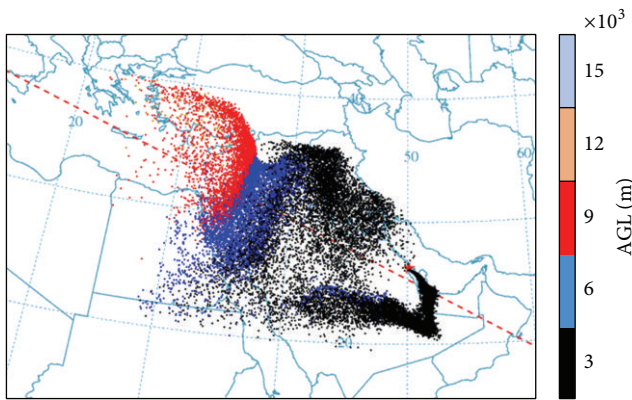


FIGURE 10: HYSPLIT backward trajectory dispersion starting from region 3 on March 09, 2009 16:00 UTC for 3 days. Heights are indicated by the legend bar.

observed from the OMI UVAI data over Saudi Arabia during March 9, 2009 dust storm event where the high UVAI values near region 3 indicate absorbing aerosols mixed with possibly desert dust, where the contribution of small particles from industrial emissions is attributed to the land-breeze circulations in this area [65] (Figure 9). Furthermore, particles' dispersion at different altitudes was observed at 16:00 UTC on March 09, 2009 by examining 3-day back trajectories originating from region 3. The trajectories computed by the HYSPLIT model initiated at 50 m above the ground level show that dust originated from the North West of Saudi Arabia and the east of Egypt where aerosols showed high dominance at ~ 3000 m (Figure 10). However, the middle of the desert where Solar Village is located exhibits mixed particles at 3000 (black) and 6000 (blue) m showing higher deposition as aerosols approach the EP and agreeing with the small AERONET AE values around the springtime favoring dust presence (Figure 10).

MISR AOD, size, and shape fractions data was used to characterize the types of aerosol based on their physical and

TABLE 2: MISR AOD monthly mean size fractions for the period 2003–2013.

	MISR AOD average size fractions		
	Small	Medium	Large
January	0.0418	0.0418	0.1202
February	0.0418	0.0418	0.165
March	0.085	0.0983	0.2667
April	0.275	0.1583	0.3583
May	0.333	0.2733	0.385
June	0.3267	0.2233	0.33
July	0.3633	0.2033	0.3883
August	0.3367	0.075	0.3067
September	0.2233	0.05	0.18
October	0.1283	0.05	0.16
November	0.0633	0.05	0.0933
December	0.05	0.05	0.0783

optical properties to study aerosols microphysics. The MISR AOD at 558 nm data categorizes particles into small, medium, and large sizes as well as to spherical and nonspherical. Figures 11(a) and 11(b) present the monthly size and shape averages, from 2003 to 2013 over region 3 where the large and small size particles' fraction showed higher dominance than the medium ones (Figure 11(a)) with even more large size particles abundance during spring season. Such particle size occurrence agrees with the AE values with distinct dusty versus anthropogenic episodes as compared to mixed ones. It is also noticed that spherical particles are higher than nonspherical and show a more stable value all year round indicating high pollution levels. However, the nonspherical particles are significantly higher during March–July than the rest of the year (Figure 11(b)) which is consistent with the dust storms season extending from March till late summer [14]. The AOD of nonspherical particles reaches a maximum in June with a value of $\sim 0.3517 \pm 0.01$, where the maximum of the spherical fraction AOD occurs in July with a value of $\sim 0.4867 \pm 0.01$. The large AOD fractions are higher during March–May with a significant contribution from the desert dust, while during the rainy season, November–February, the AOD of small, medium and large particles significantly drops as expected.

During spring and summer seasons the MISR AOD generally shows higher values for large and small size particles as compared to the medium ones shown in Table 2. These high values during these seasons disclose that most particles are of large sizes with a radius larger than $1 \mu\text{m}$ especially for April and May. However, the October distribution shows that both small and large particles exist with more domination of large particles as can be revealed from the two peaks at ~ 0.1 and $\sim 4 \mu\text{m}$ (Figure 12). The above results related to AOD, AE, and size distribution during spring and other seasons agrees with the spring maximum local desert-dust activity as well as mixed scenarios during other seasons [66].

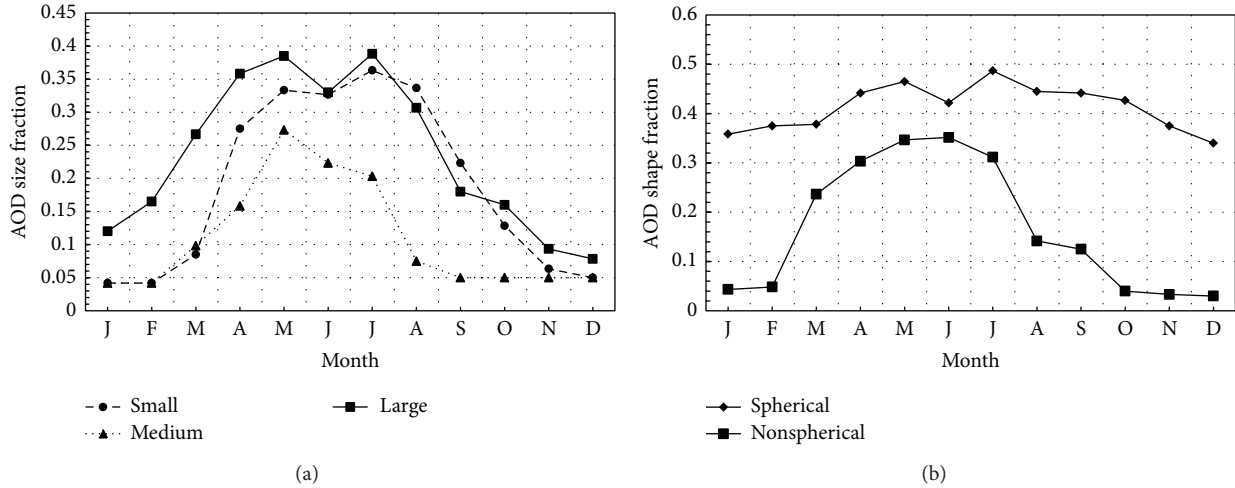


FIGURE 11: Climatology of AOD shape fraction and size over region 3 using MISR Level 3 at 558 nm (green band) (2003–2013): (a) size and (b) shape.

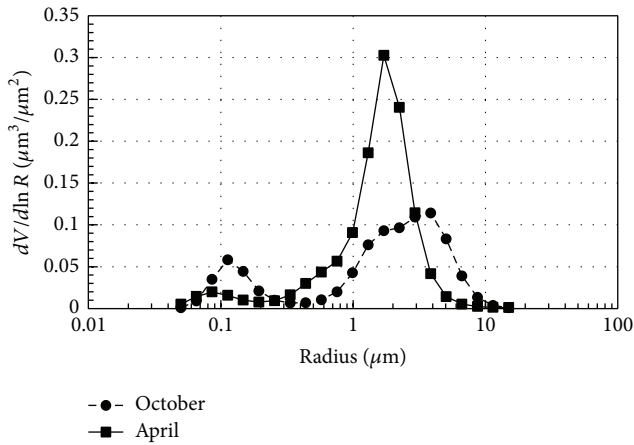


FIGURE 12: Size distribution of AERONET station at Solar Village in April 2012 and October 2012.

4. Conclusions

Sand-dust storms (SDSs) over the gulf region affect human life in various aspects including health and economy. They can be associated with climate change and result in different feedback mechanisms as well as with air pollution. Therefore, early detection and monitoring of SDSs is a matter of the utmost importance for possible risk reduction caused by these hazardous phenomena. Generally, satellite sensing using various sensors equipped for different purposes, provides synthetic ways of monitoring SDSs most effectively. In this study, multisensor approach is applied to severe SDS cases, which originated in Arabia and from the surroundings, to investigate characteristics of the case storm and to explore the capability of such approaches for its detection and monitoring. For this purpose, we employ several satellite sensors, namely, MODIS, OMI, and the lidar instrument and visible-infrared imagers on-board CALIPSO and data

from the AERONET ground stations. Information on aerosol loading is provided by AOD retrieved from the Terra/Aqua MODIS. For retrieving AOD over bright land surface, DB algorithm was adopted. For the dust storm event, information on dust clouds was obtained by the standard AOD except over the bright surface areas around Rub al Khali (Empty Quarter) Desert, which were covered by DB AOD. This indicates that combined aerosol loading information available from other algorithms (and sensors) provide more continuous and complete detection of severe SDSs.

Overall the multisensor approach using satellite remote sensing provides useful information on various properties of the dust storm event, including location and magnitude of aerosol loading, size mode of aerosols, the behavior of long-lived absorbing aerosols, and the vertical structure. This enables us to make more continuous and complete detection of severe SDSs. In addition, our approach provides information on anthropogenic aerosols and pollutants, not just dust particles. Early detection of such aerosols and pollutants is especially very useful and important for health protection in the areas located downstream from the source region.

Conflict of Interests

The authors declare that there is no conflict of interests regarding the publication of this paper.

Acknowledgments

The authors would like to acknowledge the support provided by King Abdulaziz City for Science and Technology (KACST) for funding this work under Grant no. MT-32-76. The support provided by the Deanship of Research at King Fahd University of Petroleum & Minerals (KFUPM) is gratefully acknowledged. Analyses and visualizations used in this study were produced with the Giovanni online data

system, developed and maintained by the NASA GES DISC. They also acknowledge the MODIS mission scientists and associated NASA personnel for the production of the data used in this research effort. Furthermore, the authors would like also to acknowledge the use of the Samueli Laboratory in Computational Sciences in the Schmid College of Science and Technology, Chapman University, for image processing and data analysis.

References

- [1] M. D. King, Y. J. Kaufman, D. Tanré, and T. Nakajima, "Remote Sensing of Tropospheric Aerosols from Space: Past, Present, and Future," *Bulletin of the American Meteorological Society*, vol. 80, no. 11, pp. 2229–2259, 1999.
- [2] Y. J. Kaufman, D. Tanré, and O. Boucher, "A satellite view of aerosols in the climate system," *Nature*, vol. 419, no. 6903, pp. 215–223, 2002.
- [3] K. K. Moorthy, V. S. Nair, S. S. Babu, and S. K. Satheesh, "Spatial and vertical heterogeneities in aerosol properties over oceanic regions around india: implications for radiative forcing," *Quarterly Journal of the Royal Meteorological Society*, vol. 135, no. 645, pp. 2131–2145, 2009.
- [4] P. Ginoux, D. Garbuzov, and N. C. Hsu, "Identification of anthropogenic and natural dust sources using moderate resolution imaging spectroradiometer (MODIS) deep blue level 2 data," *Journal of Geophysical Research D: Atmospheres*, vol. 115, no. 5, 2010.
- [5] T. M. Saeed, H. Al-Dashti, and C. Spyrou, "Aerosol's optical and physical characteristics and direct radiative forcing during a shamal dust storm: a case study," *Atmospheric Chemistry and Physics*, vol. 14, no. 7, pp. 3751–3769, 2014.
- [6] J. Heinrich and R. Slama, "Fine particles, a major threat to children," *International Journal of Hygiene and Environmental Health*, vol. 210, no. 5, pp. 617–622, 2007.
- [7] Y. Aboel Fetouh, H. El Askary, M. El Raey, M. Allali, W. A. Sprigg, and M. Kafatos, "Annual patterns of atmospheric pollutions and episodes over Cairo Egypt," *Advances in Meteorology*, vol. 2013, Article ID 984853, 11 pages, 2013.
- [8] W. A. Sprigg, S. Nickovic, J. N. Galgiani et al., "Regional dust storm modeling for health services: the case of valley fever," *Aeolian Research*, vol. 14, pp. 53–73, 2014.
- [9] H. El-Askary, R. Gautam, R. P. Singh, and M. Kafatos, "Dust storms detection over the Indo-Gangetic basin using multi sensor data," *Advances in Space Research*, vol. 37, no. 4, pp. 728–733, 2006.
- [10] A. I. Rushdi, K. F. Al-Mutlaq, B. R. T. Simoneit et al., "Characteristics of lipid tracer compounds transported to the Arabian Gulf by runoff from rivers and atmospheric dust transport," *Arabian Journal of Geosciences*, vol. 3, no. 2, pp. 113–131, 2010.
- [11] A. I. Rushdi, K. F. Al-Mutlaq, M. Al-Otaibi, A. H. El-Mubarak, and B. R. T. Simoneit, "Air quality and elemental enrichment factors of aerosol particulate matter in Riyadh City, Saudi Arabia," *Arabian Journal of Geosciences*, vol. 6, no. 2, pp. 585–599, 2013.
- [12] J. M. Prospero, P. Ginoux, O. Torres, S. E. Nicholson, and T. E. Gill, "Environmental characterization of global sources of atmospheric soil dust identified with the Nimbus 7 Total Ozone Mapping Spectrometer (TOMS) absorbing aerosol product," *Reviews of Geophysics*, vol. 40, no. 1, pp. 2-1-2-31, 2002.
- [13] P. P. Pease, V. P. Tchakerian, and N. W. Tindale, "Aerosols over the Arabian Sea: geochemistry and source areas for aeolian desert dust," *Journal of Arid Environments*, vol. 39, no. 3, pp. 477–496, 1998.
- [14] B. H. Alharbi, A. Maghrabi, and N. Tapper, "The march 2009 dust event in Saudi Arabia: precursor and supportive environment," *Bulletin of the American Meteorological Society*, vol. 94, no. 4, pp. 515–528, 2013.
- [15] M. Notaro, F. Alkolibi, E. Fadda, and F. Bakhrijy, "Trajectory analysis of Saudi Arabian dust storms," *Journal of Geophysical Research D: Atmospheres*, vol. 118, no. 12, pp. 6028–6043, 2013.
- [16] A. Maghrabi, B. Alharbi, and N. Tapper, "Impact of the March 2009 dust event in Saudi Arabia on aerosol optical properties, meteorological parameters, sky temperature and emissivity," *Atmospheric Environment*, vol. 45, no. 13, pp. 2164–2173, 2011.
- [17] T. A. Jones and S. A. Christopher, "Seasonal variation in satellite-derived effects of aerosols on clouds in the Arabian Sea," *Journal of Geophysical Research D: Atmospheres*, vol. 113, no. 9, Article ID D09207, 2008.
- [18] I. Sabbah and F. M. Hasan, "Remote sensing of aerosols over the Solar Village, Saudi Arabia," *Atmospheric Research*, vol. 90, no. 2-4, pp. 170–179, 2008.
- [19] A. Smirnov, B. N. Holben, O. Dubovik et al., "Atmospheric aerosol optical properties in the Persian Gulf," *Journal of the Atmospheric Sciences*, vol. 59, no. 3, pp. 620–634, 2002.
- [20] H. Kutiel and H. Furman, "Dust storms in the Middle East: sources of Origin and their temporal characteristics," *Indoor and Built Environment*, vol. 12, no. 6, pp. 419–426, 2003.
- [21] J. Barkan, H. Kutiel, and P. Alpert, "Climatology of dust sources in North Africa and the Arabian Peninsula, based on TOMS data," *Indoor and Built Environment*, vol. 13, no. 6, pp. 407–419, 2004.
- [22] H. M. El-Askary, S. Sarkar, M. Kafatos, and T. A. El-Ghazawi, "A multisensor approach to dust storm monitoring over the Nile delta," *IEEE Transactions on Geoscience and Remote Sensing*, vol. 41, no. 10, pp. 2386–2391, 2003.
- [23] H. El-Askary and M. Kafatos, "Dust storm and black cloud influence on aerosol optical properties over Cairo and the greater Delta Region, Egypt," *International Journal of Remote Sensing*, vol. 29, no. 24, pp. 7199–7211, 2008.
- [24] H. El-Askary, R. Farouk, C. Ichoku, and M. Kafatos, "Inter-continental transport of dust and pollution aerosols across Alexandria, Egypt," *Annales Geophysicae*, vol. 27, no. 7, pp. 2869–2879, 2009.
- [25] S. A. Christopher and T. A. Jones, "Satellite and surface-based remote sensing of Saharan dust aerosols," *Remote Sensing of Environment*, vol. 114, no. 5, pp. 1002–1007, 2010.
- [26] H. S. Marey, J. C. Gille, H. M. El-Askary, E. A. Shalaby, and M. E. El-Raey, "Study of the formation of the 'black cloud' and its dynamics over Cairo, Egypt, using MODIS and MISR sensors," *Journal of Geophysical Research D: Atmospheres*, vol. 115, no. 21, Article ID D21206, 2010.
- [27] A. K. Prasad, H. El-Askary, and M. Kafatos, "Implications of high altitude desert dust transport from Western Sahara to Nile Delta during biomass burning season," *Environmental Pollution*, vol. 158, no. 11, pp. 3385–3391, 2010.
- [28] H. S. Marey, J. C. Gille, H. M. El-Askary, E. A. Shalaby, and M. E. El-Raey, "Aerosol climatology over Nile Delta based on MODIS, MISR and OMI satellite data," *Atmospheric Chemistry and Physics*, vol. 11, no. 20, pp. 10637–10648, 2011.

- [29] T. M. Saeed and H. Al-Dashti, "Optical and physical characterization of 'Iraqi freedom' dust storm, a case study," *Theoretical and Applied Climatology*, vol. 104, no. 1-2, pp. 123–137, 2011.
- [30] R. R. Draxler, D. A. Gillette, J. S. Kirkpatrick, and J. Heller, "Estimating PM10 air concentrations from dust storms in Iraq, Kuwait and Saudi Arabia," *Atmospheric Environment*, vol. 35, no. 25, pp. 4315–4330, 2001.
- [31] S. M. Mohalfi, H. S. Bedi, T. N. Krishnamurti, and S. D. Cocke, "Impact of shortwave radiative effects of dust aerosols on the summer season heat low over Saudi Arabia," *Monthly Weather Review*, vol. 126, no. 12, pp. 3153–3168, 1998.
- [32] A. S. Ahmed, A. A. Adel, and A. A. Mohammed, "Airborne dust size analysis for tropospheric propagation of millimetric waves into dust storms," *IEEE Transactions on Geoscience and Remote Sensing*, vol. GE-25, no. 5, pp. 593–599, 1987.
- [33] H. A. Al-Jeelani, "Air quality assessment at Al-Taneem area in the Holy Makkah City, Saudi Arabia," *Environmental Monitoring and Assessment*, vol. 156, no. 1–4, pp. 211–222, 2009.
- [34] H. A. Al-Jeelani, "The impact of traffic emission on air quality in an urban environment," *Journal of Environmental Protection*, vol. 4, no. 2, pp. 205–217, 2013.
- [35] A. I. Rushdi, A. H. El-Mubarak, L. Lijotra et al., "Characteristics of organic compounds in aerosol particulate matter from Dhahran city, Saudi Arabia," *Arabian Journal of Chemistry*, 2014.
- [36] B. N. Holben, T. F. Eck, I. Slutsker et al., "AERONET—a federated instrument network and data archive for aerosol characterization," *Remote Sensing of Environment*, vol. 66, no. 1, pp. 1–16, 1998.
- [37] R. R. Draxler, B. Stunder, G. Rolph, A. Stein, and A. Taylor, *HYSPLIT4 User's Guide Version 4.9*, 2009, http://www.arl.noaa.gov/documents/reports/hysplit_user_guide.pdf.
- [38] L. A. Remer, Y. J. Kaufman, D. Tanré et al., "The MODIS aerosol algorithm, products, and validation," *Journal of the Atmospheric Sciences*, vol. 62, no. 4, pp. 947–973, 2005.
- [39] R. C. Levy, L. A. Remer, R. G. Kleidman et al., "Global evaluation of the Collection 5 MODIS dark-target aerosol products over land," *Atmospheric Chemistry and Physics*, vol. 10, no. 21, pp. 10399–10420, 2010.
- [40] Y. J. Kaufman, D. Tanré, L. A. Remer, E. F. Vermote, A. Chu, and B. N. Holben, "Operational remote sensing of tropospheric aerosol over land from EOS moderate resolution imaging spectroradiometer," *Journal of Geophysical Research D: Atmospheres*, vol. 102, no. 14, pp. 17051–17067, 1997.
- [41] Y. J. Kaufman, A. E. Wald, L. A. Remer, B.-C. Gao, R.-R. Li, and L. Flynn, "MODIS 2.1- μm channel-correlation with visible reflectance for use in remote sensing of aerosol," *IEEE Transactions on Geoscience and Remote Sensing*, vol. 35, no. 5, pp. 1286–1298, 1997.
- [42] N. C. Hsu, S.-C. Tsay, M. D. King, and J. R. Herman, "Aerosol properties over bright-reflecting source regions," *IEEE Transactions on Geoscience and Remote Sensing*, vol. 42, no. 3, pp. 557–569, 2004.
- [43] N. C. Hsu, S. C. Tsay, M. D. King, and J. R. Herman, "Deep blue retrievals of Asian aerosol properties during ACE-Asia," *IEEE Transactions on Geoscience and Remote Sensing*, vol. 44, no. 11, pp. 3180–3195, 2006.
- [44] R. C. Levy, S. Mattoo, L. A. Munchak et al., "The Collection 6 MODIS aerosol products over land and ocean," *Atmospheric Measurement Techniques*, vol. 6, no. 11, pp. 2989–3034, 2013.
- [45] J. V. Martonchik, D. J. Diner, K. A. Crean, and M. A. Bull, "Regional aerosol retrieval results from MISR," *IEEE Transactions on Geoscience and Remote Sensing*, vol. 40, no. 7, pp. 1520–1531, 2002.
- [46] J. V. Martonchik, D. J. Diner, R. A. Kahn, B. J. Gaitley, and B. N. Holben, "Comparison of MISR and AERONET aerosol optical depths over desert sites," *Geophysical Research Letters*, vol. 31, no. 16, 2004.
- [47] J. V. Martonchik, R. A. Kahn, and D. J. Diner, "Retrieval of aerosol properties over land using MISR observations," in *Satellite Aerosol Remote Sensing Over Land*, A. Kokhanovsky, Ed., pp. 267–293, Springer, Berlin, Germany, 2009.
- [48] R. A. Kahn, B. J. Gaitley, M. J. Garay et al., "Multiangle Imaging Spectroradiometer global aerosol product assessment by comparison with the Aerosol Robotic Network," *Journal of Geophysical Research D: Atmospheres*, vol. 115, no. 23, Article ID D23209, 2010.
- [49] R. A. Kahn, B. J. Gaitley, J. Martonchik, D. Diner, K. Crean, and B. N. Holben, "MISR global aerosol optical depth validation based on two years of coincident AERONET observations," *Journal of Geophysical Research—Atmospheres*, vol. 110, Article ID D10S04, 2005.
- [50] D. M. Winker, J. Pelon, and M. P. McCormick, "The CALIPSO mission: spaceborne lidar for observation of aerosols and clouds," in *3rd Lidar Remote Sensing for Industry and Environment Monitoring*, vol. 4893 of *Proceedings of SPIE*, pp. 1–11, Hangzhou, China, March 2003.
- [51] P. F. Levelt, G. H. J. van den Oord, M. R. Dobber et al., "The ozone monitoring instrument," *IEEE Transactions on Geoscience and Remote Sensing*, vol. 44, no. 5, pp. 1093–1100, 2006.
- [52] O. Torres, P. K. Bhartia, A. Sinyuk, E. J. Welton, and B. N. Holben, "Total Ozone Mapping Spectrometer measurements of aerosol absorption from space: comparison to SAFARI 2000 ground-based observations," *Journal of Geophysical Research D: Atmospheres*, vol. 110, no. 10, Article ID D10S18, pp. 1–12, 2005.
- [53] O. Torres, A. Tanskanen, B. Veihelmann et al., "Aerosols and surface UV products from Ozone Monitoring Instrument observations: an overview," *Journal of Geophysical Research D: Atmospheres*, vol. 112, no. 24, Article ID D24S47, 2007.
- [54] B. N. Holben, D. Tanré, A. Smirnov et al., "An emerging ground-based aerosol climatology: aerosol optical depth from AERONET," *Journal of Geophysical Research D: Atmospheres*, vol. 106, no. 11, pp. 12067–12097, 2001.
- [55] O. Dubovik, A. Smirnov, B. N. Holben et al., "Accuracy assessments of aerosol optical properties retrieved from Aerosol Robotic Network (AERONET) sun and sky radiance measurements," *Journal of Geophysical Research D: Atmospheres*, vol. 105, no. 8, pp. 9791–9806, 2000.
- [56] S. Dey and L. Di Girolamo, "A climatology of aerosol optical and microphysical properties over the Indian subcontinent from 9 years (2000–2008) of Multiangle Imaging Spectroradiometer (MISR) data," *Journal of Geophysical Research D: Atmospheres*, vol. 115, no. 15, Article ID D15204, 2010.
- [57] H. El-Askary and M. Kafatos, "Dust storm and black cloud influence on aerosol optical properties over Cairo and the Greater Delta region, Egypt," *International Journal of Remote Sensing*, vol. 29, no. 24, pp. 7199–7211, 2008.
- [58] C. D. Papadimas, N. Hatzianastassiou, N. Mihalopoulos, X. Querol, and I. Vardavas, "Spatial and temporal variability in

- aerosol properties over the Mediterranean basin based on 6-year (2000–2006) MODIS data,” *Journal of Geophysical Research D: Atmospheres*, vol. 113, no. 11, Article ID D11205, 2008.
- [59] R. Kistler, E. Kalnay, W. Collins et al., “The NCEP-NCAR 50-year reanalysis: Monthly means CD-ROM and documentation,” *Bulletin of the American Meteorological Society*, vol. 82, no. 2, pp. 247–267, 2001.
- [60] C. Ahn, O. Torres, and P. K. Bhartia, “Comparison of ozone monitoring instrument UV aerosol products with aqua/moderate resolution imaging spectroradiometer and multiangle imaging spectroradiometer observations in 2006,” *Journal of Geophysical Research D: Atmospheres*, vol. 113, no. 16, Article ID D16S27, 2008.
- [61] K. Schepanski, I. Tegen, B. Laurent, B. Heinold, and A. Macke, “A new Saharan dust source activation frequency map derived from MSG-SEVIRI IR-channels,” *Geophysical Research Letters*, vol. 34, no. 18, Article ID L18803, 2007.
- [62] O. Torres, P. K. Bhartia, J. R. Herman, Z. Ahmad, and J. Gleason, “Derivation of aerosol properties from satellite measurements of backscattered ultraviolet radiation: theoretical basis,” *Journal of Geophysical Research D: Atmospheres*, vol. 103, no. 14, pp. 17099–17110, 1998.
- [63] N. M. Mahowald and J.-L. Dufresne, “Sensitivity of TOMS aerosol index to boundary layer height: implications for detection of mineral aerosol sources,” *Geophysical Research Letters*, vol. 31, no. 3, Article ID L03103, 2004.
- [64] M. J. McGill, M. A. Vaughan, C. R. Trepte et al., “Airborne validation of spatial properties measured by the CALIPSO lidar,” *Journal of Geophysical Research D: Atmospheres*, vol. 112, no. 20, Article ID D20201, 2007.
- [65] T. F. Eck, B. N. Holben, J. S. Reid et al., “Spatial and temporal variability of column-integrated aerosol optical properties in the southern Arabian Gulf and United Arab Emirates in summer,” *Journal of Geophysical Research D: Atmospheres*, vol. 113, no. 1, 2008.
- [66] A. Smirnov, B. N. Holben, O. Dubovik et al., “Atmospheric aerosol optical properties in the Persian Gulf,” *Journal of the Atmospheric Sciences*, vol. 59, no. 3, pp. 620–634, 2002.

Research Article

Studying Air Pollutants Origin and Associated Meteorological Parameters over Seoul from 2000 to 2009

Sunmin Park,¹ Hesham El-Askary,^{2,3,4} Ismail Sabbah,^{5,6} Hanbin Kwak,⁷
Anup K. Prasad,⁸ Woo-Kyun Lee,⁷ and Menas Kafatos³

¹Department of Earth Science, University of California Riverside, Riverside, CA 92521, USA

²Schmid College of Science and Technology, Chapman University, Orange, CA 92866, USA

³Center of Excellence in Earth Systems Modeling and Observation, Chapman University, Orange, CA 92866, USA

⁴Department of Environmental Sciences, Faculty of Science, Alexandria University, Moharam Bek, Alexandria 21522, Egypt

⁵Department of Natural Sciences, College of Health Sciences, Public Authority for Applied Education and Training, Faiha, P.O. Box 14281, 72853 Kuwait, Kuwait

⁶Department of Physics, Faculty of Science, Alexandria University, Moharam Bek, Alexandria 21522, Egypt

⁷Department of Environmental Science & Ecological Engineering, Korea University, Seoul 136-713, Republic of Korea

⁸Department of Applied Geology, Indian School of Mines, Dhanbad 826004, India

Correspondence should be addressed to Woo-Kyun Lee; leewk@korea.ac.kr

Received 27 August 2014; Accepted 23 January 2015

Academic Editor: Slobodan Nickovic

Copyright © 2015 Sunmin Park et al. This is an open access article distributed under the Creative Commons Attribution License, which permits unrestricted use, distribution, and reproduction in any medium, provided the original work is properly cited.

We investigate the temporal characteristics of major air pollutants collected from 44 air quality stations over the city of Seoul, Korea, namely, nitrogen dioxide, carbon monoxide, particulate matter at 10 microns, and sulfur dioxide (SO₂) between 2000 and 2009. The corresponding satellite datasets, namely, aerosol optical depth (AOD_{sat}), Ångström exponent, and fine mode fraction, collected from moderate resolution imaging spectroradiometer (MODIS) as well as the Aeronet ground aerosol optical depth (AOD_{aeronet}), have been analyzed. Pollutants' seasonal effect has been inferred from the precipitation and temperature. The four pollutants under study show varying temporal characteristics with different annual mean concentration patterns. The monthly mean of mentioned pollutants all show similar low concentrations during the summer season and high concentrations during the winter season. We found that pollution is strongly linked to temperature and precipitation variability, especially during the fall season. Satellite data analysis provides information on the pollutants origin whether of natural or anthropogenic type. Our results indicate that the anthropogenic aerosol is dominant in the summer season even though the concentration was lower than the other seasons. AOD_{aeronet} and Ångström exponent indicated high positive and negative correlation coefficients with PM₁₀, 0.60, and -0.45, respectively. Both small and large sizes of aerosols existed in 2007; however coarse size of aerosols was the primary component in 2002.

1. Introduction

Over the last few decades we have witnessed a large increase in the amounts and types of pollutants that emitted into the atmosphere since the Industrial Revolution. Their direct and indirect influences have been of concern due to their significant harm to human health, crops, and vegetation on regional and local (microzone) scales [1–4]. Although aerosols impact the global climate via different physical processes, yet a stronger impact on regional scales is particularly expected [5].

However, the physical characteristics, spatial distribution, and dynamics of aerosols are not completely understood [6–9]. Ground-based data enable the climatology of the aerosol attributes to be observed [10, 11], which can be verified by the application of satellite data [12, 13]. The origin of aerosols' effects and relationships with meteorological factors are essential elements in the study of mesoscale modeling, as well as regional impacts [14]. They can be of either natural origin such as dust storms, forest fires, and volcanoes or anthropogenic one such as electricity generation, traffic,

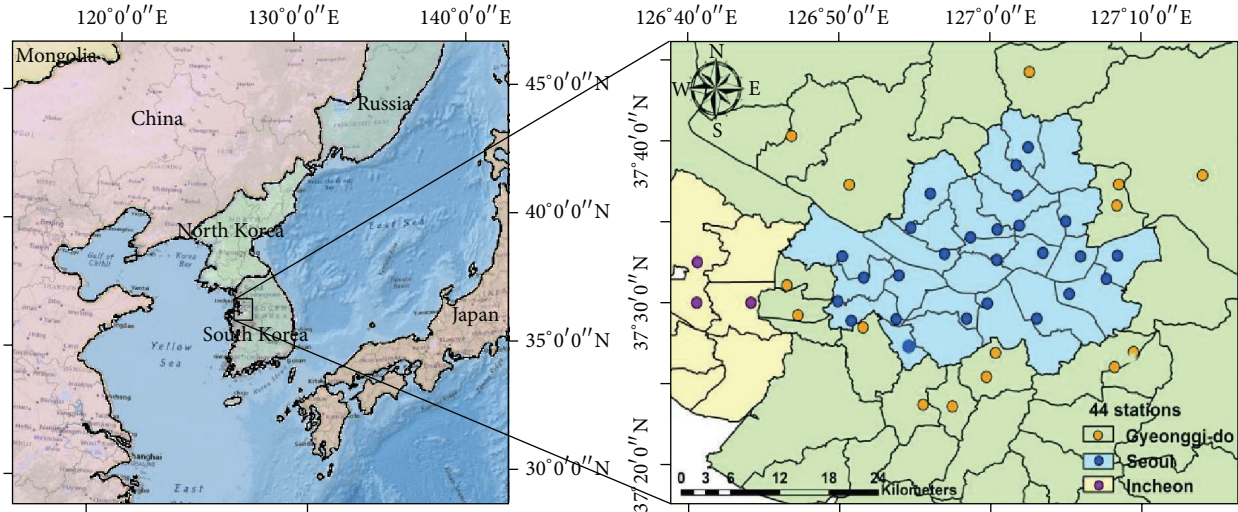


FIGURE 1: Base map of the study area, showing 44 air pollution monitoring stations.

wood fire heating, and industrial manufacturing processes [15–24].

East Asia has been experiencing frequent extremely high concentrations of sulfates, black carbon, nitrates, and organic matters due to increasing fossil fuel burning, as reported from the ACE-Asia campaign [25]. Previous work showed that the anthropogenic aerosols over the Eastern Asia were of much higher concentrations than those over Europe and the Eastern US [26, 27]. Kim et al. [28] investigated diurnal behavior and exceedance patterns of air quality criteria, ozone (O_3), and nitrogen dioxide (NO_2) in Seoul and showed that their behavior is strongly linked with geographical and meteorological factors. Harmful pollutants were observed at regional and temporal scales for particulate matter (PM_{10}) concentration over seven cities in Korea during the 2002 dust event as compared to the 2001 one [18].

Of particular concern is urban aerosol pollution, which has been the subject of many studies. Typical results of industrialization and urbanization have indicated many problems arising from urban aerosols [17, 29–33].

A great deal of research on aerosols has been carried out for several specific air pollutants in terms of their origin and relationship with meteorological parameters or seasonality using either ground or satellite observations [16, 34–38]. Using satellite observation data is an efficient way to determine and distinguish the optical properties of aerosols as it provides more complete coverage over longer time scales [32, 39–42]. Ground-based and satellite sensing of air pollutants may show different, but complementary characteristics; however, both are important in different situations, as well as for cross validation of the pollution origin [8].

Chang and Lee [34] investigated the temporal variation of air quality over Taipei city and found that primary pollutants such as carbon monoxide (CO), NO_x , and sulfur dioxide (SO_2) showed low concentration from local source activities when wind speed increases and the temperature drops. However, dusty days in Kuwait contributed to an evident decrease in temperature [43]. Choi et al. [44] found a possible

relationship between cloud formation and PM_{10} on weekly timescales when studying the interaction between PM_{10} and the meteorological parameters in the boundary layer over China. Lee et al. [45] found that the annual mean SO_2 concentration in Seoul was higher than in Hamilton, Canada, and lower than in Chicago yet with the highest values during the winter season in Seoul, which is consistent with the high winter-time fuel usage.

The main purpose of the present work is to study the sources and origin of aerosol loading, being natural or anthropogenic, over Seoul, using ground and satellite observations between 2000 and 2009. We also investigate the relationships between pollutants, namely, NO_2 , CO, SO_2 , and PM_{10} , and meteorological parameters such as temperature, precipitation, and wind speed to determine the influence of meteorological conditions on pollutants concentrations.

2. Materials

2.1. Study Area. The study area is Seoul, the capital of South Korea, and its basin area, located in $126^{\circ}62'E$, $37^{\circ}99'N$ and enclosed by mountains to the north and east (Figure 1). Seoul is characterized by noticeable distinction between the four seasons with warm weather in spring, hot and humid in summer, cool in fall, and cold and dry in winter [46].

Seoul has been experiencing serious pollution problems from local and external sources and in turns systemically polluting surrounding cities. In addition, it is one of the most densely populated cities in the world, with approximately 49% of Korea's entire population and 46% of vehicles holdings; however, it only occupies 12% of Korea's land area (605.25 km^2). Most NO_x and CO are emitted from vehicles, while SO_x and PM_{10} are emitted from manufacturing related combustion [47, 48]. Moreover, dust storms from China [49] also regularly cause an increase in the PM_{10} concentration and threaten people's health with respiratory and cardiovascular diseases [50].

TABLE 1: The characteristics and source of data used in this study.

Parameter	Time period	Frequency	Source
SO ₂	2000–2009	Hourly	National Institute of Environmental Research (NIER)
NO ₂	2000–2009	Hourly	
CO	2000–2009	Hourly	
PM ₁₀	2000–2009	Hourly	
Dust frequency	2000–2009	Monthly	
Precipitation	2000–2007	Daily	Automatic Weather System (AWS)
Temperature	2000–2007	Daily	Korea Meteorological Administration (KMA)
Relative humidity (RH)	2000–2009	Monthly	
Wind speed	2000–2007	Daily	National Oceanic and Atmospheric Administration (NOAA)
Fine mode fraction (FMF)	2000–2009	Monthly	The Moderate Resolution Imaging Spectroradiometer (MODIS) Retrieval/Terra
Aerosol optical depth (AOD _{sat})	2000–2009	Monthly	
Ångström exponent	2000–2009	Monthly	
Aerosol optical thickness (AOD _{aeronet})	2000–2007	Monthly	Aerosol Robotic Network (AERONET)

2.2. Data Sets. This work covers ten years period from 2000 to 2009 using ground and satellite observations to analyze the existing patterns and origin of pollutants over Seoul in relation to the prevailing meteorology [34]. Ground observation data, including SO₂, NO₂, PM₁₀, and CO, were measured at 44-air pollution monitoring stations, managed by the National Institute of Environmental Research (Figure 1). Twenty-six stations of which are situated within the Seoul metropolitan area while the other eighteen stations surrounding Seoul were used for correcting edge effects of air pollutants over Seoul. At these stations, the data for the four air pollutants were continuously measured during the study period (Table 1).

Temperature and precipitation have been provided from 46 Automatic Weather Systems (AWS) located in the same boundary areas as air pollutants, by the Korea Meteorological Administration (KMA), between 2000 and 2007. Wind speed data have been supplied from the US NOAA only for three locations in west, south, and center during the same time frame as temperature and precipitation. Humidity data were available only at two locations, south from NOAA and center from AWS.

In this study, the satellite data used over Seoul covers the area with following coordinates: top 37.701364, bottom 37.428478, left 126.7642, and right 127.1835. AOD_{sat} is obtained at 550 nm from the Moderate Resolution Imaging Spectroradiometer (MODIS)/Terra and AOD_{aeronet}, at 440 nm, from Aerosol Robotic Network (AERONET) (Table 1). A high correlation coefficient of 0.84 is obtained between AOD_{sat} data retrieved from MODIS/Terra satellite and AOD_{aeronet} collected at Seoul National University’s AERONET site. The Ångström exponent and fine mode fraction (FMF) are used to distinguish aerosols’ origin either natural such as dust events or anthropogenic [40]. The FMF is the fraction of

the AOD_{sat} contributed to by fine aerosols and distinguishes how the aerosols were derived, that is, from dust or anthropogenic origins, by determining the size of the aerosols [51, 52].

3. Results

3.1. Air Pollutants and Meteorological Parameters. Meteorological parameters such as temperature, precipitation, and wind speed play a pivotal role in air pollutants dynamics and distribution in many different ways [53, 54]. Here, we have carried out correlation analysis between the four pollutants mentioned in Table 1 and the corresponding meteorological parameters, namely, temperature and precipitation, over the 8-year period, from 2000 to 2007, taking seasonality into consideration.

All pollutants showed a significant negative correlation with temperature and precipitation before removing seasonality than after removing it, yet with positive correlations among pollutants (Table 2), a result that was partially found by Park et al. [55]. To further investigate the pollutants dependencies on the seasonal component, we have carried another cross-correlation analysis between the aforementioned parameters during spring, summer, fall, and winter seasons (Table 3). The negative correlation coefficient between pollutants and precipitation during all seasons suggests that removal process takes place and affects deposition to a great extent. Yet, the fall season showed the least dependency between pollutants and the meteorological parameters, implying that the local meteorology does not affect pollution concentrations during the fall season. This is owed to the fact that during fall and winter the atmosphere is less stable as compared to summer resulting in more pollutants dispersion

TABLE 2: The correlation coefficients between temperature, precipitation, and air pollutants: (a) with seasonal effects included and (b) with seasonal effects removed.

(a)					
	Pre	NO ₂	CO	SO ₂	PM ₁₀
Temp.	0.59	-0.70	-0.72	-0.82	-0.43
Precip.		-0.66	-0.46	-0.55	-0.43
NO ₂			0.61	0.72	0.69
CO				0.75	0.44
SO ₂					0.44
(b)					
	Pre	NO ₂	CO	SO ₂	PM ₁₀
Temp.	-0.03	0.19	0.07	0.07	0.16
Precip.		-0.16	-0.13	-0.26	-0.06
NO ₂			0.22	0.23	0.40
CO				0.39	0.39
SO ₂					0.06

[56]. On the other hand, summer showed a high correlation between NO₂ and PM₁₀ as compared to other pollutants during other seasons and this is owed to the high traffic experienced during summer.

The previous analysis was performed by averaging all the meteorological parameters and pollutant data over Seoul, yet we wanted to further investigate the dependence on different regions within Seoul. For that, we selected five sites at the four cardinal directions: east (127.1E, 37.5N), west (126.8E, 37.5N), south (126.9E, 37.5N), and north (127.04E, 37.6N), and at the center (126.9E, 37.6N). Each of these sites has different geological characteristics and processes, for instance, east, north, and south parts are surrounded by mountain and west is close to the ocean. In addition, vehicles and human activities vary; during the daytime the center is crowded as many companies and major offices are located within, yet, the other sites are mixed industrial and residential areas.

It is interesting that the annual mean values of CO and SO₂ at the central location decrease gradually to a minimum in 2003 and in 2002, respectively, where further investigation is needed.

Each pollutant showed different abundances over 10-year averaged concentration at each site. The CO concentration showed notable differences between pollutants. The highest CO concentration is shown at the center (0.89 ppm) then the order of south, west, east, and north (0.65, 0.62, 0.62, and 0.56 ppm, resp.). It could be due to heating from residences and vehicles, the main sources of CO emission. Generally the center and south experience heavy traffic more than the other sites and less residences and offices exist at the north. The PM₁₀ concentration indicates the highest at the center as CO; however the south site takes place for the lowest. Unexpectedly the highest concentration of NO₂ and SO₂ occurred at the south site; it could be due to vehicles and industrial activities.

We added wind speed at the center, west, and south (no data for the east and north) sites. According to other

studies concentration of the four pollutants, pollutants react sensitively with wind speed [57–59]. Moreover, wind plays an important role of air pollution dispersion [60]. However, the results show low correlation coefficient: only west site shows notable negative correlation with NO₂ (-0.45). The west site is the only one place that is not surrounded by mountains, while the other sites are crowded with skyscrapers. This indicates that geological and specific megacity's features are one of important elements to determine pollutants concentration.

3.2. Annual Mean Analysis of the Four Air Pollutant Concentrations. Various pollutants are emitted from many different sources in megacities including Seoul, where high temperature combustion processes, such as from power plants and automobiles, are the main emission sources of NO₂ that has been slightly decreasing over the last decade due to the combined effects of various control efforts. However, increasing trends were still observed in some locations with high concentrations of CO [61], derived from vehicles and forest fires as well as SO₂ emission from burning fossil fuel and some industrial activities [48]. On the other hand, PM₁₀ emission is strongly connected to different types of natural (dust storms) and anthropogenic sources [48]. Therefore, the PM₁₀ studies are associated with specific dust events [37, 62–64]: high occurrences during spring (about 87% of the annual frequency in Korea) (Figure 2).

The NO₂ annual mean in 2008 showed the highest peak (0.0363 ppm) and in 2002 and 2005 showed the lowest. The increasing population and number of cars are the reason for the variations of annual mean because vehicles contribute to more than 70% of NO₂ [48]. Figure 3 supports the variation of annual mean where the highest number of vehicles and population is experienced during 2008, low population and stable vehicles number during the 2003–2005 period, and lowest population but increasing vehicles in 2002.

The annual mean values showed that CO concentrations decreased much more than the other pollutants over the 10-year period. The maximum value (1.0 ppm) is shown in 2000 and all months observed the highest concentration with exception of March and April (the highest March and April value was in 2001). The lowest annual mean is observed during 2005 with 0.63 ppm. The CO monthly means showed high concentrations during winter and low concentrations during summer, is analogous to NO₂. These two pollutants show similar concentration tendencies in monthly mean, which is consistent with previous study [61].

SO₂ showed two peaks in 2000 (0.007 ppm) and 2007 (0.0065 ppm) whereas the lowest value is observed in 2002 (0.005 ppm). The annual concentration decreased rapidly from 2000 to 2002, which would suggest that the emission control policies are established since 1995. Nevertheless, it increased again after 2004.

In 2002, the highest PM₁₀ annual value (70.41 μg/m³) was recorded and thus could be attributed to dust events. Dust was transported from China to Korea on the 21st of March, with a concentration of 1,153 μg/m³ (Figure 4) along with the prevailing wind direction from the west with speed 5.6 m/s. Kim [37] reported that dust events have significantly

TABLE 3: The correlation coefficients between temperature and precipitation and air pollutants by season (with seasonal effects).

	Spring					Summer					Fall				
	Pre	NO ₂	CO	SO ₂	PM ₁₀	Pre	NO ₂	CO	SO ₂	PM ₁₀	Pre	NO ₂	CO	SO ₂	PM ₁₀
Temp.	0.55	-0.16	-0.38	-0.51	-0.22	0.16	-0.74	0.0	-0.32	-0.56	0.54	-0.77	-0.64	-0.79	-0.70
Precip.		-0.21	-0.47	-0.48	-0.16		-0.46	-0.14	-0.50	-0.43		-0.68	-0.46	-0.43	-0.53
NO ₂			0.45	0.38	0.33			0.35	0.48	0.80			0.58	0.78	0.80
CO				0.65	0.49				0.30	0.52				0.69	0.74
SO ₂					0.04					0.49					0.63

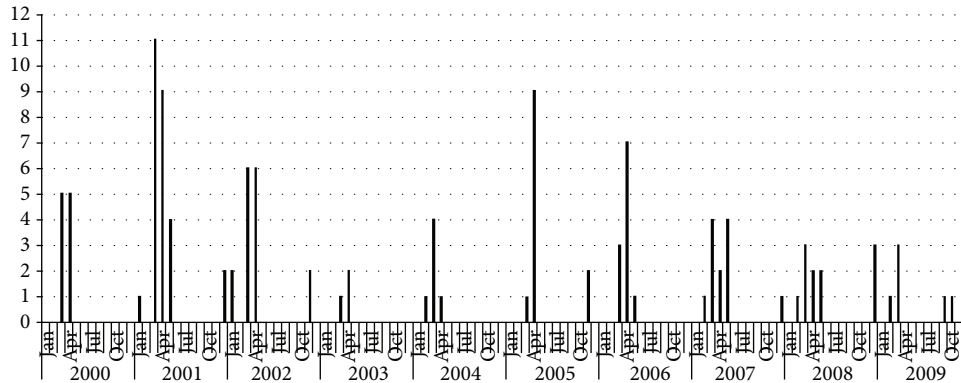


FIGURE 2: Dust event frequencies over the 10 years period.

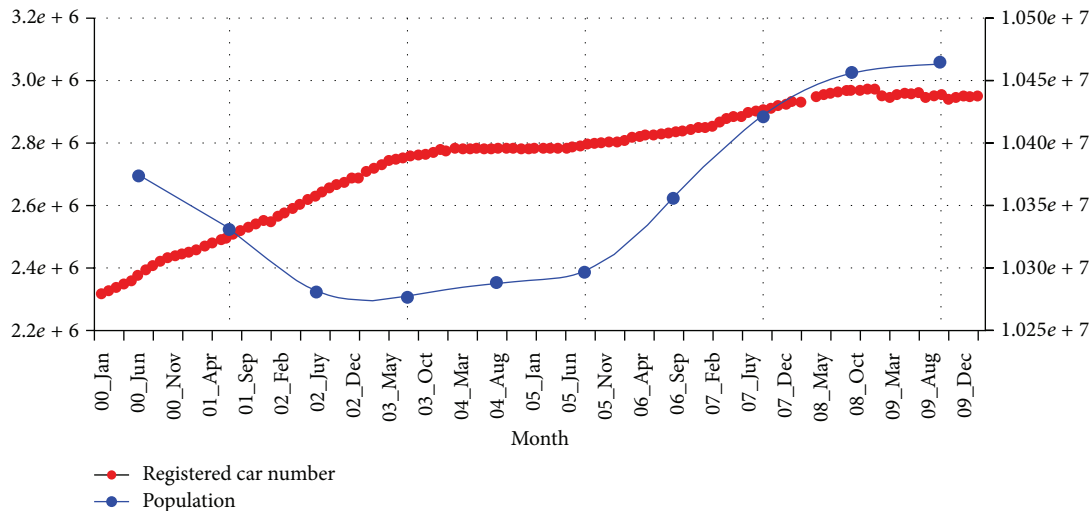


FIGURE 3: The number of registered car and population between 2000 and 2009.

increased during the 3 years from 2000 to 2002 and it has been increasing continuously since the 1980. The second highest peak was in 2007 with $62.74 \mu\text{g}/\text{m}^3$, is much lower value than first peak even though dust events were more frequent than in 2002.

3.3. Monthly Mean Analysis of the Four Air Pollutant Concentrations. The monthly NO₂ trends showed the same

pattern as previous studies, that is, low concentrations during summer and high concentrations during winter [39, 54]. Figure 6(a) indicates that the NO₂ in first (2000) and sixth (2005) low peaks showed the lowest monthly mean values during the summer. On the other hand, NO₂ in ninth peak (2007) showed the highest monthly mean value. During the summer, the rapid decreasing concentration of NO₂ is due to atmospheric conditions such as amounts of humidity and precipitation [65, 66]: according to Haberer et al. 2006 [65]

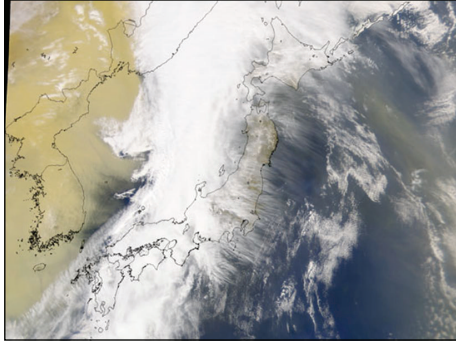


FIGURE 4: MODIS Terra image for 21 March, 2002, dust storm. Dust is lighter than the background in this true color MODIS-Terra image.

study, the minimum concentration of NO_2 investigated in July and NO_2 showed positive correlation with humidity. However, Korea experiences Monsoon every summer (this season takes most amount of annual precipitation); thus high humidity and huge amount of precipitation exist.

The CO monthly mean concentration showed the first peak during the winter of 2000 that was much higher than in the other years (Figure 6(b)). This could be due to the main sources of district heating and vehicular emission. According to the Ministry of Environment reports, the emission from vehicle takes a first rank position and the consumption of fuel is the second reason of the entire CO emission [48]. The number of registered car has been increasing since 2000; however, the trend of oil consumption has been decreasing, exactly same pattern as the CO annual mean, except for the year 2000 (Figure 5). It indicates that CO concentration is significantly dependent on human activities.

The monthly pattern of the SO_2 concentration mostly showed the same behavior as that of CO and NO_2 , with the highest concentrations during winter and the lowest during the summer (Figure 6(c)). According to Lalas et al. [67], in Greece, a low concentration was observed in late summer and early fall because of rain combined with a deep mixed layer. We mentioned above that the monsoon influences Korea during the summer; thus precipitation could explain that the low concentration was observed during summer and could be related to amount of rain and it reacts with precipitation dissimilar to other pollutants.

Figures 4 and 6(d) show that the 2002 dust storm was recorded as an intense event much stronger than other dust events in other years [68, 69]. The monthly mean of PM_{10} during spring season always takes high values during a year; during the winter it is of higher values than summer and fall seasons. However, the lowest concentrations always occurred during summer season due to the wash-out effect of summer rainfall: the lowest values were recorded in August in 2008, at $31.96 \mu\text{g}/\text{m}^3$. Dust storms were definitely one of the main sources of high PM_{10} concentration [70, 71] during spring season. Sabbah and Hasan [72] found that the increase in wind speed is related to the increase of the concentration of dust particles during spring over the Solar Village (Riyadh,

Saudi Arabia). Generally, during the spring the wind blows strongly from west to east over Korea.

3.4. Analysis of Pollutant Sources. In Sections 3.2 and 3.3, we show temporal characteristic of each pollutant with some possible reasons for 10 years period in Seoul metropolitan area. However, it has limitation of recognizing their origin; therefore we used satellite data (AOD_{sat} , Ångström exponent, and FMF) to distinguish their origins.

The satellite results indicate that AOD_{sat} increased from March to May, as expected due to the dust storms during the spring. All years during this time show AOD increasing with both low and high Ångström exponent and FMF representing a possible mixing scenario. During March 2002, a strong dust storm occurred (Figure 4), where the Ångström exponent, AOD_{sat} , and FMF values were 0.9, 0.45, and 0.1, respectively (Figure 7). These values suggest that this dusty event contains aerosols derived not only from natural sources but also from anthropogenic ones.

Unlikely, all Ångström exponent values were higher than 1 with decreasing AOD_{sat} values, while the FMF showed highest values (Figure 7) during the summer. For better understanding of distribution and origin of air pollution, we categorized the condition of atmospheric using AOD_{sat} and Ångström exponent values as same as “clean” with $\text{AOD} \leq 0.06$, “dust” with $\text{AOD} > 0.06$ and Ångström exponent < 0.25 , and “pollution” with Ångström exponent > 1.0 , and other cases are classified as “mixed” [21]. The results show that the conditions of atmospheric over Seoul only have the cases of “mixed” and “pollution.” In addition, most of the pollution occurs from May to October and mixed condition exists from November to April.

3.5. Volume Size Distribution Variability. Here we investigate the variation of the volume size distributions (VSD) as a function of the particle geometric mean radius for Anmyeon located 180 km from Seoul during the period 2000 to 2007 except for 2003 over west-ward direction as well as over Seoul for 4 years from 2000 till 2003 (Figure 8). The VSD was inverted from the AERONET observations at Anmyeon and Seoul, it helps understand local aerosol properties and variation [73, 74]. Figure 8(b) displays the variation of the VSD ($dV/d \ln R$) with a high magnitude of coarse mode peaking during the years 2005, 2006, and 2007 as compared to the previous years. The year 2002 has the highest concentration of coarse particles at Anmyeon due to the dust storm of 21 March, 2002. It peaks at $\sim 3 \mu\text{m}$ geometric mean radius with partial contribution for the fine particles fraction.

We got a good correlation ($r = 0.60$) between the monthly values of $\text{AOD}_{\text{aeronet}}$ collected at Seoul National University’s AERONET site and the corresponding PM_{10} values during 2002, when a major dust event occurred, observed close to Seoul National University (Latitude: 37.45, Longitude: 126.9), and a correlation coefficient of -0.45 between Ångström exponent and PM_{10} . Sabbah et al. 2012 [75] found a good inverse correlation ($r = -0.62$) between the Ångström exponent and AOD_{sat} using Terra/MODIS satellite collections. They interpreted that as evidence of high

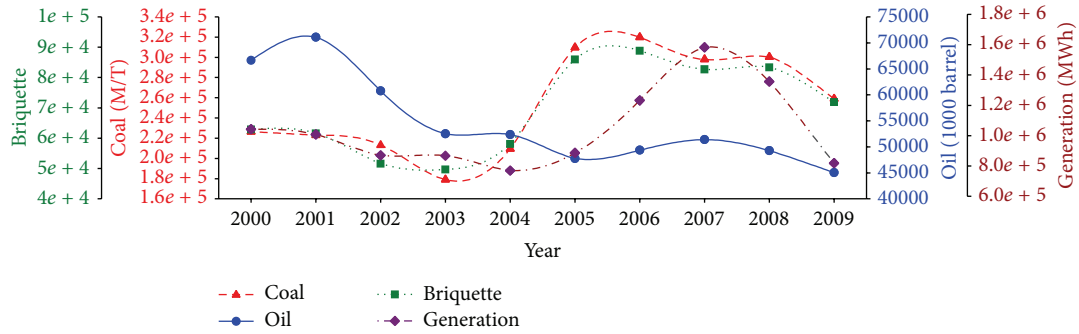


FIGURE 5: Annual means of coal and oil consumption and yield of briquette and generated.

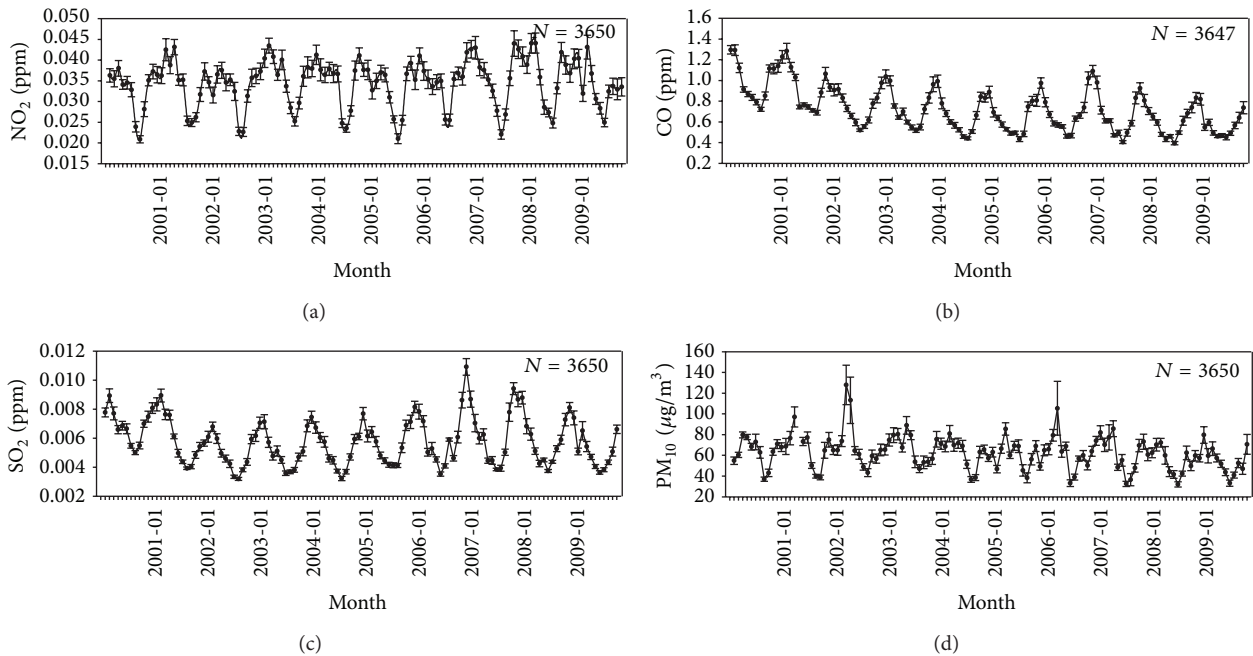


FIGURE 6: Monthly mean variations of (a) NO_2 , (b) CO , (c) SO_2 , and (d) PM_{10} between 2000 and 2009.

dust concentration. It supports that the dust storm in 2002 was high dust concentration. The year 2004 over Anmyeon exhibits the highest concentration of fine particles where the VSD peaks at $0.1 \mu\text{m}$. Figure 8(d) illustrates the variation of the volume size distributions over Seoul for dust storm occurring on 21 March, 2002. We see a substantial increase in the concentration of the coarse particles at $2.9 \mu\text{m}$ that dominates the aerosol loadings on March 21 as evident from the major dust event over Seoul (Figure 4).

4. Discussion and Conclusions

In this study, major air pollutants over Seoul, including NO_2 , CO , SO_2 , and PM_{10} , were examined, revealing specific tendencies and characteristics, which can be attributed to natural and anthropogenic sources, as well as changing meteorological factors. The significant relationships between air pollution and temperature/precipitation exist due to

the seasonality particularly; the strongest impacts were observed during the fall.

The annual mean results showed peak in different year related to different anthropogenic sources. This is evident from the increase in the cumulative number of registered car per month, rapid increase in population, high coal consumption, and the briquette yield. The dust storms, during the spring and winter, indicate mixed or pollution conditions. It means that even though dust storm contains not only natural aerosols but also aerosols from anthropogenic sources [15, 20, 76, 77]. Therefore, the reason for the peaks and minimum values are due to both natural and anthropogenic sources playing a role in the same year. The atmospheric condition during the summer is clearly identified as pollution, although all four pollutants show the lowest concentration. On the other hand, during the fall (highly affected by seasonality), it showed the mixed condition.

Satellite data analysis distinguished the pollutants origins and VSD. It indicates that the year 2007 contains small

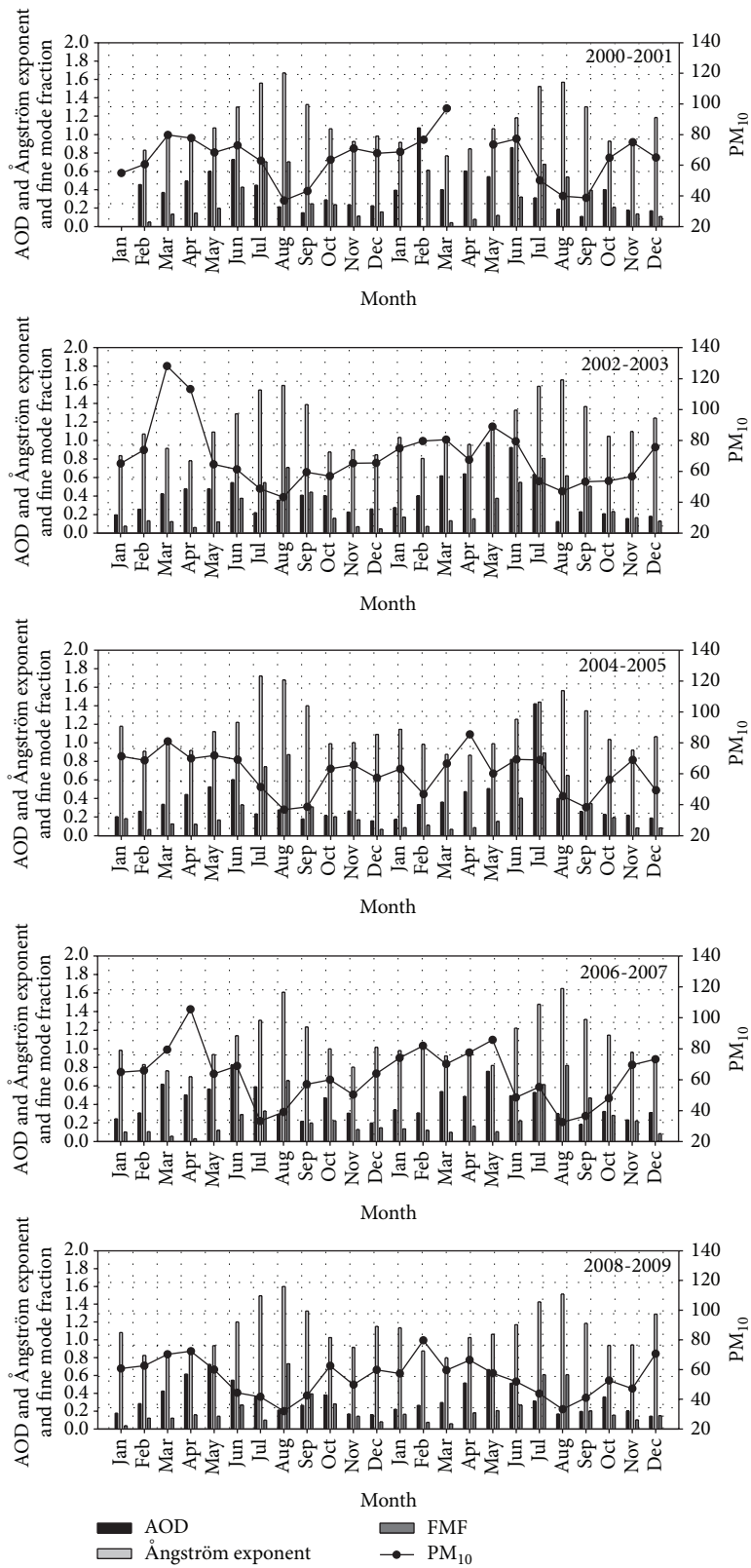


FIGURE 7: Satellite data (AOD_{sat}, Ångström exponent, and FMF) with PM₁₀ (2000 to 2009).

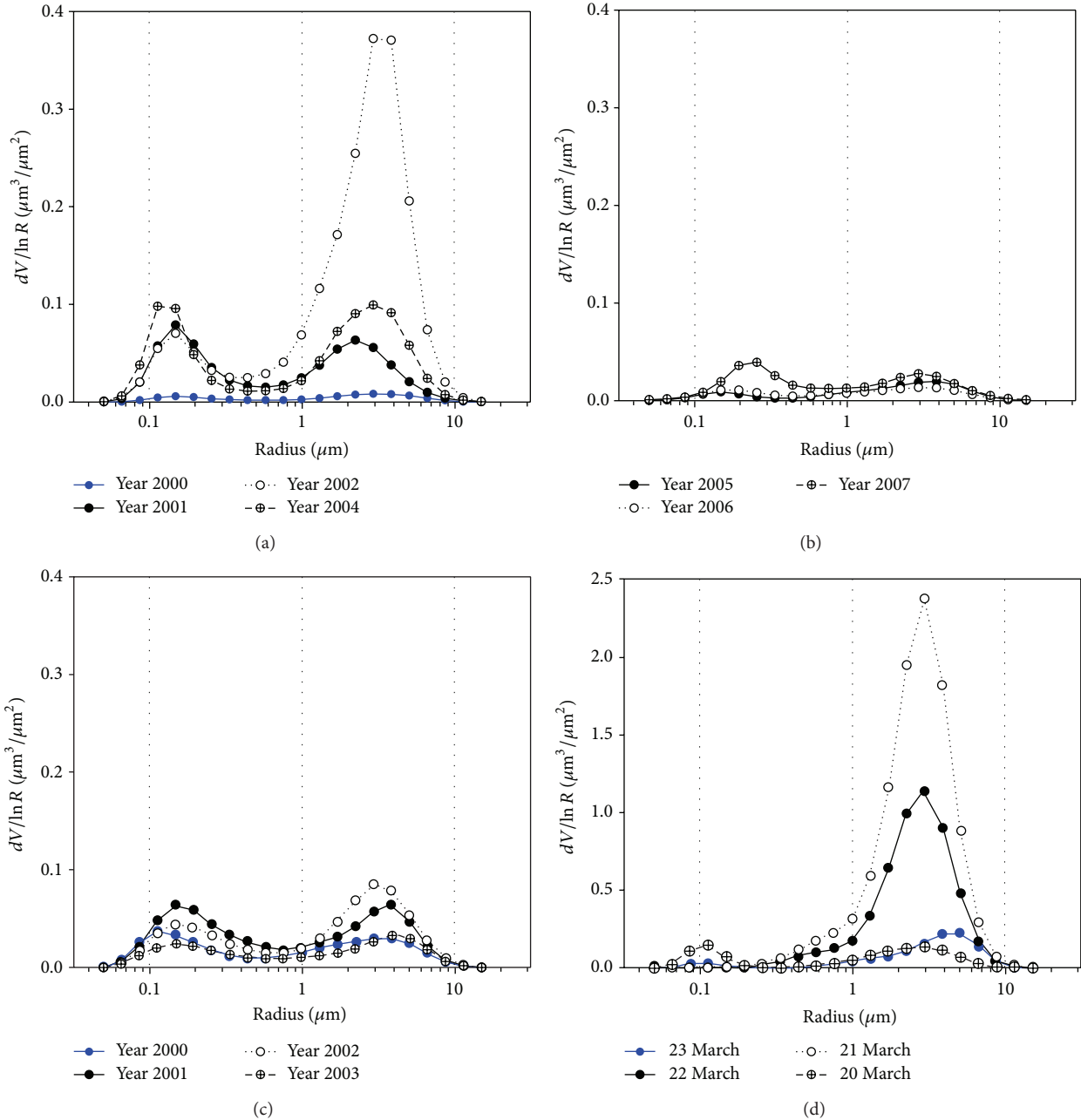


FIGURE 8: Variation of aerosol volume size distribution: (a) annual variation over Anmyeon for $N = 63$, 2000, $N = 177$, 2001, $N = 42$, 2002, and $N = 209$, 2004, (b) over Anmyeon for $N = 117$, 2005, $N = 174$, 2006, and $N = 189$, 2007, (c) over Seoul from for $N = 15$, 2000, $N = 8$, 2001, $N = 106$, 2002, and $N = 14$, 2003, and (d) daily variation over Seoul before, during, and after the dust storm of 21 March 2002. N is the number of days used.

size particle more than the other years: it implies that anthropogenic aerosol was predominant. In addition, anthropogenic aerosols increased in 2004 at Anmyeon rather than 2000, even though many policies have been established for air pollution: the radius of anthropogenic aerosols was found between 0.1 and 0.25 μm [78, 79]. The effective controls for air pollution in megacities, such as Seoul, must consider natural as well as anthropogenic sources when formulating laws to restrict pollutant emissions. Therefore, policy decisions need to be more elaborated to result in better air quality over Seoul.

Conflict of Interests

The authors declare that there is no conflict of interests regarding the publication of this paper.

Acknowledgments

Dr. El-Askary would like to acknowledge the partial support of this work for the US collaborators by the NSF Grant 0922772. Furthermore, the authors would like also

to acknowledge the use of the Samuelli Laboratory in Computational Sciences in the Schmid College of Science and Technology, Chapman University, for image processing and data analysis. The authors would like also to acknowledge Ms. Hyun-Ah Choi and Mr. Taehyub Kwon for helping in the ground data preparation process.

References

- [1] T. Abe, Y. Tokuda, S. Ohde, S. Ishimatsu, T. Nakamura, and R. B. Birrer, "The relationship of short-term air pollution and weather to ED visits for asthma in Japan," *American Journal of Emergency Medicine*, vol. 27, no. 2, pp. 153–159, 2009.
- [2] B. R. Gurjar, T. M. Butler, M. G. Lawrence, and J. Lelieveld, "Evaluation of emissions and air quality in megacities," *Atmospheric Environment*, vol. 42, no. 7, pp. 1593–1606, 2008.
- [3] K.-H. Kim, Y.-J. Choi, and M.-Y. Kim, "The exceedance patterns of air quality criteria: a case study of ozone and nitrogen dioxide in Seoul, Korea between 1990 and 2000," *Chemosphere*, vol. 60, no. 4, pp. 441–452, 2005.
- [4] M. Lee, J.-A. Kim, Y.-M. Kim, and G. Lee, "Characteristics of atmospheric hydrogen peroxide variations in Seoul megacity during 2002–2004," *Science of the Total Environment*, vol. 393, no. 2–3, pp. 299–308, 2008.
- [5] T. Takemura, T. Nakajima, T. Nozawa, and K. Aoki, "Simulation of future aerosol distribution, radiative forcing, and long-range transport in East Asia," *Journal of the Meteorological Society of Japan*, vol. 79, no. 6, pp. 1139–1155, 2001.
- [6] S. B. Mazon, I. Riipinen, D. M. Schultz et al., "Classifying previously undefined days from eleven years of aerosol-particle-size distribution data from the SMEAR II station, Hyytiälä, Finland," *Atmospheric Chemistry and Physics*, vol. 9, no. 2, pp. 667–676, 2009.
- [7] J. Huang, C. Zhang, and J. M. Prospero, "Large-scale effect of aerosols on precipitation in the West African Monsoon region," *Quarterly Journal of the Royal Meteorological Society*, vol. 135, no. 640, pp. 581–594, 2009.
- [8] C. Ichoku, R. Levy, Y. J. Kaufman et al., "Analysis of the performance characteristics of the five-channel Microtops II Sun photometer for measuring aerosol optical thickness and precipitable water vapor," *Journal of Geophysical Research D: Atmospheres*, vol. 107, no. 13, pp. AAC-5-1–AAC-5-17, 2002.
- [9] O. Torres, P. K. Bhartia, J. R. Herman, A. Sinyuk, P. Ginoux, and B. Holben, "A long-term record of aerosol optical depth from TOMS observations and comparison to AERONET measurements," *Journal of the Atmospheric Sciences*, vol. 59, no. 3, pp. 398–413, 2002.
- [10] G. A. D'Almeida, P. Koepke, and E. P. Shettle, *Atmospheric Aerosols: Global Climatology and Radiative Characteristics*, A. Deepak Publishing, Hampton, Va, USA, 1991.
- [11] E. P. Shettle, "Optical and radiative properties of a desert aerosol model," in *Proceedings of the International Radiation Symposium on Current Problems in Atmospheric Radiation August 1984*, vol. 1, pp. 21–28, 1986.
- [12] D. Tanre, P. Y. Deschamps, C. Devaux, and M. Herman, "Estimation of Saharan aerosol optical thickness from blurring effects in Thematic Mapper data," *Journal of Geophysical Research: Atmospheres*, vol. 93, no. 12, pp. 15955–15964, 1988.
- [13] D. Tanré and M. Legrand, "On the satellite retrieval of Saharan dust optical thickness over land: two different approaches," *Journal of Geophysical Research: Atmospheres*, vol. 96, no. 3, pp. 5221–5227, 1991.
- [14] A. Vukovic, M. Vujadinovic, G. Pejanovic et al., "Numerical simulation of 'an American haboob,'" *Atmospheric Chemistry and Physics*, vol. 14, no. 7, pp. 3211–3230, 2014.
- [15] H. El-Askary, R. Farouk, C. Ichoku, and M. Kafatos, "Transport of dust and anthropogenic aerosols across Alexandria, Egypt," *Annales Geophysicae*, vol. 27, no. 7, pp. 2869–2879, 2009.
- [16] H. El-Askary and M. Kafatos, "Dust storm and black cloud influence on aerosol optical properties over Cairo and the Greater Delta region, Egypt," *International Journal of Remote Sensing*, vol. 29, no. 24, pp. 7199–7211, 2008.
- [17] B. Grobéty, R. Gieré, V. Dietze, and P. Stille, "Airborne particles in the urban environment," *Elements*, vol. 6, no. 4, pp. 229–234, 2010.
- [18] B. K. Lee, H. K. Lee, and N.-Y. Jun, "Analysis of regional and temporal characteristics of PM10 during an Asian dust episode in Korea," *Chemosphere*, vol. 63, no. 7, pp. 1106–1115, 2006.
- [19] G. M. Marazzan, S. Vaccaro, G. Valli, and R. Vecchi, "Characterisation of PM₁₀ and PM_{2.5} particulate matter in the ambient air of Milan (Italy)," *Atmospheric Environment*, vol. 35, no. 27, pp. 4639–4650, 2001.
- [20] A. K. Prasad and R. P. Singh, "Changes in aerosol parameters during major dust storm events (2001–2005) over the Indo-Gangetic Plains using AERONET and MODIS data," *Journal of Geophysical Research D: Atmospheres*, vol. 112, no. 9, Article ID D09208, 2007.
- [21] I. Sabbah, C. Ichoku, Y. J. Kaufman, and L. Remer, "Full year cycle of desert dust spectral optical thickness and precipitable water vapor over Alexandria, Egypt," *Journal of Geophysical Research D: Atmospheres*, vol. 106, no. 16, pp. 18305–18316, 2001.
- [22] H. El-Askary, "Air pollution impact on Aerosol Variability over mega cities using Remote Sensing Technology: case study, Cairo," *Journal of Remote Sensing and Space Science*, vol. 9, pp. 31–40, 2006.
- [23] Y. Aboel Fetouh, H. El Askary, M. El Raey, M. Allali, W. A. Sprigg, and M. Kafatos, "Annual patterns of atmospheric pollutions and episodes over Cairo Egypt," *Advances in Meteorology*, vol. 2013, Article ID 984853, 11 pages, 2013.
- [24] W. A. Sprigg, S. Nickovic, J. N. Galgiani et al., "Regional dust storm modeling for health services: the case of valley fever," *Aeolian Research*, vol. 14, pp. 53–73, 2014.
- [25] S. W. Kim, S. C. Yoon, J. Kim, and S. Y. Kim, "Seasonal and monthly variations of columnar aerosol optical properties over east Asia determined from multi-year MODIS, LIDAR, and AERONET Sun/sky radiometer measurements," *Atmospheric Environment*, vol. 41, no. 8, pp. 1634–1651, 2007.
- [26] J. Kim, S. C. Yoon, A. Jefferson, and S. W. Kim, "Aerosol hygroscopic properties during Asian dust, pollution, and biomass burning episodes at Gosan, Korea in April 2001," *Atmospheric Environment*, vol. 40, no. 8, pp. 1550–1560, 2006.
- [27] S. Ramachandran and T. A. Rajesh, "Black carbon aerosol mass concentrations over Ahmedabab, an urban location in western India: comparison with urban sites in Asia, Europe, Canada, and the United States," *Journal of Geophysical Research D: Atmospheres*, vol. 112, no. 6, 2007.
- [28] S.-W. Kim, S.-C. Yoon, A. Jefferson et al., "Aerosol optical, chemical and physical properties at Gosan, Korea during Asian dust and pollution episodes in 2001," *Atmospheric Environment*, vol. 39, no. 1, pp. 39–50, 2005.
- [29] J. M. Baldasano, E. Valera, and P. Jiménez, "Air quality data from large cities," *Science of the Total Environment*, vol. 307, no. 1–3, pp. 141–165, 2003.

- [30] S. K. Guttikunda, G. R. Carmichael, G. Calori, C. Eck, and J. H. Woo, "The contribution of megacities to regional sulfur pollution in Asia," *Atmospheric Environment*, vol. 37, no. 1, pp. 11–22, 2003.
- [31] W. K. Jo, I. H. Yoon, and C. W. Nam, "Analysis of air pollution in two major Korean cities: trends, seasonal variations, daily 1-hour maximum versus other hour-based concentrations, and standard exceedances," *Environmental Pollution*, vol. 110, no. 1, pp. 11–18, 2000.
- [32] A. K. Prasad, H. El-Askary, and M. Kafatos, "Implications of high altitude desert dust transport from Western Sahara to Nile Delta during biomass burning season," *Environmental Pollution*, vol. 158, no. 11, pp. 3385–3391, 2010.
- [33] K.-H. Tseng, J.-L. Wang, M.-T. Cheng, and B.-J. Tsuang, "Assessing the relationship between air mass age and summer ozone episodes based on photochemical indices," *Aerosol and Air Quality Research*, vol. 9, no. 2, pp. 149–171, 2009.
- [34] S.-C. Chang and C.-T. Lee, "Evaluation of the temporal variations of air quality in Taipei City, Taiwan, from 1994 to 2003," *Journal of Environmental Management*, vol. 86, no. 4, pp. 627–635, 2008.
- [35] H. El-Askary, A. K. Prasad, G. Kallos, M. El-Raey, and M. Kafatos, "Analyzing black cloud dynamics over Cairo, Nile Delta region and Alexandria using aerosols and water vapor data," in *Air Quality-Models and Applications*, chapter 12, InTECH, Vienna, Austria, 2011.
- [36] F. Geng, Q. Zhang, X. Tie et al., "Aircraft measurements of O₃, NO_x, CO, VOCs, and SO₂ in the Yangtze River Delta region," *Atmospheric Environment*, vol. 43, no. 3, pp. 584–593, 2009.
- [37] J. Kim, "Transport routes and source regions of Asian dust observed in Korea during the past 40 years (1965–2004)," *Atmospheric Environment*, vol. 42, no. 19, pp. 4778–4789, 2008.
- [38] D. Mage, G. Ozolins, P. Peterson et al., "Urban air pollution in megacities of the world," *Atmospheric Environment*, vol. 30, no. 5, pp. 681–686, 1996.
- [39] J. An, H. Ueda, Z. Wang, K. Matsuda, M. Kajino, and X. Cheng, "Simulations of monthly mean nitrate concentrations in precipitation over East Asia," *Atmospheric Environment*, vol. 36, no. 26, pp. 4159–4171, 2002.
- [40] H. M. El-Askary, S. Sarkar, M. Kafatos, and T. A. El-Ghazawi, "A multisensor approach to dust storm monitoring over the Nile Delta," *IEEE Transactions on Geoscience and Remote Sensing*, vol. 41, no. 10, pp. 2386–2391, 2003.
- [41] H. S. Marey, J. C. Gille, H. M. El-Askary, E. A. Shalaby, and M. E. El-Raey, "Aerosol climatology over Nile Delta based on MODIS, MISR and OMI satellite data," *Atmospheric Chemistry and Physics*, vol. 11, no. 20, pp. 10637–10648, 2011.
- [42] H. S. Marey, J. C. Gille, H. M. El-Askary, E. A. Shalaby, and M. E. El-Raey, "Study of the formation of the 'black cloud' and its dynamics over Cairo, Egypt, using MODIS and MISR sensors," *Journal of Geophysical Research D: Atmospheres*, vol. 115, no. 21, 2010.
- [43] I. Sabbah, "Impact of aerosol on air temperature in Kuwait," *Atmospheric Research*, vol. 97, no. 3, pp. 303–314, 2010.
- [44] Y.-S. Choi, C.-H. Ho, D. Chen, Y.-H. Noh, and C.-K. Song, "Spectral analysis of weekly variation in PM₁₀ mass concentration and meteorological conditions over China," *Atmospheric Environment*, vol. 42, no. 4, pp. 655–666, 2008.
- [45] H. S. Lee, C.-M. Kang, B.-W. Kang, and H.-K. Kim, "Seasonal variations of acidic air pollutants in Seoul, South Korea," *Atmospheric Environment*, vol. 33, no. 19, pp. 3143–3152, 1999.
- [46] Korea Meteorological Administration, *Annual Climate Report*, Korea Meteorological Administration, 2000, (Korean), <http://www.kma.go.kr>.
- [47] Y. Chae, "Co-benefit analysis of an air quality management plan and greenhouse gas reduction strategies in the Seoul metropolitan area," *Environmental Science and Policy*, vol. 13, no. 3, pp. 205–216, 2010.
- [48] Ministry of Environment Republic of Korea, Annual report of ambient air quality in Korea, 2002, 2003, 2007, 2008 and 2009 (Korean), <http://library.me.go.kr>.
- [49] A. Agarwal, H. M. El-Askary, T. El-Ghazawi, M. Kafatos, and J. Le-Moigne, "Hierarchical PCA techniques for fusing spatial and spectral observations with application to MISR and monitoring dust storms," *IEEE Geoscience and Remote Sensing Letters*, vol. 4, no. 4, pp. 678–682, 2007.
- [50] H.-J. Kwon, S.-H. Cho, Y. Chun, F. Lagarde, and G. Pershagen, "Effects of the Asian dust events on daily mortality in Seoul, Korea," *Environmental Research*, vol. 90, no. 1, pp. 1–5, 2002.
- [51] T. A. Jones and S. A. Christopher, "MODIS derived fine mode fraction characteristics of marine, dust, and anthropogenic aerosols over the ocean, constrained by GOCART, MOPITT, and TOMS," *Journal of Geophysical Research D: Atmospheres*, vol. 112, no. 22, Article ID D22204, 2007.
- [52] Y. J. Kaufman, O. Boucher, D. Tanré, M. Chin, L. A. Remer, and T. Takemura, "Aerosol anthropogenic component estimated from satellite data," *Geophysical Research Letters*, vol. 32, no. 17, Article ID L17804, pp. 1–4, 2005.
- [53] H. S. Lee, C.-M. Kang, B.-W. Kang, and H.-K. Kim, "Seasonal variations of acidic air pollutants in Seoul, South Korea," *Atmospheric Environment*, vol. 33, no. 19, pp. 3143–3152, 1999.
- [54] X. K. Wang and W. Z. Lu, "Seasonal variation of air pollution index: Hong Kong case study," *Chemosphere*, vol. 63, no. 8, pp. 1261–1272, 2006.
- [55] I. S. Park, D. G. Rhee, and I. G. Kang, "The meteorological factors covering SO₂ concentrations during the wintertime in Seoul area," *Journal of Korean Society for Atmospheric Environment*, vol. 7, pp. 96–104, 1991 (Korean).
- [56] H. K. Elminir, "Dependence of urban air pollutants on meteorology," *Science of the Total Environment*, vol. 350, no. 1–3, pp. 225–237, 2005.
- [57] L. Huang, C.-S. Yuan, G. Wang, and K. Wang, "Chemical characteristics and source apportionment of PM₁₀ during a brown haze episode in Harbin, China," *Particuology*, vol. 9, no. 1, pp. 32–38, 2011.
- [58] Y. Ma, Y. Wang, N. Liu, and Y. Hong, "Analysis of inhalable particulate matter PM₁₀ and PM_{2.5} pollution levels in grouped cities of Central Liaoning Province," *China Powder Science and Technology*, no. 1, pp. 9–13, 2010.
- [59] C.-C. Wen and H.-H. Yeh, "Comparative influences of airborne pollutants and meteorological parameters on atmospheric visibility and turbidity," *Atmospheric Research*, vol. 96, no. 4, pp. 496–509, 2010.
- [60] P. Kastner-Klein, R. Berkowicz, and E. J. Plate, "Modelling of vehicle-induced turbulence in air pollution studies for streets," *International Journal of Environment and Pollution*, vol. 14, no. 1–6, pp. 496–507, 2000.
- [61] A. Bigi and R. M. Harrison, "Analysis of the air pollution climate at a central urban background site," *Atmospheric Environment*, vol. 44, no. 16, pp. 2004–2012, 2010.
- [62] C.-H. Kim, S.-U. Park, and C.-K. Song, "A simple semi-empirical photochemical model for the simulation of ozone

- concentration in the Seoul metropolitan area in Korea,” *Atmospheric Environment*, vol. 39, no. 30, pp. 5597–5607, 2005.
- [63] S.-W. Kim, S.-C. Yoon, J. Kim, J.-Y. Kang, and N. Sugimoto, “Asian dust event observed in Seoul, Korea, during 29–31 May 2008: analysis of transport and vertical distribution of dust particles from lidar and surface measurements,” *Science of the Total Environment*, vol. 408, no. 7, pp. 1707–1718, 2010.
- [64] O. Yi, Y.-C. Hong, and H. Kim, “Seasonal effect of PM10 concentrations on mortality and morbidity in Seoul, Korea: a temperature-matched case-crossover analysis,” *Environmental Research*, vol. 110, no. 1, pp. 89–95, 2010.
- [65] K. Haberer, L. Jaeger, and H. Rennenberg, “Seasonal patterns of ascorbate in the needles of Scots Pine (*Pinus sylvestris* L.) trees: correlation analyses with atmospheric O₃ and NO₂ gas mixing ratios and meteorological parameters,” *Environmental Pollution*, vol. 139, no. 2, pp. 224–231, 2006.
- [66] M. E. Hazenkamp-Von Arx, T. Götschi, U. Ackermann-Liebrich et al., “PM_{2.5} and NO₂ assessment in 21 European study centres of ECRHS II: annual means and seasonal differences,” *Atmospheric Environment*, vol. 38, no. 13, pp. 1943–1953, 2004.
- [67] D. P. Lalas, V. R. Veirs, G. Karras, and G. Kallos, “An analysis of the SO₂ concentration levels in Athens, Greece,” *Atmospheric Environment*, vol. 16, no. 3, pp. 531–544, 1982.
- [68] H. J. Ahn, S. U. Park, and L. S. Chang, “Effect of direct radiative forcing of Asian dust on the meteorological fields in East Asia during an Asian dust event period,” *Journal of Applied Meteorology and Climatology*, vol. 46, no. 10, pp. 1655–1681, 2007.
- [69] Z. Batjargal, J. Dulam, and Y. S. Chung, “Dust storms are an indication of an unhealthy environment in East Asia,” *Environmental Monitoring and Assessment*, vol. 114, no. 1–3, pp. 447–460, 2006.
- [70] K. Bouchlaghem, B. Nsom, N. Latrache, and H. Haj Kacem, “Impact of Saharan dust on PM10 concentration in the Mediterranean Tunisian coasts,” *Atmospheric Research*, vol. 92, no. 4, pp. 531–539, 2009.
- [71] S. Rodríguez, X. Querol, A. Alastuey, G. Kallos, and O. Kakaliagou, “Saharan dust contributions to PM₁₀ and TSP levels in Southern and Eastern Spain,” *Atmospheric Environment*, vol. 35, no. 14, pp. 2433–2447, 2001.
- [72] I. Sabbah and F. A. Hasan, “Remote sensing of aerosols over the Solar Village, Saudi Arabia,” *Atmospheric Research*, vol. 90, no. 2–4, pp. 170–179, 2008.
- [73] I. Sabbah, A. Nermina, A. A. Mona, A. E. Ali, A. H. Aneesah, and A. A. Nada, “Influence of air quality conditions on asthmatic patient visits in Kuwait,” *Journal of Allergy and Therapy*, vol. 5, no. 6, article 197, 2014.
- [74] X. Yang and M. Wenig, “Study of columnar aerosol size distribution in Hong Kong,” *Atmospheric Chemistry and Physics*, vol. 9, no. 16, pp. 6175–6189, 2009.
- [75] I. Sabbah, H. F. Al-Mudhaf, A. Al-Kandari, and F. Al-Sharifi, “Remote sensing of desert dust over Kuwait: long-term variation,” *Atmospheric Pollution Research*, vol. 3, no. 1, pp. 95–104, 2012.
- [76] E. Hamonou, P. Chazette, D. Balis et al., “Characterization of the vertical structure of Saharan dust export to the Mediterranean basin,” *Journal of Geophysical Research D: Atmospheres*, vol. 104, no. 18, pp. 22257–22270, 1999.
- [77] D. G. Kaskaoutis, H. D. Kambezidis, P. T. Nastos, and P. G. Kosmopoulos, “Study on an intense dust storm over Greece,” *Atmospheric Environment*, vol. 42, no. 29, pp. 6884–6896, 2008.
- [78] R. G. Kleidman, N. T. O’Neill, L. A. Remer et al., “Comparison of Moderate Resolution Imaging Spectroradiometer (MODIS) and Aerosol Robotic Network (AERONET) remote-sensing retrievals of aerosol fine mode fraction over ocean,” *Journal of Geophysical Research D: Atmospheres*, vol. 110, no. 22, pp. 1–6, 2005.
- [79] D. Tanré, Y. J. Kaufman, B. N. Holben et al., “Climatology of dust aerosol size distribution and optical properties derived from remotely sensed data in the solar spectrum,” *Journal of Geophysical Research D: Atmospheres*, vol. 106, no. 16, pp. 18205–18217, 2001.

Research Article

Origin and Distribution of PAHs in Ambient Particulate Samples at High Mountain Region in Southern China

Peng-hui Li,¹ Yan Wang,² Yu-hua Li,³ Hong-li Li,³ and Xianliang Yi^{4,5}

¹School of Environmental Science and Safety Engineering, Tianjin University of Technology, Tianjin 300384, China

²School of Environmental Science and Engineering, Shandong University, Jinan 250100, China

³Shandong Environmental Monitoring Center, Jinan 250101, China

⁴The Swire Institute of Marine Science, The University of Hong Kong, Pokfulam, Hong Kong

⁵State Key Laboratory of Environmental Criteria and Risk Assessment, Chinese Research Academy of Environmental Sciences, Beijing 100012, China

Correspondence should be addressed to Peng-hui Li; lipenghui406@163.com and Yan Wang; wy@sdu.edu.cn

Received 6 June 2014; Revised 21 November 2014; Accepted 21 November 2014

Academic Editor: Hesham El-Askary

Copyright © 2015 Peng-hui Li et al. This is an open access article distributed under the Creative Commons Attribution License, which permits unrestricted use, distribution, and reproduction in any medium, provided the original work is properly cited.

To understand the deposition and transport of PAHs in southern China, a measurement campaign was conducted at a high-elevation site (the summit of Mount Heng, 1269 m A.S.L.) from April 4 to May 31, 2009, and a total of 39 total suspended particulate samples were collected for measurement of PAH concentrations. The observed particulate-bound PAHs concentrations ranged from 1.63 to 29.83 ng/m³, with a mean concentration of 6.03 ng/m³. BbF, FLA, and PYR were the predominant compounds. Good correlations were found between individual PAHs and meteorological parameters such as atmospheric pressure, relative humidity, and ambient temperature. The backward trajectory analysis suggested that particulate samples measured at the Mount Heng region were predominantly associated with the air masses from southern China, while the air masses transported over northern and northwestern China had relative higher PAHs concentrations. Based on the diagnostic ratios and factor analysis, vehicular emission, coal combustion, industry emission, and unburned fossil fuels were suggested to be the PAHs sources at Mount Heng site. However, the reactivity and degradation of individual PAHs could influence the results of PAH source profiles, which deserves further investigations in the future.

1. Introduction

Polycyclic aromatic hydrocarbons (PAHs) are a group of widespread environmental contaminants, originating from both natural (e.g., forest fires and volcanoes) and anthropogenic sources (e.g., incomplete combustion and pyrolysis of fossil fuels or organic materials). Between the two sources, human activities (i.e., anthropogenic sources) contribute the most to PAHs emissions. This is particularly the case in urban area or industrial areas, where the PAHs sources can be entirely anthropogenic [1–4]. PAHs are persistent and accumulative in environment, and they can cause carcinogenic and mutagenic effects to living things. Thus, these compounds have received more and more attention by environmental scientists for the last several decades. The emission abatement of PAHs has been listed on the agenda of

international convention processes, such as the 1979 Geneva Convention on Long-Range Transboundary Air Pollution. Since 1990, reduction of PAHs emission has been reported in U.S. and European countries. In contrast to those developed countries, the PAH emissions in China have been continuously increasing due to the rapid industrialization and economic development [5–7]. The total PAH emission in China was estimated to be about 25,300 tons in the year of 2003 and the major sources were suggested to be domestic coal combustion, biofuel burning, and industry emission [5].

Once released into the atmosphere, PAHs can partition between vapor and particle phases, which is dependent on temperature and vapor pressure of the chemicals [8, 9]. PAHs with high molecular weight (4–6 rings) tend to be associated with particle phase, while those with lower molecular weight (2–3 rings) are often concentrated in the vapor phase

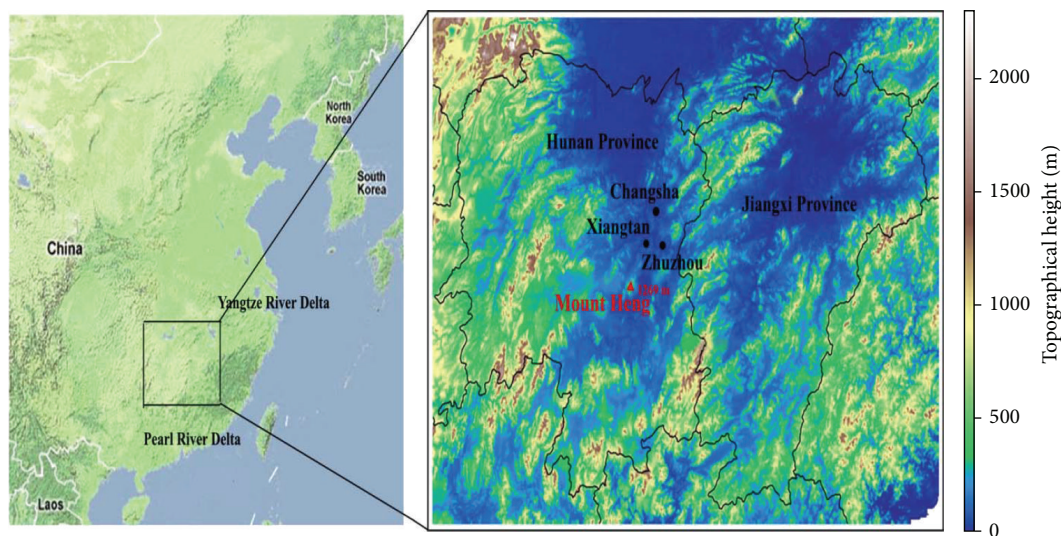


FIGURE 1: Geographical location of Mount Heng (cited from [36]).

[10]. During the course of their transport, PAHs could be removed from the atmosphere due to precipitation and/or dry deposition. Through the grasshopper effect, PAHs can be transported to very long ranges from their original sources [11].

Although a considerable number of studies have been conducted on measurements of PAHs in urban environment, little work has been done in rural sites. Remote mountain regions, particularly with altitude in the free troposphere, are the unique environments for the study of atmospheric pollution load over continental areas, and the study at remote mountain regions can help to get full assessment of the role of the atmosphere in the global distribution of PAHs [12, 13]. In this study, atmospheric particulate samples were collected at the summit of Mt. Heng, which is in the transition region between the free troposphere and boundary layer, and serve as a regionally representative site for studying the long-range transport of pollutants in Southern China. The objectives of the present study were (1) to gain a primary understanding on the distribution of particulate-bound PAHs at Mt. Heng and (2) to examine the possible sources and transport patterns of PAHs in the region.

2. Materials and Methods

2.1. Site Description and Sample Collection. The Mount Heng is located in Hunan Province, south China, and it is between two major polluted industrial/urban areas—the Pearl River and Yangtze River deltas. There are two big cities, Shanghai and Guangzhou, situated 900 km to the east and 400 km to the south of the Mount Heng, respectively. The sampling site was located at a meteorological station ($27^{\circ}18'N$, $112^{\circ}42'E$), which was set up in the 1937 at the summit of Mount Heng (1269 m A.S.L.) (Figure 1).

The sampling period was carried out from April 4 to May 31, 2009. Total suspended particulate (TSP) samples were collected on glass fibre filters by a middle-volume air

sampler (KC-300, Qingdao Laoshan Electronic Instrument Company) daily (22 hours, from 10 a.m. to 8 a.m.). The sampler was operated at a flow rate of 225 L/min and a total of 39 TSP samples were collected. Prior to sampling, all the glass fibre filters were combusted at $450^{\circ}C$ in an oven for 6 h to volatilize any organic contaminants. After sampling, the glass fibre filters were wrapped in aluminum foils and frozen at $-20^{\circ}C$, and PAHs analysis was then conducted within two weeks after sampling.

2.2. Sample Preparation and Analysis. The glass fibre filters were extracted by Accelerated Solvent Extractor (Dionex ASE 300) with acetone/*n*-hexane (1:1, v/v) solvents, and the elute was purified using silica gel columns and condensed to exactly 1 mL with rotary evaporation and nitrogen stream technique. PAHs were then determined using gas chromatography coupled to mass spectrometry (Shimadzu 2010 plus). The details of the extraction and analysis procedure were described elsewhere [1]. Fifteen individual PAHs were detected in this study (Table 1).

2.3. Quality Control. Deuterated perylene-d₁₂ was spiked to all the samples to monitor procedural performance. The mean recoveries based on surrogates in samples were $98.4 \pm 6.4\%$.

Field and method blanks were analyzed using the same procedure as particulate samples, and all the PAHs concentrations were corrected for blanks. The control calibration standards were measured regularly to ensure the performance of instrument during sample analysis.

3. Results and Discussion

3.1. Concentrations of PAHs in Particulate Samples. Descriptive statistics for all valid observations of PAHs concentrations in particulate samples collected at Mount Heng are summarized in Table 2. The concentrations of PAHs varied

TABLE 1: The abbreviations for PAH compounds and their detection limits.

PAHs	Abbreviation	Detection limit (ng)
Acenaphthylene	ACY	4
Acenaphthene	ACE	5
Fluorene	FLU	5
Phenanthrene	PHE	3
Anthracene	ANT	4
Fluoranthene	FLA	7
Pyrene	PYR	4
Benz[a]anthracene	BaA	2
Chrysene	CHR	7
Benzo[b]fluoranthene	BbF	3
Benzo[k]fluoranthene	BkF	4
Benzo[a]pyrene	BaP	4
Dibenz[a,h]anthracene	DahA	6
Benzo[g,h,i]perylene	BghiP	4
Indeno[1,2,3-cd]pyrene	IcdP	5

from 1.63 to 29.83 ng/m³, with a mean concentration of 6.03 ng/m³. BbF was the predominant compound, with a mean concentration of 0.86 ng/m³, contributing to 14.26% of the total PAH concentration. FLA, PHE, and PYR comprised the second tier of dominant compounds, with mean concentrations of 0.77, 0.74, and 0.60 ng/m³, respectively. Similar distribution of individual PAHs has been reported in previous studies in China. For the research done by our group at the Mount Tai (the highest mountain at northern China, 1534 m A.S.L.), BbF, FLA, and PYR were the most abundant PAH compounds in PM_{2.5} samples, accounting for 23.55%, 14.21%, and 10.39% of the total PAH concentration, respectively [1]. Wang et al. [14] also suggested that BbF was the predominant compound of PAHs in PM₁₀ samples in Beijing. In 2012, China Environmental Protection Agency has published the latest ambient air quality standards, in which the BaP daily and annual concentration limits were set at 2.5 ng/m³ and 1.0 ng/m³, respectively. The BaP concentration found in this study met the standard. Together with BaP, several other PAHs compounds, including BaA, BbF, BkF, IcdP, and DahA, were suggested as potential carcinogenic compounds by the International Agency for Research on Cancer (IARC). The total concentration of these six compounds was 2.30 ng/m³, accounting for 38.14% of the total PAHs.

The observed PAHs concentrations at the Mount Heng are comparable with our previous studies done at the Mount Tai (fine particles, 6.88 ng/m³; Table 3) [1]. When comparing with other areas, the PAHs concentrations at Mount Heng are much lower than the results reported in urban cities or areas in China, including Beijing [14], Guangzhou [15], and Northern Plain [16]. In contrast, the PAHs concentrations at Mount Heng were higher than the observed concentrations at Waliguan (a global standard observation site, 3810 m A.S.L., 2.08 ng/m³) [17], high mountain regions of Europe (0.07–1.10 ng/m³, 2240–2413 m) [18], Mt. Bachelor Observatory (MBO, <6 ng/m³, 2763 m) [19], Far East Asia

TABLE 2: Statistical description of PAH concentrations in particulate samples at Mount Heng.

Species	PAHs concentrations (ng/m ³)		
	Range	Mean	SD
ACY	Nd-0.11	0.02	0.03
ACE	Nd-0.56	0.10	0.15
FLU	Nd-0.85	0.22	0.23
PHE	0.17–2.83	0.74	0.71
ANT	Nd-0.41	0.12	0.12
FLA	0.15–4.88	0.77	0.97
PYR	0.13–3.62	0.60	0.72
BaA	0.05–1.68	0.27	0.33
CHR	Nd-3.80	0.52	0.80
BbF	Nd-4.24	0.86	0.88
BkF	0.11–1.25	0.36	0.30
BaP	0.08–1.47	0.35	0.31
IcdP	Nd-1.80	0.39	0.39
DahA	Nd-0.53	0.07	0.11
BghiP	0.21–2.60	0.64	0.51
PAHs	1.63–29.83	6.03	5.87

(0.32 ng/m³), North Pacific Ocean (0.14 ng/m³), and the Arctic area (0.48 ng/m³) [20].

3.2. Correlations of Particulate-Bound PAH Levels with Meteorological Parameters. The meteorological conditions are important factors that can affect the deposition levels of pollutants [21–23]. In the present study, meteorological parameters including atmospheric pressure (press.), relative humidity (RH), and ambient temperature (T) were measured during the sampling period. The correlation coefficients between these meteorological parameters and particulate-bound PAHs were analyzed (Table 4). Good correlation was found between atmospheric pressure and several individual PAHs including BkF, BaP, IcdP, and BghiP, suggesting that high atmospheric pressure enhanced the bound of these compounds to the particulate phase. In the study of Tian et al. [21], significant negative correlation was observed between particulate-bound PAHs and ambient temperature, suggesting the temperature dependence for PAHs. Some other studies also highlighted the important role of temperature in PAHs partitioning between gas and particulate phase [24, 25]. However, in this present study, only five individual PAH compounds including ACY, ACE, BkF, IcdP, and BghiP presented significant negative correlation with temperature. In addition, ACE and FLU had good positive relationships with RH, indicating their RH dependence.

3.3. Transport Pattern and Sources of Particulate-Bound PAHs. In previous studies, atmospheric samples always have higher deposition concentrations when they came from the more polluted area [2, 10]. Back trajectory analysis was conducted in this study to characterize the particulate deposition character influenced by different source regions.

TABLE 3: Comparison of particulate-bound PAH levels between Mount Heng and other studies.

Sampling site	Sample type	Altitude (m A.S.L.)	\sum PAHs	PAHs concentrations (ng/m ³)	Reference
Mount Heng, China	TSP	1269 m	\sum 15	6.03	This research
Mount Tai, China	PM _{2.5}	1534 m	\sum 15	6.88	[1]
Waliguan, China	TSP	3810 m	\sum 14	2.08	[17]
High Mountain Regions, Europe	TSP	2240 m–2413 m	\sum 20	0.07–1.10	[18]
MBO, US	TSP	2763 m	\sum 14	<4	[19]
Far East Asia	TSP	NA	\sum 15	0.32	[20]
North Pacific Ocean	TSP	NA	\sum 15	0.14	[20]
Arctic	TSP	NA	\sum 15	0.48	[20]
Beijing, China	PM ₁₀	NA	\sum 15	44.9	[14]
Northern Plain, China	TSP	NA	\sum 16	346	[16]
Guangzhou, China	TSP	NA	\sum 16	19.5	[15]

TABLE 4: The correlation coefficients between particulate bound-PAH concentrations and meteorological parameters.

	Press. (Pa)	T (°C)	RH (%)
PAHs	0.627	-0.639	0.226
ACY	0.551	-0.764*	0.665
ACE	-0.025	-0.234	0.940**
FLU	-0.078	-0.166	0.938**
PHE	0.389	-0.554	0.700
ANT	0.472	-0.641	0.621
FLA	0.541	-0.571	0.119
PYR	0.555	-0.564	0.076
BaA	0.572	-0.537	0.050
CHR	0.531	-0.475	0.015
BbF	0.688	-0.644	0.174
BkF	0.733*	-0.718*	0.233
BaP	0.722*	-0.706	0.221
IcdP	0.767*	-0.783*	0.336
DahA	0.626	-0.656	0.363
BghiP	0.751*	-0.784*	0.310

Significance level: * $P < 0.05$, ** $P < 0.01$.

Forty-eight-hour backward trajectories were calculated using the HYSPLIT (hybrid single-particle Lagrangian integrated trajectory) model at a height of 1269 m A.S.L.

Based on the analysis, four major trajectory categories were classified for the samples: N/NW, continental air masses from northern and northwestern China, the most polluted region of China; EA, air masses from eastern China, where Shanghai and its surrounding cities located here; S, air masses from the Southern China, transported through the Pearl River Delta region; and L, samples with looped and short trajectories that stayed within a radius of 500 km of sampling site (Figure 2).

Among the four classified trajectory categories, S happened most frequently, accounting for 42.9% of the total, followed by N/NW (37.1%), EA (14.3%), and L (5.7%). As presented in Figure 3, the order of PAHs concentrations among the trajectory categories was N/NW, L, EA, and S.

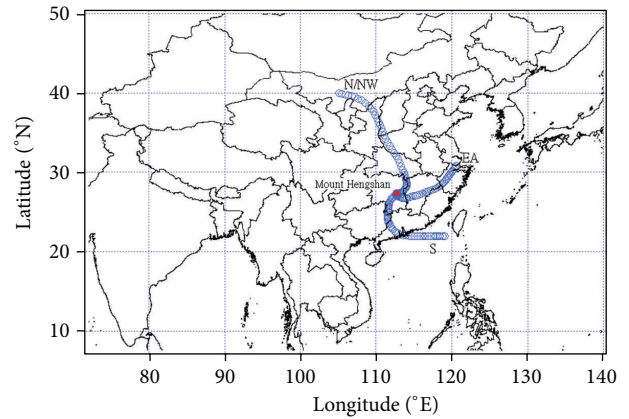


FIGURE 2: Classified pathway of each trajectory category.

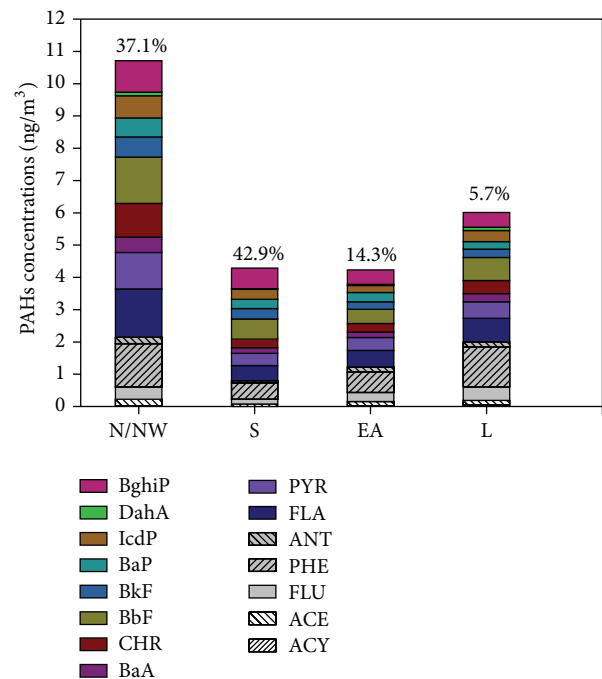


FIGURE 3: PAHs concentrations based on different trajectory categories.

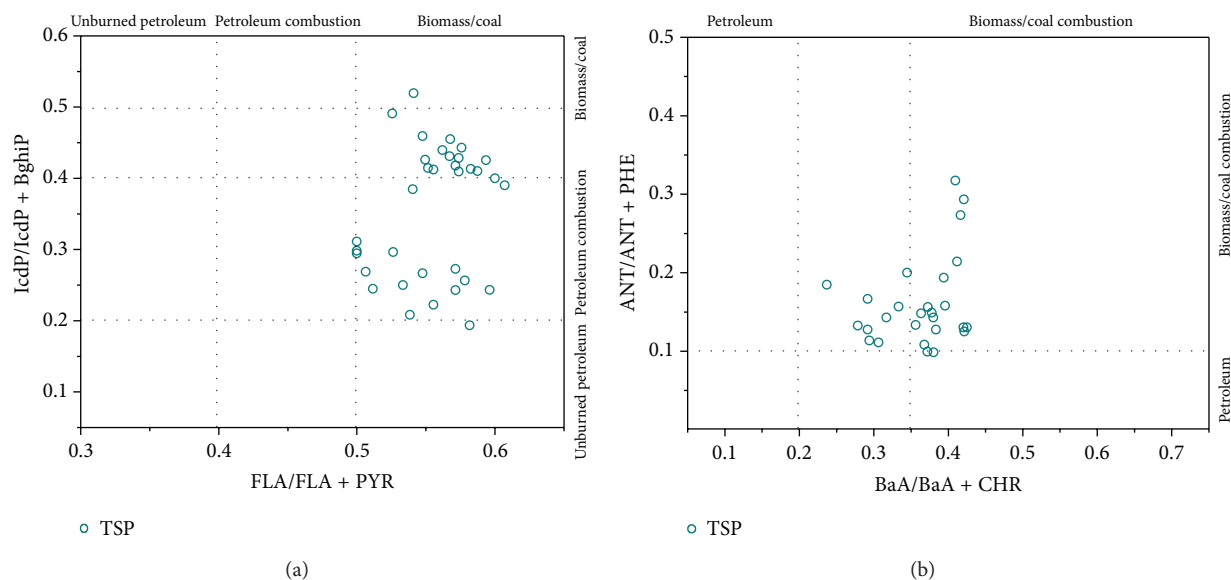


FIGURE 4: Diagnostic PAH ratios for TSP samples collected at Mount Heng.

The air masses of N/NW group originated from the northern and northwestern China, where most industrial activities of China are located and burning of coal and biomass was the dominant energy source. So, particulate samples of this group had the highest PAHs concentrations, reaching 10.71 ng/m^3 . Unexpectedly, the group of L had higher PAHs concentrations than EA and S groups, and the average concentration reached 6.01 ng/m^3 . PHE was the predominant compound of L group, contributing over 20% of the total concentration. As presented in the study of Lin et al. [26], PHE is a major component of emissions from incense burning. There are several temples located in the Mount Heng region, and most of them are crowded with visitors. Therefore, incense burning inside or outside the temples is suggested to be an important local PAHs emission source. It should be noted that the relative fewer sample numbers of L group could cause uncertainties to some degree. Air mass from eastern and southern China, the two most developed areas in China, had lower PAHs concentrations, which are 4.23 and 4.29 ng/m^3 , respectively.

3.4. Diagnostic Ratios of PAH. As suggested in prior studies, the concentrations and ratios of some tracer PAHs could be used to identify the contribution of different sources. Four common diagnostic ratios including $FLA/(PYR + FLA)$, $IcdP/(BghiP + IcdP)$, $ANT/(PHE + ANT)$, and $BaA/(BaA + CHR)$ were used to analyze the PAHs in particulate samples, and the results are presented in Figure 4.

According to the study of Yunker et al. [27], the ratio of $FLA/(PYR + FLA)$ lower than 0.4 implies the unburned petrogenic sources and the ratio higher than 0.5 signals the coal and wood combustion, and a ratio between 0.4 and 0.5 indicates the liquid fossil fuel combustion sources. In this study, the ratio was 0.56 for particulate sample, indicating wood and coal combustion was the main source.

For $IcdP/(BghiP + IcdP)$, the ratio lower than 0.2 suggests unburned petrogenic sources, the ratio between 0.2 and 0.4 indicates liquid fossil fuel combustion sources, and the ratio higher than 0.5 signals the contribution of coal or wood combustion [6]. The ratio value was 0.38 for the sample, indicating comprehensive contributions from coal and liquid fossil fuel combustion sources. For another common used indicator $ANT/(PHE + ANT)$, a ratio lower than 0.1 signals the liquid fossil fuel sources and a ratio higher than 0.1 indicates the combustion sources. As presented in Figure 4, the ratios were all above 0.1 for particulate samples, indicating the combustion source contributions. In previous study, the ratio of $BaA/(BaA + CHR)$ higher than 0.35 indicates the coal or other biomass combustion sources, while the ratio lower than 0.2 signals the liquid fossil fuel sources [28]. In this study, the ratio was 0.29 for particulate sample, indicating the coal and liquid fossil fuel combustion contribution.

Based on the results of diagnostic ratios analysis, coal combustion and emissions from liquid fossil fuel consumption were suggested to be the dominating sources of particulate-bound PAHs at Mount Heng site. In our previous studies conducted at Mount Tai, the highest mountain in northern China, coal combustion and vehicular emissions were the main sources of PAHs in atmospheric samples as well [1, 2]. The results obtained from the high altitude background sites could reflect an overall picture of PAH possible sources in China. However, special caution should be given when using diagnostic ratios. The ratio values could be altered as PAHs can react with other atmospheric compounds, such as hydroxyl radicals and/or ozone [29, 30]. In addition, degradation during the transport can modify the concentrations and ratios of PAHs, which is another limitation of using diagnostic ratios [31]. For example, BaA and ANT have been proved to degrade more quickly than their isomers-CHR and PHE, respectively [32, 33].

TABLE 5: Factor analysis for particulate-bound PAHs.

PAHs	Factor 1	Factor 2
ACY		0.735
ACE		0.977
FLU		0.962
PHE		0.790
ANT		0.846
FLA	0.857	
PYR	0.882	
BaA	0.940	
CHR	0.922	
BbF	0.954	
BkF	0.709	
BaP	0.810	
IcdP	0.851	
DahA	0.895	
BghiP	0.833	
% of variance	70.77	15.43
Sources	Vehicular and coal combustion emission	Unburned fossil fuels and incense burning

3.5. Factor Analysis. As stated above, several constraints exist when using diagnostic ratios to identify PAHs sources. Factor analysis, which served as an exploratory tool, can be used to quantify the major sources of PAHs. In this present study, the total concentrations of 15 PAHs compounds detected in particulate samples were subjected to factor analysis using SPSS version 16 (SPSS Inc.). Factor analysis was conducted with Varimax rotation, and factors with eigenvalue >1 were considered. The results of rotated factors are listed in Table 5.

Two factors were separated, accounting for 86.2% of the total variance in the data. Factor 1, which explained 70.77% of the variance, presented high loading for individual PAHs with higher molecular weight, including FLA, PYR, BaA, CHR, BbF, BkF, BaP, IcdP, DahA, and BghiP. According to previous studies, BbF, BkF, IcdP, and BghiP are the major components of vehicular emission, and the presence of FLA, PYR, BaA, and CHR could point to coal and wood combustion sources [1, 34, 35]. Thus, factor 1 could represent sources from vehicular and coal combustion emission. Factor 2, which explained 15.43% of the variance, is highly loaded on ACY, ACE, FLU, PHE, and ANT. ACY and ACE could signal the contribution of unburned fossil fuels. PHE and ANT have been identified in industry emission in previous studies [1, 6]. PHE is also a major component of emissions from incense burning [26], while Flu could originate from different sources.

Based on the results of factor analysis, vehicular emission, coal combustion, industry emission, and unburned fossil fuels were suggested to be the PAHs sources at Mount Heng site. However, as mentioned earlier, the reactivity and degradation of individual PAHs could influence the results for profiles of PAH sources, and thus much work still needs to be conducted in the future.

4. Conclusion

Particulate-bound PAHs concentrations were investigated at high mountain region in Southern China from April to May 2009. The PAH concentrations ranged from 1.63 to 29.83 ng/m³, with a mean concentration of 6.03 ng/m³. The meteorological parameters including atmospheric pressure, relative humidity, and ambient temperature had good correlations with individual PAHs. The results obtained from air mass back trajectories and PAHs concentrations highlighted the importance of air mass origin. The air masses of N/NW group, transported over the most polluted region of China, had relatively higher PAH concentrations. Both the diagnostic ratio and factor analysis suggested that vehicular emission, coal combustion, industry emission, and unburned fossil fuels were the possible sources of PAHs at Mount Heng site.

Conflict of Interests

The authors declare that there is no conflict of interests regarding the publication of this paper.

Acknowledgments

The authors are grateful to Mount Heng Meteorological Station for providing meteorological data and other support in the field observation. They thank Jinan Institute of Environmental Protection for the support of sample analysis. They appreciate the assistance from Zaifeng Wang, Houyong Zhang, Likun Xue, Xiaomei Gao, Wei Nie, and Shengzhen Zhou. This study was supported by the National Natural Science Foundation of China (21177073, 41475115), Tianjin 131 creative talents project, and Tianjin High School Science & Technology Fund Planning Project (20140515).

References

- [1] P.-H. Li, Y. Wang, Y.-H. Li et al., "Characterization of polycyclic aromatic hydrocarbons deposition in PM_{2.5} and cloud/fog water at Mount Taishan (China)," *Atmospheric Environment*, vol. 44, no. 16, pp. 1996–2003, 2010.
- [2] Y. Wang, P.-H. Li, H.-L. Li, X.-H. Liu, and W.-X. Wang, "PAHs distribution in precipitation at Mount Taishan. China. Identification of sources and meteorological influences," *Atmospheric Research*, vol. 95, no. 1, pp. 1–7, 2010.
- [3] S. S. Park, Y. J. Kim, and C. H. Kang, "Atmospheric polycyclic aromatic hydrocarbons in Seoul, Korea," *Atmospheric Environment*, vol. 36, no. 17, pp. 2917–2924, 2002.
- [4] C. Vasilakos, N. Levi, T. Maggos, J. Hatzianestis, J. Michopoulos, and C. Helmis, "Gas-particle concentration and characterization of sources of PAHs in the atmosphere of a suburban area in Athens, Greece," *Journal of Hazardous Materials*, vol. 140, no. 1-2, pp. 45–51, 2007.
- [5] S. Xu, W. Liu, and S. Tao, "Emission of polycyclic aromatic hydrocarbons in China," *Environmental Science and Technology*, vol. 40, no. 3, pp. 702–708, 2006.
- [6] K. Ravindra, R. Sokhi, and R. van Grieken, "Atmospheric polycyclic aromatic hydrocarbons: source attribution, emission

- factors and regulation,” *Atmospheric Environment*, vol. 42, no. 13, pp. 2895–2921, 2008.
- [7] P.-H. Li, S.-F. Kong, C.-M. Geng et al., “Health risk assessment for vehicle inspection workers exposed to airborne polycyclic aromatic hydrocarbons (PAHs) in their work place,” *Environmental Sciences: Processes and Impacts*, vol. 15, no. 3, pp. 623–632, 2013.
- [8] J. He and R. Balasubramanian, “Semi-volatile organic compounds (SVOCs) in ambient air and rainwater in a tropical environment: concentrations and temporal and seasonal trends,” *Chemosphere*, vol. 78, no. 6, pp. 742–751, 2010.
- [9] M. F. Simcik, T. P. Franz, H. Zhang, and S. J. Eisenreich, “Gas-particle partitioning of PCBs and PAHs in the Chicago urban and adjacent coastal atmosphere: states of equilibrium,” *Environmental Science and Technology*, vol. 32, no. 2, pp. 251–257, 1998.
- [10] M. À. Olivella, “Polycyclic aromatic hydrocarbons in rainwater and surface waters of Lake Maggiore, a subalpine lake in Northern Italy,” *Chemosphere*, vol. 63, no. 1, pp. 116–131, 2006.
- [11] J. He and R. Balasubramanian, “A study of precipitation scavenging of semivolatile organic compounds in a tropical area,” *Journal of Geophysical Research D: Atmospheres*, vol. 114, no. 12, Article ID D12201, 2009.
- [12] G. L. Daly and F. Wania, “Organic contaminants in mountains,” *Environmental Science and Technology*, vol. 39, no. 2, pp. 385–398, 2005.
- [13] B. L. van Drooge, J. O. Grimalt, C. J. Torres García, and E. Cuevas, “Semivolatile organochlorine compounds in the free troposphere of the Northeastern Atlantic,” *Environmental Science and Technology*, vol. 36, no. 6, pp. 1155–1161, 2002.
- [14] W. Wang, S. L. M. Simonich, W. Wang et al., “Atmospheric polycyclic aromatic hydrocarbon concentrations and gas/particle partitioning at background, rural village and urban sites in the North China Plain,” *Atmospheric Research*, vol. 99, no. 2, pp. 197–206, 2011.
- [15] Y. Yang, P. Guo, Q. Zhang, D. Li, L. Zhao, and D. Mu, “Seasonal variation, sources and gas/particle partitioning of polycyclic aromatic hydrocarbons in Guangzhou, China,” *Science of the Total Environment*, vol. 408, no. 12, pp. 2492–2500, 2010.
- [16] S. Liu, S. Tao, W. Liu et al., “Atmospheric polycyclic aromatic hydrocarbons in north China: a winter-time study,” *Environmental Science and Technology*, vol. 41, no. 24, pp. 8256–8261, 2007.
- [17] H.-R. Cheng, G. Zhang, X. Liu, J. Li, S.-H. Qi, and Y.-C. Zhao, “Studies on polycyclic aromatic hydrocarbons in the atmosphere of Waliguan, Qinghai,” *China Environmental Science*, vol. 26, no. 6, pp. 646–649, 2006.
- [18] P. Fernández, J. O. Grimalt, and R. M. Vilanova, “Atmospheric gas-particle partitioning of polycyclic aromatic hydrocarbons in high mountain regions of Europe,” *Environmental Science & Technology*, vol. 36, no. 6, pp. 1162–1168, 2002.
- [19] T. Primbs, A. Piekarz, G. Wilson et al., “Influence of Asian and Western United States urban areas and fires on the atmospheric transport of polycyclic aromatic hydrocarbons, polychlorinated biphenyls, and fluorotelomer alcohols in the Western United States,” *Environmental Science and Technology*, vol. 42, no. 17, pp. 6385–6391, 2008.
- [20] X. Ding, X. M. Wang, Z. Q. Xie et al., “Atmospheric polycyclic aromatic hydrocarbons observed over the North Pacific Ocean and the Arctic area: Spatial distribution and source identification,” *Atmospheric Environment*, vol. 41, no. 10, pp. 2061–2072, 2007.
- [21] F. Tian, J. Chen, X. Qiao et al., “Sources and seasonal variation of atmospheric polycyclic aromatic hydrocarbons in Dalian, China: factor analysis with non-negative constraints combined with local source fingerprints,” *Atmospheric Environment*, vol. 43, no. 17, pp. 2747–2753, 2009.
- [22] K. Ravindra, L. Bencs, E. Wauters et al., “Seasonal and site-specific variation in vapour and aerosol phase PAHs over Flanders (Belgium) and their relation with anthropogenic activities,” *Atmospheric Environment*, vol. 40, no. 4, pp. 771–785, 2006.
- [23] A. Motelay-Massei, D. Ollivon, B. Garban, and M. Chevreuil, “Polycyclic aromatic hydrocarbons in bulk deposition at a suburban site: assessment by principal component analysis of the influence of meteorological parameters,” *Atmospheric Environment*, vol. 37, no. 22, pp. 3135–3146, 2003.
- [24] M. Tsapakis and E. G. Stephanou, “Occurrence of gaseous and particulate polycyclic aromatic hydrocarbons in the urban atmosphere: study of sources and ambient temperature effect on the gas/particle concentration and distribution,” *Environmental Pollution*, vol. 133, no. 1, pp. 147–156, 2005.
- [25] A. Li, J.-K. Jang, and P. A. Scheff, “Application of EPA CMB8.2 model for source apportionment of sediment PAHs in Lake Calumet, Chicago,” *Environmental Science and Technology*, vol. 37, no. 13, pp. 2958–2965, 2003.
- [26] T.-C. Lin, F.-H. Chang, J.-H. Hsieh, H.-R. Chao, and M.-R. Chao, “Characteristics of polycyclic aromatic hydrocarbons and total suspended particulate in indoor and outdoor atmosphere of a Taiwanese temple,” *Journal of Hazardous Materials*, vol. 95, no. 1-2, pp. 1–12, 2002.
- [27] M. B. Yunker, R. W. Macdonald, R. Vingarzan, R. H. Mitchell, D. Goyette, and S. Sylvestre, “PAHs in the Fraser River basin: a critical appraisal of PAH ratios as indicators of PAH source and composition,” *Organic Geochemistry*, vol. 33, no. 4, pp. 489–515, 2002.
- [28] H. H. Soclo, P. Garrigues, and M. Ewald, “Origin of polycyclic aromatic hydrocarbons (PAHs) in coastal marine sediments: case studies in Cotonou (Benin) and Aquitaine (France) Areas,” *Marine Pollution Bulletin*, vol. 40, no. 5, pp. 387–396, 2000.
- [29] A. L. Robinson, R. Subramanian, N. M. Donahue, A. Bernardo-Bricker, and W. F. Rogge, “Source apportionment of molecular markers and organic aerosol—1. Polycyclic aromatic hydrocarbons and methodology for data visualization,” *Environmental Science and Technology*, vol. 40, no. 24, pp. 7803–7810, 2006.
- [30] A. L. Robinson, N. M. Donahue, and W. F. Rogge, “Photochemical oxidation and changes in molecular composition of organic aerosol in the regional context,” *Journal of Geophysical Research D: Atmospheres*, vol. 111, no. 3, Article ID D03302, 2006.
- [31] M. Tsapakis and E. G. Stephanou, “Collection of gas and particle semi-volatile organic compounds: use of an oxidant denuder to minimize polycyclic aromatic hydrocarbons degradation during high-volume air sampling,” *Atmospheric Environment*, vol. 37, no. 35, pp. 4935–4944, 2003.
- [32] R. M. Kamens, Z. Guo, J. N. Fulcher, and D. A. Bell, “Influence of humidity, sunlight, and temperature on the daytime decay of polyaromatic hydrocarbons on atmospheric soot particles,” *Environmental Science and Technology*, vol. 22, no. 1, pp. 103–108, 1988.
- [33] J. J. Schauer, W. F. Rogge, L. M. Hildemann, M. A. Mazurek, G. R. Cass, and B. R. T. Simoneit, “Source apportionment of airborne particulate matter using organic compounds as tracers,” *Atmospheric Environment*, vol. 30, no. 22, pp. 3837–3855, 1996.

- [34] H. Guo, S. C. Lee, K. F. Ho, X. M. Wang, and S. C. Zou, "Particle-associated polycyclic aromatic hydrocarbons in urban air of Hong Kong," *Atmospheric Environment*, vol. 37, no. 38, pp. 5307–5317, 2003.
- [35] W. Zhang, S. Zhang, C. Wan, D. Yue, Y. Ye, and X. Wang, "Source diagnostics of polycyclic aromatic hydrocarbons in urban road runoff, dust, rain and canopy throughfall," *Environmental Pollution*, vol. 153, no. 3, pp. 594–601, 2008.
- [36] J. Zhou, Y. Wang, T. X. Yue, Y. H. Li, K.-M. Wai, and W. X. Wang, "Origin and distribution of trace elements in high-elevation precipitation in Southern China," *Environmental Science and Pollution Research*, vol. 19, no. 8, pp. 3389–3399, 2012.

Research Article

Atmospheric Error Correction of the Laser Beam Ranging

J. Saydi,¹ A. Lotfalian,² M. Abedi,² J. Khalilzadeh,¹ and H. Saghafifar³

¹ Physics Department, Imam Hosein University, P.O. Box 16575-347, Tehran, Iran

² Malek-Ashtar University of Technology, Isfahan, Iran

³ Center of Optics and Laser Researches, Malek-Ashtar University of Technology, Isfahan, Iran

Correspondence should be addressed to J. Khalilzadeh; jkhalil@ihu.ac.ir

Received 24 April 2014; Revised 28 July 2014; Accepted 12 August 2014; Published 7 September 2014

Academic Editor: Hesham El-Askary

Copyright © 2014 J. Saydi et al. This is an open access article distributed under the Creative Commons Attribution License, which permits unrestricted use, distribution, and reproduction in any medium, provided the original work is properly cited.

Atmospheric models based on surface measurements of pressure, temperature, and relative humidity have been used to increase the laser ranging accuracy by ray tracing. Atmospheric refraction can cause significant errors in laser ranging systems. Through the present research, the atmospheric effects on the laser beam were investigated by using the principles of laser ranging. Atmospheric correction was calculated for 0.532, 1.3, and 10.6 micron wavelengths through the weather conditions of Tehran, Isfahan, and Bushehr in Iran since March 2012 to March 2013. Through the present research the atmospheric correction was computed for meteorological data in base of monthly mean. Of course, the meteorological data were received from meteorological stations in Tehran, Isfahan, and Bushehr. Atmospheric correction was calculated for 11, 100, and 200 kilometers laser beam propagations under 30°, 60°, and 90° rising angles for each propagation. The results of the study showed that in the same months and beam emission angles, the atmospheric correction was most accurate for 10.6 micron wavelength. The laser ranging error was decreased by increasing the laser emission angle. The atmospheric correction with two Marini-Murray and Mendes-Pavlis models for 0.532 nm was compared.

1. Introduction

Through the laser range finding systems, the distance was calculated by computation of the round-trip time of emitted beam and reflected from the target. From this point of view, this class of systems had two basic parts: the pulse generator and emitter including its optical system and attached equipment and detector and received pulses analyzer including receiving telescope and beam time of flight measuring unit [1]. The laser range finder system at large distances was developed and used in the USA between 1961 and 1962 for first time for satellites ranging specially. The applied satellite was BE-B (BEACONEXPLORER-B). The first successful received signal was achieved in 1965. The atmosphere through the most recent models has been assumed to be symmetric and spherical to simplify the calculations of range finding and delay caused by atmosphere. In these models, horizontal gradients in atmosphere index of reflection would be ignored because it led to error less than a centimeter in angles less than 10 degrees [2]. Due to the atmosphere and turbulence, beam

refraction induced error through the laser range finding systems. Atmospheric refraction index increased the mean optical path. The group velocity error ranged from 2.5 meters at zenith to almost 13 meters at elevation of 10 degrees. Intense atmospheric turbulences caused a random error in the optical path length which probably would be a few centimeters at 10 degrees. Many models have been developed to correct laser range measurements because of mean atmospheric index of refraction. The atmospheric measuring data resulting from range finding sites were used through the mentioned models and their accuracy received a few centimeters at 20 degrees. In order to increase the accuracy of these measurements, it was shown that the accuracy was limited by the atmospheric propagation and turbulence effects and also by the system hardware. For single-frequency satellite laser ranging systems, Marini and Murray proposed a model containing the precision requirements at that time. Therefore, all known developments of the improved atmospheric correction formulae have been based on the Marini-Murray scheme [3–5]. Mendes and Pavlis developed a new

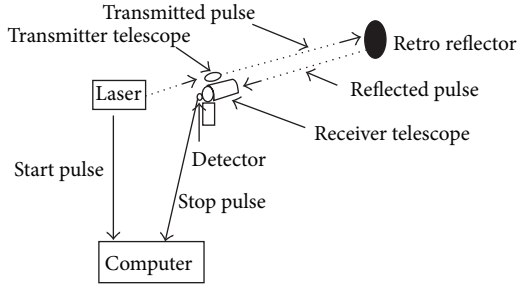


FIGURE 1: Laser tracking system scheme.

modified model based on the Marini-Murray [6]. For gradients with horizontal refraction and also for refractions with spherical symmetry, many accurate models could be used to correct errors. Of course, the mentioned models required many meteorological data. The models based on the surface measurements depended on near earth surface topography and other atmospheric effects. For its high accuracy, the laser range finding was one of the best range measuring methods [7, 8]. The mentioned technique was used to air born platform ranging at short ranges and to space born platform ranging at long ranges. Refractive index difference between layers of atmosphere was one of the error factors in the accurate range finding. The atmospheric correction method was applied in order to minimize errors and compute accurate distance between ground site and target. Through the present method, to achieve a real value of the distance between ground site and target, the error value has been calculated and encountered in the final measurement due to atmospheric effects (AC). Through the present work, the atmospheric effects on laser propagation were investigated based on the Marini-Murray model. Group refractive index error was calculated by using the Mendes and Pavlis modified model for comparison. Due to atmosphere, the occurred error on accurate measuring has been studied considering weather conditions of laser emitter site. The atmospheric correction for weather conditions in one year of Tehran, Isfahan, and Bushehr was calculated. Weather conditions, that is, mean pressure, mean temperature, mean precipitation, and mean relative humidity were 664 (mmHg), 18°C, 225 mm, and 41%, for Tehran, 630 (mmHg), 16°C, 160 mm, and 52% for Isfahan, and 760 (mmHg), 25°C, 280 mm, and 71% for Bushehr, respectively. The atmospheric correction was calculated for laser beams at several wavelengths and for 11, 100, and 200 km propagation path lengths. Calculations were done for three laser beam emission angles, that is, 30, 60, and 90 degrees. Because of this, the real meteorological data of the above mentioned states was used.

2. Laser Range Finding Fundamentals

In laser range finding of distance between a ground site and a target, a very short laser pulse is guided to a telescope for sending to target. Sent pulses back-scatter from the target surface to receiver telescope. This telescope is equipped to a beam recording detector which determines pulse time of

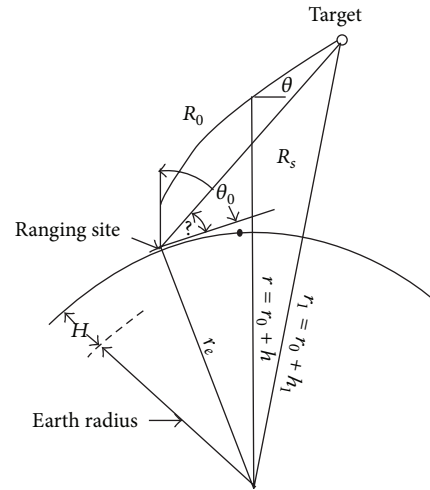


FIGURE 2: Curved and straight path of beam.

light. Figure 1 shows a schematic diagram of this system. The measured time multiplied by speed of light gives two time of distance between laser emitter site and the target [9, 10]. Because of large distance between ground site and target, the pick power of pulse must be large enough to reach reflecting surface and then back scatter to detector. One of the important parameters in accurate measuring is the pulse width of the sent pulse. Thus a very short pulse with width of about a few tens picoseconds is selected. According to $\tau \times c/2$, 0.45 cm measuring accuracy will be achieved with a 30 picosecond pulse width [1].

3. Atmospheric Correction Theory

The laser beam which is the same as the other electromagnetic radiations was affected by its propagating medium. When the light transmits from a medium to another one, its speed was varied. Instead of the direct propagation of light path, the mentioned speed variation caused refraction or concaving of it. Rate of the concave merely was affected by the concentration difference of two mediums and frequency (or wavelength) of light. The earth atmosphere was not a homogeneous medium. It also included gases and other fine particles, making evaluating medium variation effect complicated. This nonhomogeneity of medium caused refraction of beam in propagation path. This path at long distances became concave. Figure 2 shows the concaved path of beam (R_0) and straight path (R_s) that will travel in vacuum. The traveled optical path by laser beam can be evaluated from the following equation [11]:

$$R_0 = \int_{r_0}^{r_1} \frac{n_g}{\sin \theta} dr, \quad (1)$$

where, n_g is the group refractive index and θ is the angle that could be evaluated by Snell's law for a layered spherical medium using (2):

$$nr \cos \theta = n_0 r_0 \cos \theta_0, \quad (2)$$

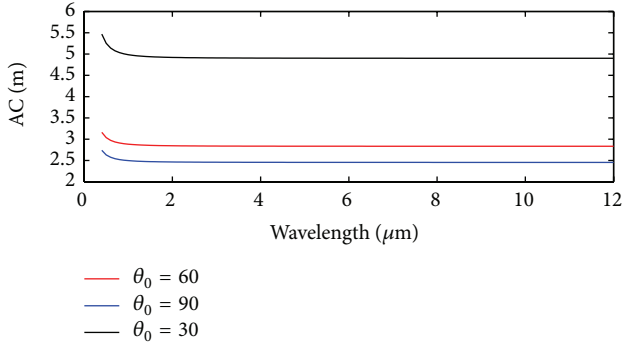


FIGURE 3: Wavelength dependence of AC in Isfahan weather conditions.

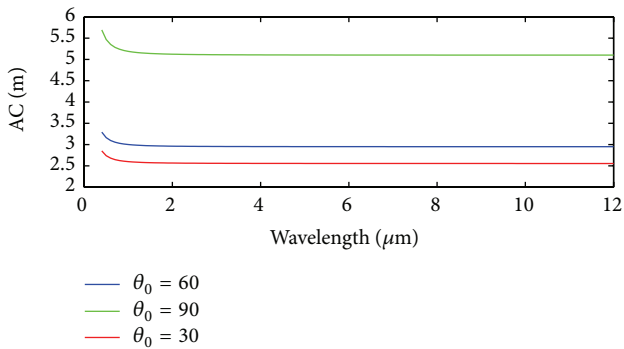


FIGURE 4: Wavelength dependence of AC in Tehran weather conditions.

where, n_0 is refractive index and θ_0 is the rising angle of beam at measuring site according to Figure 2. Group refractive index (n_g) can be evaluated from the following equation [12]:

$$n_g = 1 + 10^{-6} N_g, \quad (3)$$

where, N_g is the group refractive parameter. Calculating group refractive index, atmospheric correction (AC) can be achieved from (4):

$$\begin{aligned} AC &= R_0 - R_s \\ &= 10^{-6} \int_{r_0}^{r_1} \frac{N_g}{\sin \theta} dr + \left[\int_{r_0}^{r_1} \frac{dr}{\sin \theta} - R_s \right]. \end{aligned} \quad (4)$$

First term in (4) is the group velocity error. Due to the variation of laser, the mentioned error is pulse group velocity which is because of atmospheric transmittance. Second term is the difference between direct beam path (R_s) and beam traveled optical path (R_0) as indicated in Figure 2. Because of the second term, the error value is about 3-4 cm for 10 degrees rising angle. For grater angles, it is negligible compared to first term error [11-13].

The group refractive parameter N_g can be evaluated by Marini and Murray relation [14]:

$$N_g = \left(\frac{273.15 P}{1013.25 T} n_{gs} \right) - 11.27 \left(\frac{e}{T} \right), \quad (5)$$

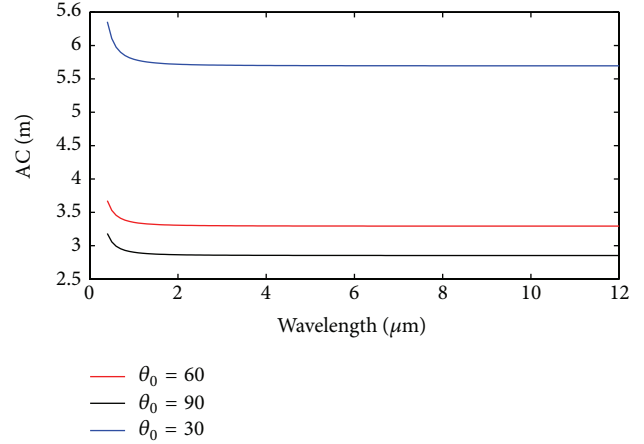


FIGURE 5: Wavelength dependence of AC in Bushehr weather conditions.

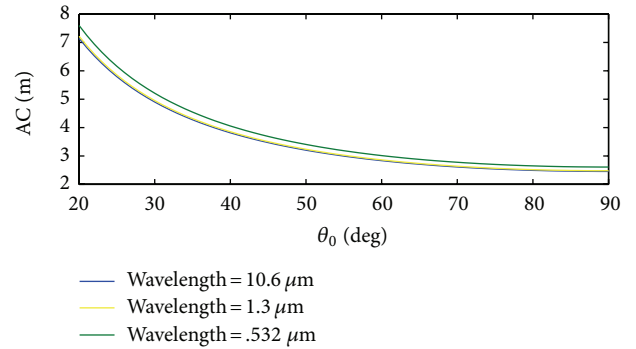


FIGURE 6: Rise angle (θ_0) dependence of AC in Isfahan weather conditions (two curves are overlapped and are not distinguishable).

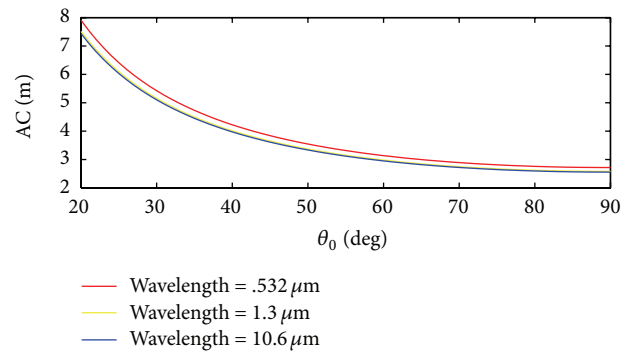


FIGURE 7: Rise angle (θ_0) dependence of AC in Tehran weather conditions (two curves are overlapped and are not distinguishable).

where P is the overall pressure in hectopascal, T is the temperature in Kelvin, e is the partial water vapor pressure, and n_{gs} is the group refraction index at standard conditions; that is, $T = 273.15$ K and 1 atm. pressure. n_{gs} can be evaluated

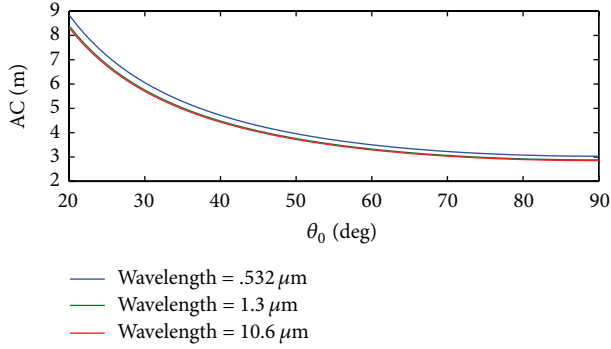


FIGURE 8: Rise angle (θ_0) dependence of AC in Bushehr weather conditions (two curves are overlapped and are not distinguishable).

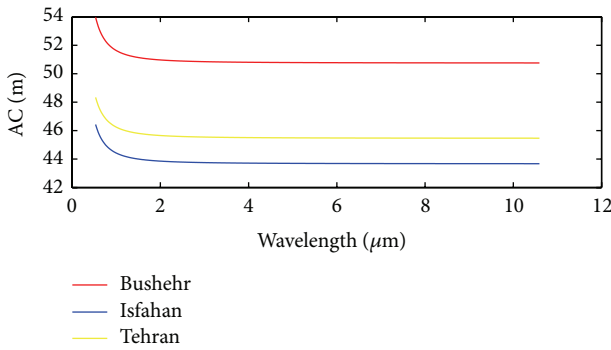


FIGURE 9: AC versus wavelength for 100 km altitude and laser beam emission angle of 30 degrees.

using (6) in which λ is laser range finder wavelength in micrometer [15]. Consider the following:

$$n_{gs} = 287.6155 + \frac{4.8866}{\lambda^2} + \frac{0.068}{\lambda^4}, \quad (6)$$

$$e = 0.01 \exp^{\alpha}, \quad (7)$$

$$\alpha = 1.2378847 \times 10^{-5} T^2 - 1.9121316 \times 10^{-2} T + 33.93711047 - 6.34316453 \times 10^3 T^{-1}. \quad (8)$$

4. Results and Discussion

AC value of Tehran, Isfahan, and Bushehr states was computed by using (1)–(8) and real meteorological monthly average data, that is, temperature, pressure, and relative humidity, during one year. AC value for the laser beams was calculated at 0.532, 1.3, and 10.6 microns and for 11, 100, and 200 km propagation path lengths. Calculations were done for three laser beam emission angles, that is, 30, 60, and 90 degrees. Results are presented in Figures 3, 4, 5, 6, 7, 8, 9, 10, 11, 12, 13, and 14. One can see from (4) and results show that the AC value obviously depends on the laser wavelength, emission angle, and propagation path length. As it can be seen through Figures 3–14, the atmospheric correction for 10.6 μm at same emission angles and same propagation path length was the least one with respect to the other wavelengths. This

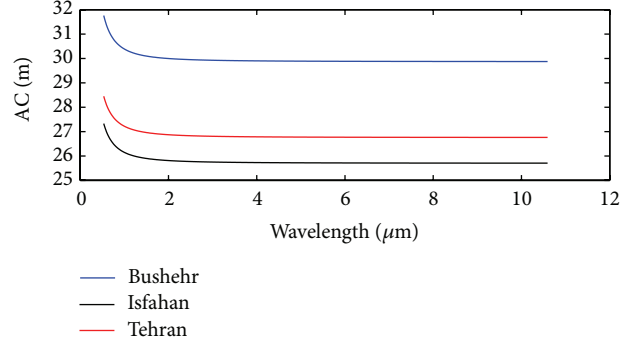


FIGURE 10: AC versus wavelength for 100 km altitude and laser beam emission angle of 60 degrees.

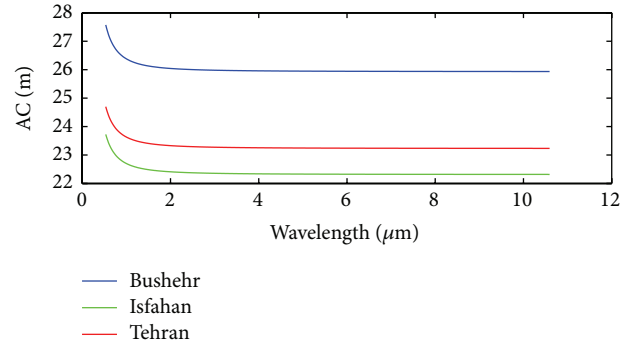


FIGURE 11: AC versus wavelength for 100 km altitude and laser beam emission angle of 90 degrees.

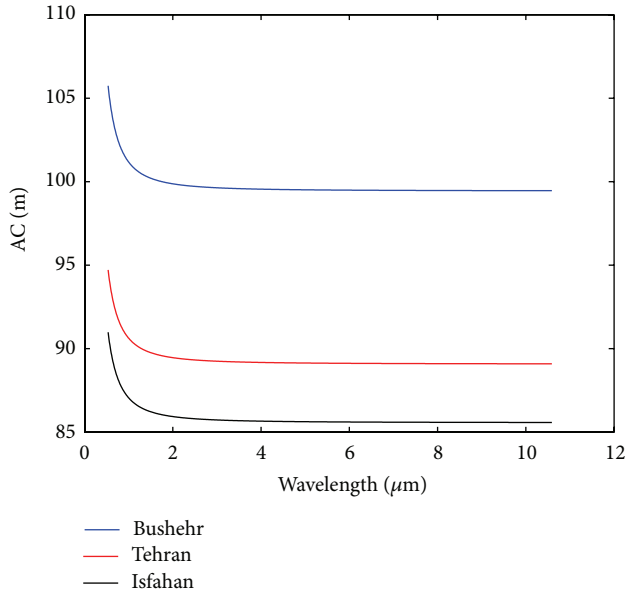


FIGURE 12: AC versus wavelength for 200 km altitude and laser beam emission angle of 30 degrees.

means that the 10.6 μm needs less atmospheric correction. In the same manner 1.3 μm needs less atmospheric correction with respect to 0.532 μm wavelength. Figures 3–5 and Figures 9–14 are atmospheric corrections versus wavelength curves. These curves are plotted for 11, 100, and 200 km propagation path lengths under three laser beam emission angles of 30,

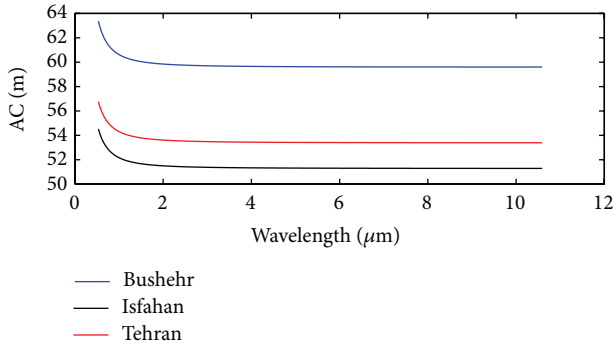


FIGURE 13: AC versus wavelength for 200 km altitude and laser beam emission angle of 60 degrees.

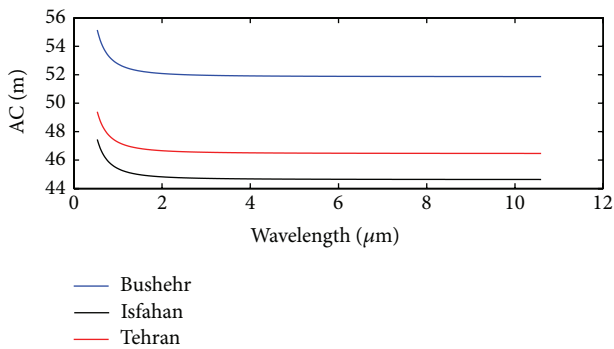


FIGURE 14: AC versus wavelength for 200 km altitude and laser beam emission angle of 90 degrees.

60, and 90 degrees, respectively. These curves were figured for three numbered states (Tehran, Isfahan, and Bushehr) by utilizing metrological organization data.

According to (4) and (2), the AC value depends on the rising angle θ_0 , too. This dependency can be seen qualitatively in Figures 6–8. Results show that for a given propagation path length, increasing the rising angle decreases the atmospheric correction (see Figures 6–14). Atmospheric effect on laser beams is also investigated. Figures 6–8, depict atmospheric correction versus rising angle θ_0 diagrams for 0.532, 1.3, and 10.6 μm wavelengths at 11 km propagation path length for three states. The group refraction parameter versus wavelength in Isfahan, Tehran, and Bushehr states weather conditions were calculated and are depicted in Figure 15. Mendes and Pavlis modified model has been used for AC correction of 0.532 μm range finding and its results were compared with results of Marini–Murray model, which is depicted in Table 1. AC values in Table 1 show a distinguishable difference between two models and better results for Mendes and Pavlis model.

5. Conclusion

Through the present paper, the laser range finding system was investigated. Also errors due to the laser plus width and atmospheric effects at metrological conditions of laser beam emitter site were studied. Atmospheric correction for

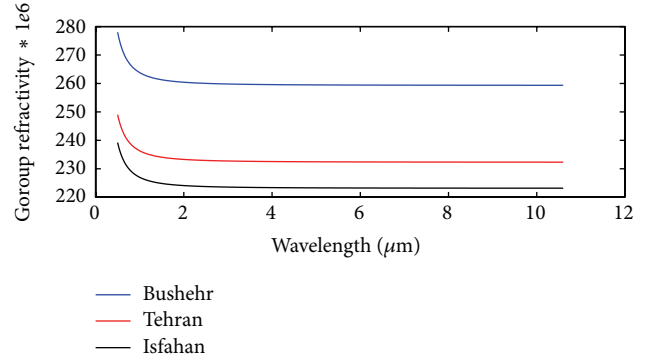


FIGURE 15: Group refraction parameter versus wavelength in Isfahan, Tehran, and Bushehr states weather conditions.

TABLE 1: AC comparison for two different applied models at 532 nm wavelength and 0° zenith angle.

City	Used model	Atmospheric path (km)	AC (m)
Tehran	Mendes-Pavlis	11	2.2166
		100	2.3242
		200	2.3932
	Marini-Murray	11	2.5942
		100	23.5834
		200	47.1667
Esfahan	Mendes-Pavlis	11	2.1756
		100	2.2323
		200	2.2985
	Marini-Murray	11	2.4898
		100	22.6349
		200	45.2698
Bushehr	Mendes-Pavlis	11	2.6355
		100	2.7031
		200	2.7832
	Marini-Murray	11	2.7562
		100	25.0566
		200	50.1131

monthly average metrological data of Tehran, Isfahan, and Bushehr states were calculated during a year. The atmospheric correction was calculated for 0.532, 1.3, and 10.6 μm laser wavelengths and 11, 100, and 200 km propagation path lengths under three emission angles. The atmospheric correction values at same emission angles and propagation path lengths were increased from 10.6 μm to 0.532 μm ; therefore, it was concluded that the atmosphere is approximately a window for first wavelength. For given states, the differences between AC values showed that it depended on the atmospheric conditions, that is, temperature and pressure of measuring site. According to the accessed results, the minimum group refraction parameter was for Isfahan and maximum for Bushehr. It was concluded that the weather conditions of Bushehr, that is, high pressure, high temperature, and high humidity, corresponded to the high group parameter and consequently high group refractive index. This high group

refractive index needs more atmospheric correction for the laser beams. The overall conclusion is that the various weather conditions cause error in the laser range finding and must be calculated and compensated.

Conflict of Interests

The authors declare that there is no conflict of interests regarding the publication of this paper.

References

- [1] L. Combrinck, *Satellite Laser Ranging, Sciences of Geodesy-I*, Springer, Berlin, Germany, 2010.
- [2] Z. Altamimi, P. Sillard, and C. Boucher, "ITRF2000: a new release of the International Terrestrial Reference Frame for earth science applications," *Journal of Geophysical Research B: Solid Earth*, vol. 107, no. 10, pp. 2–19, 2002.
- [3] D. D. Wijaya and F. K. Brunner, "Atmospheric range correction for two-frequency SLR measurements," *Journal of Geodesy*, vol. 85, no. 9, pp. 623–635, 2011.
- [4] J. W. Marini, "Correction of satellite tracking data for an arbitrary tropospheric profile," *Radio Science*, vol. 7, pp. 223–231, 1972.
- [5] J. W. Marini and C. W. Murray, "Correction of laser range tracking data for atmospheric refraction at elevations above 10 degrees," NASA Technical Memorandum NASA-TM-X-70555, 1973.
- [6] V. B. Mendes and E. C. Pavlis, "High-accuracy zenith delay prediction at optical wavelengths," *Geophysical Research Letters*, vol. 31, no. 14, 2004.
- [7] H. J. Rim and B. E. Schutz, *Geoscience Laser Altimeter System (GLAS), Algorithm Theoretical Basis Document, Version 2.2*, The University of Texas at Austin, Austin, Tex, USA, 2002.
- [8] G. C. Hulley and E. C. Pavlis, "A ray-tracing technique for improving Satellite Laser Ranging atmospheric delay corrections, including the effects of horizontal refractivity gradients," *Journal of Geophysical Research B: Solid Earth*, vol. 112, article B6, 2007.
- [9] J. J. Degnan, "Asynchronous laser transponders for precise interplanetary ranging and time transfer," *Journal of Geodynamics*, vol. 34, no. 3-4, pp. 551–594, 2002.
- [10] W. Colin and J. Julian, *Handbook of Laser Technology*, IOP Press, Bristol, UK, 2004.
- [11] A. B. Mark, *Development of the portable satellite laser ranging system [M.S. Thesis]*, Curtin University of Technology, 2003.
- [12] S. Svanberg, *Atomic and Molecular Spectroscopy: Basic Aspects and Practical Applications*, Springer, New York, NY, USA, 4th edition, 2003.
- [13] J. J. Degnan, "Satellite laser ranging current status and future prospects," *IEEE Transactions on Geoscience and Remote Sensing*, vol. 23, no. 4, pp. 398–413, 1985.
- [14] J. B. Abshire and C. S. Gardner, "Chester, Atmospheric refractivity correction in satellite laser ranging," *IEEE Transactions on Geoscience and Remote Sensing*, vol. 23, no. 4, pp. 414–425, 1985.
- [15] V. B. Mendes and E. C. Pavlis, "Atmospheric refraction at optical wavelengths: problems and solutions," in *Proceedings of the 13th International Laser Ranging Workshop*, 2002.

Research Article

Dust Identification over Arid and Semiarid Regions of Asia Using AIRS Thermal Infrared Channels

Hui Xu, Tianhai Cheng, Donghai Xie, Jiaguo Li, Yu Wu, and Hao Chen

Institute of Remote Sensing and Digital Earth, Chinese Academy of Sciences, Haidian District, Beijing 100101, China

Correspondence should be addressed to Tianhai Cheng; cthy@irsa.ac.cn

Received 5 June 2014; Revised 10 August 2014; Accepted 12 August 2014; Published 31 August 2014

Academic Editor: Hesham El-Askary

Copyright © 2014 Hui Xu et al. This is an open access article distributed under the Creative Commons Attribution License, which permits unrestricted use, distribution, and reproduction in any medium, provided the original work is properly cited.

Asia dust generated in northern China exerts significant influences on regional air quality, weather, and climate. In this study, a dust identification algorithm over arid and semiarid regions of Asia was proposed based on the thermal observations of atmospheric infrared sounder (AIRS). Firstly, a combination of the line-by-line (LBL) and discrete ordinates radiative transfer (DISORT) model was utilized to investigate the thermal infrared signatures of dust and cloud in 800–1250 cm^{-1} region. Secondly, six channels in the thermal infrared region were selected from AIRS to monitor dust from space, and a further sensitivity analysis for dust and cloud under different conditions was also performed. Then, the description of the detailed identification method was provided based on distinct thermal infrared signature of dust. At last, several dust events that observed in northern China between the period of 2008 and 2012 were analyzed, and the usefulness of monitoring the outbreaks of Asian dust was emphasized through the comparison with moderate resolution imaging spectroradiometer (MODIS) visible observations and cloud aerosol lidar with orthogonal polarization (CALIOP) data in this study.

1. Introduction

In spring, the arid and semiarid regions of northern China are dry and often windy [1], providing the favorable conditions for the development of dust activities [2, 3] and making China the most important dust source regions in Eastern Asia [4–6]. The elevated mineral dust which is mainly distributed in the troposphere [7–10] can affect climate on various spatial and temporal scales [11] through a series of complex direct and indirect radiative forcing [12–15]. Recently, owing to the climate change and excessive land use, dust events occur more frequently around the world [16, 17]. Therefore, it is necessary to monitor its distribution and study how it changes.

Since the advent of satellite technology, monitoring dust from space has become one of the most important focuses among the many atmospheric scientific issues [18]. In last decade, much progress has been made in the remote sensing of dust using various VIR (visible and near-infrared) and TIR (thermal infrared) techniques [19–27]. Recently, the potential possibility of utilizing the microwave and Lidar measurements to monitor dust from space was also discussed

by many researchers [28–30]. Among the many techniques, it has been proved that the infrared hyperspectral resolution remote sensing has the distinct advantage in monitoring dust over arid and semiarid surfaces and even in the nighttime [31–37]. Sokolik [31] carried out the research on the infrared hyperspectral radiative signature of wind-blown mineral dust, concluding that dust has a significant influence on the retrieval accuracy of surface and atmospheric parameters. Hong et al. [32] made a deep investigation on the infrared signature of overlapping cirrus clouds and mineral dust, which finds that the thermal infrared spectral features in the 1100–1200 cm^{-1} and 1400–1850 cm^{-1} regions can be used to retrieve the optical thicknesses of the dust and cirrus cloud, respectively. Pierangelo et al. [26, 33, 34] proposed an algorithm to retrieve the optical depth, effective radius, and height of dust over the Atlantic Ocean from AIRS data based on the fast line-by-line Automated Atmospheric Absorption Atlas (4A) model. DeSouza-Machado et al. [35, 36] using AIRS observations developed fast optical depth and height retrieval methods through the analysis of infrared dust spectral signatures over ocean, and the results show good

correlation with MODIS products. Based on the RTTOV IDVAR algorithm, Yao et al. [37] retrieved the Asia dust top height and infrared optical depth over land from AIRS observations, and the optical depths retrieved from AIRS correlate favorably with the visible optical depths from OMI.

Although remote sensing dust using hyperspectral infrared measurement has made considerable progress in the last decade, more efforts still need to do both in the forward simulation and retrieval method, especially at nighttime and even when the condition of dust and cloud are cooccurrence in the same atmospheric column. As the accurate dust detection result is critically important for the properties retrieval, this study focuses on the dust identification over arid and semiarid regions using thermal infrared hyperspectral sounding data from AIRS. The paper is organized as follows: a description of used satellite remote sensing dataset is given in Section 2; Section 3 makes a comprehensive analysis on the thermal infrared signatures of dust and cloud, and the detailed dust identification algorithm is also given in this section; detection results and comparison with MODIS and CALIOP observations are performed in Section 4; summary and conclusions are given in the closing section.

2. Satellite Remote Sensing Data

2.1. AIRS. The AIRS instrument [38] on board Earth Observing System (EOS) Aqua platform in the A-Train constellation which launched on May 4, 2002, is the first new generation of high spectral resolution of infrared sounder. It has 2378 infrared channels which can measure the earth outgoing radiation in 3.7–15.4 μm region (3.75–4.58, 6.2–8.2, and 8.8–15.4 μm) with a spectral resolution of $\lambda/\Delta\lambda = 1200$ and spatial resolution of 13.5 km (nadir field of view). The primarily task of AIRS is to obtain the highly accurate temperature profiles within the atmosphere plus a variety of additional Earth/atmosphere products (surface temperature, water vapor, and cloud properties) [39–41] to conduct the further research on climate changes and weather forecasting. Additionally, AIRS can also measure the information of dust properties by taking advantage of the high spectral resolution longwave dust-sensitive radiance measurements as described above. In this study, the daily level 1B datasets which are downloaded from Goddard Earth Sciences Data and Information Services Center (GES DISC) are used to monitor and analyse the dust of Asia.

2.2. MODIS. The MODIS sensor shares the Aqua satellite with AIRS (there are no temporal artefacts on the observed scene between the two instruments) which has 36 channels with wavelengths from 0.41 to 14.385 μm and nadir spatial resolutions of 0.25 km, 0.5 km, and 1 km [42]. It is considered as a key instrument to improve our understanding of global dynamics and processes occurring on the land, in the oceans, and in the lower atmosphere. Its level 2 aerosol products [43] use three different algorithms (Ocean, Dark Target, and Deep Blue) to monitor the ambient aerosol optical thickness over the oceans globally and over the continents. The Deep Blue algorithm [20] was developed to get the aerosol optical depth

over bright land areas. Generally speaking, high values of the deep blue optical depth over the arid and semiarid regions are usually related to more dust loading in the atmosphere, vice versa. Here, the level 1B RGB composition images (R: channel 1, G: channel 4, and B: channel 3) and level 2 deep blue aerosol optical depth product (MYD04) which are downloaded from International Cancer Alliance for Research and Education (ICARE) is used to evaluate and analyse the results of proposed dust identification algorithm.

2.3. CALIOP. The Cloud Aerosol Lidar with Orthogonal Polarization (CALIOP) instrument on board the CALIPSO platform which can provide the unique measurements of the global vertical distributions of clouds and aerosols both at day and night [36]. It is a two-wavelength Lidar that transmits and receives backscattered light at laser wavelengths of 532 nm and 1064 nm. The vertical resolutions are 30 m from the surface to 8 km altitude and 60 m above the 8 km altitude. The minimum horizontal resolution of a single profile is 330 m, and a typical horizontal averaging interval is 5 km for aerosol and dust. CALIOP is a nadir only sensor which follows a similar ground track to AIRS (offset by 170 km from AIRS nadir). It is also a member of the A-Train constellation, which means that measurements from AIRS and CALIOP can be easily compared to each other. In this paper, the L1 532 nm backscatter data and L2 aerosol subtype products from the CALIPSO Search and Subsetting web application are used to evaluate the dust identification results during nighttime.

3. Physical Basis and Method

3.1. Physical Basis. Generally, almost all dust events, especially the dust storms, are related to cold front and cyclone activities [1]; consequently, dust and cloud more often coexist in the same scene. In order to differentiate dust from other targets, the thermal infrared signatures of dust and cloud are investigated. To acquire the spectral brightness temperatures at the top of atmosphere, the discrete ordinates radiative transfer (DISORT) model in conjunction with a line by line (LBL) model is used to simulate the thermal infrared signatures of dust and cloud in the 800–1250 cm^{-1} region with a spectral resolution of 0.1 cm^{-1} .

Considering that the optical properties of dust are mainly depending on the mineralogical composition and particle radius (the nonspherical effect is small over IR spectral range [44]), accurate refractive indices and size distribution are required for the simulation. Han et al. [45] founded that the Volz dust-like refractive indices [46] can well represent the optical properties of Asia dust. Therefore, the bulk extinction coefficient, single scattering albedo, and phase function of Asia dust are calculated with Lorentz-Mie scattering based on the dust-like refractive indices and OPAC typical accumulated dust size distribution [47]. For the description of cloud, the water and ice cloud is investigated. The optical properties of water cloud are calculated through Lorentz-Mie scattering with an effective radius of 10 μm [48], and the optical properties of ice cloud are derived from Baum et al. [49, 50] with an effective radius of 30 μm .

Many researches have proved that dust is generally located around the 1–5 km in altitude [22, 26, 34, 37], and sometimes it can be transported to the 8–10 km [51] levels of atmosphere when the conditions permit. In present simulation, the spectral brightness temperatures of dust for a 3 km height in conjunction with an optical thickness of 1.0 (at infrared wavelength of $10 \mu\text{m}$, 1000 cm^{-1} in wavenumber) are simulated. In addition, the thermal infrared signatures of typical water and ice cloud [48] are also studied for the purpose of comparing and analyzing the spectrum difference between dust and cloud. The water cloud layer with an optical depth of 15.0 in an altitude of 1 km height was assumed, and the ice cloud layer is considered at a 10 km height atmosphere with an optical depth of 3.0. Moreover, the atmospheric molecular absorption is calculated from the LBL model based on the middle latitude winter standard atmospheric profile, the surface temperature, and emissivity are assumed as 290 K and 1.0, respectively. At last, the nadir infrared spectral brightness temperatures of clear sky, dust, and cloud are calculated through the DISORT and LBL models. Figure 1 shows the forward simulation results, and all the input variables are listed in Table 1.

From Figure 1(a), it is easy to see that the spectral segment of clear sky in $800\text{--}1250 \text{ cm}^{-1}$ region is essentially flat except for the ozone strong absorption region (nearly around the region of $1000\text{--}1060 \text{ cm}^{-1}$). However, in the present dust (Figure 1(b)), it not only decreases the brightness temperatures in the whole spectral region of $800\text{--}1250 \text{ cm}^{-1}$ but also displays a “V” spectral shape which is resulted from a negative spectral slope in $800\text{--}1000 \text{ cm}^{-1}$ subregion and a positive spectral slope in $1060\text{--}1250 \text{ cm}^{-1}$ subregion. In addition, the overall variation patterns of the two subregions are nearly symmetric although the slope in the positive region is a little bit sharper. Unlike the spectral variation caused by dust, clouds reveal some different characteristics. In Figure 1(c), it is obvious to see that ice cloud generally shows a reversed spectral feature with dust. The spectrum in $800\text{--}1000 \text{ cm}^{-1}$ region is marked with a positive slope whereas the variation of brightness temperatures in $1060\text{--}1250 \text{ cm}^{-1}$ region is generally flat. For the spectral signature of water cloud, it is much more similar to the clear sky, even though the brightness temperatures in the subregion of $800\text{--}1000 \text{ cm}^{-1}$ are generally higher than the subregion of $1060\text{--}1250 \text{ cm}^{-1}$ (Figure 1(d)).

Actually, the obvious “V” spectral shape of dust in the region of $800\text{--}1250 \text{ cm}^{-1}$ probably provides us an opportunity to monitor it from space.

3.2. Channel Selection. It is common to know that water vapor and ozone are the main absorption gases in the thermal infrared region of $800\text{--}1250 \text{ cm}^{-1}$. Thus, the selected dust observation channels should be either highly sensitive to dust or less/no sensitive to water vapor and ozone. Actually, there are many channels that may satisfy the criteria. However, as the extinction abilities of dust in the adjacent channels are basically similar, consequently, the brightness temperature differences between these channels are generally small, and then the spectral shape of dust can be easily affected by

TABLE 1: The input parameters of dust and cloud for the brightness temperature simulation.

	Dust	Ice cloud	Water cloud
Optical depth	1.0	3.0	15.0
Layer height	3 km	10 km	1 km
Particle effective radius	$1.3 \mu\text{m}$	$30 \mu\text{m}$	$10 \mu\text{m}$
Surface temperature	290 K		
Surface emissivity	1.0		
Atmosphere profile	Middle latitude winter atmospheric profile		

TABLE 2: The selected AIRS dust observation channels.

Chanel (id)	Wavenumber (cm^{-1})	Wavelength (μm)	Transmittance
504	811.78	12.32	0.90
761	901.00	11.09	0.95
953	980.36	10.20	0.93
1179	1092.92	9.15	0.90
1237	1123.13	8.90	0.92
1307	1239.68	8.06	0.67

nondust factors. Therefore, in order to more accurately depict the unique “V” spectral shape of dust in the $800\text{--}1250 \text{ cm}^{-1}$ region, six channels with obviously different dust extinction abilities are selected, as shown in Table 2. And the redundant channels with similar transmittance to these six channels are removed, even though they also can be used to monitor dust from space.

It is interesting to note that all the selected channels have a high transmittance except for the 1239.68 cm^{-1} channel. Under the condition of clear sky, the radiances measured in this channel will generally low than the others. However, as it has less dust extinction compared with other channels, the relative changes in radiances observed in this channel can be used as a good indicator of dust.

3.3. Sensitivity Analysis. Based on the selected AIRS observation channels, the spectrum variation patterns of dust and cloud under different conditions are further discussed. The high resolution monochromatic radiances of the scenes are integrated with the filter function over the bandwidth of selected channels to acquire the channel brightness temperatures. Specially, if not specified, the default input parameters of the following simulation are set as values listed in Table 1, and one parameter changes, and the others keep constant.

3.3.1. Dust. Figure 2 shows the dependence of the channel spectral brightness temperatures on the optical depth, layer height, and effective radius of dust. In addition to the “V” spectral shape of dust that is discussed in Section 3.1, other interesting features can be also noticed from Figure 2.

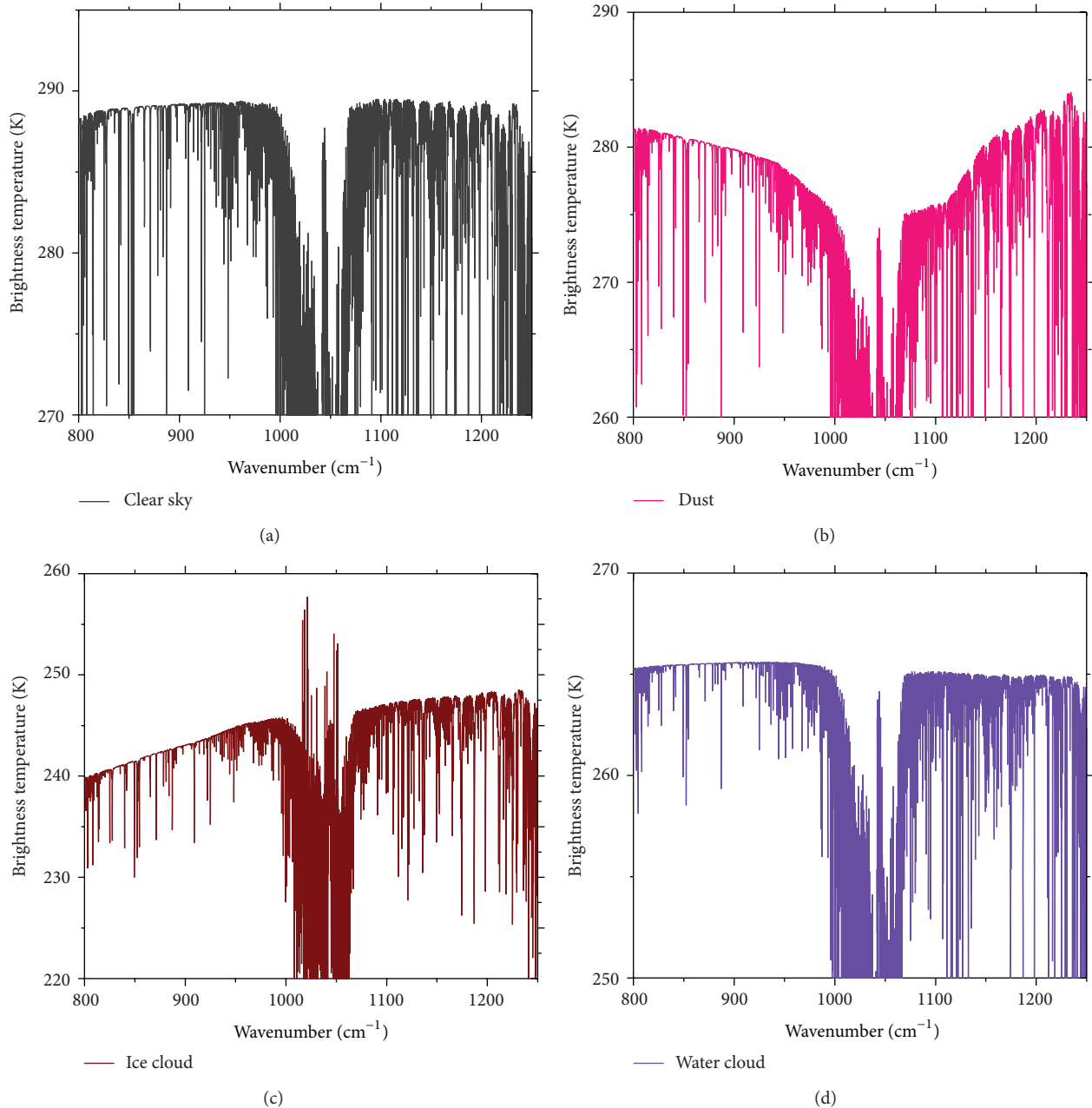


FIGURE 1: The simulated nadir-viewed spectral brightness temperatures of (a) clear sky, (b) dust, (c) ice cloud, and (d) water cloud.

Figures 2(a) to 2(d) show the spectral variation of dust with optical depth. It is easy to see that the “V” spectral shape is not particularly obvious when dust has a low optical depth. However, with the increase of the optical depth, the slopes of the spectrum in both the 800–1000 cm^{-1} and 1060–1200 cm^{-1} regions become more and more sharp, and this variation characteristic is also applicable to the changes of dust layer height. As shown in Figure 2(e), with the increase of dust layer altitude, the “V” spectral shape becomes more and more clear. These indicate that the thermal infrared measurements are especially suitable for the detection of dust with high optical depth and altitude; however, dust layer close to the surface

with a low optical depth can be hardly identified. Figure 2(f) shows the variation of channel brightness temperatures with the change of dust effective radius. In Figure 2(f), another interesting point to be noted is that the spectral brightness temperature differences between channels become smaller with the increase of particle effective radius. That is to say, the coarse particles can weaken the particular “V” spectral shape of dust.

3.3.2. *Cloud.* For the detailed spectrum analysis of cloud in the selected channels, not only ice and water clouds are discussed (Figures 3 and 4) but also the mixed-phase cloud is

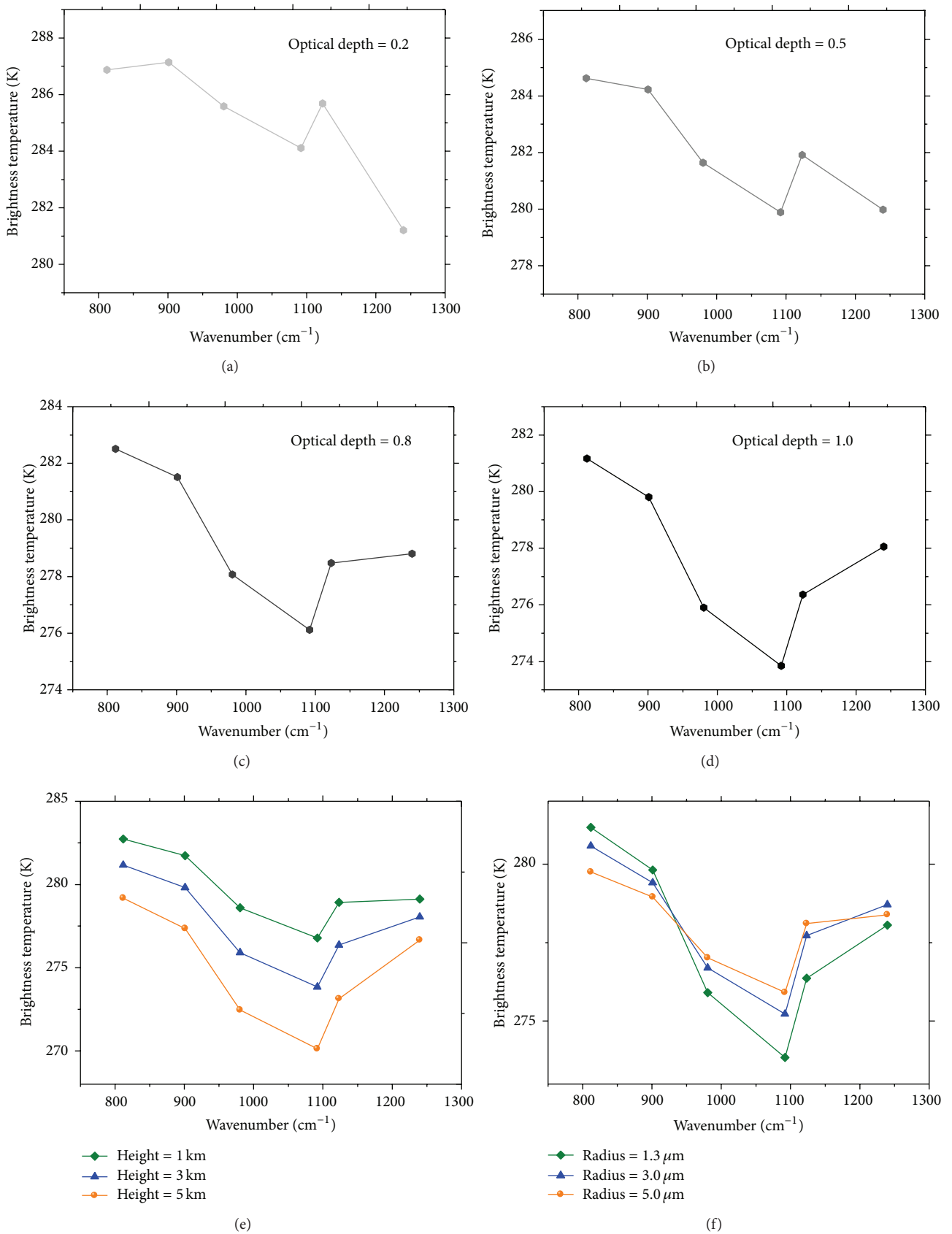


FIGURE 2: The effects of (a–d) optical depth, (e) layer height, and (f) effective radius on the spectrum of dust.

investigated (Figure 5), as the mixed-phase clouds are more frequent in the cold front coexist with dust storms over the semiarid region.

Like the case for dust, the spectral signature of ice cloud becomes more pronounced as the optical depth (shown in Figures 3(a) to 3(d)) and layer height (shown in Figure 3(e)) increase, and the spectrum in 800–1000 cm^{-1} subregion is gradually featured with a positive slope. It is also interesting to see that the slopes of the spectrum in both the 800–1000 cm^{-1} and 1060–1250 cm^{-1} subregions are sensitive to the variation of ice particle effective radius (as shown in Figure 3(f)). Specially, ice particles with small effective radius (radius = 10 μm in Figure 3(f)) will reveal a reversed spectral shape with dust, as evident from Figure 3(f) (positive slope in 800–1000 cm^{-1} subregion and negative slope in 1060–1250 cm^{-1} subregion).

The thermal infrared signature of water cloud is shown in Figure 4. In general, the spectral brightness temperatures in the 800–1000 cm^{-1} subregion gradually become higher than them in the 1060–1250 cm^{-1} subregion, with the increase of water cloud optical depth (shown from Figures 4(a) to 4(d)). Moreover, it is evident from Figure 4 that the slope of the spectrum in 1060–1250 cm^{-1} subregion is becoming nearly zero along with the increasing of water cloud optical depth and layer height. Similar to the dust and ice cloud cases, the increase of water droplet effective radius will decrease the brightness temperature differences in these selected channels, as shown in Figure 4(f).

For the case of mixed-phase cloud, the optical properties are calculated following the formulations developed by Liou [52], and Ou et al. [53] using the optical model developed a mixed-phase cloud retrieval method for the sensor of Visible Infrared Imaging Radiometer Suite (VIIRS):

$$\begin{aligned}\omega_{\text{mix}} &= \frac{\tau_s}{\tau} = \frac{\omega_i \tau_i + \omega_w \tau_w}{\tau_i + \tau_w}, \\ l_{\text{mix}} &= \frac{\omega_i \tau_i l_i + \omega_w \tau_w l_w}{\tau_s}, \\ f_{\text{mix}} &= \frac{\omega_i \tau_i f_i + \omega_w \tau_w f_w}{\tau_s},\end{aligned}\quad (1)$$

where ω_{mix} , l_{mix} , and f_{mix} are the mixed-phase single scattering albedo, Legendre polynomial expansion coefficients, and phase function. Parameters τ_s and τ are the scattering optical depth and total optical depth of mixed-phase cloud, respectively, with subscripts i and w denoting ice and water clouds. Figures 5(a) and 5(b) show the spectral brightness temperatures of mixed-phase clouds with 1 km and 10 km in altitude, respectively.

From Figure 5, it is clear to see that the spectral variation of mixed-phase cloud is generally between the spectral shapes of ice (Ice_(optical depth) = 10.0, Water_(optical depth) = 0.0) and water cloud (Ice_(optical depth) = 0.0, Water_(optical depth) = 10.0), and the spectral characteristic of mixed-phase cloud is basically determined by the fractions of ice and water cloud particles in it. Another interesting point that can be intuitively identified is that the thermal infrared signature of low level mixed-phase

cloud is generally consistent with that of water cloud (shown in Figure 5(a)); however, if the mixed-phase cloud locates at a high level atmosphere, it would reveal a spectral signature more similar to the ice cloud (shown in Figure 5(b)).

3.3.3. Cloud over Dust. Many dust monitor researches have focused on the cases of cloud and dust layers which are not cooccurring in the same atmospheric column. However, they are frequently cooccurring over the northwest of China. To investigate the impact of cloud on spectral signature of dust, forward simulation experiments in the cases of thin (optical depth set as 1.0) and thick (optical depth set as 3.0) ice cloud overlapping low level dust are conducted, as shown in Figures 6(a) and 6(b), respectively.

In Figure 6(a), it is intuitive to see that the spectral brightness temperatures are depressed with increasing the optical depth of underlying dust. And the spectral shape is gradually transformed from ice cloud only to dust only. As shown in Figure 6(a), when the optical depth of the underlying dust is larger than that of the thin ice cloud, the spectral signatures of cloud-dust coexisting are highly consistent with that of dust only. However, if the dust layer is covered by a thick ice cloud, as shown in Figure 6(b), the spectral signatures of cloud-dust coexisting conditions are different from those for ice cloud only or dust alone, especially in the 800–1000 cm^{-1} subregion. This implies that the case of thick ice cloud overlapping low level dust cannot be easily detected by the thermal infrared measurements.

3.4. Method. In general, the spectral characteristics discussed in the preceding context imply that dust has a unique thermal infrared signature in the region of 800–1250 cm^{-1} . Indeed, this distinct spectral shape provides us a reliable way to monitor dust through the thermal infrared measurements. Based on the analysis of channel spectral signature, several thresholds and combinations of selected ARIS channels were chosen to identify dust over arid and semiarid region, which are listed in Table 3. The entire dust test that is listed in Table 3 should generally provide an almost unique signature of dust in the thermal infrared. For any AIRS FOV, if test passes the threshold, it denotes that the pixel is contaminated by dust; otherwise, the FOV is flagged as not dust contaminated, finally.

4. Results and Discussion

4.1. Case: 30 March 2008. Taklamakan Desert is the world's largest shifting sand desert which is located in Central Asia (northwest China). Figure 7(a) shows a dust event on 30 March, 2008, sweeping across the northern Taklimakan Basin (red arrows in Figure 7(a)) which is surrounded by Kunlun Mountains in south and Tian Shan Mountains in north.

In order to evaluate the discussed Asia dust thermal infrared signature in the preceding context (Section 3), the brightness temperatures of the selected six channels in the dust region (the blue box region depicted in Figure 7(a)) are extracted from AIRS observation, as shown in Figure 7(b). The distinct “V” shape of dust can be directly acquired from

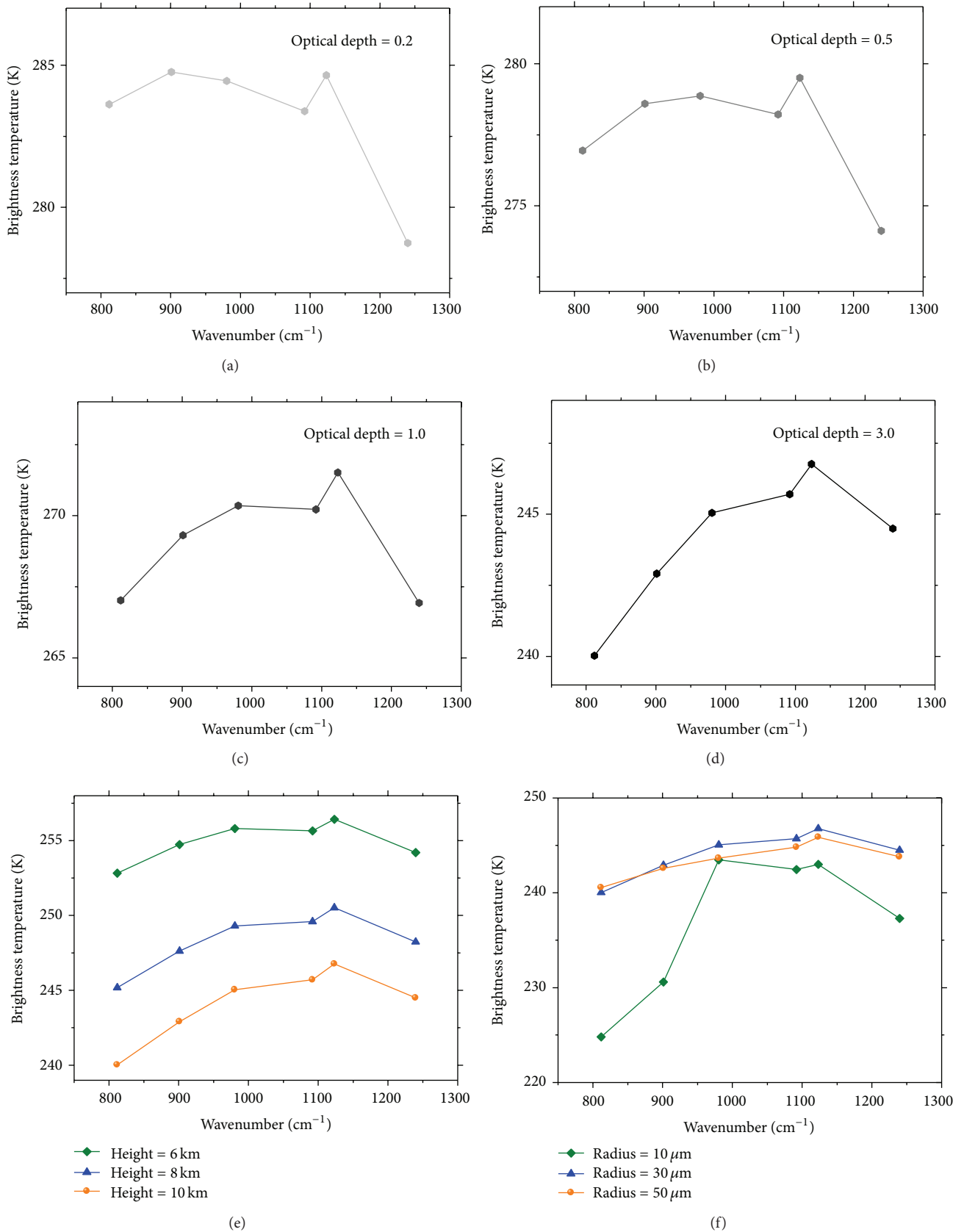


FIGURE 3: The effects of (a-d) optical depth, (e) layer height, and (f) effective radius on the spectrum of ice cloud.

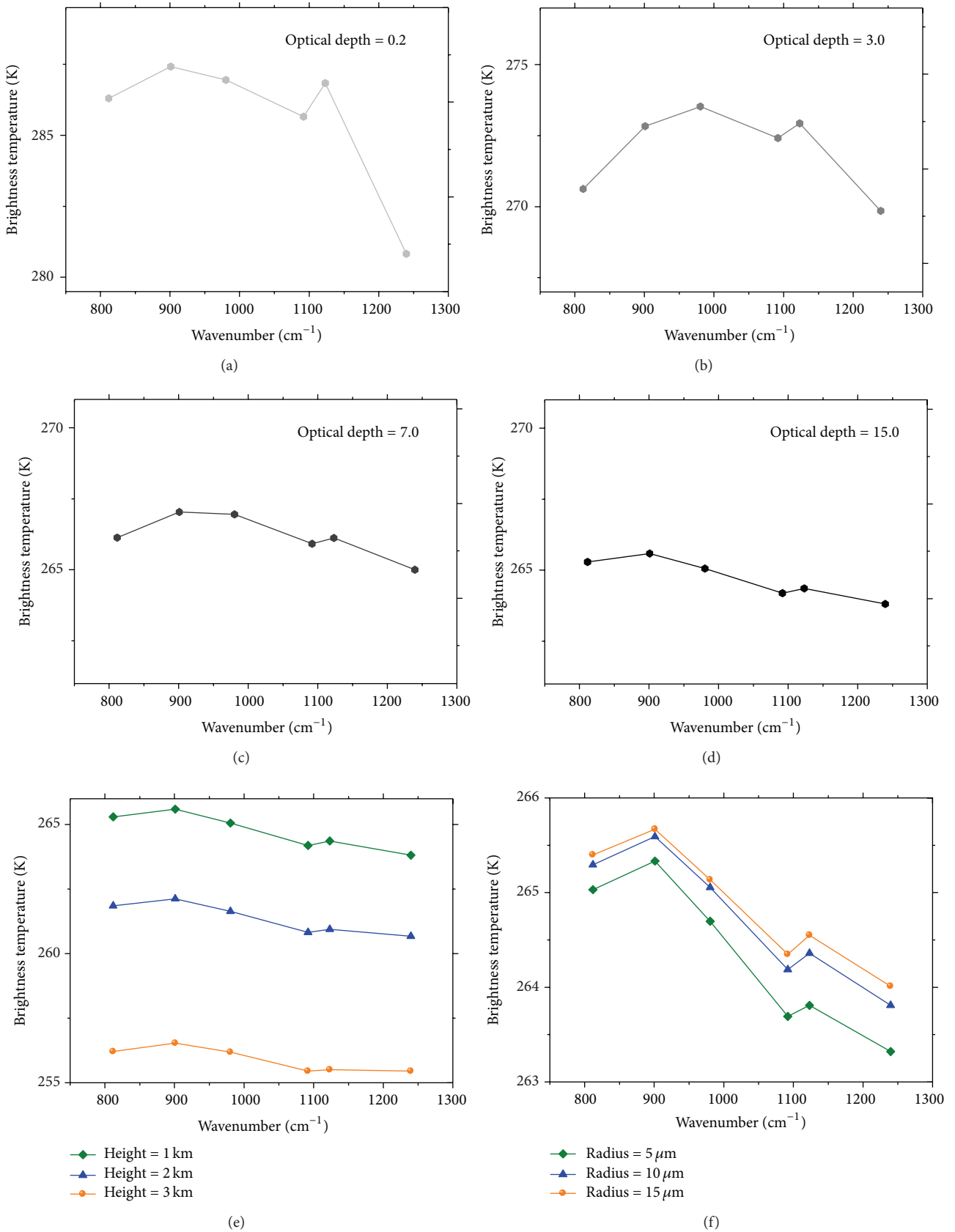


FIGURE 4: The effects of (a–d) optical depth, (e) layer height, and (f) effective radius on the spectrum of water cloud.

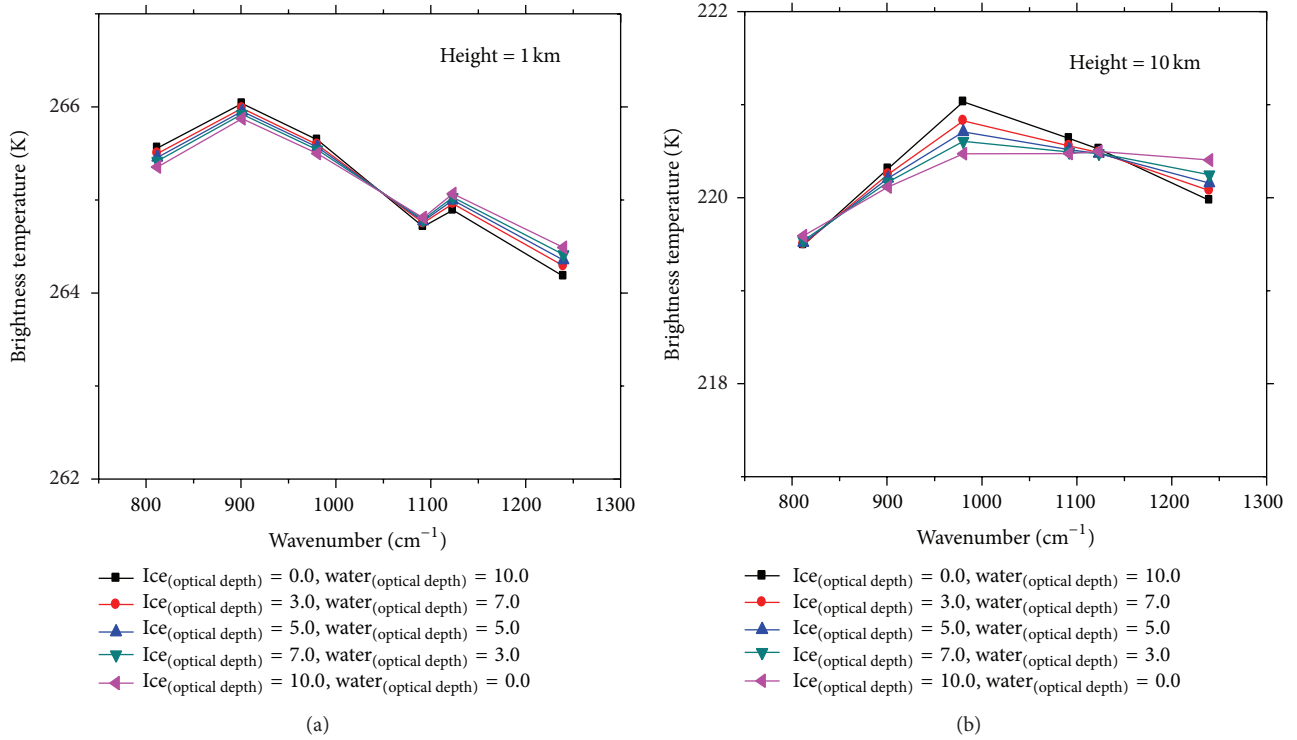


FIGURE 5: The spectrums of (a) low and (b) high mixed-phase clouds.

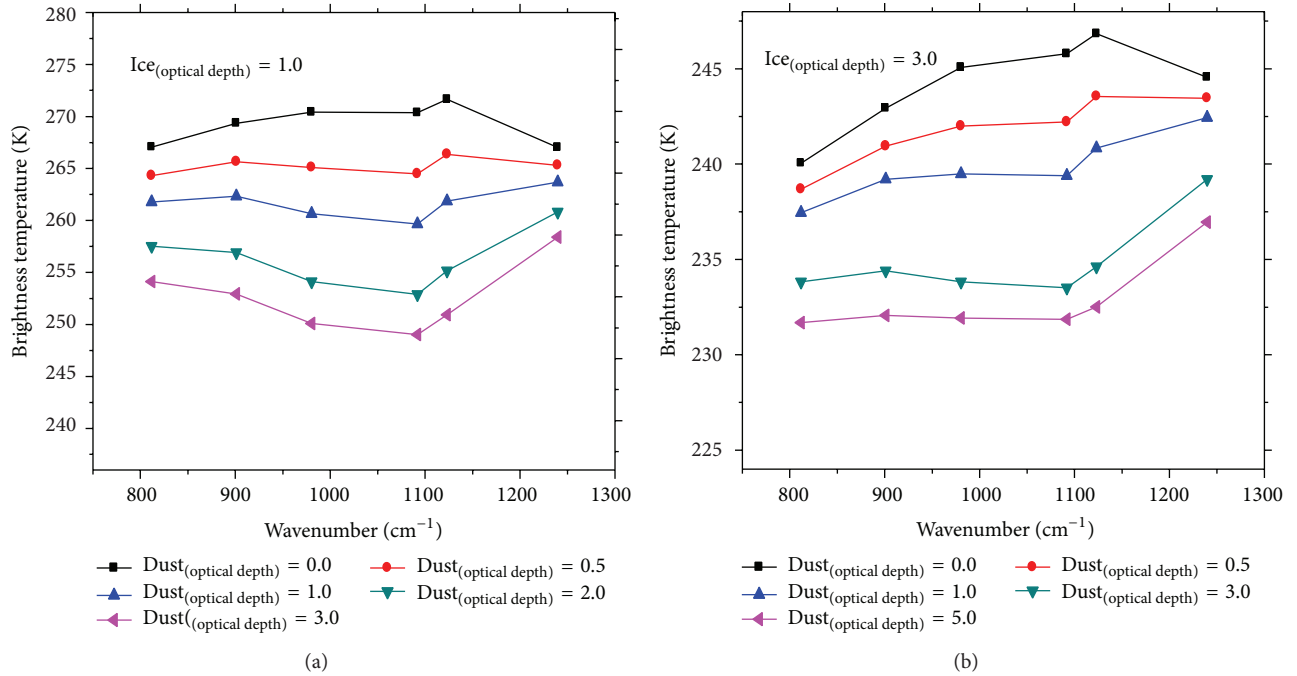


FIGURE 6: The spectrums of (a) thin and (b) thick ice clouds overlapping underlying dust.

this figure. Moreover, through the comparison of Figures 7(b) and 2, the spectral variation feature that is observed by AIRS is highly corresponding with the forward simulation experiments. This not only implies the correctness of the results

discussed in previous context but also indicates that the “V” shape is the true spectral signature of Asia dust in 800–1250 cm⁻¹ region, which gives us more confidence to monitor the Asia dust using this particular characteristic.

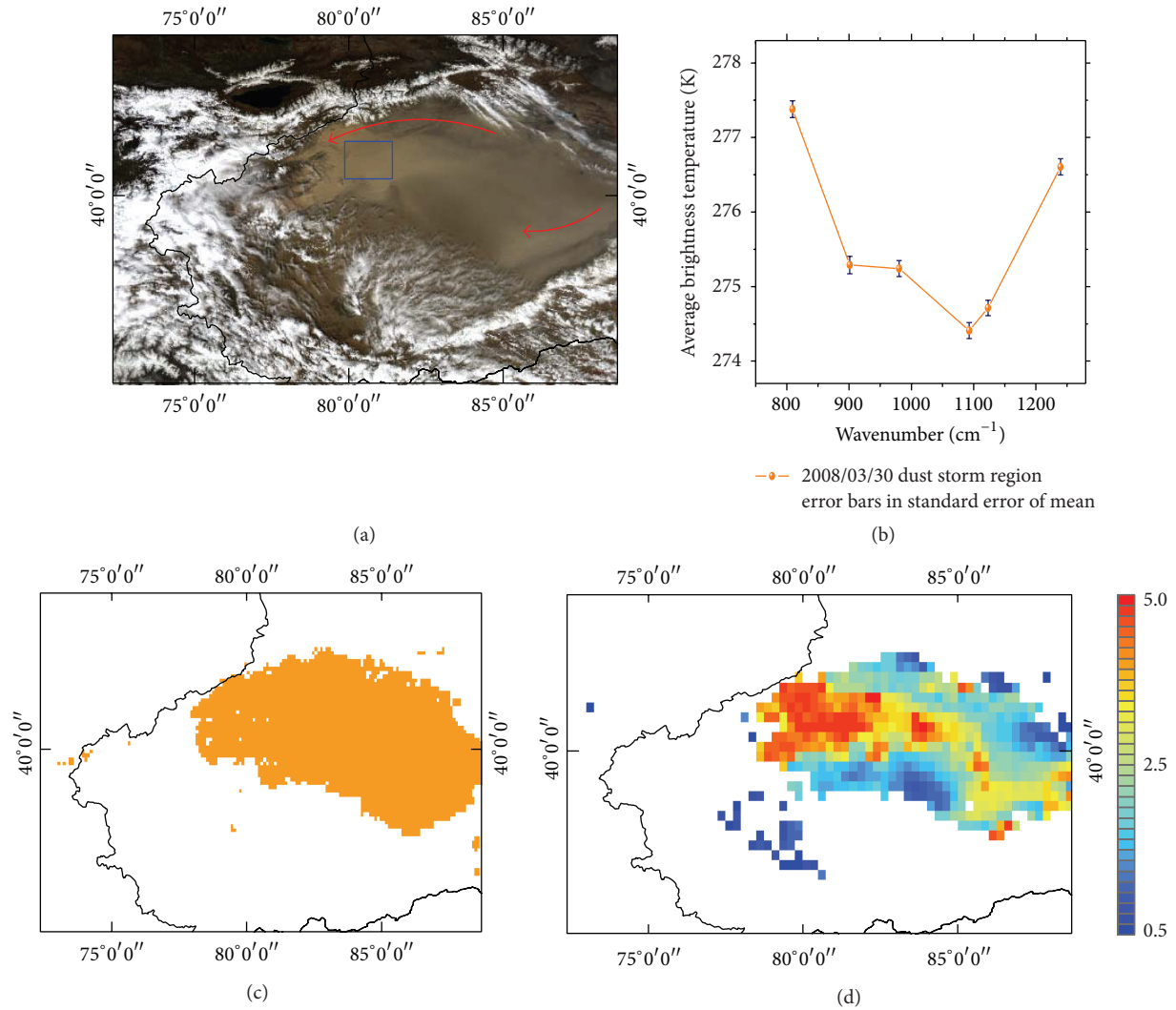


FIGURE 7: (a) March 30, 2008, dust RGB composite image form MODIS, (b) AIRS observation brightness temperature within dust region, (c) dust identification results, and (d) MODIS deep blue aerosol optical depth results.

TABLE 3: The combinations of ARIS channels and dust identification thresholds.

Dust test	Channel combinations	Threshold
dustflag1	$BT_{811.78 \text{ cm}^{-1}} \text{ minus } BT_{901 \text{ cm}^{-1}}$	Positive
dustflag2	$BT_{811.78 \text{ cm}^{-1}} \text{ minus } BT_{1092.92 \text{ cm}^{-1}}$	Positive
dustflag3	$BT_{901 \text{ cm}^{-1}} \text{ minus } BT_{980.36 \text{ cm}^{-1}}$	Positive
dustflag4	$BT_{901 \text{ cm}^{-1}} \text{ minus } BT_{1092.92 \text{ cm}^{-1}}$	Positive
dustflag5	$BT_{1092.92 \text{ cm}^{-1}} \text{ minus } BT_{1123.13 \text{ cm}^{-1}}$	Negative
dustflag6	$BT_{1092.92 \text{ cm}^{-1}} \text{ minus } BT_{1239.68 \text{ cm}^{-1}}$	Negative
dustflag7	$BT_{1123.13 \text{ cm}^{-1}} \text{ minus } BT_{1239.68 \text{ cm}^{-1}}$	Negative

Figure 7(c) displays the dust identification result based on the proposed method. It is obvious to see that the light brownish dust plumes (red arrow cover region in Figure 7(a)) have been clearly identified by the infrared dust identification algorithm from AIRS observations. Besides, the highly consistent spatial distribution between the dust identification

results and MODIS deep blue aerosol optical depth results (Figure 7(d)) also confirms the point. This demonstrates that the selected thermal infrared AIRS channels can effectively identify the dust from other scenes.

4.2. Case: 19 April 2008. On April 19, 2008, a combination of dust and cloud hovered over the most of Taklimakan Desert. The RGB composite image captured by Aqua's MODIS instrument is shown in Figure 8(a). As seen in this image, the strong dust activity originates from eastern Taklimakan Desert, blowing massive loose sand and dust particles to the atmosphere and carrying them to the western areas; red arrows denote the coverage of dust.

Figure 8(b) shows the spectral brightness temperatures within dust regions (the blue box region depicted in Figure 8(a)) observed by the selected infrared channels of AIRS. The thermal infrared signature of this selected dusty area also reveals a similar variation characteristic with the forward simulation results which are displayed in

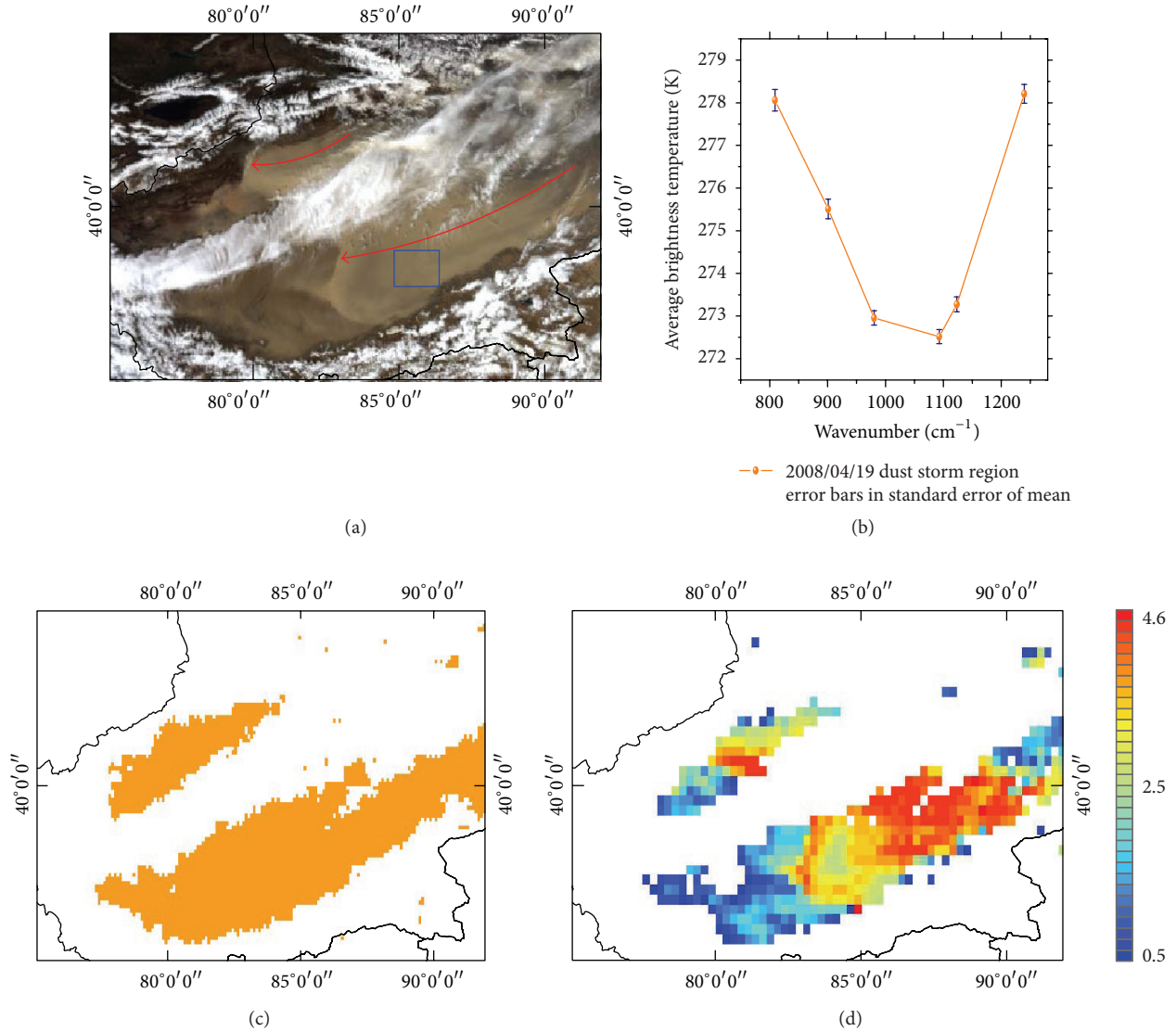


FIGURE 8: (a) April 19, 2008, dust RGB composite image from MODIS, (b) AIRS observation brightness temperature within dust region, (c) dust identification results, and (d) MODIS deep blue aerosol optical depth results.

Figure 2. This phenomenon proved again that the spectral characteristic of Asia dust discussed in the preceding context is overall correct.

Based on the proposed method, the coverage of this dust event is identified by the selected AIRS channels, which is shown in Figure 8(c). Through the comparison with MODIS composite image, it is clear to see that the dusty areas can be accurately distinguished from cloud and clear sky regions, and the detected results agree well with those shown in the visible observations. In addition, the distribution pattern of retrieved MODIS deep blue optical depth results (Figure 8(d)) is also highly consistent with the AIRS dust identification results. This indicates that the thermal infrared measurements are indeed able to successfully pick out the dusty regions over bright surface of arid and semiarid regions.

4.3. Case: 25 April 2009. The particular nighttime dust imagery around the Taklimakan desert region on 25 April, 2009, is selected to illustrate the capability of dust identification at night. Figure 9(a) shows the CALIOP track path (black line), and the pink line segment represents the local footprints in the study areas. The AIRS dust identification results, CALIOP 532 nm backscatter data (in units of km⁻¹sr⁻¹), and retrieved aerosol subtype results are given in Figures 9(b), 9(c), and 9(d), respectively.

Through the comparison of Figures 9(b) and 9(d), it is intuitive to see that the nighttime AIRS dust identification results along the track agree well with the aerosol type results retrieved from CALIOP, and both of the results indicate that dust exists in large areas from the latitude of 52.25° to 28.30°. Indeed, as evidently shown in the Lidar

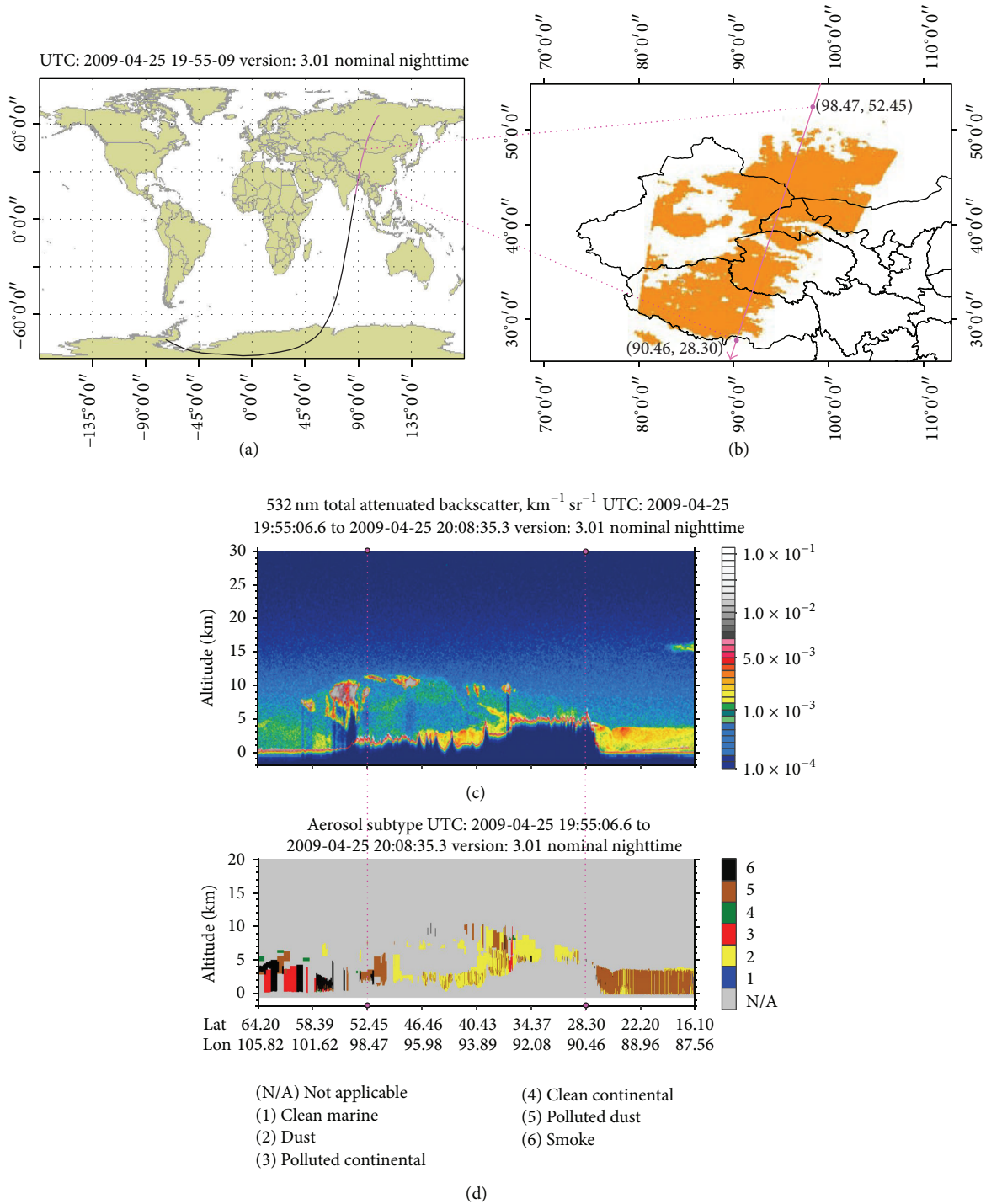


FIGURE 9: (a) April 25, 2009, CALIPSO track path, (b) AIRS dust identification results along the CALIPSO track, (c) the vertical backscatter data observed by the CALIOP 532 nm channel, and (d) the level 2 aerosol subtype results retrieved from CALIOP.

backscatter data (Figure 9(c)), thin dusts (yellow signals) with a top height between 1 km and 10 km are present between 52.45° and 46.46° latitude, and the ice clouds (pale signals) with geometric depth ranging from 500 m to 1 km are also existing in the same region. In addition, the thick dust layer (red signals) located between 1 km and 2 km from the latitude

of 46.46° to 34.37° is observed, and an extra tenuous dust layer (yellow signals) distributed at a high altitude on top of the thick one was also captured by the sensor of CALIOP. In the latitude region of 34.37° to 28.30°, however, relatively weak backscatter signals were received by the 532 nm channel, which indicates that little dusts exist in the area.

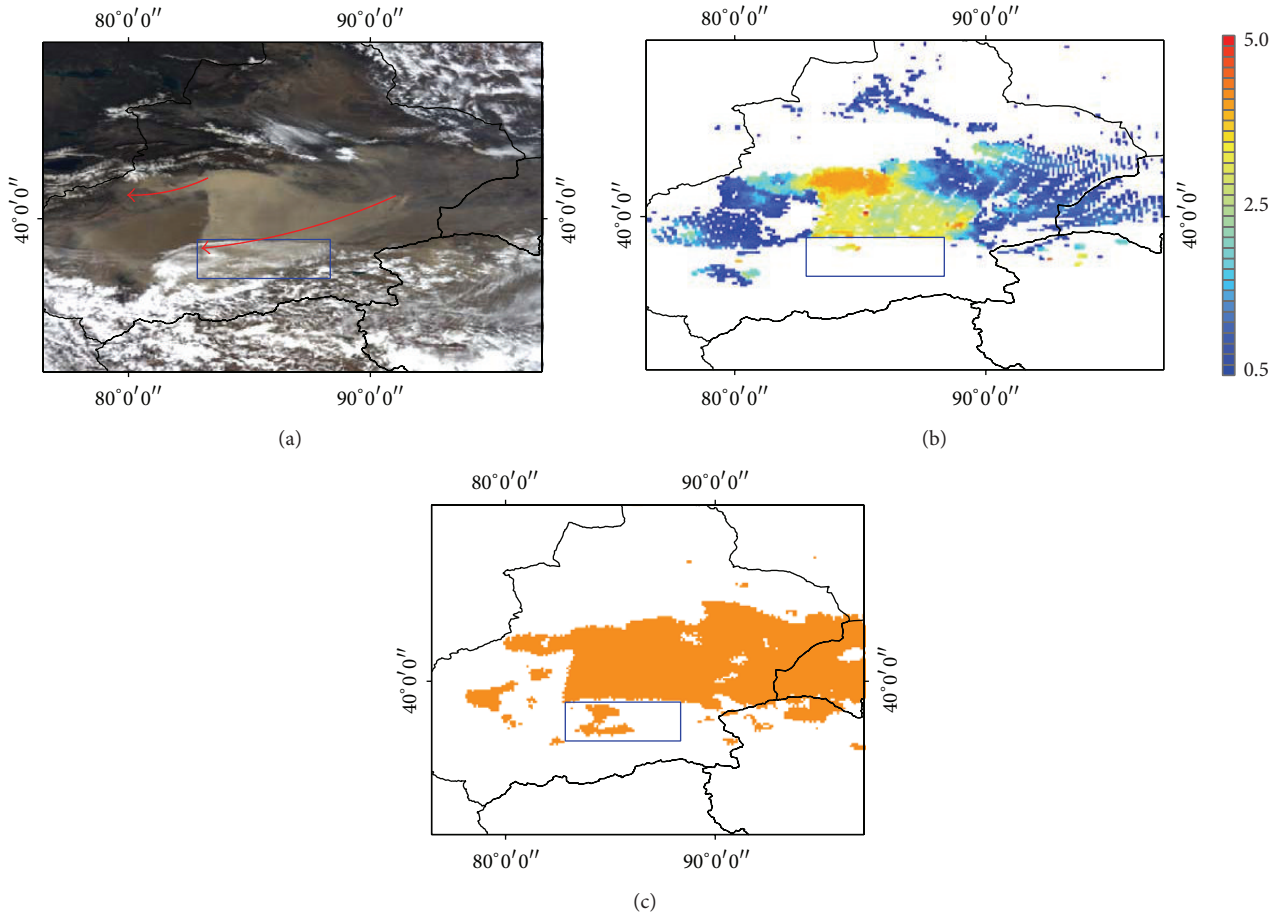


FIGURE 10: (a) April 23, 2012, dust RGB composite image from MODIS, (b) dust identification results, and (c) MODIS deep blue aerosol optical depth results.

The accurate identification results demonstrate that dust which occurred during nighttime can also be effectively detected through the thermal infrared channels of AIRS.

4.4. Case: 23 April 2012. On 23 April, 2007, dust plumes blew out of the Taklimakan desert toward the west. They are captured by the MODIS image shown in Figure 10(a). In the blue rectangle region, it is clear to see that the clouds and dusts coexisted in the same scene. Figures 10(b) and 10(c) show the spatial distribution of dust identification results from AIRS and deep blue aerosol optical depth results from MODIS.

From Figures 10(b) and 10(c), it is interesting to see that both the infrared and visible measurements can easily detect the outbreaks of dust in the areas of cloud and dust layers which are not cooccurring in the same atmospheric column. However, in the blue rectangle region where dust is overlapped by cloud, only little dusty areas can be identified through the infrared or visible observations, even though some thin ice cloud overlapping areas can be successfully detected by the proposed thermal infrared method. This is because cloud can absolutely cover the visible and infrared spectral signature of underlying dust when its optical depth is very high, as discussed in Section 3.3. Thus, dust events might

be underestimated under the particular condition, and more remote sensing techniques are required in addition to the visible and infrared to solve this problem, such as the infrared and microwave combined method developed by Huang et al. [28] and the active Lidar and infrared combined method developed by Chen et al. [30].

4.5. Case: 2009~2012. In order to make a further validation on the accuracy of proposed dust identification algorithm, several other dust events that occurred during the period of 2009 and 2012 are performed in the following content. Figure 11 shows the three dust events over different regions of northern China on 15 March, 2009, 11 May, 2011, and 24 April, 2012, respectively. From left to right, the images are MODIS RGB composite image, AIRS dust identification results, and MODIS deep blue aerosol optical depth results.

It is interesting to note that all the light brownish dusty regions (red arrow cover regions) in the MODIS RGB composite images can be well detected by the proposed infrared AIRS dust identification method, and all the detection results are generally consistent with the MODIS deep blue visible optical depth in spatial distribution. As a whole, all the above analyzed dust cases demonstrate that the proposed

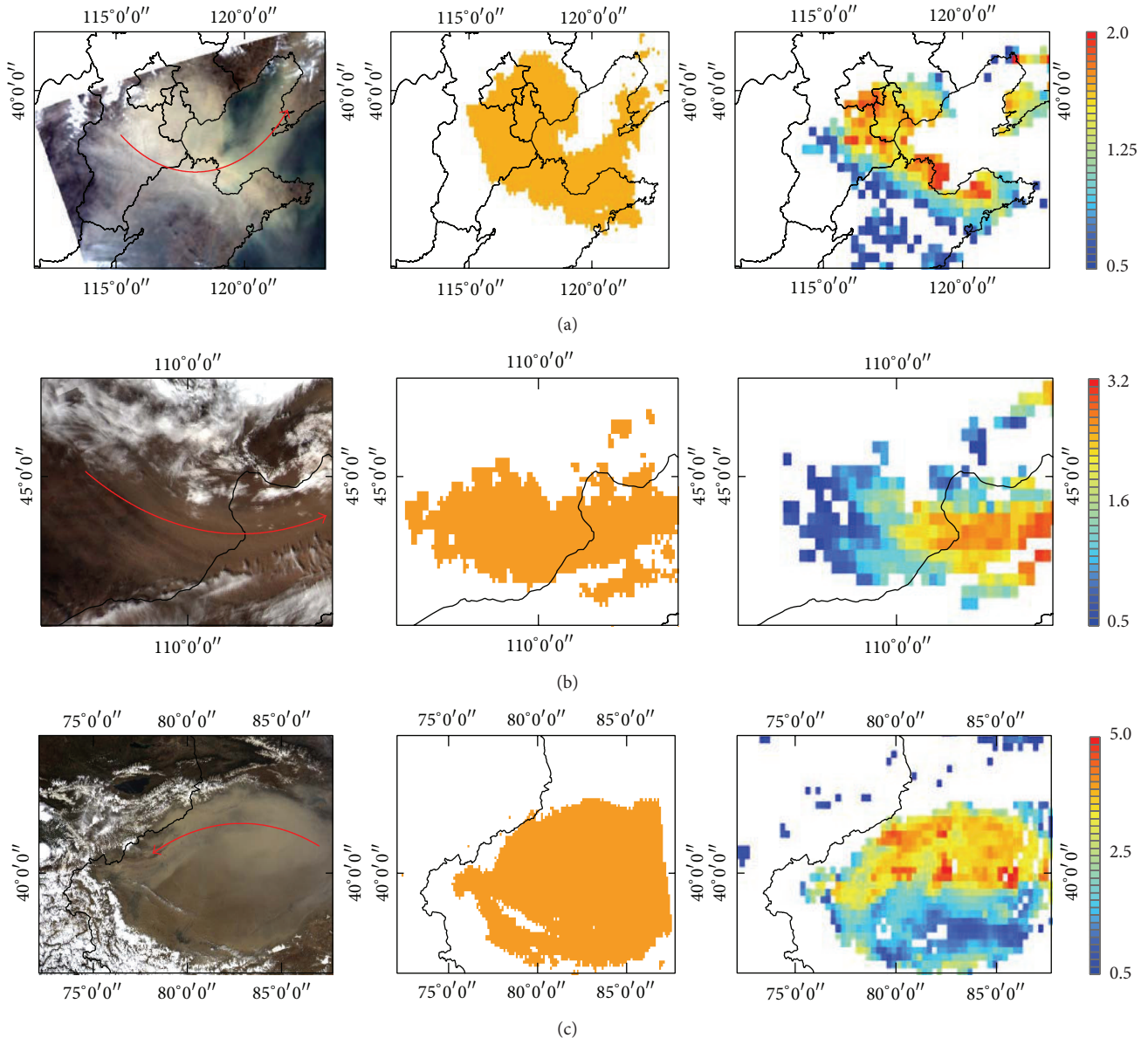


FIGURE 11: Asia dust events occurred in northern China from 2009 to 2012. (a) 15 March, 2009, (b) 11 May, 2011, and (c) 24 April, 2012.

identification algorithm in this study is indeed useful and reliable for monitoring the outbreaks and dispersion of Asian dust over arid and semiarid regions.

5. Conclusion

The developed thermal infrared dust identification algorithm has been successfully applied to Asia dust in this paper. This method relies on the distinct “V” spectral signature of dust in the $800\text{--}1250\text{ cm}^{-1}$ region, which is resulted from a negative spectral slope in $800\text{--}1000\text{ cm}^{-1}$ subregion and a positive spectral slope in $1060\text{--}1250\text{ cm}^{-1}$ subregion. Through the comparison of dust identification results from AIRS with MODIS visible observations, it suggests that

the identification criteria determined from the analysis of the forward simulation experiments are suitable for Asia dust monitoring. In addition to this, the detected nighttime dust results have been evaluated and validated by comparing the CALIOP vertical backscattered data and aerosol subtype results, which reveals that the identification algorithm is also accurate in dust detection at night.

Even so, more efforts and improvements of the algorithm still need to be pursued in the future. (1) Applying the identification method to other active dust regions (e.g., the Sahara region of Africa) and given that the optical properties of dust are highly depending on the dust source regions, more dust models should be considered in this algorithm to extend the applicability of the algorithm. (2) Exploring the ability of dust detection under the condition of cloud

and dust coexisting in the same atmospheric column and as the cloud can make a great impact on the spectral signature of underlying dust, therefore, more sensors, channel combinations, and identification criteria are needed to accurately detect dust under this particular scene.

Conflict of Interests

The authors declare that there is no conflict of interests regarding the publication of this paper.

Acknowledgments

This study was funded by the Major State Basic Research Development Program of China (no. 2010CB950800) and Natural Science Foundation (no. 41371015). Additionally, the authors thank the GES-DISC and ICARE for providing AIRS and MODIS remote sensing data. At last, they thank the reviewer a lot for all the work done to this paper and are highly appreciating his generous help.

References

- [1] P. Zhang, N.-M. Lu, X.-Q. Hu, and C.-H. Dong, "Identification and physical retrieval of dust storm using three MODIS thermal IR channels," *Global and Planetary Change*, vol. 52, no. 1-4, pp. 197-206, 2006.
- [2] L. Natsagdorj, D. Jugder, and Y. S. Chung, "Analysis of dust storms observed in Mongolia during 1937-1999," *Atmospheric Environment*, vol. 37, no. 9-10, pp. 1401-1411, 2003.
- [3] X. Wang, J. Huang, M. Ji, and K. Higuchi, "Variability of East Asia dust events and their long-term trend," *Atmospheric Environment*, vol. 42, no. 13, pp. 3156-3165, 2008.
- [4] J. Xuan and I. N. Sokolik, "Characterization of sources and emission rates of mineral dust in Northern China," *Atmospheric Environment*, vol. 36, no. 31, pp. 4863-4876, 2002.
- [5] X. Y. Zhang, S. L. Gong, Z. X. Shen et al., "Characterization of soil dust aerosol in China and its transport and distribution during 2001 ACE-Asia: 1. Network observations," *Journal of Geophysical Research D: Atmospheres*, vol. 108, no. 9, pp. -1-13, 2006.
- [6] Y. Shao and C. H. Dong, "A review on East Asian dust storm climate, modelling and monitoring," *Global and Planetary Change*, vol. 52, no. 1-4, pp. 1-22, 2006.
- [7] J. Zhou, G. Yu, C. Jin et al., "Lidar observations of Asian dust over Hefei, China, in spring 2000," *Journal of Geophysical Research D: atmospheres*, vol. 107, no. 15, pp. -1-8, 2002.
- [8] T. Murayama, N. Sugimoto, I. Uno et al., "Ground-based network observation of Asian dust events of April 1998 in East Asia," *Journal of Geophysical Research*, vol. 106, no. D16, pp. 18345-18360, 2001.
- [9] T. Murayama, D. Müller, K. Wada, A. Shimizu, M. Sekiguchi, and T. Tsukamoto, "Characterization of Asian dust and Siberian smoke with multi-wavelength Raman lidar over Tokyo, Japan in spring 2003," *Geophysical Research Letters*, vol. 31, no. 23, pp. 1-5, 2004.
- [10] A. Shimizu, N. Sugimoto, I. Matsui et al., "Continuous observations of Asian dust and other aerosols by polarization lidars in China and Japan during ACE-Asia," *Journal of Geophysical Research: Atmospheres*, vol. 109, no. D19, pp. D19-S17, 2004.
- [11] Y. Gu, W. I. Rose, and G. J. S. Bluth, "Retrieval of mass and sizes of particles in sandstorms using two MODIS IR bands: a case study of April 7, 2001 sandstorm in China," *Geophysical Research Letters*, vol. 30, no. 15, p. 1805, 2003.
- [12] J. Huang, B. Lin, P. Minnis et al., "Satellite-based assessment of possible dust aerosols semi-direct effect on cloud water path over East Asia," *Geophysical Research Letters*, vol. 33, no. 19, Article ID L19802, 2006.
- [13] J. Huang, Y. Wang, T. Wang, and Y. Yi, "Dusty cloud radiative forcing derived from satellite data for middle latitude regions of East Asia," *Progress in Natural Science*, vol. 16, no. 10, pp. 1084-1089, 2006.
- [14] J. Huang, P. Minnis, B. Lin et al., "Possible influences of Asian dust aerosols on cloud properties and radiative forcing observed from MODIS and CERES," *Geophysical Research Letters*, vol. 33, no. 6, Article ID L06824, 2006.
- [15] A. Zhu, V. Ramanathan, F. Li, and D. Kim, "Dust plumes over the Pacific, Indian, and Atlantic oceans: climatology and radiative impact," *Journal of Geophysical Research D*, vol. 112, no. 16, Article ID D16208, 2007.
- [16] T. D. Jickells, Z. S. An, K. K. Andersen et al. et al., "Global iron connections between desert dust, ocean biogeochemistry, and climate," *Science*, vol. 308, no. 5718, pp. 67-71, 2005.
- [17] E.-H. Lee and B.-J. Sohn, "Recent increasing trend in dust frequency over Mongolia and Inner Mongolia regions and its association with climate and surface condition change," *Atmospheric Environment*, vol. 45, no. 27, pp. 4611-4616, 2011.
- [18] J. J. Qu, X. Hao, M. Kafatos, and L. Wang, "Asian dust storm monitoring combining terra and aqua MODIS SRB measurements," *IEEE Geoscience and Remote Sensing Letters*, vol. 3, no. 4, pp. 484-486, 2006.
- [19] O. Torres, P. K. Bhartia, J. R. Herman, Z. Ahmad, and J. Gleason, "Derivation of aerosol properties from satellite measurements of backscattered ultraviolet radiation: theoretical basis," *Journal of Geophysical Research*, vol. 103, no. 14, pp. 17099-17110, 1998.
- [20] N. C. Hsu, S.-C. Tsay, M. D. King, and J. R. Herman, "Aerosol properties over bright-reflecting source regions," *IEEE Transactions on Geoscience and Remote Sensing*, vol. 42, no. 3, pp. 557-569, 2004.
- [21] M. Legrand, A. Plana-Fattori, and C. N'Doumé, "Satellite detection of dust using the IR imagery of Meteosat 1. Infrared difference dust index," *Journal of Geophysical Research D: Atmospheres*, vol. 106, no. 16, pp. 18251-18274, 2001.
- [22] J. K. Roskovensky and K. N. Liou, "Differentiating airborne dust from cirrus clouds using MODIS data," *Geophysical Research Letters*, vol. 32, no. 12, Article ID L12809, 2005.
- [23] H. E. Brindley and J. E. Russell, "Improving GERB scene identification using SEVIRI: infrared dust detection strategy," *Remote Sensing of Environment*, vol. 104, no. 4, pp. 426-446, 2006.
- [24] J. Li, P. Zhang, T. J. Schmit, J. Schmetz, and W. P. Menzel, "Quantitative monitoring of a Saharan dust event with SEVIRI on Meteosat-8," *International Journal of Remote Sensing*, vol. 28, no. 10, pp. 2181-2186, 2007.
- [25] X. Q. Hu, N. M. Lu, T. Niu, and P. Zhang, "Operational retrieval of Asian sand and dust storm from FY-2C geostationary meteorological satellite and its application to real time forecast in Asia," *Atmospheric Chemistry and Physics*, vol. 8, no. 6, pp. 1649-1659, 2008.
- [26] C. Pierangelo, A. Chédin, S. Heilliette, N. Jacquinet-Husson, and R. Armante, "Dust altitude and infrared optical depth from

- AIRS," *Atmospheric Chemistry and Physics*, vol. 4, no. 7, pp. 1813–1822, 2004.
- [27] L. Klüser, D. Martynenko, and T. Holzer-Popp, "Thermal infrared remote sensing of mineral dust over land and ocean: a spectral SVD based retrieval approach for IASI," *Atmospheric Measurement Techniques*, vol. 4, no. 5, pp. 757–773, 2011.
- [28] J. Huang, J. Ge, and F. Weng, "Detection of Asia dust storms using multisensor satellite measurements," *Remote Sensing of Environment*, vol. 110, no. 2, pp. 186–191, 2007.
- [29] J. Ge, J. Huang, F. Weng, and W. Sun, "Effects of dust storms on microwave radiation based on satellite observation and model simulation over the Taklamakan desert," *Atmospheric Chemistry and Physics*, vol. 8, no. 16, pp. 4903–4909, 2008.
- [30] B. Chen, J. Huang, P. Minnis et al., "Detection of dust aerosol by combining CALIPSO active lidar and passive IIR measurements," *Atmospheric Chemistry and Physics*, vol. 10, no. 9, pp. 4241–4251, 2010.
- [31] I. N. Sokolik, "The spectral radiative signature of wind-blown mineral dust: implications for remote sensing in the thermal IR region," *Geophysical Research Letters*, vol. 29, no. 24, pp. 7-1-7-4, 2002.
- [32] G. Hong, P. Yang, H.-L. Huang, S. A. Ackerman, and I. N. Sokolik, "Simulation of high-spectral-resolution infrared signature of overlapping cirrus clouds and mineral dust," *Geophysical Research Letters*, vol. 33, no. 4, Article ID L04805, 2006.
- [33] C. Pierangelo, M. Mishchenko, Y. Balkanski, and A. Chédin, "Retrieving the effective radius of Saharan dust coarse mode from AIRS," *Geophysical Research Letters*, vol. 32, no. 20, Article ID L20813, pp. 1–4, 2005.
- [34] S. Peyridieu, A. Chédin, D. Tanré et al., "Saharan dust infrared optical depth and altitude retrieved from AIRS: a focus over North Atlantic-comparison to MODIS and CALIPSO," *Atmospheric Chemistry and Physics*, vol. 10, no. 4, pp. 1953–1967, 2010.
- [35] S. G. DeSouza-Machado, L. L. Strow, S. E. Hannon, and H. E. Motteler, "Infrared dust spectral signatures from AIRS," *Geophysical Research Letters*, vol. 33, no. 3, Article ID L03801, 2006.
- [36] S. G. Desouza-Machado, L. L. Strow, B. Imbiriba et al., "Infrared retrievals of dust using AIRS: comparisons of optical depths and heights derived for a North African dust storm to other collocated EOS A-Train and surface observations," *Journal of Geophysical Research*, vol. 115, no. 15, Article ID D15201, 2010.
- [37] Z. Yao, J. Li, H.-J. Han, A. Huang, B. J. Sohn, and P. Zhang, "Asian dust height and infrared optical depth retrievals over land from hyperspectral longwave infrared radiances," *Journal of Geophysical Research D: Atmospheres*, vol. 117, Article ID D19202, 2012.
- [38] M. T. Chahine, T. S. Pagano, H. H. Aumann et al., "AIRS: improving weather forecasting and providing new data on greenhouse gases," *Bulletin of the American Meteorological Society*, vol. 87, no. 7, pp. 911–926, 2006.
- [39] J. Susskind, C. D. Barnet, and J. M. Blaisdell, "Retrieval of atmospheric and surface parameters from AIRS/AMSU/HSB data in the presence of clouds," *IEEE Transactions on Geoscience and Remote Sensing*, vol. 41, no. 2, pp. 390–409, 2003.
- [40] J. Li, H.-L. Huang, C.-Y. Liu et al., "Retrieval of cloud microphysical properties from MODIS and AIRS," *Journal of Applied Meteorology*, vol. 44, no. 10, pp. 1526–1543, 2005.
- [41] E. Weisz, J. Li, J. Li et al., "Cloudy sounding and cloud-top height retrieval from AIRS alone single field-of-view radiance measurements," *Geophysical Research Letters*, vol. 34, no. 12, Article ID L12802, 2007.
- [42] W. L. Barnes, T. S. Pagano, and V. V. Salomonson, "Prelaunch characteristics of the moderate resolution imaging spectroradiometer (MODIS) on EOS-AMI," *IEEE Transactions on Geoscience and Remote Sensing*, vol. 36, no. 4, pp. 1088–1100, 1998.
- [43] L. A. Remer, Y. J. Kaufman, D. Tanré et al., "The MODIS aerosol algorithm, products, and validation," *Journal of the Atmospheric Sciences*, vol. 62, no. 4, pp. 947–973, 2005.
- [44] P. Yang, Q. Feng, G. Hong et al., "Modeling of the scattering and radiative properties of nonspherical dust-like aerosols," *Journal of Aerosol Science*, vol. 38, no. 10, pp. 995–1014, 2007.
- [45] H.-J. Han, B.-J. Sohn, H.-L. Huang, E. Weisz, R. Saunders, and T. Takamura, "An improved radiance simulation for hyperspectral infrared remote sensing of Asian dust," *Journal of Geophysical Research D*, vol. 117, no. 9, Article ID D09211, 2012.
- [46] F. E. Volz, "Infrared refractive index of atmospheric aerosol substances," *Applied Optics*, vol. 11, no. 4, pp. 755–759, 1972.
- [47] M. Hess, P. Koepke, and I. Schult, "Optical properties of aerosols and clouds: the software package OPAC," *Bulletin of the American Meteorological Society*, vol. 79, no. 5, pp. 831–844, 1998.
- [48] B. Mayer and A. Kylling, "Technical note: the libRadtran software package for radiative transfer calculations—description and examples of use," *Atmospheric Chemistry and Physics*, vol. 5, no. 7, pp. 1855–1877, 2005.
- [49] B. A. Baum, A. J. Heymsfield, P. Yang, and S. T. Bedka, "Bulk scattering properties for the remote sensing of ice clouds. Part I: microphysical data and models," *Journal of Applied Meteorology*, vol. 44, no. 12, pp. 1885–1895, 2005.
- [50] B. A. Baum, P. Yang, A. J. Heymsfield et al., "Bulk scattering properties for the remote sensing of ice clouds. part II: narrow-band models," *Journal of Applied Meteorology*, vol. 44, no. 12, pp. 1896–1911, 2005.
- [51] J. P. Huang, P. Minnis, B. Chen et al., "Long-range transport and vertical structure of Asian dust from CALIPSO and surface measurements during PACDEX," *Journal of Geophysical Research D: Atmospheres*, vol. 113, no. 23, Article ID D23212, 2008.
- [52] K. N. Liou, "Parameterization of the radiative properties of cirrus clouds," *Journal of the Atmospheric Sciences*, vol. 50, no. 13, pp. 2008–2025, 1993.
- [53] S. S. C. Ou, K. N. Liou, X. J. Wang et al., "Retrievals of mixed-phase cloud properties during the National Polar-Orbiting Operational Environmental Satellite System," *Applied Optics*, vol. 48, no. 8, pp. 1452–1462, 2009.

Research Article

Source Allocation of Long-Range Asian Dusts Transportation across the Taiwan Strait by Innovative Chemical-Assisted Identification Methods

Yi-Hsiu Jen,¹ Yi-Chi Liu,¹ Iau-Ren Ie,¹ Chung-Shin Yuan,¹ and Chung-Hsuang Hung²

¹ Institute of Environmental Engineering, National Sun Yat-Sen University, Kaohsiung 80424, Taiwan

² Department of Safety, Health and Environmental Engineering, National Kaohsiung First University, Kaohsiung 824, Taiwan

Correspondence should be addressed to Chung-Shin Yuan; ycsngi@mail.nsysu.edu.tw

Received 13 June 2014; Accepted 8 August 2014; Published 27 August 2014

Academic Editor: Hesham El-Askary

Copyright © 2014 Yi-Hsiu Jen et al. This is an open access article distributed under the Creative Commons Attribution License, which permits unrestricted use, distribution, and reproduction in any medium, provided the original work is properly cited.

This study used the backward trajectory calculation to obtain the transportation routes of Asian dusts and further combined the chemical composition with the enrichment factor (EF) and the grey relational analysis (GR) to identify the potential sources of eighteen Asian dust storm (ADS) events. The results showed that the chemical compositions of atmospheric particles sampled at the Pescadore Islands were very similar to source soils fugitively emitted from Inner Mongolia, which could assist in identifying the source regions of Asian dusts. This study further compared the source allocation of Asian dusts obtained from EF, GR, and backward trajectory, which showed that the source regions of Asian dusts obtained from these three methods were quite similar. The similarity of backward trajectory and GR reached as high as 83.3%. Moreover, the similarity of backward trajectory calculation and EF or GR was up to 77.8% while that of the GR and EF was up to 83.3%. Overall, these three methods can successfully allocate the source regions of Asian dusts by 66.7%. Moreover, these innovative chemical-assisted methods can be successfully applied to identify the source regions of Asian dusts for 18 ADS events.

1. Introduction

At the beginning (February–May) of each year, Asian dusts are frequently blown from hyperarid, arid, and semiarid lands located at Northwest and North China, South Mongolia, and South Siberia [1–3]. For the past half-century, the frequency of Asian dust storms (ADS) occurring in China increased significantly from 0.5 (1950') to 14 (2000) times per year, especially the strong and/or super ADS. This phenomenon is correlated mainly to climate change both locally and globally [4, 5]. It is estimated that approximately 800 million metric tons of sands were emitted to the atmosphere by ADS, which accounts for almost half of natural fugitive sands globally [6, 7].

ADS could transport in the upper troposphere easterly to Korea, Japan, and even North America and may also transport southerly to Okinawa, Taiwan, Hong Kong, and Philippine due to anticyclone of atmospheric circulation [8–11]. Although many sands might be settled down to the ocean and provided nutrients (e.g., Fe^{2+}) to the oceanic

biosphere, which actually benefits the circulation of global geochemistry, ADS could deteriorate ambient air quality, reduce atmospheric visibility, cause adverse effects on human health, and result in poor scenery and public welfare [12–14]. Additionally, great losses of national economy due to ADS are constantly reported in the West Pacific regions, including crop damage, soil productivity losses, livestock losses, mass migration, human health impacts, and impacts on climate [15–18].

In general, ADS invades Taiwan 2–3 times per year and lasts for about 1–2 days for each invasion. The concentration of suspended particles (PM_{10}) in the events of ADS increases approximately 2–3-fold when compared to normal days [7, 19, 20]. During the ADS periods, significant increases of atmospheric aerosols, particularly PM_{10} , have been frequently observed in Taiwan [7, 8, 19, 21]. Particularly, yellow rain episodes have been reported both in Japan and Taiwan at the end of March 2000 [22]. The morphology and apparent color of dust particles filtered from the yellow rain were similar to yellow sands at their source [22]. Furthermore, the results

obtained from the investigation on source apportioning atmospheric aerosols at an Asian dust episode in metro Kaohsiung indicated that the percentage of fugitive dusts increased significantly from 8.5% (regular periods) to 26.2% (Asian dust periods) [23]. Moreover, during the transportation of ADS across continents, the physicochemical characteristics of Asian dusts might be changed by mixing with anthropogenic particles emitted from typical stationary and mobile sources [24, 25]. Yuan et al. [19] reported that the size distribution of atmospheric aerosols sampled at the Pescadores Islands located in the middle of the Taiwan Strait during the period of ADS switched from bimode to single mode with a peak in coarse particles. Besides, the sulfate (SO_4^{2-}) and ammonia (NH_4^+) of coarse particles ($\text{PM}_{2.5-10}$) increase significantly during the period of ADS when compared to non-ADS periods [7, 26, 27].

In order to investigate the feasibility of chemical-assisted ADS source identification methods which can be used to trace back the soil source regions of ADS, this study compared the transportation routes of ADS event from the backward trajectory calculation to the chemical composition of atmospheric particles and soil sources. Top soils collected in three soil source regions of Inner Mongolia were resuspended and sampled to analyze their chemical composition for further conducting the enrichment factor analysis (EF) and grey relational analysis (GR). Ultimately, this study revealed and discussed the similarity percentages from the backward trajectory calculation, EF, and GR and further obtained the source regions of Asian dusts for 18 ADS events.

2. Methodologies

2.1. Sampling Sites of Atmospheric Particles and Soil Dusts.

Located at the middle of Taiwan Strait between southeastern China and Taiwan Island, the Pescadores Islands have an area of 127.97 km², which has the subtropical weather being mainly influenced by East Asian monsoons. During the 18 ADS events, the atmospheric particles were sampled at Hsiao-men site (23°38'471" N; 119°30'316" E), which is located at the northwestern coastline of the Pescadores Islands and is approximately 12 m above the ground and 500 m and 50 m far from the coastline and the major roads, respectively. At the sampling sites, this study used to simultaneously collect PM_{10} (including $\text{PM}_{2.5-10}$ and $\text{PM}_{2.5}$) with dichotomous samplers (Anderson, Model Series 241). The sampling flow rate of the sampler was 16.7 L/min for a total of 24 hours, and the filters used in this study were 37 mm quartz filters.

The soil samples were collected from three ADS source regions in the western (38°13'19 to 39°06'45 N; 115°21'47 to 116°53'38 E), central (40°06'49 to 41°39'0 N; 110°28'35 to 111°32'20 E), and eastern (43°03'27 to 43°28'37 N; 116°41'41 to 119°02'09 E) Inner Mongolia, China [7]. Among them, strong winds and dry climate result in serious soil erosion and thus cause heavy ADS frequently (Inner Mongolia Web Site, 2003). A total of thirty soil samples were taken at the top 10–15 cm surface of open sand lands and were then separately stored in labeled sampling bags. The soil samples were then sent back to the Air Pollution Laboratory at the Institute of Environmental

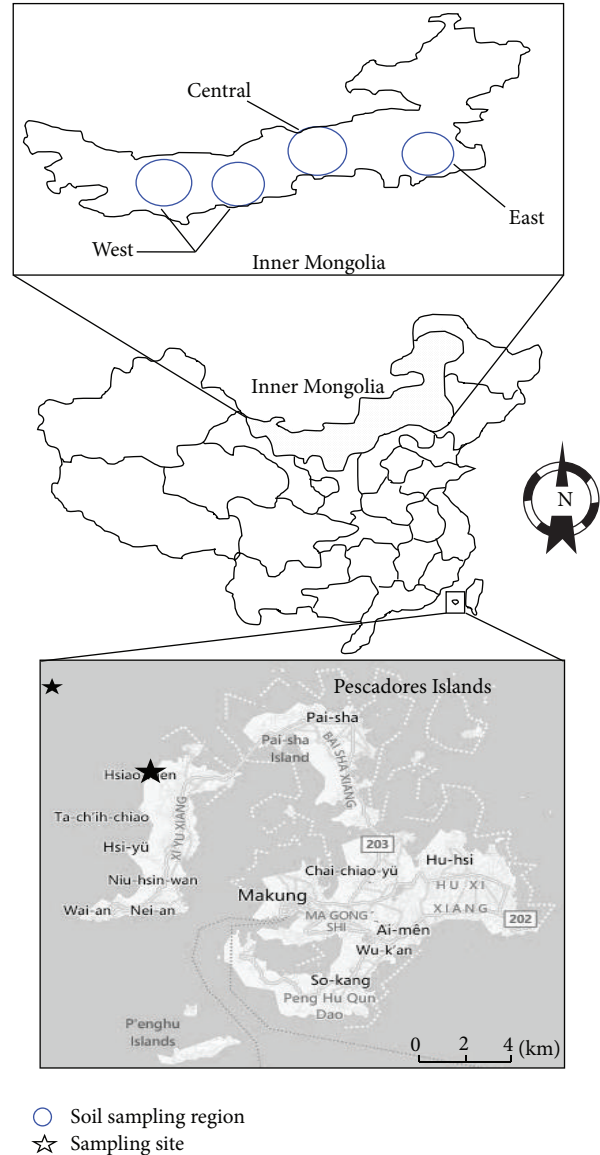


FIGURE 1: Location of atmospheric particles (★) at the Pescadores Islands and soil source regions (○) in the Inner Mongolia.

Engineering in National Sun Yat-Sen University, Taiwan, for further chemical analyses. The locations of all soil sampling sites are illustrated in Figure 1.

2.2. Backward Trajectory Calculation. In order to trace the transportation of air parcel, backward trajectories from a specific receptor site were commonly used in this study, which could be used to identify the air mass transportation routes from specific source regions. A hybrid single-particle Lagrangian integrated trajectory (HYSPPLIT) has been a widely used model that plots the trajectory of a single air parcel from a specific location and height above ground over a period of time [28, 29]. Backward trajectory calculation used the interpolated measured or modeled meteorological fields to estimate the most likely route over the geographical

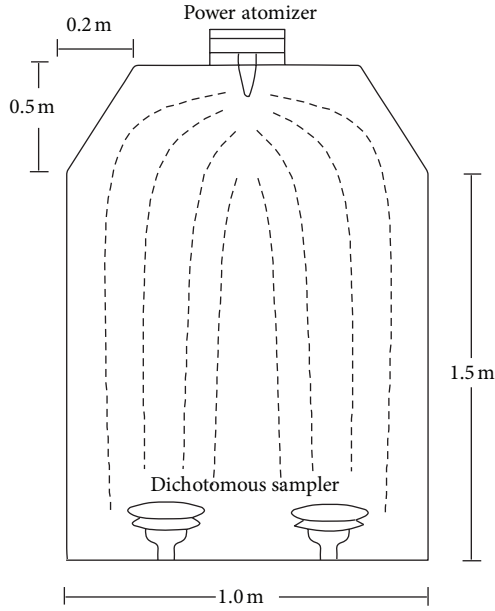


FIGURE 2: Schematic diagram of the resuspension chamber.

areas that provided air parcels from its source to a receptor at a given time. The method essentially follows a parcel of air backward in hourly steps for a specified length of time [10, 30]. Moreover, HYSPLIT uses archived 3-dimensional meteorological fields generated from observations and short-term forecasts. HYSPLIT can be run to generate either forward or backward trajectories using several available meteorological data archives, which is developed by the National Oceanic and Atmospheric Administration's (NOAA) Air Resources Laboratory (ARL). All backward trajectories were drawn at an arrival height of 50 m above the sea level in this study. By using the NOAA-HYSPLIT model, the dates with high particle concentration at the Pescadores Islands were determined and the transportation routes of air parcels toward the Pescadores Islands during the sampling periods were then simulated. This information was further applied to examine the possible long-range transportation routes conveying ADS from several long-range soil source regions to the Pescadores Islands.

2.3. Enrichment Factor Analysis. Soil samples collected from the eastern, central, and western parts of the Inner Mongolia were sent back to the Air Pollution Laboratory at National Sun Yat-Sen University for further soil resuspension and chemical analyses. The soil samples were resuspended with a dry powder atomizer at the top of a resuspension chamber ($2\text{ m} \times 1\text{ m}^2$), which is illustrated in Figure 2. The resuspended dusts were then sampled as $\text{PM}_{2.5-10}$ and $\text{PM}_{2.5}$ for a total of 0.5 hours by two dichotomous samplers with a total volumetric flow rate of 16.7 L/min, which was located at the bottom of the resuspension chamber. Particulate matter with diameters larger than $10\ \mu\text{m}$ tended to settle down at the bottom of the resuspension chamber. Besides, the resuspended soil dusts were further characterized chemically

to apply for the identification of Asian dusts at the downwind sites by using an enrichment factor (EF). The enrichment factor (EF) defined by (1) was used to correlate the downwind atmospheric particles sampled at the Pescadores Islands, Taiwan, to ADS originated from Inner Mongolia, China:

$$\text{EF} = \frac{(\text{Tr}/\text{Ref})_{\text{PM}}}{(\text{Tr}/\text{Ref})_{\text{crust}}}, \quad (1)$$

where EF is the enrichment factor; Tr is the trace element; Ref is the reference element; and subscripts PM and crust represents atmospheric particles and crustal soils. Among them, the reference element has to be initially determined. Previous studies reported that the mass ratio of Mg, K, and Fe (or Al) to Al (or Fe) showed a relatively narrow range for coarse particles, but not for fine particles, which can be used as the fingerprints of Asian dusts originated from the Inner Mongolia [7]. Generally, the enrichment factor close to unity ($\text{EF} \approx 1$) indicates that the elements consider very high possibility from the specific sources. It is also defined that the elements might come from the specific source when the EF ranged from 0.1 to 10.

2.4. Grey Relational Analysis. The technique of grey relational analysis is suitable for unascertained problems with poor information [31]. It provides an efficient solution to the uncertainty, multi-input, and discrete data problem. This kind of interaction is mainly through the connection among parameters and some conditions that are already known. Also, it will indicate the relational degree between two sequences with the help of the grey relational analysis. Moreover, the grey relational grade could utilize the discrete measurement method to judge the distance.

When the range of the sequence is too large or the standard value is too enormous, it will cause the influence of some factors to be neglected. Also, in the sequence, if the factors' goals and directions are different, the grey relational analysis might also produce unexpected incorrect results. Therefore, preprocessing of all the data is highly required. This process is called the grey relational generating. An ideal sequence is $x_0(k)$ ($k = 1, 2, 3$) for three responses. The definition of the grey relational grade in the grey relational analysis is to show the relational degree between n sequences ($x_0(k)$ and $x_i(k)$, $i = 1, 2, \dots, n$; $k = 1, 2, 3, \dots, n$). The grey relational coefficient $\xi_i(k)$ could be calculated by the following equation:

$$\xi_i(k) = \frac{\Delta_{\min} + \zeta \Delta_{\max}}{\Delta_{0i}(k) + \zeta \Delta_{\max}}, \quad (2)$$

where $\Delta_{0i}(k) = |x_0(k) - x_i(k)|$ is the difference of absolute value between $x_0(k)$ and $x_i(k)$; ξ is the distinguishing coefficient (0, 1); Δ_{\min} is the smallest value of $\Delta_{0i}(k)$; and Δ_{\max} is the largest value of $\Delta_{0i}(k)$. After averaging the grey relational coefficients, the grey relational grade Y_i can be obtained as

$$Y_i = \sum_{k=1}^m \beta_k \xi_i(k), \quad (3)$$

where m is the number of process responses and β_k is the weight value.

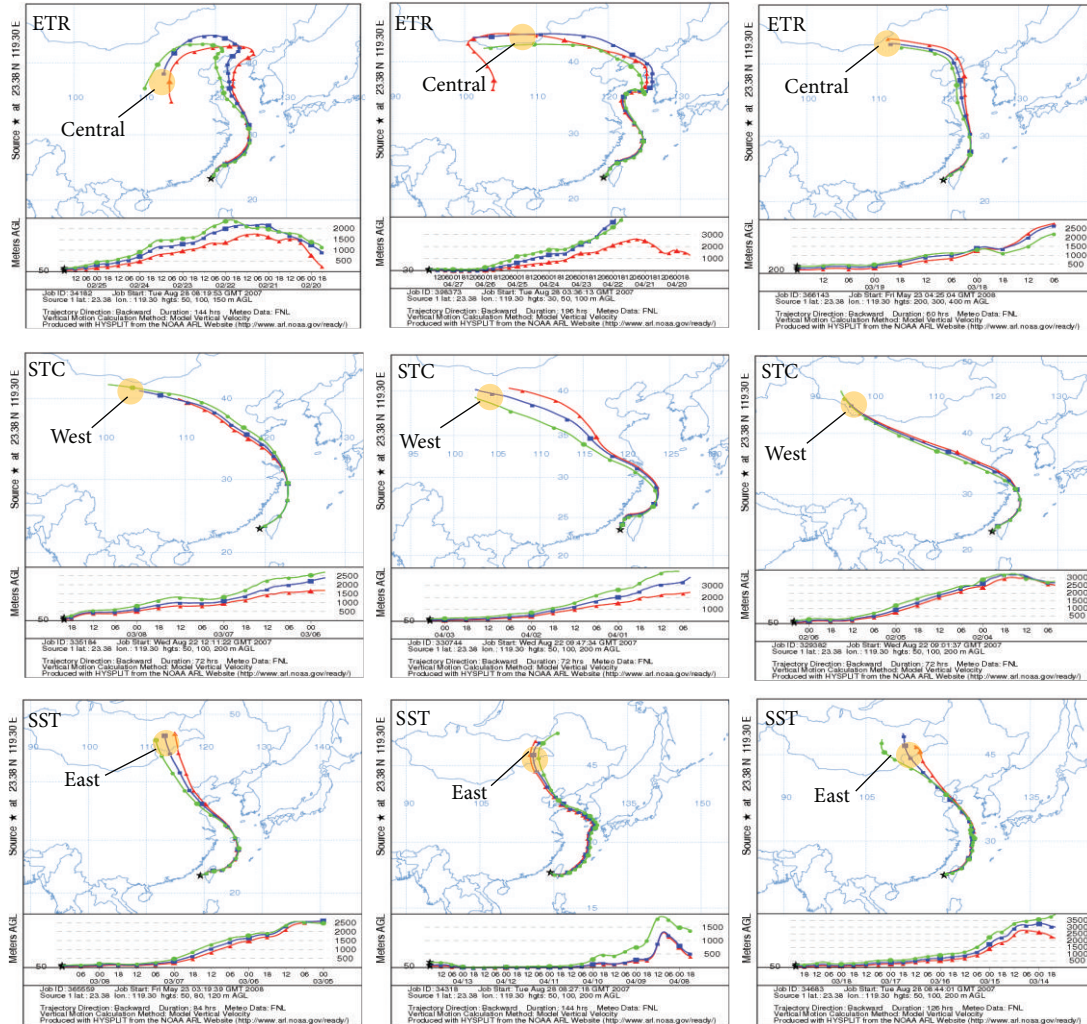


FIGURE 3: Backward trajectories for three types of ADS transportation routes from the Inner Mongolia to the Pescadores Islands.

3. Results and Discussion

3.1. Correlation of Chemical Composition with Backward Trajectory Calculation. A total of 18 ADS events were observed at the Pescadores Islands from November 2002 to April 2006. Results obtained from the backward trajectory calculation indicated that three main types of routes dominated the Asian dusts transported from the Inner Mongolia to the Pescadores Islands, which included the eastward transportation and retraced route (ETR), southeastern transportation and circumrotated route (STC), and straight southeastern transportation route (SST), as illustrated in Figure 3.

Table 1 summarizes that the ETR-type ADS events accounted for approximately 33.3% of the total of 18 ADS events, which were mostly accompanied with strong northeastern monsoons occurring from late February to April. When the ADS transported toward the east, the transportation routes would detour toward the southwest due to atmospheric circulation, which usually passed through the Pescadores Islands. The STC-type ADS events were mainly

affected by the strength of the northeastern monsoons mostly observed from November to next April, accounting for about 22.2% of the total of 18 ADS events. Weakening the northeastern monsoons would result in a smooth curvature of the backward trajectories. The SST-type ADS events occurred mostly from December to next April, in which air parcels transported almost directly from northern China to the Pescadores Islands, Taiwan.

According to the probability of transportation routes, it showed that the SST-type ADS was dominant in all ADS transportation routes, accounting for approximately 44.5% of the 18 ADS events. The ETR- and STC-type ADS were ordered the second and third routes, respectively. Moreover, this study further aggregated the routes of 18 ADS events and tried to trace them back to their major source regions. All of the ADS routes were transported along the coastline or passed through the major mega cities of North and/or East China, which could alter the chemical composition of atmospheric dusts while transporting from the Inner Mongolia to the Pescadores Islands. During the transportation processes,

TABLE 1: The transportation types and soil sources of 18 ADS events in this study.

Transportation route types	Events	Routes probability	Predilection periods	Asian dust source region
ETR	$n = 18$	33.3%	Late Feb.~April	Central (83%)
STC		22.2%	Nov.~next April	West (75%)
SST		44.5%	Dec.~next April	East (88%)

(1) ETR is the eastward transportation and retraced route.

(2) STC is the southeastern transportation and circumrotated route.

(3) SST is the straight southeastern transportation route.

Asian dusts would mix with particulate matter emitted from local anthropogenic, industrial, and mobile sources. This study further compared the chemical composition of resuspended source soils and atmospheric dusts for similar transportation route type, as illustrated in Figure 4.

The results indicated that the most abundant chemical composition of source soils were EC, SO_4^{2-} , Cl^- , NO_3^- , OC, and Ca^{2+} in the eastern source region of Inner Mongolia; EC, Fe, Al, SO_4^{2-} , Ca, and Ca^{2+} were in the central source region; EC, SO_4^{2-} , OC, NO_3^- , Cl^- , and Ca were in the western source region, respectively. On the other hand, the most abundant chemical composition for different transportation routes were SO_4^{2-} , Ca^{2+} , NO_3^- , Cl^- , Na^+ , and EC for the ETR-type ADS; SO_4^{2-} , Cl^- , Na^+ , NO_3^- , Al, and Fe for the STC-type ADS; and SO_4^{2-} , EC, NO_3^- , Na^+ , Cl^- , and Ca^{2+} for the SST-type ADS, respectively. The chemical composition between the soils collected in the eastern and western soil sources of Inner Mongolia and Asian dusts sampled at the Pescadores Islands were similar, except the water-soluble Ca^{2+} and metal Ca. The chemical composition of soils collected at each soil source region was similar but not identical, which could cause the chemical composition variation of atmospheric dusts. Thus, the chemical composition from each soil source was similar to the chemical composition of atmospheric dust on their corresponding transportation route. Among them, the air masses traveled through several major industrial cities of China and transported along the coastal regions by the backward trajectories. Previous studies [29, 30, 32, 33] showed that the chemical proportion on the atmospheric dust was changed by the anthropogenic pollutions or nature sources emission, such as SO_4^{2-} and NO_3^- originated from direct emissions of major industries (such as petrochemical, power plant, and incinerator) or mobile sources (including onshore and offshore). Calcium and aluminum were dominated by stone processing, construction, and the cement industry. EC was originated primarily from direct emissions of fuel and coal combustion.

This study further compared the chemical composition of the source soils and atmospheric dusts sampled for different transportation routes. The results showed that the chemical fingerprints of the most soil sources and atmospheric dusts were coincided, except some chemical species were different. Actually, the chemical composition of atmospheric dusts could be influenced by the anthropogenic emission sources for different ADS transportation routes, thus resulting in the increase of the portion of SO_4^{2-} , NO_3^- , and EC. Moreover, Asian dusts could be long-range transported across the

ocean to the Pescadores Islands, which could increase the proportion of Na^+ and Cl^- due to oceanic spray. As a whole, the source soils were not exactly the same in their chemical composition between the eastern, central, or western Inner Mongolia, but the chemical species of the source soils in the Inner Mongolia and atmospheric dusts in the Pescadores Islands were similar in the same transportation routes. It could be explained that both backward trajectory calculation and chemical composition can be used to decide the ADS transportation routes concurrently.

3.2. Correlation of Chemical Composition with Enrichment Factors and Grey Relational Analysis. The enrichment factor was further applied to identify the ADS source region in the Inner Mongolia toward the Pescadores Islands in this study. During the transportation processes, water-soluble ions and carbonaceous components of Asian dusts could be interfered by the anthropogenic emissions. However, the characteristics of metallic elements are less likely varied in the ambient air. Consequently, this study selected Al or Fe as trace metals, which are fairly representative in the earth crust, and can be used to calculate the EF of 15 metals of Asian dusts originated from the Inner Mongolia during the 18 ADS events, as shown in Table 2. The EF values of 15 metal compositions in the range of 0.1 to 10 were shown to be highly relevant, as illustrated in Figure 5. Source identification results showed that 72% of ADS out of 18 events were originated from the central soil source region of the Inner Mongolia. However, three ADS events (numbers 3, 7, and 8) were not consistently identified for their source regions by using Al and Fe as reference elements. The source regions identified by EF values were either the western or the central Inner Mongolia. It might be attributed that Asian dusts could be mixed with other anthropogenic particles during the ADS transportation processes.

This study further applied the grey relational analysis to allocate the source regions of 18 ADS events, as summarized in Table 3. The results indicated that approximately 27, 23, and 50% of Asian dusts were originated from the eastern, western, and central Inner Mongolia for the 18 ADS events, respectively. Moreover, if the results of grey relational analysis were close to 1, the soil source of ADS events could be identified with relatively high correlation. Unlike the results of EF analysis, the source regions would be determined decisively by the grey relational analysis. However, if the grey relational grades of three soil source regions were close to each other, it could be difficult to allocate their

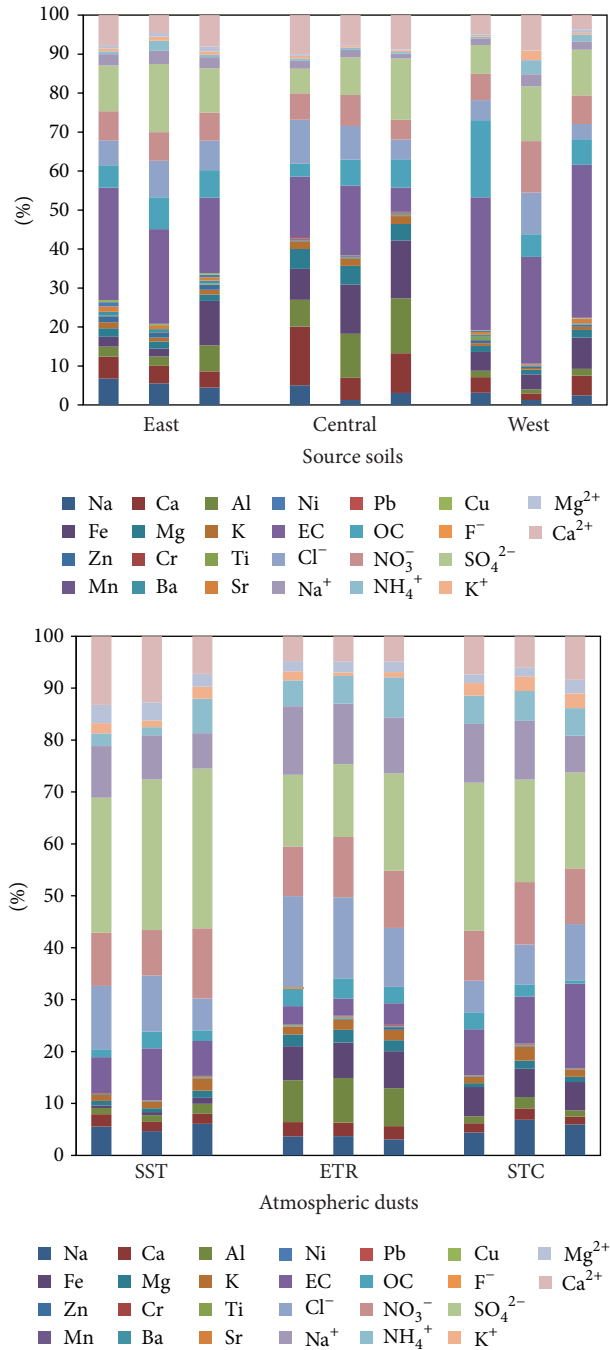


FIGURE 4: Chemical fingerprints of resuspended source soils and atmospheric dusts during the ADS events.

sources in this specific case. For example, number 13 ADS event was identified from the central region of the Inner Mongolia by backward trajectory calculation. Its GR grades were shown as 0.78, 0.91, and 0.89 for the eastern, central, and western soil source regions, respectively. Similar results were obtained from EF analysis, indicating that the chemical composition of Asian dusts played a crucial role in identifying the soil source regions of Asian dusts. Overall, the chemical-based enrichment factor and the grey relational analysis both showed that the soil source region of number 13 ADS

event was highly likely emitted from the central Inner Mongolia.

3.3. Comparison of Three Source Identification Methods. Figure 6 illustrates and compares three methods for identifying the source regions of 18 ADS events. Through the backward trajectory calculation, enrichment factor and grey relational analysis could be applied to identify the ADS events numbers 1, 2, 6, 8, 9, 11, and 13–18, which accounted for 66.7% of the

TABLE 2: Source allocation of 18 ADS events in the Inner Mongolia by enrichment factor analysis.

ADS events	Dates of ADS events	Reference elements	ADS source region			Identified sources
			East	Central	West	
1	Mar. 8-9, 2002	Al	14	9	12	East
		Fe	13	9	12	
2	Mar. 18–20, 2002	Al	14	11	13	East
		Fe	14	13	13	
3*	Mar. 31, 2002	Al	11	12	13	West, central
		Fe	11	12	11	
4	Apr. 13, 2002	Al	7	9	8	Central
		Fe	7	9	7	
5	Apr. 17–19, 2002	Al	11	13	12	East
		Fe	11	8	9	
6	Feb. 25, 2003	Al	12	15	12	Central
		Fe	13	14	12	
7*	Mar. 7-8, 2003	Al	12	15	15	West, central
		Fe	13	13	13	
8*	Mar. 26-27, 2003	Al	13	15	15	West, central
		Fe	13	13	13	
9	Apr. 26-27, 2003	Al	12	14	14	Central
		Fe	12	13	12	
10	Feb. 6, 2004	Al	10	12	10	Central
		Fe	10	12	9	
11	Feb. 15-16, 2004	Al	10	13	10	Central
		Fe	11	11	11	
12	Apr. 2, 2004	Al	11	13	10	Central
		Fe	10	13	11	
13	Apr. 13–15, 2004	Al	11	14	14	Central
		Fe	12	14	12	
14	Nov. 29, 2005	Al	12	15	14	Central
		Fe	12	15	13	
15	Dec. 21–26, 2005	Al	13	14	15	West
		Fe	13	11	13	
16	Mar. 14–17, 2006	Al	9	13	9	Central
		Fe	10	12	12	
17	Mar. 19, 2006	Al	8	13	8	Central
		Fe	8	13	12	
18	Apr. 24-25, 2006	Al	10	15	10	East
		Fe	12	15	12	

* Different source regions determined by EF values using Al and Fe as reference elements.

18 ADS events. Comparing backward trajectory calculation with enrichment factor, the similarity percentage was 77.8% for 18 ADS events, including ADS events numbers 1, 2, 5–9, 11, 12, and 14–18 in this study. In terms of enrichment factor and grey relational analysis, it was shown that they were coincident for 83.3% of 18 ADS events, including ADS events numbers 1, 2, 4–6, 8–11, 12, and 14–18. In terms of grey relational analysis and backward trajectory calculation, it was shown that they were coincident for 77.8% of 18 ADS events, including ADS events numbers 1, 2, 4–6, 8–11, and 14–18. Generally speaking, the source allocation methods of ADS transported from Inner Mongolia to the Pescadores Islands

were relatively accurate, especially for simultaneous application of enrichment factor and grey relational analysis. More importantly, accurate chemical fingerprints of source soils and atmospheric particles are highly required for chemically allocating the source regions of the ADS events.

In order to further confirm the above three optimal methods feasible for allocating the mostly possible sources of ADS events, this study used the past general method to compare with the above three methods, which calculated the mass ratios of Al and Sr (Al/Sr), which had the highest differences in the 15 metals for 18 ADS events. Table 4 lists the mass ratio of Al/Sr for resuspended soils collected in the Inner Mongolia

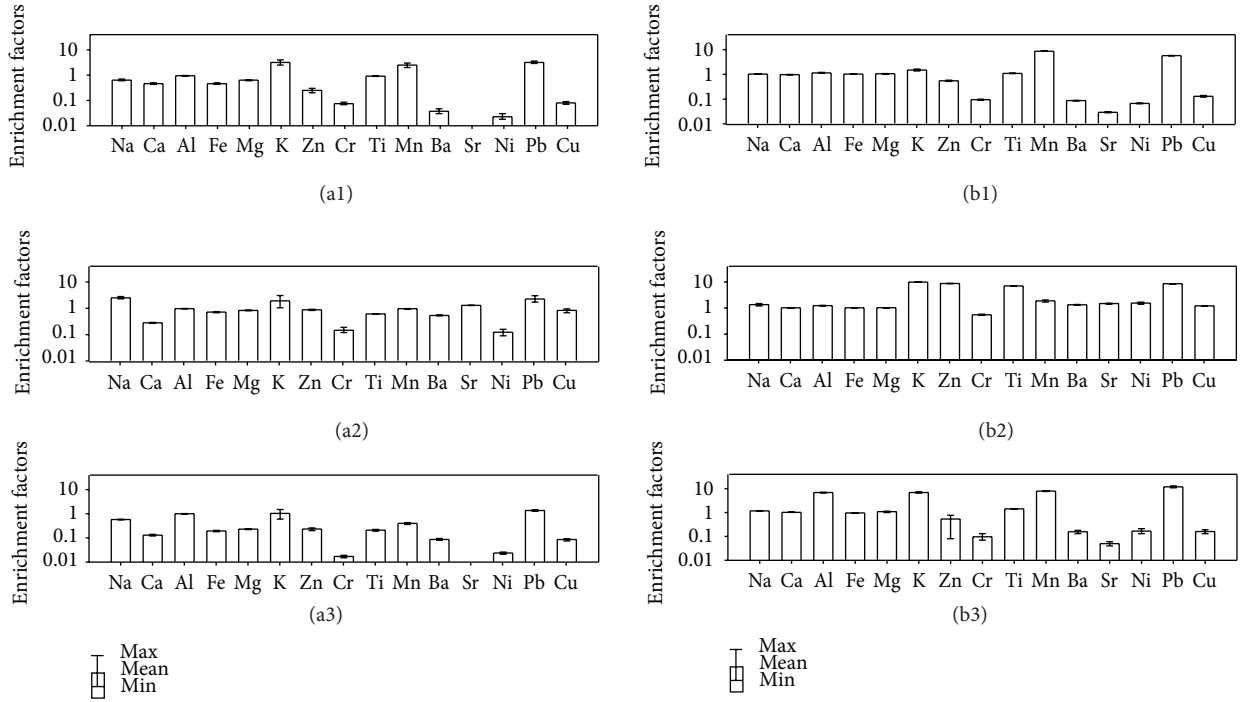


FIGURE 5: EF values of 15 metals with Al or Fe as reference elements at the Pescadores Islands. For example, (a1)~(a3) are the EF of eastern, central, and western source regions calculated by using aluminum as reference element; (b1)~(b3) are the EF of eastern, central, and western source regions calculated by using iron as reference element.

TABLE 3: Source allocation of 18 ADS events in the Inner Mongolia by grey relational calculation.

ADS events	Dates of ADS events	ADS source regions			Identified sources
		East	Central	West	
1	Mar. 8-9, 2002	0.90	0.87	0.82	East
2	Mar. 18-20, 2002	0.81	0.76	0.74	East
3	Mar. 31, 2002	0.79	0.84	0.87	West
4	Apr. 13, 2002	0.81	0.74	0.79	East
5	Apr. 17-19, 2002	0.79	0.78	0.71	East
6	Feb. 25, 2003	0.85	0.92	0.84	Central
7	Mar. 7-8, 2003	0.87	0.91	0.89	Central
8	Mar. 26-27, 2003	0.78	0.91	0.83	Central
9	Apr. 26-27, 2003	0.65	0.87	0.83	Central
10	Feb. 6, 2004	0.77	0.83	0.85	West
11	Feb. 15-16, 2004	0.70	0.84	0.78	Central
12	Apr. 2, 2004	0.83	0.86	0.93	West
13	Apr. 13-15, 2004	0.78	0.91	0.89	Central
14	Nov. 29, 2005	0.76	0.87	0.83	Central
15	Dec. 21-26, 2005	0.72	0.78	0.89	West
16	Mar. 14-17, 2006	0.63	0.87	0.84	Central
17	Mar. 19, 2006	0.69	0.79	0.80	Central
18	Apr. 24-25, 2006	0.92	0.89	0.83	East

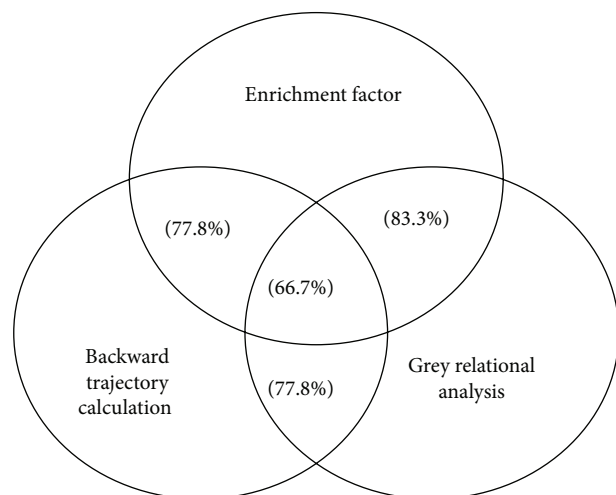


FIGURE 6: Comparison of the correlation percentages among backward trajectory calculation, enrichment factor, and grey relational analysis.

TABLE 4: Comparison of the Al/Sr ratios for source soils and atmospheric particles sampled in the Inner Mongolia and at the Pescadores Islands.

Source regions	Soil samples Al/Sr	Dust samples Al/Sr	Number of ADS events
East	55.6 ± 4.3	33.0 ± 93.3	1, 2, 4, 5, 18
Central	325.0 ± 118.0	161.1 ± 65.1	6–9, 11–14, 16, 17
West	2.5 ± 0.8	132.9 ± 42.6	7, 10, 12, 15

and atmospheric particles sampled at the Pescadores Islands. The results showed that the resuspended soil samples in the central Inner Mongolia had relatively higher Al/Sr ratio (325.0 ± 118.0) and observed simultaneously with the higher Al/Sr ratio (161.1 ± 65.1) of atmospheric particles at the Pescadores Islands. Furthermore, the resuspended soils and Asian dusts in the eastern Inner Mongolia both had high relative standard deviation (RSD) of 77 and 283%, respectively. The Al/Sr ratios of the resuspended soils and Asian dusts in the eastern and central Inner Mongolia had their significant characteristics, which could be used to identify the soil source regions of ADS events, while the Al/Sr ratios in the western Inner Mongolia were relatively broad. Overall, although the Al/Sr ratio could assist in identifying the sources of ADS, its confidence level was relatively lower than the backward trajectory calculation, enrichment factor, and grey relational analysis. Finally, this study has selected the mostly possible analysis methods to identify the sources of ADS events, which could be used to trace the source areas of ADS event in the future.

4. Conclusions

This study successfully combined backward trajectory calculation, enrichment factor, and grey relational analysis to allocate the potential source(s) of 18 ADS events, and identified

the transportation routes of Asian dusts transported from the Inner Mongolia to the Pescadores Islands. Three major transportation routes observed for 18 ADS events included ETR, STC, and SST. The variations of chemical components of the atmospheric dusts or source soils were correlated to their transportation routes, in which the chemical characteristics of Asian dusts could be influenced by anthropogenic particles emitted from local stationary and mobile sources during the ADS transportation processes. However, most of chemical components between source soils and atmospheric dusts for the same transportation routes were coincident. Moreover, source identification results showed that 50–72% out of 18 ADS events were originated from the central region of Inner Mongolia. Comparison of the three methods showed that the chemical-assisted methods demonstrated the accuracy of 66.7% for identifying the source regions of ADS events. Particularly, simultaneous application of enrichment factor and grey relational analysis raised the accuracy up to 83.3%. Overall, these three chemical-assisted tracing methods were feasible for identifying the soil source regions of ADS events.

Conflict of Interests

The authors declare that there is no conflict of interests regarding the publication of this paper.

Acknowledgments

The authors gratefully acknowledge the financial support from the National Science Council and kind assistance from the Institute of Environmental Engineering at National Sun Yat-Sen University. The authors would like to express their sincere appreciation for its financial and technological support to accomplish this study.

References

- [1] H. Bian, X. Tie, J. Cao, Z. Ying, S. Han, and Y. Xue, "Analysis of a severe dust storm event over China: application of the WRF-dust model," *Aerosol and Air Quality Research*, vol. 11, no. 4, pp. 419–428, 2011.
- [2] J. J. Cao, J. C. Chow, J. G. Watson et al., "Size-differentiated source profiles for fugitive dust in the Chinese Loess Plateau," *Atmospheric Environment*, vol. 42, no. 10, pp. 2261–2275, 2008.
- [3] M. T. Cheng, W. C. Chou, C. P. Chio et al., "Compositions and source apportionments of atmospheric aerosol during Asian dust storm and local pollution in central Taiwan," *Journal of Atmospheric Chemistry*, vol. 61, no. 2, pp. 155–173, 2008.
- [4] R. A. Duce, C. K. Unni, B. J. Ray, J. M. Prospero, and J. T. Merrill, "Long-range atmospheric transport of soil dust from Asia to the tropical North Pacific: temporal variability," *Science*, vol. 209, no. 4464, pp. 1522–1524, 1980.
- [5] X. Y. Zhang, S. L. Gong, Z. X. Shen et al., "Characterization of soil dust aerosol in China and its transport and distribution during 2001 ACE-Asia: 1. Network observations," *Journal of Geophysical Research D: Atmospheres*, vol. 108, no. 9, pp. 4261–4274, 2003.
- [6] X. Y. Zhang, R. Arimoto, and Z. S. An, "Dust emission from Chinese desert sources linked to variations in atmospheric

- circulation,” *Journal of Geophysical Research D*, vol. 102, no. 23, pp. 28041–28047, 1997.
- [7] C. S. Yuan, C. X. Hai, and M. Zhao, “Source profiles and fingerprints of fine and coarse sands resuspended from the soils sampled in the central inner mongolia,” *Particuology*, vol. 4, pp. 304–311, 2006.
- [8] Y. I. Tsai and C. L. Chen, “Characterization of Asian dust storm and non-Asian dust storm $PM_{2.5}$ aerosol in southern Taiwan,” *Atmospheric Environment*, vol. 40, no. 25, pp. 4734–4750, 2006.
- [9] I. Mori, M. Nishikawa, T. Tanimura, and H. Quan, “Change in size distribution and chemical composition of kosa (Asian dust) aerosol during long-range transport,” *Atmospheric Environment*, vol. 37, no. 30, pp. 4253–4263, 2003.
- [10] S. Tan, G. Shi, and H. Wang, “Long-range transport of spring dust storms in Inner Mongolia and impact on the China seas,” *Atmospheric Environment*, vol. 46, pp. 299–308, 2012.
- [11] F. Tsai, G. T. J. Chen, T. H. Liu, W. D. Lin, and J. Y. Tu, “Characterizing the transport pathways of Asian dust,” *Journal of Geophysical Research*, vol. 113, Article ID D17311, 2008.
- [12] R. D. Brook, “Is air pollution a cause of cardiovascular disease? Updated review and controversies,” *Reviews on Environmental Health*, vol. 22, no. 2, pp. 115–137, 2007.
- [13] C. Kang, W. Kim, H. Ko, and S. Hong, “Asian Dust effects on Total Suspended Particulate (TSP) compositions at Gosan in Jeju Island, Korea,” *Atmospheric Research*, vol. 94, no. 2, pp. 345–355, 2009.
- [14] S. Wang, S. Tsay, N. Lin et al., “First detailed observations of long-range transported dust over the northern South China Sea,” *Atmospheric Environment*, vol. 45, no. 27, pp. 4804–4808, 2011.
- [15] M. V. K. Sivakumar, “Impacts of sand storms/dust storms on agriculture,” in *Natural Disasters and Extreme Events in Agriculture*, pp. 159–177, 2005.
- [16] D. Y. Jeong, “Socio-economic costs from yellow dust damages in South Korea,” *Transborder Environmental and Natural Resource Management*, pp. 185–198, 2008.
- [17] H. Mu, S. Otani, M. Shinoda et al., “Long-term effects of livestock loss caused by dust storm on mongolian inhabitants: a survey 1 year after the dust storm,” *Yonago Acta Medica*, vol. 56, no. 1, pp. 39–42, 2013.
- [18] H. Lee, Y. Honda, Y. H. Lim, Y. L. Guo, M. Hashizume, and H. Kim, “Effect of Asian dust storms on mortality in three Asian cities,” *Atmospheric Environment*, vol. 89, pp. 309–317, 2014.
- [19] C. S. Yuan, C. C. Sau, M. C. Chen et al., “Mass concentration and size-resolved chemical composition of atmospheric aerosols sampled at the Pescadores Islands during Asian dust storm periods in the years of 2001 and 2002,” *Terrestrial, Atmospheric and Oceanic Sciences*, vol. 15, no. 5, pp. 857–879, 2004.
- [20] B. Lee, H. K. Lee, and N. Jun, “Analysis of regional and temporal characteristics of PM_{10} during an Asian dust episode in Korea,” *Chemosphere*, vol. 63, no. 7, pp. 1106–1115, 2006.
- [21] S. Chen, L. Hsieh, M. Kao, W. Lin, K. Huang, and C. Lin, “Characteristics of particles sampled in southern Taiwan during the Asian dust storm periods in 2000 and 2001,” *Atmospheric Environment*, vol. 38, no. 35, pp. 5925–5934, 2004.
- [22] C. J. Ma, M. Kasahara, S. Tohno, R. Holler, and T. Kamiya, “Chemical composition of single raindrops fallen in yellow rainfall episode in Japan,” in *Proceedings of the 2nd Asian Aerosol Conference*, pp. 185–186, Pusan, Republic of Korea, 2001.
- [23] S. H. Liu and C. S. Yuan, *Source apportionment and optical properties of atmospheric aerosols in metro Kaohsiung [M.S. thesis]*, Institute of Environmental Engineering, National Sun Yat-sen University, Kaohsiung, Taiwan, 2000, (Chinese).
- [24] G. McTainsh, Y. Chan, H. McGowan, J. Leys, and K. Tews, “The 23rd October 2002 dust storm in eastern Australia: characteristics and meteorological conditions,” *Atmospheric Environment*, vol. 39, no. 7, pp. 1227–1236, 2005.
- [25] Z. X. Shen, J. J. Cao, R. Arimoto et al., “Ionic composition of TSP and $PM_{2.5}$ during dust storms and air pollution episodes at Xi’an, China,” *Atmospheric Environment*, vol. 43, pp. 2911–2918, 2009.
- [26] T. Nakamura, K. Matsumoto, and M. Uematsu, “Chemical characteristics of aerosols transported from Asia to the East China Sea: An evaluation of anthropogenic combined nitrogen deposition in autumn,” *Atmospheric Environment*, vol. 39, no. 9, pp. 1749–1758, 2005.
- [27] R. Zhang, Z. Shen, T. Cheng, M. Zhang, and Y. Liu, “The elemental composition of atmospheric particles at Beijing during Asian dust events in spring 2004,” *Aerosol and Air Quality Research*, vol. 10, no. 1, pp. 67–75, 2010.
- [28] S. F. Kong, B. Han, Z. P. Bai, L. Chen, J. W. Shi, and Z. Xu, “Receptor modeling of $PM_{2.5}$, PM_{10} and TSP in different seasons and long-range transport analysis at a coastal site of Tianjin, China,” *Science of the Total Environment*, vol. 408, no. 20, pp. 4681–4694, 2010.
- [29] L. Zhu, X. Huang, H. Shi, X. Cai, and Y. Song, “Transport pathways and potential sources of PM_{10} in Beijing,” *Atmospheric Environment*, vol. 45, no. 3, pp. 594–604, 2011.
- [30] H. H. Tsai, C. S. Yuan, C. H. Hung, and Y. C. Lin, “Physicochemical properties of $PM_{2.5}$ and $PM_{2.5-10}$ at inland and offshore sites over Southeastern coastal region of Taiwan strait,” *Aerosol and Air Quality Research*, vol. 11, no. 6, pp. 664–678, 2011.
- [31] J. L. Deng, *A Course on Grey System Theory*, HUST Press, Wuhan, China, 1990.
- [32] G. Dongarrà, E. Manno, D. Varrica, M. Lombardo, and M. Vultaggio, “Study on ambient concentrations of PM_{10} , $PM_{10-2.5}$, $PM_{2.5}$ and gaseous pollutants: trace elements and chemical speciation of atmospheric particulates,” *Atmospheric Environment*, vol. 44, no. 39, pp. 5244–5257, 2010.
- [33] T. C. Li, W. H. Chen, C. S. Yuan, S. P. Wu, and X. H. Wang, “Physicochemical characteristics and source apportionment of atmospheric aerosol particles in Kinmen-Xiamen Airshed,” *Aerosol and Air Quality Research*, vol. 13, no. 1, pp. 308–323, 2013.

Research Article

Ground-Based Polarimetric Remote Sensing of Dust Aerosol Properties in Chinese Deserts near Hexi Corridor

Hua Xu, Zhengqiang Li, Donghui Li, Li Li, Xingfeng Chen, Yisong Xie,
Kaitao Li, Cheng Chen, and Yuhuan Zhang

State Environmental Protection Key Laboratory of Satellite Remote Sensing, Institute of Remote Sensing and Digital Earth,
Chinese Academy of Sciences, Beijing 100101, China

Correspondence should be addressed to Zhengqiang Li; lizq@radi.ac.cn

Received 28 February 2014; Revised 4 July 2014; Accepted 23 July 2014; Published 18 August 2014

Academic Editor: Hesham El-Askary

Copyright © 2014 Hua Xu et al. This is an open access article distributed under the Creative Commons Attribution License, which permits unrestricted use, distribution, and reproduction in any medium, provided the original work is properly cited.

One-year observation of dust aerosol properties near Hexi Corridor was obtained from polarimetric measurements by ground-based sunphotometer in the county of Minqin in northwestern China from March 2012 to February 2013. We observed an annual mean AOD of 0.22 ± 0.22 at $0.50 \mu\text{m}$ and Ångström exponents of 0.1–1.0 fitting a bimode normal distribution centered at 0.18 and 0.50, respectively. The effective radii of fine ($0.13\text{--}0.17 \mu\text{m}$) and coarse ($2.49\text{--}3.49 \mu\text{m}$) modes were found stable at all seasons together with the appearance of a third mode of particle radius at $0.4\text{--}1.0 \mu\text{m}$ when AOD was larger than 0.6. It is noticeable that the real ($1.5\text{--}1.7$) and imaginary (0.0005 to 0.09) parts of complex refractive indices were higher than other studies performed in other desert regions of China, while single scattering albedo was relatively lower ($\sim 0.84\text{--}0.89$) at wavelengths of 0.44 , 0.67 , 0.87 , and $1.02 \mu\text{m}$. This is partially due to calcite or hematite in the soil in Minqin or the influence of anthropogenic aerosols containing carbon. Moreover, from our novel polarimetric measurement, the scattering phase function (F_{11}) and degree of linear polarization for incident unpolarized light ($-F_{12}/F_{11}$) of dust aerosols were also obtained within this deserted area.

1. Introduction

Dust aerosols are common natural particles suspending in terrestrial atmosphere. According to mineralogy, there are thousands of mineral species in global crust such as illite, kaolinite, gypsum, smectite, quartz, calcite, and hematite, each of which has a specific chemical composition, molecular structure, and physical morphology [1]. The abundance of minerals usually varies spatiotemporally. Dust aerosols originate from eroding rocks in deserts or arid soils and are emitted from the bare surface by updraft, then transported in a long-range way, and finally deposited by gravity or rainout. The atmospheric dust aerosols interact with light and influence the radiative forcing in global/regional scale [2]. However, knowledge of optical properties of Chinese dust aerosols is not enough and the radiative impact is poorly known as well. This is in part due to the complexity of the properties of mineral dust aerosols which depend on size, shape, and orientation [3] and in part due to the lack of long-term rigorous observation in this region.

Many researchers have improved our knowledge of dust aerosols in worldwide locations. Sokolik et al. [4, 5] compared refractive indices of atmospheric dust aerosols from various geographic locations and then modeled the radiative properties accounting for their compositions. Databases containing experimental scattering matrices of mineral dust particles were developed [6, 7]. Apart from these high-quality laboratory measurements, the optical and physical properties of dust aerosols can be retrieved by ground-based sunphotometer [8–10]. The optical properties of dust aerosols in Sahara Desert [11], Middle East [12], and Asian regions [13] were studied. In China, there were several observations in northern arid areas such as Taklimakan Desert [14] and Hunshan Dake Desert [15].

With a goal of studying the optical and microphysical properties of dust aerosols, we deployed a ground-based sunphotometer in northwestern China. The location was surrounded by deserts where the aerosol properties and climatology of mineral dusts were thought to be obvious. We took one year observation from March 2012 to February



FIGURE 1: Geographical location of Hexi Corridor, Badain Jaran Desert, and Tengger Desert. The Minqin site (38.6°N , 103.1°E) is marked as a red pentagram.

2013 and the results and analysis are shown in the following sections.

2. Measurement and Data

2.1. Polarimetric Sunphotometer Measurement. The sunphotometer (CIMEL CE318-DP) is a polarized instrument with nine channels of 0.34, 0.38, 0.44, 0.50, 0.67, 0.87, 0.93, 1.02, and $1.64\ \mu\text{m}$. The radiometer is capable of measuring both the direct-sun radiances and diffuse-sky radiances with a 1.2° full field of view [16]. When automatic mode performs, the collimator of sunphotometer tracks the sun each 15 minutes and scans following almucantar (ALM) and solar principle plane (SPP) geometry procedures approximately each hour. For the SPP procedure, the instrument measures sky radiation at different solar elevation angles at a fixed solar azimuthal angle and large scattering angles are attainable at noon. Moreover, the sunphotometer is a new polarized version which can measure polarization at all bands by combining rotation of polarizer and filter wheels [17].

The site (referred to as Minqin site hereafter) is located at 38.6°N , 103.1°E in Gansu province in China (Figure 1), neighbored by Hexi Corridor. It has a peculiar geographical position because it lies on a junction of Badain Jaran Desert and Tengger Desert which are the third and fourth biggest desert in China, respectively. The climatology is a typical continental arid climate with adequate solar energy, scarce rainfall, and large evaporation. Therefore, the site is vulnerable to dust aerosols. According to meteorological records since 2006, the dust storms have happened nineteen times averagely every year. The instrument is installed in downtown which has a population of about 300,000.

2.2. Data Processing. We use one-year measurements from March 2012 to January 2013 at Minqin site to investigate the properties of mineral dust aerosols. Unscreened measurements are frequently contaminated by clouds or obstruction. Therefore we apply cloud screening procedures which include

triplet measurements (a sequence of three direct-sun measurements are taken 30 s apart per wavelength [16]) and check the symmetry of the ALM measurements. The latter way is suited to find whether the sky is clear because the presence of cloud would cause disparities between symmetrical pairs of ALM measurements. Following these methods, the data is upgraded from level 1.0 to 1.5. To ensure the quality, three kinds of calibrations are applied to the direct-sun measurement, diffuse-sky measurement, and polarization measurements [16–19], respectively. The uncertainty of direct-sun measurements makes the AOD error less than 0.01–0.02, while the uncertainty of sky radiances is estimated to be about 3%. The maximum uncertainty of DOLP measurements is estimated to be less than ~ 0.01 .

In reality, dust particles are not spherical and seldom isotropic or homogeneous. Dubovik et al. [9] established a spheroid model accounting for nonsphericity in ground-based remote sensing of aerosols. Hence, in this study we use this model for retrieving the properties of dust aerosols by spectral and angular observation of both intensity and polarization. The results will be discussed in Section 3, including AOD, Ångström exponent, size distribution, complex refractive index, single scattering albedo, phase function (F_{11}), and the degree of linear polarization ($-F_{12}/F_{11}$).

In this work, we totally select 7040 AODs and Ångström exponents records (level 1.5) out of 15309 measurements (level 1.0). For the retrieval of aerosol size distribution, complex refractive index, single scattering albedo, phase function, and the degree of linear polarization, we select only 478 records filtered by residuals threshold of 5% according to Dubovik et al. [9].

3. Results and Discussion

3.1. AOD and Ångström Exponent

3.1.1. Histogram and Monthly Variation of AOD. Following Beer-Lambert-Bouguer's law, aerosol optical depth can be derived by excluding the atmospheric molecules optical depth and gas absorption optical depth from the total optical

depth measured by sunphotometer. About forty-five percent, 7040 records (level 1.5), of all instantaneous measurements are used for investigation in Minqin.

Figure 2 shows the frequency distribution of AODs at $0.5 \mu\text{m}$ (τ_{500}) with both relative frequency and accumulated frequency in left and right axis, respectively. The distribution is well fitted by a normal function centered at $0.22 (\mu)$ with the standard deviation of $0.22 (\sigma)$. It is explicit that $0.15 < \tau_{500} \leq 0.20$ occur most frequently with the probability beyond 16%. When $0 < \tau_{500} \leq 0.44$ (i.e., $\mu - \sigma < \tau_{500} < \mu + \sigma$), the accumulated frequency is beyond 80%, while when $0 < \tau_{500} \leq 0.88$ (i.e., $\mu - \sigma < \tau_{500} < \mu + 3\sigma$), it reaches up to 97%. Moreover, the distributions of AOD at other wavelengths are similar. Che et al. [14] exhibited the frequency distribution of AODs over Taklimakan Desert in China. Their histogram was fitted by two peaks; that were the mode centered at ~ 0.23 probably corresponding to nondust atmospheric and the mode centered at ~ 0.50 caused by higher mineral dust burden in atmosphere. Our average is very close to their first peak. In Figure 2 we can find that AODs within the range of $0.4\text{--}0.7$ are obviously higher than the fitting curve which may correspond to their second peak. Similarly, at wavelength of $1.02 \mu\text{m}$, the mean AOD is 0.21 that is close to Dubovik et al. [10] study in which the mean AOD is 0.22 in Persian Gulf and 0.17 in Saudi Arabia.

Heavy dust storms are an apparent meteorological process, but from Figure 2, it is hard to make out them because we use data of level 1.5. High-quality data and dust activities are not compatible causing a selection effect. First, large AODs corresponding to active dust events may be excluded as cloud contamination. Second, the dust storms with turbulence windy condition may cause unstable measurements. For example, in the case of heavy dust loading, due to FOV uncertainty, errors of AODs can be significant because of large forward scattering of large particles [19]. Third, due to the default digital gain of CE318 under automatic mode, the maximal AOD is suggested to be no more than 4.0 . For another example, when an active dust storm happened on March 20, 2012, in Minqin, our ground-based sunphotometer only totally took down 48 records. The level 1.0 data showed that the daily average of AODs (τ_{500}) was 2.3 and the maximum even reached up to 4.7 . Therefore, from this point of view, we probably lose the opportunity to investigate the heavy dust aerosol burden in this area if we want to insure data quality.

The monthly variation of AOD (τ_{500}) is shown in Figure 3. The error bars stand for one standard deviation range ($\pm\sigma$) of monthly averaged AODs. The entire observation period (from Mar. 2012 to Feb. 2013) can be divided into four seasons which are spring (from Mar. 2012 to May. 2012), summer (from Jun. 2012 to Aug. 2012), autumn (from Sep. 2012 to Nov. 2012), and winter (from Dec. 2012 to Feb. 2013). At the bottom of Figure 3, the number of monthly records (corresponding to the right coordinate) is counted. Each month has approximately equal numbers ($\sim 500\text{--}800$) of AODs except December (83 counts) and January (23 counts). This is because we carried out instrument calibration in Beijing from Dec. 8, 2012 to Jan. 30, 2013.

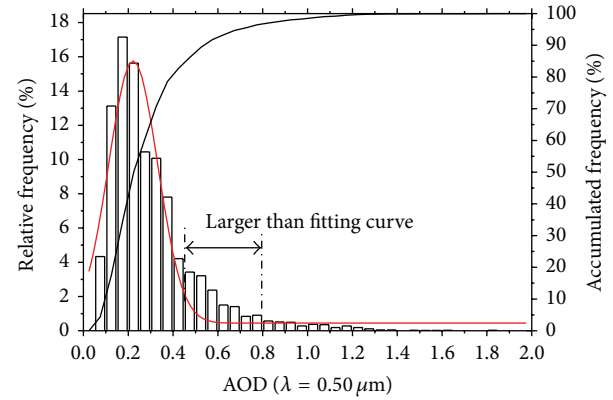


FIGURE 2: The histogram of AOD at $0.50 \mu\text{m}$ in the form of relative frequency and accumulated frequency.

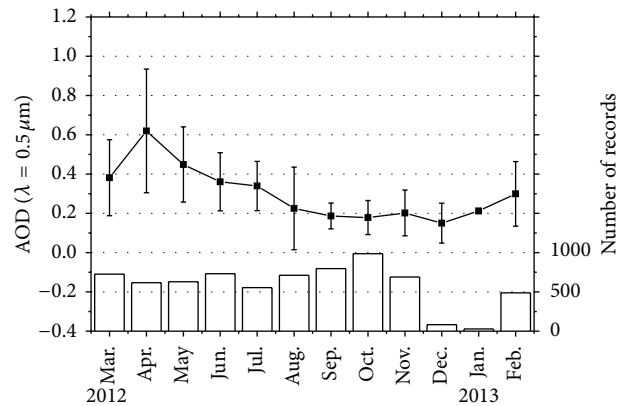


FIGURE 3: The monthly variation of AOD. The left axis corresponding to AOD and the right axis corresponding to number of records.

A clear pattern for monthly variation of AOD (τ_{500}) can be found in Figure 3. In spring, dust aerosol load is always the heaviest among four seasons. The AOD values change from 0.4 to 0.6 with the biggest standard deviation (~ 0.3) in April. A probable explanation is that Minqin suffers from drought and active windy events in spring. From summer to autumn the AODs decrease. In October, AODs are the lowest, that is, 0.18 ± 0.09 . Because of quiet weather, from September to November, the measurements are very stable which is reflected by small standard deviations. In winter, the AODs begin to increase slightly till the next spring. It should be noted that in January there are the fewest records and the smallest standard deviations for the sake of calibration experiment.

3.1.2. Histogram and Monthly Variation of Ångström Exponent. Ångström exponent (α) reflects the aerosol size and its spectral dependence. The frequency histogram of Ångström exponents, derived from AODs at wavelength of 0.44 and $0.87 \mu\text{m}$, can be seen in Figure 4. It illustrates the main range of α from 0.1 to 1.0 . The distribution is fitted by a bimode normal distribution centered at about 0.18 and 0.50 , comparable to Che et al. [14] results of 0.17 and 0.50 ,

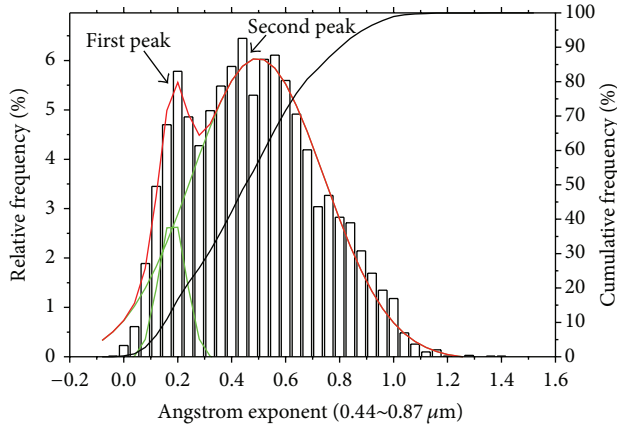


FIGURE 4: The frequency distribution of Ångström exponents (0.44–0.87 μm) in the form of relative histogram and accumulated frequency.

respectively. Two peaks in Figure 4, corresponding to larger size and smaller size particles, are perhaps associated with two aerosol types in desert area. The peak 0.50 can be explained as dust particles emitted into atmosphere by wind, while another peak 0.18 may be related to suspending particles by floating dust or dust flowing. Also, the threshold is very consistent with other desert locations such as Saudi Arabia (0.1–0.9) [10]. It is also found that the peak 0.18 corresponds to most of large dust aerosols ($-0.05 < \alpha < 0.25$) discovered by Li et al. [11] among 5 sites in Africa arid areas.

Dust aerosols have an obvious trend of increasing AOD versus decreasing Ångström exponent. This phenomenon is caused by large particles. The monthly variation of Ångström exponent is plotted in Figure 5. Compared with Figure 3, Ångström exponent behaves contrary to the AOD trend at all seasons. The minimum value of Ångström exponent is in April (0.29 ± 0.15), while the maximum value is in September (0.64 ± 0.22). In general, the size of dust aerosol is larger in winter-spring than in summer-autumn. In conjunction with Figure 4, the peak of the histogram of Ångström exponent ($\alpha \sim 0.2$) is likely from winter-spring. When the wind blows from north to south in winter-spring season, the influence of dust particles is more noticeable resulting in lower values of Ångström exponent. Whereas, when the wind blows from south to north in summer-autumn, the anthropogenic influence is more obvious causing the values of Ångström exponent to be higher.

3.2. Size Distribution

3.2.1. Size Distribution versus AOD. The size of dust aerosols is normally expressed by the effective radius (r_{eff}) ranging from a few nanometers to 100 microns. An ensemble of dust particles can be classified as clay ($r < 1 \mu\text{m}$), silt ($1 < r < 25 \mu\text{m}$), and sand ($r > 25 \mu\text{m}$) fractions in terms of size distribution [3]. In OPAC model [20] (tabulated in Table 1c therein), there are four mineral modes: nucleus mode, accumulation mode, mineral-transported mode, and coarse mode whose volume radii are 0.27, 1.6, 3.0, and 11.0 μm ,

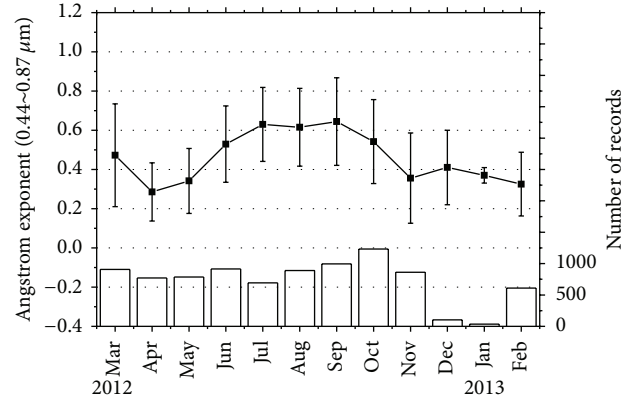


FIGURE 5: The monthly variation of Ångström exponent (0.44–0.87 μm). The left axis corresponding to Ångström exponent and the right axis corresponding to number of records.

respectively. In fact, the size distribution of dust particle is related to a few characteristics such as shape, composition, mixture manner, and AOD. For instance, tiny particles of clay are believed to stay suspended in atmosphere for a long time and then can transport further than large particles of sands. Dust aerosols may be agglomerated or aggregated through physicochemical transformation which can lead to size change.

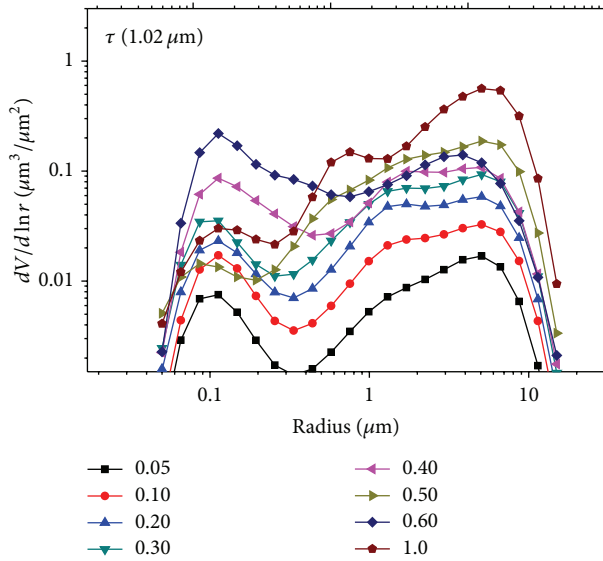
We use a bimodal lognormal function for modeling. The size distribution is divided into twenty-two bins with radii from 0.05 to 15 μm [9]. On average of all retrievals of size distributions, the effective radius of fine mode (r_f) is 0.14 μm with the standard deviation $\sigma_f = 0.5$ while the coarse mode (r_c) is 2.82 μm with $\sigma_c = 0.75$. Dubovik et al. [10] summarized a couple of size distributions of dust aerosols in Arabian Peninsula (Saudi Arabia and Cape Verde) and Bahrain-Persian Gulf, which were $r_f \sim 0.12\text{--}0.15 \mu\text{m}$ and $r_c \sim 1.90\text{--}2.54 \mu\text{m}$, respectively. Large aerosols are dominant because of $V_c/V_f \sim 2\text{--}8$. Our results agree with several previous observations [15, 21]. However, the volume content of coarse mode in Minqin is lower than regions mentioned above ($V_c/V_f \sim 10\text{--}50$).

In this study, we divide measurements into eight categories in terms of AODs ($\tau \leq 0.05$, $0.05 < \tau \leq 0.1$, $0.1 < \tau \leq 0.2$, $0.2 < \tau \leq 0.3$, $0.3 < \tau \leq 0.4$, $0.4 < \tau \leq 0.5$, $0.5 < \tau \leq 0.6$, and $0.6 < \tau \leq 1.0$) (Figure 6). In general, most series exhibit the dominance of large particles in dust aerosols. When AODs increase, both the concentrations of the fine and coarse modes increase. Despite changes in AODs, the aerosol size distributions are approximately consistent in shape except for $0.6 < \tau \leq 1.0$. The third mode (except for fine and coarse modes) at particle radius of 0.4–1.0 μm begins to appear when AODs are larger than 0.6. This change is most likely to attribute to abundance of the accumulation and mineral-transported components in dust aerosols [22].

3.2.2. Monthly Variation of Size Distribution. The monthly variation of size distribution is plotted in Figure 7 and the parameters of mean and standard deviation of effective radii

TABLE 1: The monthly variation of effective radius, standard deviation, and volume concentration of fine mode and coarse mode.

Month	r_f (μm)	r_c (μm)	σ_f	σ_c	V_f ($\mu\text{m}^3/\mu\text{m}^2$)	V_c ($\mu\text{m}^3/\mu\text{m}^2$)
Mar. (2012)	0.15	2.59	0.51	0.74	0.04	0.12
Apr.	0.15	2.81	0.57	0.76	0.05	0.43
May	0.16	2.64	0.57	0.76	0.04	0.14
Jun.	0.13	3.06	0.51	0.75	0.05	0.15
Jul.	0.17	3.49	0.51	0.77	0.05	0.09
Aug.	0.14	3.02	0.46	0.77	0.02	0.07
Sep.	0.14	3.01	0.47	0.76	0.02	0.07
Oct.	0.14	2.76	0.51	0.73	0.02	0.07
Nov.	0.14	2.49	0.53	0.72	0.01	0.07
Dec.	0.15	2.75	0.50	0.71	0.01	0.04
Jan. (2013)	0.15	2.93	0.49	0.66	0.01	0.15
Feb.	0.16	2.64	0.53	0.74	0.01	0.05

FIGURE 6: The size distribution of dust aerosol is divided into eight categories in terms of AODs ($\tau \leq 0.05$, $0.05 < \tau \leq 0.1$, $0.1 < \tau \leq 0.2$, $0.2 < \tau \leq 0.3$, $0.3 < \tau \leq 0.4$, $0.4 < \tau \leq 0.5$, $0.5 < \tau \leq 0.6$, and $0.6 < \tau \leq 1.0$).

and volume ratios of fine mode and coarse mode are listed in Table 1. From the table, we find that both the effective radii of two modes are stable from spring to winter ($r_f \sim 0.13\text{--}0.17 \mu\text{m}$, $r_c \sim 2.49\text{--}3.49 \mu\text{m}$). The volume concentration of fine mode (V_f) decreases from spring to winter. The volume concentration of coarse mode (V_c) exhibits a similar tendency only if we disregard March (0.43) and January (0.15). Moreover, V_c is significantly high (~ 0.43) in April because of dust activities.

3.3. Complex Refractive Index

3.3.1. Histogram of Complex Refractive Index. The histograms of real parts of the complex refractive indices at 0.44, 0.67, 0.87, and $1.02 \mu\text{m}$ are given in Figure 8. It should be pointed out that the threshold of real parts used in our processing is

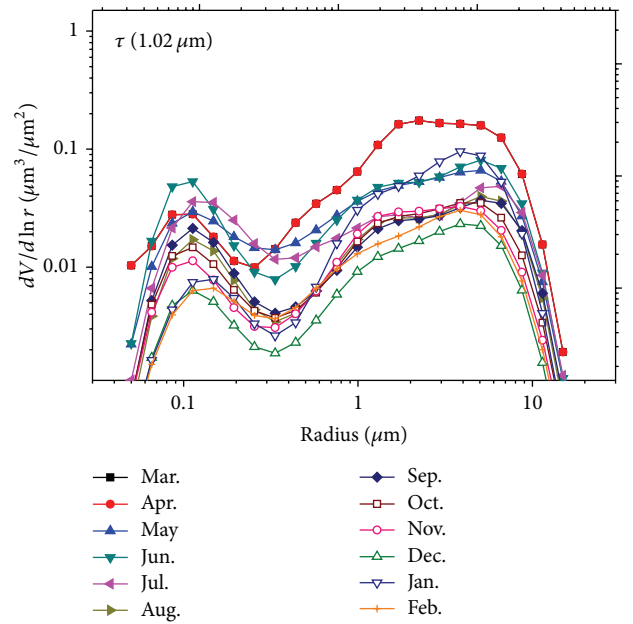


FIGURE 7: Monthly variation of size distribution of dust aerosols from Mar. 2012 to Feb. 2013.

set as 1.33–1.70, which is different from AERONET's threshold (1.33–1.60). In many models [21], the real part of dust aerosol is thought to be constantly 1.53 in visible spectrum or accompanying a slight fluctuation with a range of 0.05 in accordance with *in situ* measurements [4]. Nevertheless, in Figure 9, the real parts of complex refractive indices seem to be higher than expected. Additionally, the real parts of complex refractive indices in the range ($\sim 1.6\text{--}1.7$) have a pronounced spectral variation from visible to infrared spectrum.

For imaginary parts of refractive indices, our results are given in Figure 9 with values ranging from 0.0005 to 0.09 at four wavelengths of 0.44, 0.67, 0.87, and $1.02 \mu\text{m}$. In the WMO model, the imaginary part of refractive index in visible spectrum is 0.008 which is thought to be larger than measurements by Dubovik et al. [10]. Otterman et al.

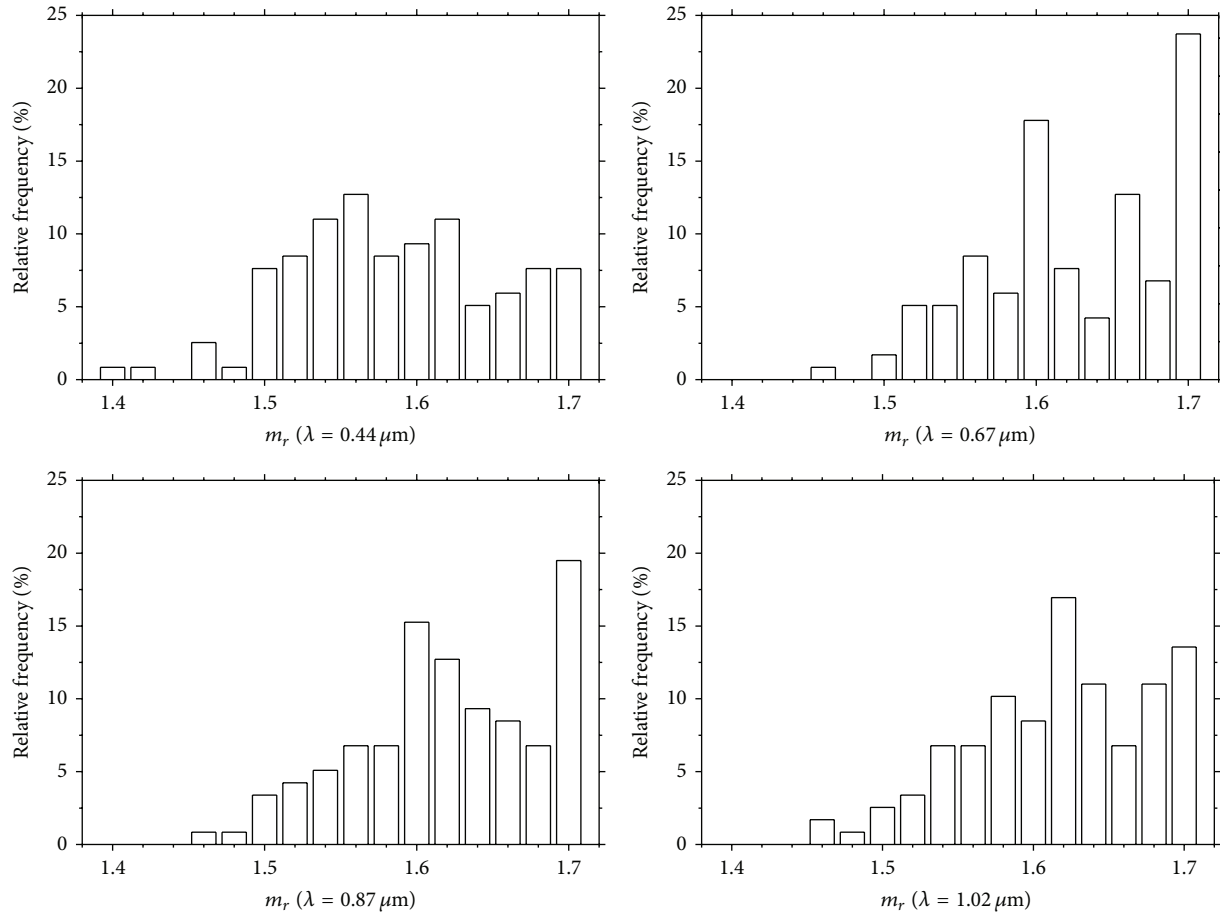


FIGURE 8: The histograms of the real part of complex refractive index for dust aerosol at 0.44, 0.67, 0.87, and 1.02 μm .

[23] gave the value of 0.001 and sometimes 0.003 [24] when heavy dust happened. In China, Cheng et al. [15] observed a value of about 0.0007–0.0033 at four wavelengths in Hunshan Dake Desert. Nevertheless, as explicated in Figure 9, the imaginary parts tend to be larger than previous studies. Only approximately 30% of our observations fall into the bin of 0.001–0.008.

3.3.2. Analysis of Dust Constituents. The complex refractive index of dust aerosol is relevant to its constituents. Dust aerosol is always a natural mixture of various constituents which are mainly illite, kaolinite, smectite, calcite, and quartz as major species for clays and quartz, feldspars, calcite, hematite, and gypsum for silts. The abundance of each dust mineral depends on sources, mobilization processes, and physicochemical transformations during transport. For convenience of comparison, we list complex refractive indices of various common species of dust minerals in Table 2 as well as citations. At visible wavelength the real part of mineral is about 1.4–1.6 for all aforementioned species except for limestone (~ 1.655 only *o*-ray) and hematite (~ 3.0), while the imaginary part is very close to zero except for hematite (~ 0.1 – 0.01). Limestone (98% calcite), due to its property of birefringence, has two measured values of real

parts, while the distribution of real parts also shows bimode. From this similarity in phenomenon, we speculated that the birefringence exists.

Looking back to our measurements, the real part is higher than 1.5. It is implicit that the limestone (calcite) may be a dominant constituent in dust aerosols in Minqin. The evidence is convincing according to the global high-resolution mineralogical database of dust-productive soils [25]. The values of 1.7 may be due to our thresholds for the real part. Thus, another reason is that hematite whose real part (~ 3.0) is uniquely large than other minerals that may exist in Minqin. As Table 2 shows, the imaginary part is larger than most mineral species implying the occurrence of absorptive particles, perhaps anthropogenic aerosols due to human activities or hematite. Xiao-peng and Hai-bing [26] found that iron oxides are an important constituent of dust aerosols in Minqin, which demonstrates our speculation to some extent. Finally, the other possibility why the modeled refractive indices may turn out higher is the effect of surface roughness [3] which is not considered in Dubovik's spheroidal model.

3.4. Single Scattering Albedo. Single scattering albedo (SSA, ω_0) is a synthetic optical parameter for particle scattering

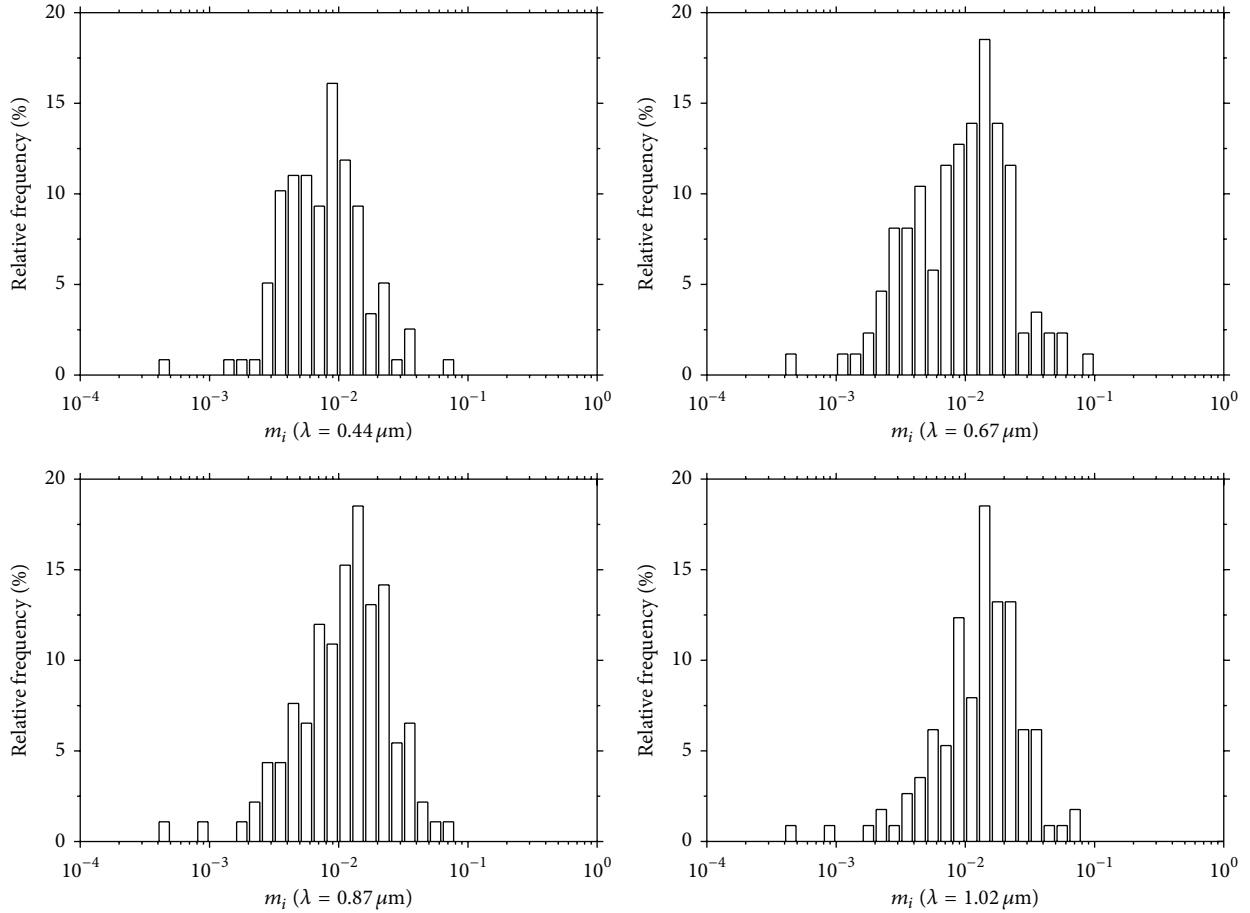


FIGURE 9: The histograms of the imaginary part of complex refractive index for dust aerosol at 0.44, 0.67, 0.87, and 1.02 μm .

TABLE 2: Complex refractive indices of minerals derived from some references.

Mineral dust	m_r	m_i	References
Illite	1.413	0.000773	[5]
Kaolinite	1.493	0.000048	[5]
Montmorillonite	1.523	0.000038	[5]
Limestone (98% Calcite)	1.655	0 (<i>o</i> -ray)	[27]
	1.485	0 (<i>e</i> -ray)	
Feldspar	1.5-1.6	0.001-0.00001	[28]
Hematite	3.0	0.1-0.01	[29]
Quartz	1.54	0	[28]
White clay	1.50-1.70	0.00001-0.001	[30]
Green clay	1.50-1.70	0.00001-0.001	[30]

depending on its size, shape, orientation, and composition. Dubovik et al. [10] found that the SSA value of dust *in situ* measurement was above 0.90 at wavelengths of 0.44–0.87 μm . His results were significantly less absorptive than models (~ 0.63 –0.89 at 0.55 μm [21]). Generally speaking, dust aerosol is thought to be weakly absorbing except hematite. The SSAs of dust aerosols in Minqin are 0.89 ± 0.05 , 0.87 ± 0.06 , 0.85 ± 0.07 , and 0.84 ± 0.07 at wavelengths of 0.44, 0.67,

0.87, and 1.02 μm , respectively. The results are closed to models, but lower than Dubovik et al. [10] observation as shown in Figure 10. The figure exhibits different tendency of SSA spectrum between fine mode ($<1 \mu\text{m}$) and coarse mode ($>1 \mu\text{m}$) particles. For large particles, the trend of SSA increases compared to λ , agreeing well with Li et al. [11] statistics. In the case of nondust dominated fine aerosols, we expect $\omega_0(\lambda)$ to show a tendency to decrease.

According to our results, the single scattering albedo of coarse mode is obviously lower than aforementioned studies at all wavelengths. The results illustrate that dust in Minqin is likely more absorptive. In fact, the dust absorption is predetermined by the presence of hematite. Recent efforts on incorporating mineralogical composition into models of radiative properties of dust [5] emphasize that the way hematite is mixed with quartz or clay is complicated and strongly impacts the resulting absorption.

3.5. Scattering Matrix. One of the advantages in polarimetric measurement by sunphotometer is to retrieve elements from 4×4 scattering matrix, that is, Mueller matrix, which reveals important microphysical properties of an ensemble of dust aerosols. Assuming that the particles have their mirror positions in equal number and in random orientations, the matrix

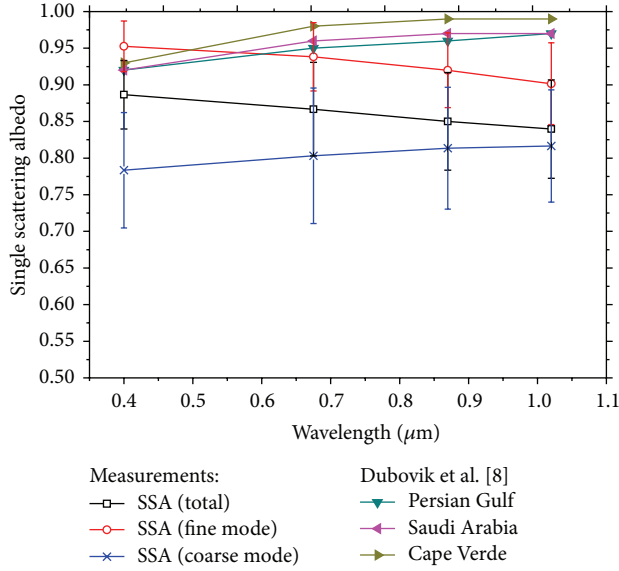


FIGURE 10: The total SSA, SSA of fine mode, SSA of coarse mode of dust aerosol at 0.44, 0.67, 0.87, and 1.02 μm and measurements from Dubovik et al. [10] work.

can concisely be written with six independent dimensionless elements as

$$F = \begin{bmatrix} F_{11} & -F_{12} & 0 & 0 \\ F_{12} & F_{22} & 0 & 0 \\ 0 & 0 & F_{33} & F_{34} \\ 0 & 0 & F_{34} & F_{44} \end{bmatrix}. \quad (1)$$

The complete scattering matrix has been investigated as a function of the scattering angle of aerosols in laboratory and published via website [7, 31]. Two matrix elements as a function of the scattering angle, the scattering phase function (F_{11}) normalized to 1 at 30 degrees, and the degree of linear polarization for unpolarized incident light ($-F_{12}/F_{11}$) can be obtained by polarimetric ground-based observations. In the inversion algorithm [10], sky radiance and polarized radiance (the maximum scattering angle depends on solar zenith angle) are fitted simultaneously with model to yield column aerosol microphysical parameter, like aerosol size distribution, refractive index, and shape. F_{11} and $-F_{12}/F_{11}$ also could be calculated from these aerosol parameters by radiative transfer model, with 83 scattering angle from 0 to 180°.

We average all instantaneous measurements of F_{11} and $-F_{12}/F_{11}$ at the wavelength of 0.67 μm and plot them with one standard deviation shown in Figure 11. Moreover, we calculate the mean values of F_{11} and $-F_{12}/F_{11}$ under various conditions of Ångström exponent (three classes: $\alpha < 0.25$, $0.25 \leq \alpha < 0.75$, and $\alpha \geq 0.75$). As seen in Figure 11(a), as dust aerosols become larger (that is, α decreases), the forward scattering ability increases more dramatically when the scattering angle is less than 20°, while the curves are not obviously different in the angles of 90~160°. In Figure 11(b), the magnitude of

degree of linear polarization decreases with the increase in particle size.

Laboratory measurements are chosen for discussions. Figure 11 shows F_{11} and $-F_{12}/F_{11}$ of a sample of “white clay” measured by the IAA Cosmic Dust Laboratory, which is an ensemble of irregular particles with constituents of illite, kaolinite, montmorillonite, and quartz. Its size distribution is a single mode with $r_{\text{eff}} = 2.6 \mu\text{m}$ and the complex refractive index is estimated to be in the range $(1.5 \sim 1.7) - i(0.00001 \sim 0.01)$ at visual wavelengths [30]. Besides we select Volten et al. [28] sample, called “average”, adding to the Figure 11 because it represents an average case of dust particles consisting of feldspar, red clay, loess, Sahara sand, Pinatubo volcanic ash, Lokon volcanic ash. In Figure 11(a), F_{11} agrees well with laboratory result despite the fact that the “average” is slight higher in the range 90 ~ 160°. Figure 11(b) shows that the shape of $-F_{12}/F_{11}$ is consistent. “White clay” is between two classes ($\alpha < 0.25$, $0.25 \leq \alpha < 0.75$), and the corresponding Ångström exponent is estimated to be ~ 2.5 . In contrast, “average” sample is in accordance with even smaller Ångström exponent ($\alpha < 0.25$).

4. Conclusions

The field observation of dust properties is still rare in desert regions of China because of difficulties in operating and maintaining precisely long-term and continuous observation in desert environment. In this paper, we provided a complete description of column dust properties at Minqin site near Hexi Corridor based on one-year measurement obtained from a ground-based polarized type of CIMEL sun-sky radiometer (CE318-DP). The study site may be attractive for various researches because of its peculiar location where both Badain Jaran Desert and Tengger Desert contribute to sources of dust aerosols.

We used the state-of-art algorithm to retrieve aerosol optical and microphysical properties, including aerosol single scattering-albedo, size distribution, complex refractive index, scattering phase function, and degree of linear polarization for incident unpolarized light (i.e., the angular distribution of the first two elements of scattering matrix). It is found that, in Minqin, an annual mean AOD was 0.22 at 0.50 μm and the effective radii of fine (0.13–0.17 μm) and coarse (2.49–3.49 μm) modes were stable at all seasons together with the appearance of a third mode of particle radius at 0.4–1.0 μm when AOD was larger than 0.6. It is noticeable that the real (1.5–1.7) and imaginary (0.0005 to 0.09) parts of complex refractive indices were higher than other studies performed in other desert regions of China, while single scattering albedo was relatively lower (~ 0.84 – 0.89) at wavelengths of 0.44, 0.67, 0.87, and 1.02 μm . This is partially due to calcite or hematite in the soil in Minqin or the influence of anthropogenic aerosols containing carbon. These dust characteristics can provide reference for different studies not only on climate change but also on environmental and ecological researches.

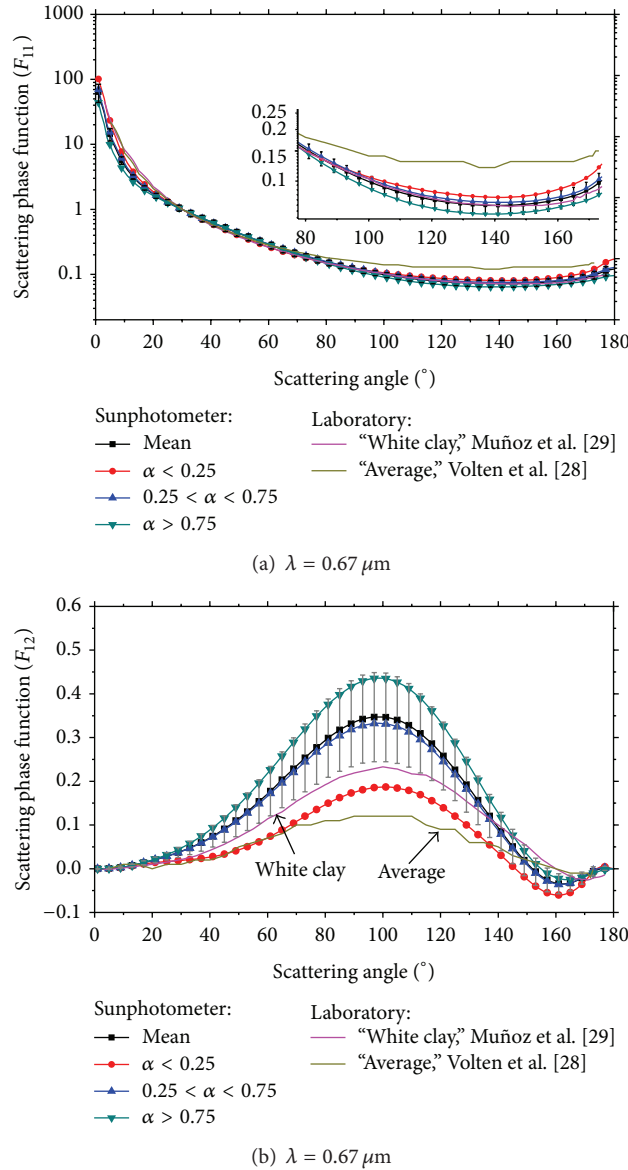


FIGURE 11: The scattering matrix of mineral dust aerosols in Minqin: (a) the scattering phase function (F_{11}) normalized to 1 at 30 degrees and (b) the degree of linear polarization for unpolarized incident light ($-F_{12}/F_{11}$).

Conflict of Interests

The authors declare that there is no conflict of interests regarding the publication of this paper.

Acknowledgments

The authors acknowledge the support of the National Basic Research Program of China (973 Program) under Grant 2010CB950800 (2010CB950801) and the National Natural Science Foundation of China (no. 41222007, no. 41301391). They are also grateful to Oleg Dubovik for providing retrieval of parameters of aerosols.

References

- [1] T. Claquin, M. Schulz, and Y. J. Balkanski, “Modeling the mineralogy of atmospheric dust sources,” *Journal of Geophysical Research: Atmospheres*, vol. 104, no. D18, pp. 22243–22256, 1999.
- [2] V. Ramanathan, P. J. Crutzen, J. T. Kiehl, and D. Rosenfeld, “Atmosphere: aerosols, climate, and the hydrological cycle,” *Science*, vol. 294, no. 5549, pp. 2119–2124, 2001.
- [3] T. Nousiainen, “Optical modeling of mineral dust particles: a review,” *Journal of Quantitative Spectroscopy and Radiative Transfer*, vol. 110, no. 14–16, pp. 1261–1279, 2009.
- [4] I. Sokolik, A. Andronova, and T. C. Johnson, “Complex refractive index of atmospheric dust aerosols,” *Atmospheric Environment—A General Topics*, vol. 27, no. 16, pp. 2495–2502, 1993.

- [5] I. N. Sokolik and O. B. Toon, "Incorporation of mineralogical composition into models of the radiative properties of mineral aerosol from UV to IR wavelengths," *Journal of Geophysical Research D: Atmospheres*, vol. 104, no. 8, pp. 9423–9444, 1999.
- [6] H. Volten, O. Munoz, J. W. Hovenier et al., "WWW scattering matrix database for small mineral particles at 441.6 and 632.8 nm," *Journal of Quantitative Spectroscopy and Radiative Transfer*, vol. 90, no. 2, pp. 191–206, 2005.
- [7] O. Muñoz, F. Moreno, D. Guirado, D. D. Dabrowska, H. Volten, and J. W. Hovenier, "The Amsterdam-Granada light scattering database," *Journal of Quantitative Spectroscopy and Radiative Transfer*, vol. 113, no. 7, pp. 565–574, 2012.
- [8] O. Dubovik, B. N. Holben, T. Lapyonok et al., "Non-spherical aerosol retrieval method employing light scattering by spheroids," *Geophysical Research Letters*, vol. 29, no. 10, pp. 541–544, 2002.
- [9] O. Dubovik, A. Sinyuk, T. Lapyonok et al., "Application of spheroid models to account for aerosol particle nonsphericity in remote sensing of desert dust," *Journal of Geophysical Research D: Atmospheres*, vol. 111, no. 11, Article ID D11208, 2006.
- [10] O. Dubovik, B. Holben, T. F. Eck et al., "Variability of absorption and optical properties of key aerosol types observed in worldwide locations," *Journal of the Atmospheric Sciences*, vol. 59, no. 3, pp. 590–608, 2002.
- [11] Z. Li, P. Goloub, L. Blarel, B. Damiri, T. Podvin, and I. Jankowiak, "Dust optical properties retrieved from ground-based polarimetric measurements," *Applied Optics*, vol. 46, no. 9, pp. 1548–1553, 2007.
- [12] T. Nakajima, G. Tonna, R. Rao, P. Boi, Y. Kaufman, and B. Holben, "Use of sky brightness measurements from ground for remote sensing of particulate polydispersions," *Applied Optics*, vol. 35, no. 15, pp. 2672–2686, 1996.
- [13] T. F. Eck, B. N. Holben, O. Dubovik et al., "Columnar aerosol optical properties at AERONET sites in central eastern Asia and aerosol transport to the tropical mid-Pacific," *Journal of Geophysical Research D: Atmospheres*, vol. 110, no. 6, Article ID D06202, 2005.
- [14] H. Che, Y. Wang, J. Sun, X. Zhang, X. Zhang, and J. Guo, "Variation of aerosol optical properties over the Taklimakan Desert in China," *Aerosol and Air Quality Research*, vol. 13, no. 2, pp. 777–785, 2013.
- [15] T. Cheng, Y. Liu, D. Lu, Y. Xu, and H. Li, "Aerosol properties and radiative forcing in Hunshan Lake desert, northern China," *Atmospheric Environment*, vol. 40, no. 12, pp. 2169–2179, 2006.
- [16] B. N. Holben, T. F. Eck, I. Slutsker et al., "AERONET—a federated instrument network and data archive for aerosol characterization," *Remote Sensing of Environment*, vol. 66, no. 1, pp. 1–16, 1998.
- [17] Z. Li, P. Goloub, O. Dubovik et al., "Improvements for ground-based remote sensing of atmospheric aerosol properties by additional polarimetric measurements," *Journal of Quantitative Spectroscopy and Radiative Transfer*, vol. 110, no. 17, pp. 1954–1961, 2009.
- [18] Z. Li, L. Blarel, T. Podvin, P. Goloub, J. Buis, and J. Morel, "Transferring the calibration of direct solar irradiance to diffuse-sky radiance measurements for CIMEL Sun-sky radiometers," *Applied Optics*, vol. 47, no. 10, pp. 1368–1377, 2008.
- [19] F. Zhao, Y. Tan, Z. Li, and C. Gai, "The effect and correction of aerosol forward scattering on retrieval of aerosol optical depth from Sun photometer measurements," *Geophysical Research Letters*, vol. 39, no. 14, Article ID L14805, 2012.
- [20] M. Hess, P. Koepke, and I. Schult, "Optical properties of aerosols and clouds: the software package OPAC," *Bulletin of the American Meteorological Society*, vol. 79, no. 5, pp. 831–844, 1998.
- [21] W. Wmo, "Radiation commission of IAMAP meeting of experts on aerosol and their climatic effects," Tech. Rep. WCP55, World Meteorological Organization, Williamsburg, Va, USA, 1983.
- [22] P. Koepke, M. Hess, I. Schult, and E. P. Shettle, *Global Aerosol Data Set*, Max-Planck-Institut für Meteorologie, Hamburg, Germany, 1997.
- [23] J. Otterman, R. S. Fraser, and O. P. Bahethi, "Characterization of tropospheric desert aerosols at solar wavelengths by multispectral radiometry from Landsat," *Journal of Geophysical Research: Oceans (1978–2012)*, vol. 87, no. C2, pp. 1270–1278, 1982.
- [24] Z. Levin, J. H. Joseph, and Y. Mekler, "Properties of Sharav (Khamsin) dust: comparison of optical and direct sampling data," *Journal of the Atmospheric Sciences*, vol. 37, no. 4, pp. 882–891, 1980.
- [25] S. Nickovic, A. Vukovic, M. Vujadinovic, V. Djurdjevic, and G. Pejanovic, "Technical note: high-resolution mineralogical database of dust-productive soils for atmospheric dust modeling," *Atmospheric Chemistry and Physics*, vol. 12, no. 2, pp. 845–855, 2012.
- [26] J. Xiao-peng and W. Hai-bing, "Analysis of atmospheric dust composition and its influence in Hexi Corridor, Gansu," *Journal of Desert Research*, vol. 29, no. 1, pp. 156–161, 2009.
- [27] D. D. Dabrowska, O. Muñoz, F. Moreno, T. Nousiainen, E. Zubko, and A. C. Marra, "Experimental and simulated scattering matrices of small calcite particles at 647 nm," *Journal of Quantitative Spectroscopy and Radiative Transfer*, vol. 124, pp. 62–78, 2013.
- [28] H. Volten, O. Muñoz, E. Rol et al., "Scattering matrices of mineral aerosol particles at 441.6 nm and 632.8 nm," *Journal of Geophysical Research D: Atmospheres*, vol. 106, no. 15, pp. 17375–17401, 2001.
- [29] O. Muñoz, H. Volten, J. W. Hovenier et al., "Experimental and computational study of light scattering by irregular particles with extreme refractive indices: hematite and rutile," *Astronomy and Astrophysics*, vol. 446, no. 2, pp. 525–535, 2006.
- [30] O. Muñoz, F. Moreno, D. Guirado, J. L. Ramos, H. Volten, and J. W. Hovenier, "The IAA cosmic dust laboratory: experimental scattering matrices of clay particles," *Icarus*, vol. 211, no. 1, pp. 894–900, 2011.
- [31] D. B. Curtis, B. Meland, M. Aycibin et al., "A laboratory investigation of light scattering from representative components of mineral dust aerosol at a wavelength of 550 nm," *Journal of Geophysical Research D: Atmospheres*, vol. 113, no. 8, Article ID D08210, 2008.